EPFL

Thèse n° 9656

FIB-Fabrication of Resonating Cantilevers to Explore Symmetry-Breaking in Quantum Materials

Présentée le 9 juin 2023

Faculté des sciences et techniques de l'ingénieur
Laboratoire des Matériaux Quantiques
Programme doctoral en science et génie des matériaux

pour l'obtention du grade de Docteur ès Sciences

par

Amelia Emily-Kay ESTRY

Acceptée sur proposition du jury

Prof. V. Michaud, présidente du jury
Prof. Ph. J. W. Moll, Prof. H.-A. Klok, directeurs de thèse
Prof. B. Ramshaw, rapporteur
Dr G. Hlawacek, rapporteur
Prof. N. Marzari, rapporteur

École polytechnique fédérale de Lausanne

2023

Acknowledgements

This thesis is possible thanks to the help and support of many people over the last few years. First and foremost, I would like to express my sincere gratitude to Philip Moll, in particular for his encouragement and advice. I have learned a great deal from Philip's innovative perspective that has helped me both improve my scientific understanding as well as develop soft skills such as organizing, time management, and presenting ideas. I have truly enjoyed working in his group and am happy to have shared the joys of FIB-fabrication. I would also like to thank Carsten Putzke for all that he has taught me about taking a careful and purposeful approach to research and also for teaching me crucial life skills. Carsten and Philip have continuously encouraged this research, challenging me to think critically and methodically.

Many thanks to all of the collaborators who have helped, on this project and on others. High-quality crystals were fabricated by Dariusz Gawryluk, Marisa Medarde, Nikolai Zhigadlo, and Stephen Hayden. I appreciate the discussions I had with Dariusz and Marisa, as well as fruitful discussions with Michele Kotiuga and Nicola Marzari. I also sincerely enjoyed collaborating with Evgeny Mikheev and David Goldhaber-Gordon.

Especial thanks goes to both the QMAT and MQM research teams. Joshua Straquadine was helpful in setting up a table-top interferometer. I really appreciate the discussions and advice of Toni Helm, Kim Modic, Tino Zimmerling, Kent Shirer, and Chunyu Guo. Thanks also to Mathieu Padlewski, Jonas Diaz, Xiangwei Huang, Hung-wei Li, Maya Bachmann, Guillaume Beaulieu, and Sofiya Konyzheva for sharing in this experience. I have truly appreciated their friendship. I also am very grateful to have had the chance to work with Ferdinand Posva and Anna Duvakina.

Finally, I would also like to express gratitude to everyone who has encouraged me throughout the years. Many thanks to my previous research groups, for motivating me to start this project. I really appreciate the support of all of my friends, in particular my best friends: Lindsay Premo and Linsey Rodenbach. Linsey has shared the PhD experience with me and Lindsay proofread this thesis. Last but not least, a heartfelt thanks to my wonderful fiancé and family for all of their support.

Abstract

Scientific progress and technological advancements on novel materials are often deterred by limitations on size and quality of samples. Materials with electronic phenomena highly attractive for applications, and presenting many open scientific questions, are often challenging to grow. Synthesizing large, high-quality samples can entail decades of research and funding. Surpassing these barriers for technological applications, or for explorations of microscopic samples, necessitates new approaches. One inherent property, particularly important for applications and fundamental science questions, is elasticity. Knowledge of a material's response to stress is critical to all forms of engineering. Furthermore, the elastic tensor is defined by attractive bonds between ions, and encodes the symmetries of the material. Phase transitions—whether magnetic, structural or electronic—are characterized by a symmetry breaking, which are reflected by changes in the elasticity. As such, elasticity measurements yield valuable insight into the symmetries of the electronic state. Unfortunately, elasticity experiments have thusfar been restricted to materials that can be grown into large, clean samples.

The goal of this thesis is to bridge this gap, by developing a micro-fabrication process to construct resonators directly from novel materials. This new technique uses a Focused Ion Beam (FIB) which can selectively etch or deposit with sub-μm precision. A process was developed to carve samples with length scales as small as ~ 10 μm into cantilevers. Because the mechanical resonance modes are dependent on geometry and elastic properties, by precisely controlling cantilever geometry, elasticity can be explored via measurements of resonance frequencies. One promising application is the study of quantum materials, in which electronic correlations give rise to remarkable phenomena such as high-temperature (high-T_c) superconductivity (SC). An experimental set-up was designed to study resonance modes of FIB-fabricated cantilevers as a function of temperature and magnetic field, such that the elastic tensor—and by corollary, the symmetry of the electronic correlations—can be probed across different phases. Measurements were conducted to explore complex electronic phenomena in the rare-earth nickelates, and the high-T_c, unconventional superconductors of the cuprates and iron pnictides.

Fundamentally, this project is intended to accelerate the transition process needed to implement novel electronic materials into research and technology. The decades of materials

research ordinarily spent on optimizing growth processes can be circumvented, focusing promptly on the microparticles available. Thus, elasticity can be probed on the sub-μm scale relevant for implementation into MEMS. The most fundamental application of this technique is elasticity studies on size and quality-limited samples. This technique enables the fabrication of cantilevers for resonance studies even for chemically complex samples when size or quality is severely restricted. For large samples, microscale elasticity can be vastly different than macroscale elasticity due to multiple-domains, defects, or compositional or strain gradients. Incorporating these materials into devices relies on knowledge of their microscale elasticity. This technique is flexible, and can be used not only for a wide range of materials, but also to create complex, 3D structures to explore functionality of different geometries. Furthermore, with some effort, FIB fabrication can be automized, opening up the possibility to incorporate quantum cantilevers directly into MEMS. To realize these goals, a robust workflow for FIB-fabrication of cantilevers was developed. FIB-fabrication compared favorably to standard lithographic techniques with FIBed Si cantilevers showing deviations from literature values on MEMS Si as low as 8%. The relative frequency resolution is superb. This is particularly significant in the study of electron states in quantum materials, in which one is most interested in the modification of the elastic components at phase transitions.

Using this technique on three correlated electronic materials, the following discoveries were made: in SmFeAs(O,F) — a family that has one of the highest T_c within the iron-based superconductors — a giant anomalous softening in the elastic shear component was observed. This softening has been reported in the lower-T_c Co and K-doped $BaFe_2As_2$ and is associated with an electronic nematic phase, which involves the breaking of rotational symmetry via electronic interactions [1]. This state occurs in close proximity to SC, raising the question of the interplay with SC and whether or not they share a common origin. These measurements are the first observations of nematicity in this high-T_c family; although remarkably, the energy of the electronic-lattice coupling is notably weaker than in the lower-T_c families. Another group of high-T_c superconductors are the cuprates. A FIB-fabricated cantilever of the cuprate, $La_{2-x}Sr_xCuO_4$, showed a large softening of 8% in Young's modulus at a structural transition and a .09% reduction at T_c. Finally, in the rare-earth nickelate, $YNiO_3$, a sharp discontinuity of Young's modulus of .2% was observed at an antiferromagnetic phase transition. These results show the potential of this novel technique in expounding upon the materials that can be studied via mechanical resonance measurements to yield further insight into intricate electronic correlations, particularly for materials such as SmFeAs(O,F) and $YNiO_3$ for which no single crystals exist with length scales above 100μm.

Key words: Focused Ion Beam, quantum materials, unconventional superconductivity, electronic nematicity, cuprates, pnictides, nickelates, elasticity, ultrasound, correlated electronic systems

Zusammenfassung

Wissenschaftlicher und technologischer Fortschritt bei neuartigen Materialien wird oft zurückgehalten durch Einschränkungen in Bezug auf Größe und Qualität der Proben. Materialien mit elektronischen Phänomenen, welche für Anwendungen sehr attraktiv sind und viele offene wissenschaftliche Fragen aufwerfen, sind oft schwer zu synthetisieren. Die Synthese großer, hochwertiger Proben kann jahrzehntelange Forschung und Finanzierung erfordern. Um diese Hindernisse für technologische Anwendungen oder die Erforschung mikroskopischer Proben überwinden zu können, sind neue Ansätze erforderlich. Eine inhärente Eigenschaft, welche besonders wichtig ist für den Anwendungsbereich, sowie grundlagenwissenschaftliche Fragestellungen, ist die Elastizität. Das Wissen um die Reaktion eines Materials auf Belastung ist für alle Formen der Ingenieursarbeit von entscheidender Bedeutung. Darüber hinaus wird der Elastizitätstensor durch attraktive Bindungen zwischen Ionen charakterisiert und kodiert die Symmetrien des Materials. Phasenübergänge, ob magnetisch, strukturell oder elektronisch, zeichnen sich durch eine Symmetriebrechung aus, die sich in Änderungen der Elastizität widerspiegelt. Somit liefern Elastizitätsmessungen wertvolle Einblicke in die Symmetrien des elektronischen Zustands. Leider waren Elastizitätsexperimente bisher auf Materialien beschränkt, die zu großen, sauberen Proben synthetisiert werden können.

Das Ziel dieser Dissertation ist es, diese Lücke zu schließen, indem ein Mikrofabrikationsprozess entwickelt wird, um Resonatoren direkt aus neuartigen Materialien zu konstruieren. Diese neue Technik verwendet einen fokussierten Ionenstrahl (Focused Ion Beam, FIB), welcher selektiv mit sub-μm Präzision ätzen und deponieren kann. Es wurde ein Verfahren entwickelt, um Proben mit einem Längenmaß von nur ~ $10\mu m$ in Ausleger einzuschnitzen. Da die mechanischen Schwingungsmoden von der Geometrie und den elastischen Eigenschaften abhängen, kann die Elastizität durch die genaue Kontrolle der Ausleger-Geometrie mit außerordentlicher Sensitivität untersucht werden, mittels Messen der Resonanzfrequenzen. Eine vielversprechende Anwendung ist die Untersuchung von Quantenmaterialien, bei denen elektronische Korrelationen zu bemerkenswerten Phänomenen wie Hochtemperatur-Supraleitung (hoch-T_c superconductor, SC) führen. Ein experimenteller Aufbau wurde entwickelt, um Schwingungsmoden von FIB-hergestellten Auslegern als Funktion von Temperatur und Magnetfeld zu untersuchen, sodass der Elastizitätstensor und damit die Symmetrie der elektronischen Korrelationen über verschiedene Phasen hinweg untersucht werden kann. Es wurden Messungen

durchgeführt, um komplexe elektronische Phänomene in seltenen Nickelaten und unkonventionellen Hoch-T_c-Supraleitern der Cuprate und Eisen-Pniktide zu untersuchen.

Grundlegend soll dieses Projekt den Übergangsprozess beschleunigen, der erforderlich ist, um neuartige elektronische Materialien in Forschung und Technologie zu implementieren. Die jahrzehntelange Materialforschung, die normalerweise für die Optimierung von Herstellungsprozessen aufgewendet wird, kann umgangen werden, indem man sich direkt auf die verfügbaren Mikropartikel konzentriert. Somit kann die Elastizität auf der Sub-μm-Skala untersucht werden, die für die Implementierung in MEMS relevant ist. Die grundlegendste Anwendung dieser Technik sind Elastizitätsstudien an größen- und qualitätslimitierten Proben. Diese Technik ermöglicht die Herstellung von Auslegern für Resonanzuntersuchungen selbst für chemisch komplexe Proben, wenn Größe oder Qualität stark eingeschränkt sind. Bei großen Proben kann sich die Elastizität im Mikromaßstab aufgrund mehrerer Domänen, Defekte oder Zusammensetzungs- oder Dehnungsgradienten stark von der Elastizität im Makromaßstab unterscheiden. Der Einbau dieser Materialien in Geräte beruht auf der Kenntnis ihrer Elastizität im Mikrobereich. Diese Technik ist flexibel und kann nicht nur für eine Vielzahl von Materialien verwendet werden, sondern auch zum Erstellen komplexer 3D-Strukturen, um die Funktionalität verschiedener Geometrien zu untersuchen. Darüber hinaus kann, mit etwas Aufwand, die Herstellung von FIB-Auslegern automatisiert werden, was die Möglichkeit eröffnet, Quantenausleger direkt in MEMS einzubauen. Um diese Ziele zu erreichen, wurde ein robuster Arbeitsablauf für die FIB-Herstellung von Auslegern entwickelt. Die FIB-Herstellung zeigte sich im Vergleich zu standardmäßigen lithografischen Techniken bei FIB-Si-Auslegern günstig, wobei Abweichungen von literaturberichteten Werten bei MEMS-Si von nur 8% auftraten. Die relative Frequenzauflösung ist hervorragend. Dies ist besonders bedeutsam bei der Untersuchung von Elektronenzuständen in Quantenmaterialien, bei denen man vor allem an der Modifikation der elastischen Komponenten bei Phasenübergängen interessiert ist.

Unter Anwendung dieser Technik wurden bei drei korrelierten elektronischen Materialien die folgenden Entdeckungen gemacht: In SmFeAs(O,F), einer Familie, die eine der höchsten T_c innerhalb der Supraleiter auf Eisenbasis hat, wurde eine enorme anomale Erweichung in der elastischen Scherkomponente beobachtet. Diese Erweichung wurde in Co- und K-substituierten $BaFe_2As_2$ mit niedrigerem Tc berichtet und ist mit einer elektronischen nematischen Phase verbunden, die das Brechen der Rotationssymmetrie durch elektronische Wechselwirkungen beinhaltet[1]. Dieser Zustand tritt in unmittelbarer Nähe zu SC auf, was die Frage nach dem Zusammenspiel mit SC aufwirft und ob sie einen gemeinsamen Ursprung haben oder nicht. Diese Messungen sind die ersten Beobachtungen von Nematizität in dieser Hoch-T_c-Familie. Bemerkenswert ist jedoch, dass die Energie der Elektronengitterkopplung deutlich schwächer ist als in den Familien mit niedrigerem Tc. Eine weitere Gruppe von Hoch-T_c-Supraleitern sind die Cuprate. Ein FIB-hergestellter Ausleger aus Cuprat, $La_{2-x}Sr_xCuO_4$, zeigte eine starke Erweichung von 8% des Youngschen Moduls bei einem strukturellen Übergang und eine Verringerung von 0,09 % bei T_c. Schließlich wurde im Seltenerd-Nickelat, $YniO_3$, eine scharfe Diskontinuität des Youngschen Moduls von 0,2% bei einem antiferromagnetischen Phasen-

übergang beobachtet. Diese Ergebnisse zeigen das Potenzial dieser neuartigen Technik zur Untersuchung von Materialien, die durch mechanische Resonanzmessungen geprüft werden können, um weitere Einblicke in komplizierte elektronische Korrelationen zu gewinnen, insbesondere für Materialien wie SmFeAs(O,F) und $YniO_3$, für die keine Einkristalle existieren mit Längenmaßen über $100\mu m$.

Stichwörter: Fokussierter Ionenstrahl, Quantenmaterialien, unkonventionelle Supraleitung, elektronische Nematizität, Cuprate, Pnictide, Nickelate, Elastizität

Contents

List of Figures

List of Tables

1 Introduction

After the discovery of a new material, available samples will often be either small, poor-quality single crystals, or polycrystals in which domains and domain walls can produce properties that deviate greatly from the underlying material physics. Developing processes for growing large single crystals can take decades of work [2]. Researching early samples to understand their complex properties and discerning in which materials to invest this time and funding is therefore a critical first step. One example of materials in which progress has been slowed by limited samples are unconventional superconductors. Their interesting electronic properties are highly desirable for technological applications but are coupled with many unanswered questions. In the 1950s, the zero-resistance ground state of the known superconductors was explained by Bardeen-Cooper-Schrieffer (BCS) theory as a coupling of electrons mediated by phonon-interactions [3]. Since then, many superconductors have been discovered in which the attractive force mediating electron coupling cannot be explained solely by phonon-interactions [4–6]. What makes these so-called "unconventional superconductors" especially remarkable is that many of them have transition temperatures, T_c, far above their conventional counterparts [7]. These high-temperature superconductors can be used for applications such as MRI magnets [8, 9], high-powered research magnets [10], and power cables [11]. Decoding the electronic correlations that give rise to high-T_c superconductivity is crucial for the eventual goal of even higher temperature superconductors that can be applied to further energy-saving projects.

A notable group are the high-T_c unconventional iron-based superconductors (FeSC). The early years following the 2008 breakthrough announcement of their superconductivity exploded with new discoveries [12, 13]. The FeSC can be considered in "families" which consist of an undoped "parent" compound that is usually not superconducting. Upon doping to add electrons, holes, or isovalent doping which applies chemical pressure, superconductivity emerges. While excitement in the FeSC was tangible, scientists interested in REFeAs(O,F) (RE1111, RE = rare-earth), faced a stumbling block. The RE = Gd, Sm, Nd families have the highest T_c ($T_c > 50$ K) of bulk crystals in the FeSC, but single crystals are extraordinarily difficult to fabricate, with an end result that is 100 μm in the longest dimension, at best [14–18].

While it is possible to create long cables of the RE1111 that could be useful for industrial applications [19], the polycrystalline nature of these cables precludes the study of the physics, which requires pure single crystals. The microscopic sample sizes of the existing single crystals deter most measurement methods.

Focus turned instead to the families in which large crystals could be grown. Doping $BaFe_2As_2$ produced a slightly lower T_c (max $T_c \approx 38$ K) [20], but the compound could be readily tuned with different dopants and the sample sizes made them workable. Research on these families developed much of the modern understanding of the FeSC which show a rich phase diagram including antiferromagnetic ordering and a quantum critical point [21]. At high temperatures, the FeSC are tetragonal, consisting of layers of Fe and a chalcogen or pnictogen stacked along the c-axis. At lower temperatures, preceding superconductivity, is a phase characterized by a large electronic anisotropy, differentiating the a and b axes [22–24]. This breaking of the rotational symmetry of the lattice by electronic interactions was coined "electronic nematicity", borrowing from the field of liquid crystals in which "nematicity" refers to a broken rotational symmetry while translational symmetry is preserved [25]. Resonant Ultrasound Spectroscopy (RUS), Pulse-Echo (PE) and three-point bending measurements (experiments which probe the elastic properties) revealed a giant anomalous softening of the elastic shear component anticipating the nematic transition [26–29]. This softening of the shear component is a result of nematic fluctuations and is indicative of a large nematic susceptibility. The existence of nematicity and its juxtaposition with superconductivity naturally suggests a competitive or collaborative correlation. This relationship can be explored by studying the strength of nematic fluctuations in FeSC with higher-T_c, such as Sm1111.

While the majority of the community targeted the large, lower-T_c FeSC, stubborn researchers resolved to explore the higher-T_c, microscopic samples of the RE1111 families. A new approach was taken: one that used a Focused Ion Beam (FIB) to sculpt electrical devices. The capacity of the FIB to locally etch away material makes it possible to carve the device to define the precise current path. The second main capability of the FIB, the ability to locally deposit material, could be used to establish the electrical contacts to the device [30–32]. Resistivity studies of microscopic crystals finally became feasible, greatly expanding the number of novel materials that could be studied. Even in samples for which large, high-quality single crystals exist, the abilities to precisely control the geometry of the device and to explore size-effects were compelling [33]. In the decade that followed, FIB-fabrication of quantum materials grew in popularity, and research expanded from the FeSC to include other unconventional superconductors [34], topological materials [35, 36], heavy fermions [37–39], and beyond [40–42]. Fabrication techniques improved as well; devices can be made strain-free [43] or with more complicated 3D geometries [44]. Yet these efforts have primarily focused on transport measurements which, however insightful, can only yield so much information about the electronic correlations. Questions such as the possible existence of electronic nematicity in Sm1111 remained unanswered. Could FIB-fabrication be used to design samples for measurements that probe the nature and symmetries of the electronic state?

This question begins the work of this thesis, which aims to establish a novel technique for elasticity measurements of microscopic samples. A key step to understanding strongly correlated states is to determine the broken symmetries —- to which the elastic tensor is exquisitely sensitive. In addition to the aforementioned nematic susceptibility measurements, elasticity techniques such PE and RUS have shown strong success in discerning complex states by decoding ordering parameters [45, 46], providing evidence for possible subtle phase transitions [47], and understanding unconventional superconductivity [48]. These techniques require high-quality macroscopic crystals. PE, for example, measures the sound velocity by recording the time taken for a vibrational wave packet to travel through a sample, necessitating that the sample is much longer than the packet [49]. In RUS, the sample is carefully balanced between two piezoelectric transducers. The bottom transducer is used to mechanically excite the sample across a range of frequencies while the top transducer converts the body's natural motion to a measurable voltage difference. When the excitation frequency equals one of the natural resonance frequencies, the response of the body is amplified. Thus, by recording the measured voltage as a function of drive frequency, the resonance spectrum can be obtained [49, 50]. Mechanical resonance modes of an object are dependent on the elastic tensor and on the geometry of the body (i.e. the boundary conditions). Extracting the elastic values from the resonance frequencies therefore requires precise knowledge of the sample geometry. Furthermore, for the sample to behave as a free resonator (with no fixed boundary conditions), the sample must be lightly balanced between the two transducers. These requirements are challenging and the risk of losing a microscopic sample is extremely high.

The alternative approach developed here is to use a FIB to fabricate cantilevers directly from single crystals. A piezoelectric transducer can be used to mechanically excite the FIB-fabricated cantilevers, while the motion is detected with an optical interferometer to obtain the resonance spectrum. With the FIB, the cantilever geometry can be precisely shaped, and FIB deposition can be used to weld the cantilever onto the sample chip, thus fixing the boundary conditions. This technique can therefore be seen as a variation on RUS, in which sample geometry is controlled by FIB processing. The use of the FIB makes it possible to explore elastic properties even in previously inaccessible microscopic samples. Fig 1.1 shows Scanning Electron Microscope (SEM) images of microscopic single crystals and FIB-fabricated cantilevers. (a) and (b) show SmFeAsO, the parent compound in Sm1111. The samples pictured in (c) and (d) are the rare-earth perovskite nickelate, $YNiO_3$, which, while not superconducting, is predicted to have ground-state coupled electric and magnetic ordering [51]. Both Sm1111 and the rare-earth nickelates require an intensive high-pressure growth method resulting in small single crystals. Fig 1.1 (a) and (c) are exemplary of the largest crystals currently available. These materials are very different electrically and chemically, but the FIB-cantilever fabrication process is flexible for a wide range of materials. As FIB-fabricated cantilevers, the elastic properties of both are now accessible. Especially interesting are the results demonstrating electronic nematicity in Sm1111.

This thesis is written to provide the necessary information such that the interested reader can reproduce or adapt this technique. A background discussion on elasticity, with particular

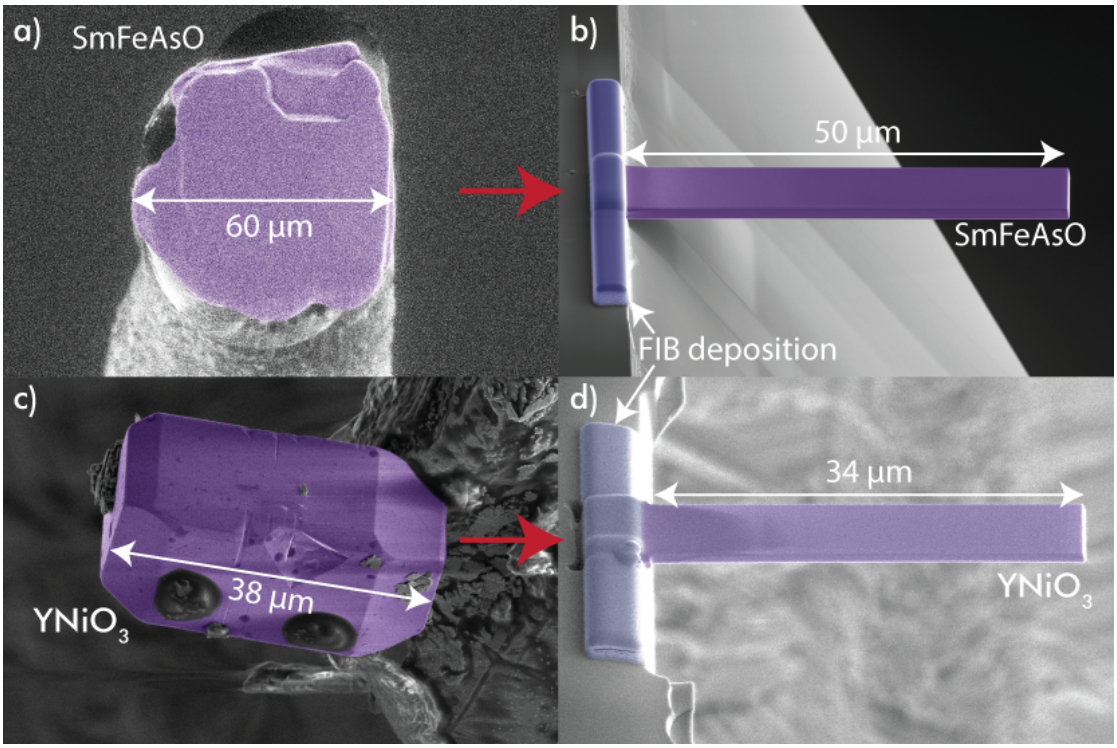

Figure 1.1: FIB cantilever fabrication enables the study of elastic properties even when samples are microscopically small. (a) FIB image of a single crystal of SmFeAsO, the parent compound of an FeSC. (b) SEM image of a FIB-fabricated SmFeAsO cantilever from a crystal similar to the one pictured in (a). (c) SEM image of a single crystal of a perovskite nickelate, $YNiO_3$ and (d) a cantilever fabricated from a similar crystal. Throughout this thesis, color has been added to show the sample in purple and FIB deposits in blue.

focus on anisotropic elasticity, cantilever beams, and elastic behavior across a phase transition, is provided in Ch 2. Simulations for a special case in which a microscale cantilever is made up of a small number of finite domains are also presented.

The FIB is a complex instrument, and the user should have a strong understanding of the etching and deposition processes, with knowledge of how the ion beam interacts with the sample in both uses. For this reason, the background explanation describing the functionality and working principles of the FIB has been allocated its own chapter (Ch 3). Parameters for patterning are discussed in depth, while highlighting possible failure mechanisms such that these can be avoided. Additionally, FIB induced depositions (FIBID) are materials with a unique microstructure. Knowledge of the elastic properties of FIBID could improve the accuracy of the technique developed here, as well as have potential uses for other FIB techniques. A process for growing FIBID cantilevers for elasticity measurements is outlined at the end of Ch 3. Ch 4 then describes the complete process flow for the FIB fabrication of cantilevers from both macroscopic and microscopic samples.

Once a cantilever has been fabricated, the symmetries of correlated electronic states can be explored by studying the resonance frequencies across phase transitions. Conducting the optical measurements down to the cryogenic temperatures at which many interesting phenomena arise required the design and construction of new measurement probe. With this micro-resonator probe, a cantilever's resonance frequencies can be tracked down to low temperatures (2K) and in high magnetic fields (up to 16T). The experimental set-up, including the micro-resonator probe and interferometric read-out, is presented in Ch 5. Discussions of experimental challenges that arose and their solutions are also provided.

In Ch 6, the fabrication method and experimental set-up is tested first on a silicon, such that the measured elasticity can be compared to the values reported in literature. This enables an accurate assessment of the capabilities and limitations of the technique. A cantilever of SmFeAsO is then measured as a function of temperature, showing a discontinuity of the resonance frequency at the phase transition. This illustrates the potential of the technique to study phase transitions in quantum materials.

The last three main chapters are dedicated to scientific explorations in three categories of materials: FeSC, high-T_c cuprates, and the rare-earth perovskite nickelates. The question of nematicity in Sm1111 is finally addressed in Ch 7. Cantilevers of SmFeAsO oriented such that the Young's modulus is dominated by the shear component show a large anomolous softening by 70%. Upon doping with fluorine, this softening is greatly reduced. These results show clear evidence of strong nematic fluctuations.

In Ch 8, cantilevers of the cuprate superconductors $La_{2-x}Sr_xCuO_4$ (LSCO) and $Tl_2Ba_2CuO_{6+x}$ (Tl2201) were fabricated. Temperature scans of LSCO show both the structural and superconducting phase transition.

In $YNiO_3$ (Ch 9), cantilevers can be annealed by laser heating, leading to a stark increase in the

resistivity, a change in the optical properties, and an increase in the stiffness by ≈ 1%. This phenomenon is attributed to oxygen dissociation and has been previously observed in thin films of $SmNiO_3$, $NdNiO_3$ and $LaNiO_3$ [52].

Ch 10 concludes with an outlook of the potential of the technique and the possibilities moving forward.

2 Theory of Elasticity

Elasticity, or the response of a body to external strain, is a fundamental property of materials. Knowledge of how an object will deform is integral to all forms of materials engineering, be it musical instruments, microscale chips or large-scale construction projects. Furthermore, elasticity measurements, such as ultrasound techniques, are often used as highly sensitive, non-destructive imaging methods that can, for example, image the human body, study the planet through seismic waves or detect defects in aircraft components [53]. Within the domain of quantum materials, elastic properties are particularly fascinating because they depend on the electronic correlations and encode the physical symmetries. A crystalline lattice of ions can be stretched and distorted, but they are bound together by virtue of their electronic interactions, which act as restoring spring forces. A change in the electronic nature, such as a phase transition from a normal metal to a superconductor, or the ordering of spins in a ferromagnet, must be accompanied by a corresponding change in the elasticity. This is due to the fact that the elastic tensor is a thermodynamic quantity.

In physics, thermodynamic quantities are particularly sought-after because of their capacity to discern phase transitions. A phase transition is usually characterized by the breaking of a symmetry between a high-temperature, symmetric phase and a low temperature, less-symmetric phase. Most transitions can be categorized as either first- or second-order (also called a continuous phase transition) [54, 55]. A first-order phase transition (such as the melting of a solid to a liquid) is distinguished by a discontinuity in the first-derivative of the free energy, e.g. in the entropy or in volume. In a second-order transition, the anomaly occurs in the second-derivative, e.g. in specific heat. Examples of second-order transitions include superconductivity and magnetic transitions. Anomalies in thermodynamic quantities can thus be used to identify both the existence of a symmetry breaking as well as the order of the transition. For example, in liquid helium, the specific heat shows a discontinuity at the transition between normal and superfluid helium [56]. These measurements distinguished superfluidity as a separate phase from normal liquid helium and showed that the transition is of the second-order.

The elastic moduli are second derivatives of the free-energy with respect to the strain, making

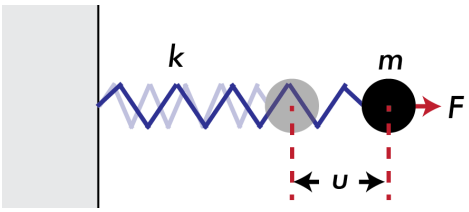

Figure 2.1: The classical example of a mass, m, connected to a spring with spring constant, k, in one dimension. An applied force, F, can be related to the displacement of the mass, u, by Hooke's law.

them sensitive especially to the second-order phase transitions. Furthermore, these moduli are particularly enticing because, unlike specific heat, the underlying symmetries of the material are inherently encoded in the elastic tensor. The symmetry broken in the phase transition can be identified via discontinuities that are present in the relevant elastic components.

2.1 Anisotropic Elasticity

1D Elasticity

A crystal is a three-dimensional lattice of atoms connected to each other by electronic interactions that act as "springs". Elastic properties of the crystal will depend on the orientation with respect to the lattice — i.e. the elasticity is anisotropic (Fig 2.2). Before considering anisotropic elasticity, it is helpful to first remember the classic example of a mass on a spring in one-dimension (Fig 2.1). Hooke's law for the spring is:

$$F_{spring} = -ku \tag{2.1}$$

$$m\ddot{u} = -ku \tag{2.2}$$

where F_{spring} is the spring force, k is the spring constant and $u = x_{final} - x_{initial}$ is the displacement of the mass. The energy stored in the spring is:

$$E = \frac{1}{2}ku^2 \tag{2.3}$$

This system will have a resonance frequency

$$f_0 = \frac{\omega_0}{2\pi} = \frac{1}{2\pi}\sqrt{\frac{k}{m}} \tag{2.4}$$

In other words, the amplitude of oscillations will be greatest for an excitation frequency of $f = f_0$. If a frequency is applied at f_0 and then switched off, the spring will continue to oscillate forever. Of course in the real world this is not possible and the spring will experience a damping force $-D\dot{u}$. For a driven oscillator with force, $F_{drive}(t) = A\sin\omega t$, the full equation of motion is:

$$F_{drive}(t) = m\ddot{u} + D\dot{u} + ku \tag{2.5}$$

If the response of the spring versus drive frequency is measured, the width of the resonance is a measure of the energy loss. This can be quantified in terms of the Q-factor:

$$Q = \frac{f}{f_{FWHM}} = \frac{\sqrt{mk}}{D} \tag{2.6}$$

Where f_{FWHM} is the full-width at half maximum of the resonance peak. Thus, by measuring the resonance spectrum, the resonance frequency can be used to calculate the spring constant, k, while the Q-factor is a measure of the dissipation of the system. A 3D anisotropic material is more complicated — the spring constant k is replaced with the rank-four elastic tensor c_{ijkl} — but fundamentally the resonance frequencies are dependent on the elastic constants. By measuring the resonance spectrum, the electronic interactions along the different directions can be explored. Furthermore, the Q-factor gives insight into the energy dissipation.

2.1.1 3D Elasticity

In the 3D example, Hooke's law can be written in terms of the stress, σ, — or the external forces on the body — and the strain, ϵ, which describes the deformation of the body. Writing the strain tensor in terms of the displacements along each direction, u_i,

$$\epsilon_{ij} = \frac{1}{2}\left(\frac{\partial u_i}{\partial x_j} + \frac{\partial u_j}{\partial x_i} + \frac{\partial u_i}{\partial x_j}\frac{\partial u_j}{\partial x_i}\right) \tag{2.7}$$

Here, $i = 1,2,3$ with $x_1 = x, x_2 = y, x_3 = z$. For small deformations, the last term can be dropped:

$$\epsilon_{ij} = \frac{1}{2}\left(\frac{\partial u_i}{\partial x_j} + \frac{\partial u_j}{\partial x_i}\right) \tag{2.8}$$

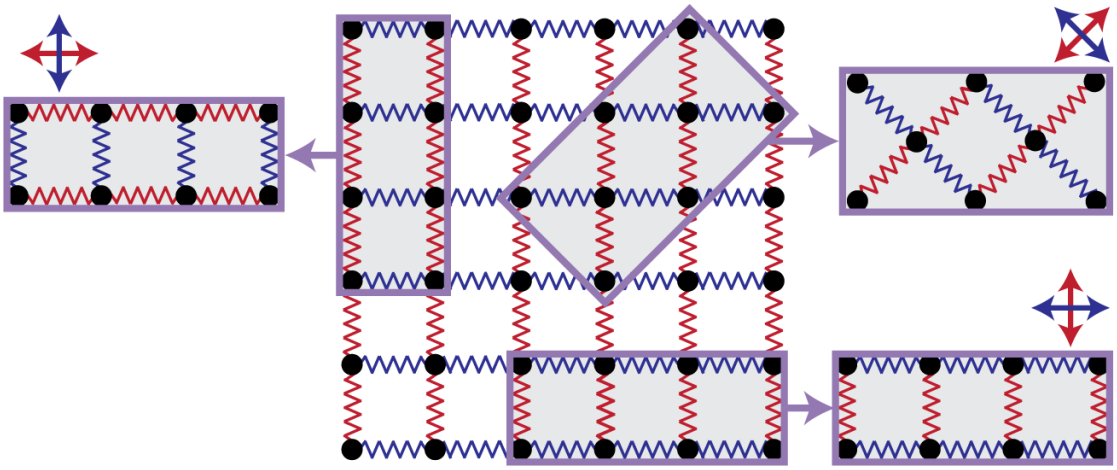

Figure 2.2: A 2D square lattice of ions (black circles) are connected by electronic interactions (red and blue springs). In this sketch, these interactions are not the same in both directions. Elastic properties are dependent on the orientation of the sample with respect to the lattice — elasticity is anisotropic.

This linear approximation is sufficient for most purposes and will be assumed from here on out. In an isotropic medium, the stress and strain tensors can be related to each other via Young's modulus, E, and Poisson's ratio, ν. For a uniaxial stress, $\sigma = \sigma_x$, Young's modulus and Poisson's ratio are

$$E = \frac{\epsilon_x}{\sigma_x} \tag{2.9}$$

$$\nu = -\frac{\epsilon_y}{\epsilon_x} = -\frac{\epsilon_z}{\epsilon_x} \tag{2.10}$$

In crystalline materials, this relationship between stress and strain must be described using the rank-four elastic modulus tensor c_{ijkl}. Hooke's law for anisotropic materials is [50, 57, 58]:

$$\sigma_{ij} = \frac{\partial F}{\partial \epsilon_{ij}} = c_{ijkl}\epsilon_{kl} \tag{2.11}$$

where $F = U - TS$ is the Helmholtz free energy. The energy of the classical 1D spring (Eqn 2.3) can be generalized for the free energy of the crystal:

$$F = \frac{1}{2} c_{ijkl}\epsilon_{ij}\epsilon_{kl} \tag{2.12}$$

where Einstein's summation notation is used. Furthermore, from Eqn 2.11:

$$c_{ijkl} = \frac{\partial^2 F}{\partial \epsilon_{ij} \partial \epsilon_{kl}} \tag{2.13}$$

The 81 components of the elastic tensor can be simplified due to symmetry. From Eqn 2.13, it can be seen that $c_{ijkl} = c_{klij}$, reducing the 81 components to 66 independent values. The symmetry of the stress and strain tensors, $\sigma_{ij} = \sigma_{ji}$ and $\epsilon_{ij} = \epsilon_{ji}$, further reduce $c_{ijkl} = c_{jikl} = c_{ijlk} = c_{jilk}$ to only 21 independent elastic moduli. Depending on the symmetries of the crystal structure, the elastic tensor may be additionally simplified. For example, the materials examined throughout this thesis have cubic, tetragonal, orthorhombic and monoclinic structures. The elastic tensor for these symmetries can be reduced to 3, 6, 9, and 13 independent elastic components, respectively [50]. The elastic tensor thus explicitly encodes the symmetry of the sample and any changes therein will be reflected in changes in the tensorial components.

2.1.2 Voigt Notation

Because symmetry relations have reduced the quantity of independent elastic components, the elastic moduli can be re-written as a matrix rather than a rank-four tensor. One of the most popular alternative notations, Voigt notation, reduces the indices as shown below:

$$11 \rightarrow 1,\ 22 \rightarrow 2,\ 33 \rightarrow 3,\ 23 \rightarrow 4,\ 31 \rightarrow 5,\ 12 \rightarrow 6 \tag{2.14}$$

where the digits on the left of the arrows are the tensorial indices and the digits on the right of the arrows are Voigt's notation. The stress and strain tensors are rewritten as vectors and Hooke's law (Eqn 2.11) becomes:

$$\sigma_i = c_{ij} \epsilon_j \tag{2.15}$$

Or, in matrix form:

$$\begin{pmatrix}\sigma_1\\ \sigma_2\\ \sigma_3\\ \sigma_4\\ \sigma_5\\ \sigma_6\end{pmatrix} = \begin{bmatrix} c_{11} & c_{12} & c_{13} & c_{14} & c_{15} & c_{16} \\ & c_{22} & c_{23} & c_{24} & c_{25} & c_{26} \\ & & c_{33} & c_{34} & c_{35} & c_{36} \\ & & & c_{44} & c_{45} & c_{46} \\ & symm & & & c_{55} & c_{56} \\ & & & & & c_{66} \end{bmatrix} \begin{pmatrix}\epsilon_1\\ \epsilon_2\\ \epsilon_3\\ \epsilon_4\\ \epsilon_5\\ \epsilon_6\end{pmatrix} \tag{2.16}$$

For a monoclinic structure, the lowest symmetry material discussed in this thesis, the elastic tensor is reduced to [57]:

$$[c] = \begin{bmatrix} c_{11} & c_{12} & c_{13} & 0 & 0 & c_{16} \\ & c_{22} & c_{23} & 0 & 0 & c_{26} \\ & & c_{33} & 0 & 0 & c_{36} \\ & & & c_{44} & c_{45} & 0 \\ & symm & & & c_{55} & 0 \\ & & & & & c_{66} \end{bmatrix} \tag{2.17}$$

and for orthorhombic:

$$[c] = \begin{bmatrix} c_{11} & c_{12} & c_{13} & 0 & 0 & 0 \\ & c_{22} & c_{23} & 0 & 0 & 0 \\ & & c_{33} & 0 & 0 & 0 \\ & & & c_{44} & 0 & 0 \\ & symm & & & c_{55} & 0 \\ & & & & & c_{66} \end{bmatrix} \tag{2.18}$$

The elastic tensor for cubic and tetragonal symmetries is the same as Eqn 2.18 with the reduction $c_{11} = c_{22} = c_{33}$, $c_{12} = c_{13} = c_{23}$ and $c_{44} = c_{55} = c_{66}$ for cubic and $c_{11} = c_{22}$, $c_{23} = c_{13}$ and $c_{44} = c_{55}$ for tetragonal.

Finally, it can sometimes be helpful to re-write the Hooke's law in terms of the compliance, $s_{ij} = c_{ij}^{-1}$

$$\epsilon_j = s_{ij}\sigma_i \tag{2.19}$$

2.1.3 Anisotropic Young's Modulus

Young's modulus is particularly useful for describing elastic problems of cantilevers, such as those studied in this thesis. For an anisotropic medium, Young's modulus is dependent on the relevant direction in the material, $\boldsymbol{n}$ and is related to the compliance tensor by:

$$\frac{1}{E_{\mathbf{n}}} = s_{ijkl} n_i n_j n_k n_l \tag{2.20}$$

where $n_{1,2,3}$ are the cosines of the angle formed between the direction n and [100], [010] and [001], respectively [59]. In Voigt notation, Young's modulus for a generic anisotropic material is [60]

$$\begin{aligned}\frac{1}{E_{\mathbf{n}}} =& s_{11} n_1^4 + s_{22} n_2^4 + s_{33} n_3^4 + (s_{44} + 2s_{23}) n_2^2 n_3^2 + (s_{55} + 2s_{13}) n_1^2 n_3^2 + (s_{66} + 2s_{12}) n_1^2 n_2^2 \\ &+ 2n_2 n_3 \left[(s_{14} + s_{56}) n_1^2 + s_{24} n_2^2 + s_{34} n_3^2 \right] \\ &+ 2n_3 n_1 \left[s_{15} n_1^2 + (s_{25} + s_{46}) n_2^2 + s_{35} n_3^2 \right] \\ &+ 2n_1 n_2 \left[s_{16} n_1^2 + s_{26} n_2^2 + (s_{36} + s_{45}) n_3^2 \right]\end{aligned} \tag{2.21}$$

Simplifying for different symmetries leads to:

Cubic:
$$\frac{1}{E_{\mathbf{n}}} = s_{11} + (s_{44} + 2s_{12} - 2s_{11})(n_1^2 n_2^2 + n_1^2 n_3^2 + n_2^2 n_3^2) \tag{2.22}$$

Tetragonal:
$$\begin{aligned}\frac{1}{E_{\mathbf{n}}} =& s_{11} + (s_{33} - s_{11}) n_3^4 + (s_{66} + 2s_{12} - 2s_{11}) n_1^2 n_2^2 \\ &+ (s_{44} + 2s_{13} - 2s_{11})(n_1^2 n_3^2 + n_2^2 n_3^2)\end{aligned} \tag{2.23}$$

Orthorhombic:
$$\begin{aligned}\frac{1}{E_{\mathbf{n}}} =& s_{11} n_1^4 + s_{22} n_2^4 + s_{33} n_3^4 + s_{44} n_2^2 n_3^2 + s_{55} n_1^2 n_3^2 + s_{66} n_1^2 n_2^2 \\ &+ 2(s_{12} n_1^2 n_2^2 + s_{13} n_1^2 n_3^2 + s_{23} n_2^2 n_3^2)\end{aligned} \tag{2.24}$$

$$\textbf{Monoclinic:} \quad \frac{1}{E_{\mathbf{n}}} = s_{11}n_1^4 + s_{22}n_2^4 + s_{33}n_3^4 + s_{44}n_2^2n_3^2 + s_{55}n_1^2n_3^2 + s_{66}n_1^2n_2^2 + 2(s_{12}n_1^2n_2^2 + s_{13}n_1^2n_3^2 + s_{23}n_2^2n_3^2) + 2n_1n_2\left[s_{16}n_1^2 + s_{26}n_2^2 + (s_{36}+s_{45})n_3^2\right] \tag{2.25}$$

In the simple cases of **n** parallel to one of the crystalline axes:

$$\frac{1}{E_{100}} = s_{11}, \frac{1}{E_{010}} = s_{22} \quad \text{and} \quad \frac{1}{E_{001}} = s_{33} \tag{2.26}$$

E.g. for cubic and tetragonal symmetries:

$$\textbf{Cubic:} \quad \frac{1}{E_{\mathbf{100}}} = s_{11} = \frac{c_{11}+c_{12}}{(c_{11}-c_{12})(c_{11}+2c_{12})} \tag{2.27}$$

$$\textbf{Tetragonal:} \quad \frac{1}{E_{\mathbf{100}}} = s_{11} = \frac{c_{13}^2 - c_{11}c_{33}}{(c_{11}-c_{12})(2c_{13}^2 - c_{11}c_{33} - c_{12}c_{33})} \tag{2.28}$$

As can be seen from the relationships between Young's Modulus and the compliance tensor, extracting the complete elastic tensor is non-trivial and requires multiple samples with different orientations and/or the measuring of many different resonance modes. However, with careful selection of **n**, the behavior of certain elastic moduli can be explored without the exact determination of all components. For example, Eqn 2.28 shows that, for tetragonal symmetries, E_{100} is dependent on c_{11}, c_{33}, c_{12} and c_{13}. A discontinuity in E_{100} therefore indicates a discontinuity in one of more of these components. When **n** = 110, the tetragonal Young's modulus becomes:

$$\frac{1}{E_{\mathbf{110}}} = \frac{1}{4}(2s_{11} + 2s_{12} + s_{66}) = \frac{1}{4}\left[\frac{1}{c_{66}} + \frac{1}{c_{11}/2 + c_{12}/2 - c_{13}^2/c_{33}}\right] \tag{2.29}$$

In contrast to E_{100}, E_{110} is dependent also on the shear modulus, c_{66}. By measuring E_{110} and E_{100}, c_{66} can be explored. This is particularly useful in the case of the iron pnictides, for which the relevant elastic modulus for electronic nematicity is c_{66}. This is discussed in detail in Ch 7, which demonstrates how measurements of E_{100} and E_{110} can be used to probe the nematicity via c_{66}.

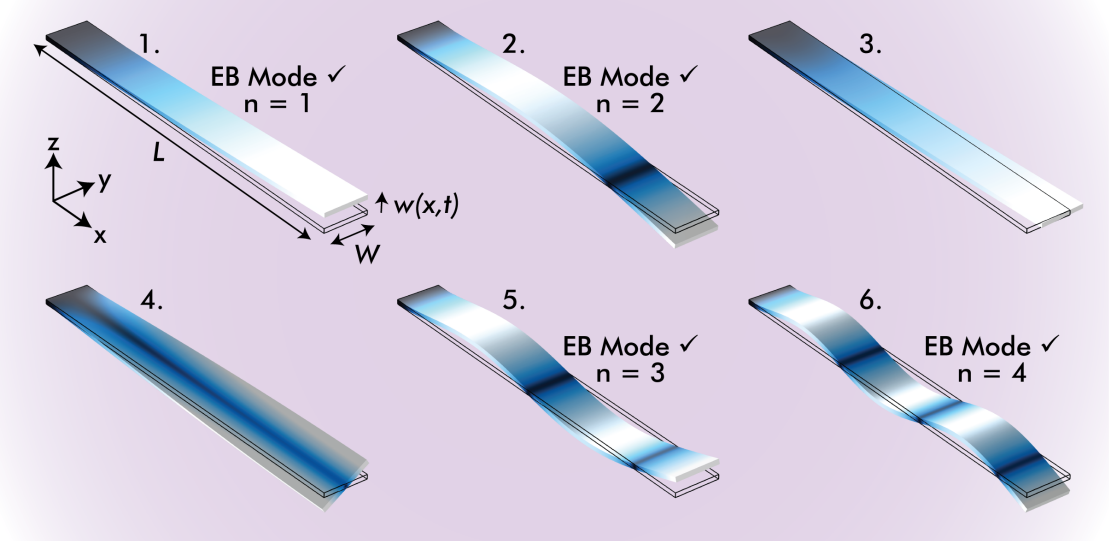

Figure 2.3: The first six resonance modes of a single-clamped cantilever beam with width W length L and thickness T simulated using Finite Element Analysis. Depending on the geometry and elastic properties, the order of these modes may vary. Euler-Bernouli Beam Theory can be used to describe the non-rotational modes whose deflection is along z. The 3rd mode depends on the shear along y and the 4th mode is rotational. For the EB modes, $w(x,t)$ describes the deflection of the beam as a function of x and time. The frequency of each can be calculated with the parameter α_n, where n is the number of the EB mode.

2.2 The Cantilever Beam

One of the simplest shapes to describe through elasticity is that of the cantilever beam. In the most general terms, a cantilever is an object that is much longer in one dimension than in the others and that is fixed on one (single-clamped) or both (double-clamped) ends while the rest of the beam is free. Cantilevers are ubiquitous, with applications ranging from architecture to microelectrical mechanical systems (MEMS). For the Focused Ion Beam fabrication of micro-mechanical resonators, the geometry of the cantilever was selected largely because of its relative simplicity, both for fabrication and modeling.

For a thin beam, the resonance frequency and Young's modulus can be directly related without knowledge of other elastic properties, by making the assumptions of negligible strain along the width of the cantilever and assuming that the beam does not rotate. Provided that the geometry and density of the beam are known, Young's modulus can therefore be calculated directly from a single measurement of one resonance mode from one cantilever. This model of a cantilever beam is called Euler-Bernouli (EB) Beam Theory (or Simple Beam Theory) [61, 62] and, depending on the frequency and geometry, the relationship between the resonance frequency and Young's modulus can often be found to within 1% accuracy. However, the resonance spectrum determined by this model is incomplete; the full spectrum requires one to consider the neglected strain and rotation (Fig 2.3). A more complete description of the

deflection of a cantilever is found in Timoshenko Beam Theory [61, 63–65] although for the application of calculating resonance modes, resonance frequencies can be more easily found through Finite Element Analysis (FEA).

This section will introduce the principles and assumptions of EB Beam Theory to relate the resonance frequency and Young's Modulus in a simple expression. FEA will also be discussed as a powerful tool for the determination of all resonance modes with a greater degree of accuracy and for more complicated geometries. Of particular interest, FEA has been used to model the resonance modes of a cantilever beam with a few large domains.

2.2.1 Euler-Bernouli Beam Theory

Simple Beam Theory relies on three main assumptions to model the deflection of a beam. (1) The beam's cross section (normal to x in Fig 2.3) remains infinitely rigid; no deformations occur in this plane. Throughout all deformations along z, the cross-section remains (2) planar and (3) normal to the deformed axis of the beam. These assumptions require that the strain along y is negligible and that there is no rotation. While no assumptions have been made about the shape, experimentally, this model works best for long and thin beams; $T << W << L$, where T, W, and L are the thickness, width and length, respectively [62, 64]. The EB beam equation relates the load q to the deflection $w(x,t)$, where t is the time.

Euler-Bernouli Beam Equation:
$$q = \frac{d^2}{dx^2}\left[EI\frac{d^2w}{d^2x}\right] \tag{2.30}$$

Here, E is Young's modulus and $I = \int\int y^2 dydz$ is the second moment of area calculated about the center of the cross-section. If E and I are independent of x, the equation of motion is:

$$\mu\frac{d^2w(x,t)}{dt^2} = EI\frac{d^4w(x,t)}{dx^4} \tag{2.31}$$

which has solution:

$$w(x,t) = w(x)e^{-i\omega t} \tag{2.32}$$

$$w(x) = C_1\sin\left(\frac{\alpha_n x}{L}\right) + C_2\sinh\left(\frac{\alpha_n x}{L}\right) + C_3\cos\left(\frac{\alpha_n x}{L}\right) + C_4\cosh\left(\frac{\alpha_n x}{L}\right) \tag{2.33}$$

The resonance modes are then given by

$$\omega_n = \alpha_n^2 \sqrt{\frac{EI}{\mu L^4}} \tag{2.34}$$

where μ is the mass per unit length and α_n can be found by solving Eqn 2.33 for the boundary conditions. For a beam with one end fixed, the boundary conditions are $w(0) = w'(0) = w''(L) = w'''(L) = 0$. A beam with both ends fixed has boundary conditions $w(0) = w'(0) = w(L) = w'(L) = 0$. The first few solutions to α_n therefore are:

single-clamped: $\alpha_n = 1.875, 4.694, 7.885...$ (2.35)

double-clamped: $\alpha_n = 4.730, 7.853, 10.996...$ (2.36)

For a perfectly rectangular cross section with width W, thickness T and for a material with known density ρ, $\mu = \rho W t$ and $I = WT^3/12$. Eqn 2.34 becomes

$$f_n = \frac{\alpha_n^2}{2\pi} \frac{T}{L^2} \sqrt{\frac{E}{12\rho}} \tag{2.37}$$

Eqn 2.37 reveals that when the strain along y is negligible, the resonance frequencies are independent of the beam width. If the beam geometry is known and the frequency is measured, Young's modulus can be calculated as:

$$E = 12\rho \left(\frac{2\pi}{\alpha_n^2} \frac{L^2}{T} \right)^2 f_n^2 \tag{2.38}$$

with error:

$$\frac{\sigma_E}{E} = 2\sqrt{\left(4\left(\frac{\sigma_L}{L}\right)^2 + \left(\frac{\sigma_T}{T}\right)^2 + \left(\frac{\sigma_f}{f}\right)^2\right)} \tag{2.39}$$

From an imperfect cantilever fabrication, the cross-section of the beam may be slightly trapezoidal (Fig 2.4) with a minimum thickness T_1 and a maximum thickness T_2. In this case, $I = \frac{WT}{24}(T_1^2 + T_2^2)$, where $T = \frac{T_1+T_2}{2}$ and Eqn 2.34 becomes

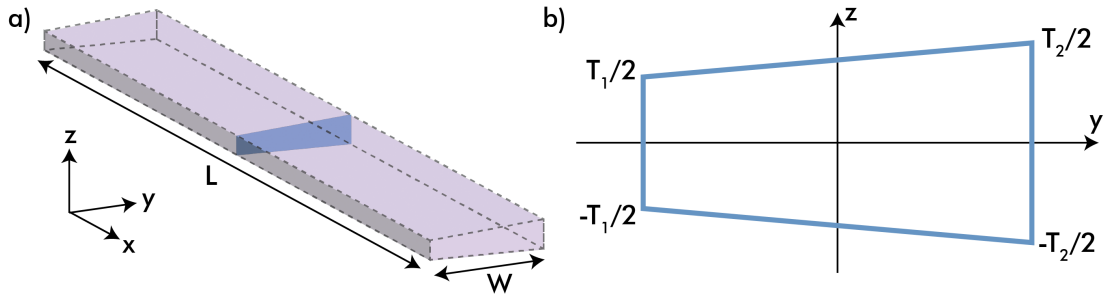

Figure 2.4: (a) Cantilever beam that is slightly trapezoidal. (b) Cross-section of (a).

$$f_n = \frac{\alpha_n^2}{2\pi L^2}\sqrt{\frac{E(T_1^2+T_2^2)}{24\rho}} \tag{2.40}$$

Young's modulus and its calculation error for the trapezoidal beam is now

$$E = \frac{24\rho}{T_1^2+T_2^2}\left(\frac{2\pi}{\alpha_n}L^2\right)^2 f^2 \tag{2.41}$$

$$\frac{\sigma_E}{E} = 2\sqrt{4\left(\frac{\sigma_L}{L}\right)^2 + \frac{T_1^2\sigma_{T1}^2 + T_2^2\sigma_{T2}^2}{(T_1^2+T_2^2)^2} + \left(\frac{\sigma_f}{f}\right)^2} \tag{2.42}$$

Note that, despite the inherent complexity of elasticity, equations 2.38 and 2.41 allow for the computation of Young's modulus from a single frequency measurement, provided that the geometry is known. Measuring higher order EB resonances, however, will only change the value of α_n. Extracting the complete elastic tensor with EB theory therefore requires measurements of cantilevers with different orientations. For an anisotropic sample, the relevant direction for Young's modulus will be the direction parallel to the length of the cantilever. For example, if one is interested in E_{100}, then the cantilever should be oriented with the longest axis along [100]. For this reason, cantilevers will sometimes be referred to by their principal direction, e.g. a [100] cantilever.

To verify that the assumptions made are reasonable for the geometry of the material, it is useful to compare EB with FEA. From the elastic constants reported for silicon (Table 2.1 [66]) and using $1/E_{100} = s_{11}$ for a cubic material, $E_{100} = 129.9$ GPa. For a cantilever with length 100 μm, width 10 μm and thickness 1 μm, Eqn 2.37 yields a fundamental resonance frequency of 120.6 kHz. FEA simulations on the same cantilever result in a fundamental frequency at 121.44 kHz. Thus Euler-Bernouli beam theory for a cantilever of these dimensions is in agreement with FEA to within 1%.

c_{11}	c_{12}	c_{44}	ρ
165.5 GPa	63.9 GPa	79.5 GPa	2330 kg/m^3

Table 2.1: Elastic moduli and density of silicon [66, 67]

2.2.2 Finite Element Analysis

FEA is particularly useful for the computation of non-EB resonance modes or for more involved geometries. In essence, FEA is a computational tool to solve differential equations across an object or physical system by dividing the system into smaller components (the elements). All elements combined form the mesh and the points where elements meet are the nodes. The differential equations are then projected onto the nodes resulting in a large number of linear equations that are solved computationally such that the boundary conditions of the system are met. Increasing the number of elements will increase the precision of the solution but also the required computation time and memory [68–71]. Comparisons between FEA and experiments show that FEA can also be more accurate than EB theory, with deviations from the measured resonance frequency < .006% for the first ten resonance modes [72, 73]. In practice, the accuracy of FEA will depend on the mesh size and the accuracy of the model.

FEA for the work in this thesis was done with Comsol Multiphysics. With a frequency sweep study, the eigenfrequencies of an object can be computed and the shape of the eigenmode visualized, provided that the geometry, boundary conditions, and the material's elastic properties and density are known. The partial differential equation used for the eigenfrequency calculations in solid mechanics is

$$-\rho\omega^2 = \nabla \cdot \mathbf{S} \tag{2.43}$$

where $\omega = 2\pi f$ and $\mathbf{S}$ is called the second Piola-Kirchhoff stress tensor. $\mathbf{S}$ is related to the stress tensor σ through the deformation gradient tensor $\mathbf{F} = \mathbf{I} + \frac{\partial \mathbf{u}}{\partial \mathbf{x}}$ and the relative volume change, $J = \det(\mathbf{F}) = dV/V_0$ [74, 75].

$$\mathbf{S} = J\mathbf{F}^{-1}\sigma\mathbf{F} \tag{2.44}$$

The dependence of the lowest six resonance frequencies on the geometry of a rectangular [100] silicon cantilever is shown in Fig 2.5. For a 1 μm × 10 μm × 100 μm beam, these frequencies correspond to the modes shown in Fig 2.3. EB theory was also used to calculate the frequency of the EB modes. When $T << W << L$, the frequency of the EB modes as determined by FEA is nearly independent of the width, in good agreement with Eqn 2.37. From the percent difference between the frequencies determined by EB Theory (f_{EB}) and FEA (f_{FEA}) plotted in

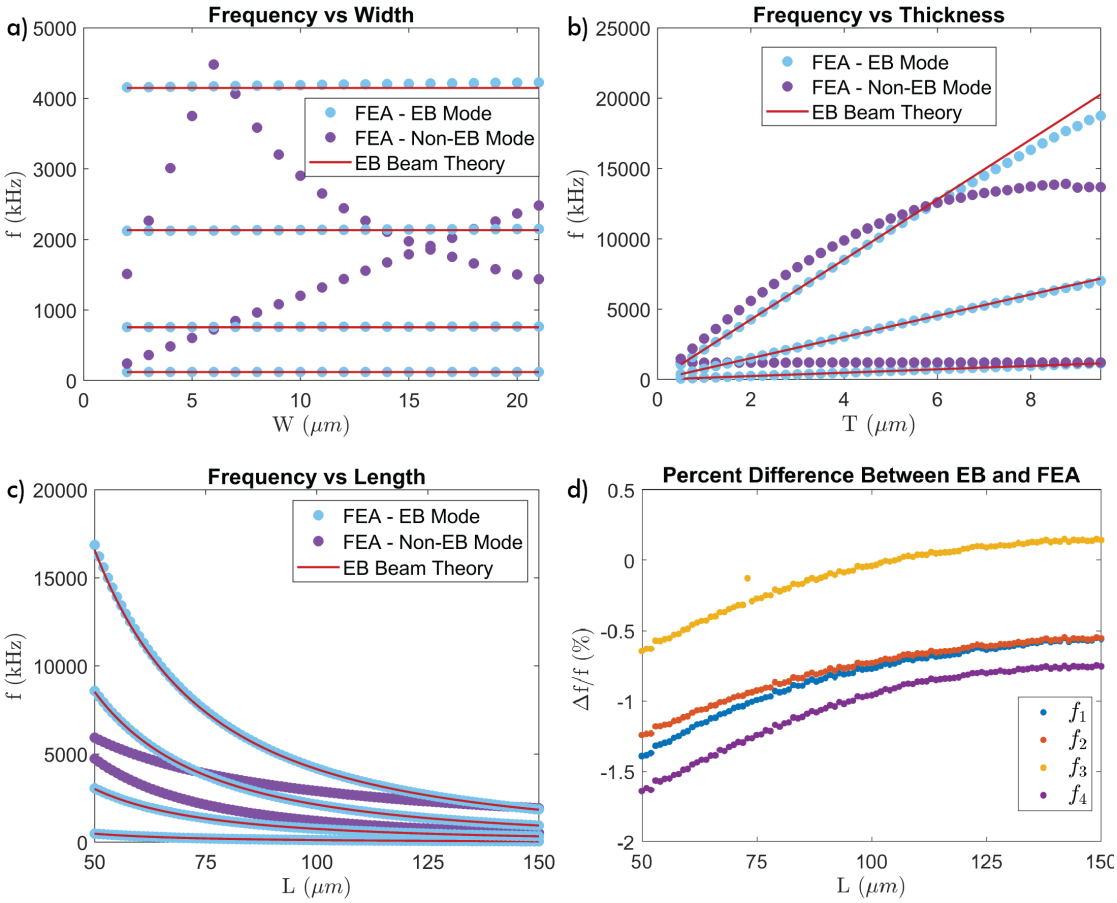

Figure 2.5: Lowest eigenfrequencies for cantilevers of different geometries calculated from Finite Element Analysis (FEA) or from Euler-Bernouli (EB) Beam Theory. FEA was done for an anisotropic rectangular cantilever of silicon using the elastic moduli shown in Table 2.1 with longest axis along [100]. Eqn 2.37 with $E_{100} = 129.9$ GPa was used for EB calculations. The four EB modes correspond to the EB modes plotted in Fig 2.3. The non-EB modes correspond to shear and torsional modes. (a) Freq vs width with constant $L = 100$ μm and $T = 1$ μm. (b) Freq vs thickness with constant $L = 100$ μm and $W = 10$ μm. (c) Freq vs length with constant $W = 10$ μm and $T = 1$ μm. (d) $(f_{EB} - f_{FEA})/f_{FEA} \times 100$ vs length for EB modes.

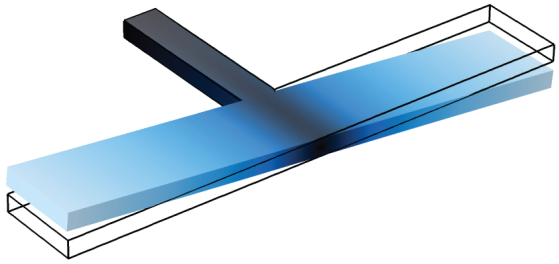

Figure 2.6: FEA is used to study cantilevers of other geometries, such as the T-beam which has a torsional mode as a fundamental resonance.

Fig 2.5 (d), it can be seen that EB theory is most accurate for large L/T.

These simulations do not take into consideration the effect of different mounting conditions — the cantilever is assumed to be rigidly fixed on one end. In reality, the boundary conditions are more complicated. For a FIB-fabricated cantilever, $5-10$ μm of the end of the cantilever is clamped between the substrate and FIB induced deposition (FIBID). This clamped cantilever can also be computed using FEA, but an accurate calculation requires that the elastic properties of the clamp are also known. A method to measure elastic properties of FIBID will be discussed in Chapter 3.

Furthermore, if enough resonance modes are measured, FEA can be used for the calculation of the elastic tensor rather than EB theory. This method can be computationally challenging; the resonance frequencies follow from the elastic properties and geometry while the inverse problem of computing the elastic constants from the frequency spectrum cannot be solved directly by analytics or simulations. In an approach to solve this problem in RUS, the frequency spectrum of sets of test elastic moduli is generated and adjusted to minimize the error between the computed and measured spectrum. One method requires approximate elastic moduli to be known, and then a gradient-based minimization is used to calculate the elastic moduli [76]. This approach has the disadvantage of possibly becoming stuck in local minima.

This risk can be reduced by using a genetic algorithm. Instead of starting at a single point, the algorithm generates a large number of parameter sets spread throughout a range of parameters in which the solution is expected. These values are solved for, and parameter sets with a minimum error are mutated to generate new sets. The process is repeated until the error on a parameter set is found to be within the tolerance. This genetic approach has been demonstrated for RUS [48, 77]; however, it may be possible to use a simplified approach for resonating cantilevers as, with interferometry, the shape of the mode can be determined reducing some of the uncertainty in the resonance spectrum. Unfortunately, these methods of solving the inverse problem require, at minimum, the number of resonance modes measured to be equal to the number of independent elastic moduli that must be found. Due to the limited frequency bandwidth of the interferometer used, this was not possible for measurements reported in this thesis. Furthermore, both EB and non-EB modes must be measured and many non-EB modes will be challenging to excite or detect. For these reasons,

elastic calculations have been performed using EB theory.

Finally, Finite Element Analysis can be used to model samples of arbitrary geometries. This can be used to reduce the error from geometric imperfections that may arise in fabrication or to design samples to explore different types of resonant modes (and thus probe different elastic values). For example, Fig 2.6 shows one example of a T-beam cantilever designed such that the fundamental resonance mode is torsional rather than shear. This geometry can be fabricated using the FIB fabrication process described in Ch 4.

2.2.3 Few-domains

An interesting peculiarity for cantilevers on the microscale to explore is the potential of domain formation with length scale on the order of, or slightly smaller than, the length scale of the cantilever (L). When cooling through a phase transition, a crystal is likely to form multiple domains with different orderings unless the symmetry is broken externally. For example, in a cubic-to-tetragonal structural transition with $a = b \neq c$, the lattice must pick a direction for c. If the sample is sufficiently strained along z (parallel to one of the crystalline axes), then z can be energetically favorable for the lattice distortion — the sample will be monodomain. In the absence of strain, there is no direction that is energetically favorable, and the sample is likely to form domains with c parallel to x, y, or z. The length scale, l_d, of these domains can vary, depending on the phase transition and the material, and it is intriguing to consider what the effect of these domains will be on a microscale cantilever.

If $l_d << L$, then the cantilever is made up of many-domains. In ultrasound measurements of many-domain samples, domain walls increase the dissipation and therefore decrease the Q-factor of the resonator. This can make it impossible to measure resonance frequency below the phase transition. At low temperatures, the domain walls can become pinned and the effective Young's modulus of the sample can be a mixture of the elastic moduli from the different domains. If $l_d >> L$, then the cantilever is monodomain, resonance can be measured and the elastic properties explored.

When $l_d \approx L$, then the sample will have few domains. FEA was used to study the effect of domain pattern and number on the fundamental frequency of a resonating cantilever. A 100 μm × 10 μm × 1 μm cantilever was divided into domains along the directions of the sample (Fig 2.7 (a)). For simplicity, these domains were assumed to be equal in size. The elastic values of silicon (Table 2.1) were distorted to simulate a tetragonal symmetry ($c_{22} = .9 * c_{11}$ and $c_{13} = .9 * c_{12}$). Domain orientations A and B of Fig 2.7 (a) represent a distortion in the plane of the cantilever, either with the distorted axis parallel (A) or perpendicular (B) to the length. Fig 2.7 (b) shows the resonance frequency versus number of domains for different domain patterns. In Pattern 1 (circles), the domain located on the fixed-end of the sample will have the biggest influence on the frequency, as this is where the strain of the fundamental resonance is most concentrated. The purple and blue circles correspond to a fixed-end domain orientation of A and B, respectively. Patterns 2 and 3 are symmetric, and the most influential domain

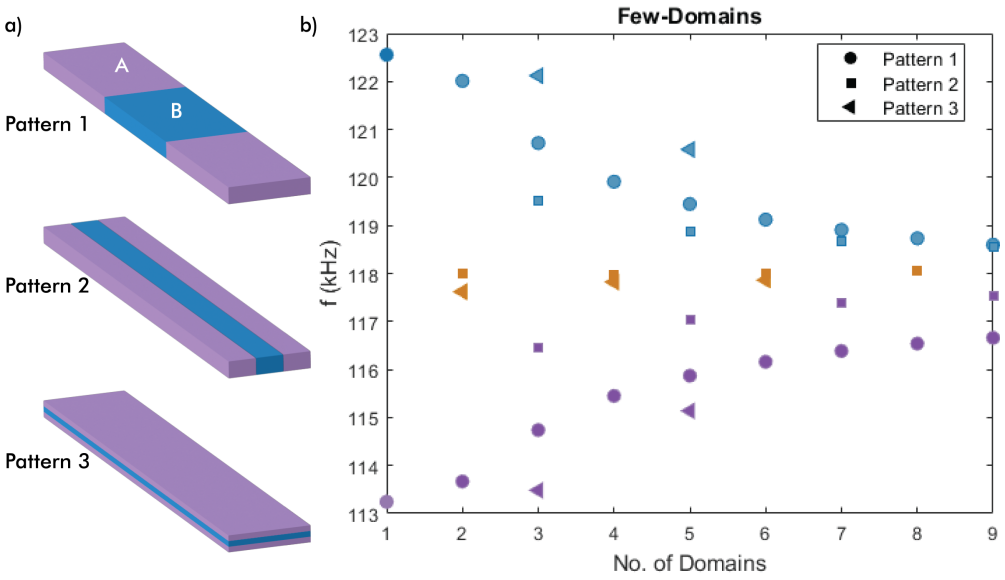

Figure 2.7: (a) Different patterns of a domain in a cantilever. (b) Resonance frequency for each pattern for different domain numbers. Purple (blue) markers indicate a dominate domain orientation of A (B). For Pattern 1, the dominant domain orientation will be the domain at the fixed-end of the cantilever. For Patterns 2 and 3, the dominant orientation will be the one with the largest volume. An even number of domains in Patterns 2 and 3 means that no orientation is clearly dominant - these are plotted in orange.

direction will be the one with the largest volume. An even number of domains (orange squares and triangles) does not break the symmetry and will have a smaller impact on the frequency. The purple (blue) markers for Patterns 2 and 3 indicate that the largest volume is orientation A (B).

While this model is simplistic (the actual domain formation is likely to be more complicated and the effect on the resonance frequency will depend on the strength of the distortion), it yields an intuitive picture of the few-domain cantilever. If the cantilever domain patterns are random, then different resonant frequencies in the ground state are possible after each cooling through the phase transition. It may also be possible to control these domain patterns (e.g. force the system into a monodomain state), perhaps with the strain gradients generated by vibrations on resonance. In this case, on-resonant vibrations of sufficient magnitude while cooling through the phase transition would cause the cantilever to reproducibly choose the same resonance frequency, while cooling without vibrations could lead to a random frequency selection.

2.3 Temperature Dependence of Elasticity

For applications of elasticity in quantum materials, one is often not only interested in the absolute value of the elastic constants, but also the dependence of the elastic properties on

temperature. Understanding elasticity at phase transitions requires first understanding the elasticity dependence on temperature in the absence of thermodynamic transitions. In a normal material, the anharmonicity of the lattice gives rise to a stiffening upon cooling. This property is usually described phenomenologically and can be fit and subtracted from the data such that the raw effect of phase transitions can be examined. Many types of phase transitions, such as superconductivity, can be well-described by Landau Theory, which proposes that the Free energy about a phase transition can be expanded in terms of an ordering parameter that is zero above the transition and non-zero below. As suggested by Landau Theory, when cooling through a phase transition, the change in the elastic moduli gives indication on the nature of the phase transition and on the coupling of the ordering parameter with the lattice.

2.3.1 Phonon Anharmonicity

In order to look at the dependence of elasticity on temperature in correlated systems, it is useful to understand the background elasticity, i.e. the temperature dependence of elasticity that arises from thermal phonons [50, 78–80]. In the harmonic approximation of a lattice, the Hamiltonian takes the form:

$$H = H_{el} + H_{ph} = \frac{1}{2}\sum_{ij} c_{ij}\epsilon_i\epsilon_j + \frac{1}{2}\sum_q \hbar\omega_q(n_q + 1/2) \tag{2.45}$$

Here, H_{el} and H_{ph} are the contributions to the Hamiltonian due to strains and harmonic phonons, respectively, and ω_q are the phonon frequencies. Under this approximation, the elastic tensor is constant in temperature. Recovering the temperature dependence of elasticity requires a quasi-harmonic approach [78]. With this approach, the elastic constants take the form:

$$c_{ij} = c^0_{ij} - \frac{1}{2}\Gamma U(T) + \frac{1}{4}\gamma_{ph}\Big[U(T) - TC_v(T)\Big] \tag{2.46}$$

with phonon-Grüneisen parameter

$$\gamma_{kl} = \frac{\partial \ln\langle\omega^2\rangle}{\partial\epsilon_{kl}}, \quad \Gamma_{klk'l'} = -\frac{\partial^2 \ln\langle\omega^2\rangle}{\partial\epsilon_{kl}\partial\epsilon_{k'l'}} \tag{2.47}$$

γ_{ph} is the average phonon-Grüneisen parameter, $U(T)$ is the internal energy and C_v is the specific heat. At large temperatures ($T >> \Theta_D$, Θ_D = Debye temperature), C_v is constant and $c_{ij} \sim -T$. When $T << \Theta_D$, $C_v \sim T^3$ and $c_{ij} \sim -T^4$ [50]. However, the low-temperature

relationship of c_{ij} can deviate from the predicted T^4 dependence when other interactions become dominant. For example, the electronic contribution to the low temperature elastic constants in normal metals results in a T^2 temperature dependence [79].

In practice, phenomenological expressions are used to fit the temperature dependence of elastic constants, with the most well known expression given by Varshni [80]:

$$c_{ij} = c_{ij}^0 - \frac{s}{e^{t/T} - 1} \tag{2.48}$$

where s, t are fitting parameters. The theoretical justification for this equation is as follows: Leibfried and Ludwig showed that the temperature dependence of adiabatic elastic constants that arises from the lattice can be expressed as [80]:

$$c_{ij} = c_0(1 - D\bar{\epsilon}) \tag{2.49}$$

D is a parameter depending on the model and $\bar{\epsilon}$ is the average energy per oscillator. The average energy from the Einstein model of a solid is

$$\bar{\epsilon} = \frac{1}{2}h\nu + \frac{h\nu}{e^{h\nu/kT} - 1} \tag{2.50}$$

Substituting this equation into Eqn 2.49 yields Eqn. 2.48. Because Eqn. 2.48 is meant to represent the total temperature dependence including the electronic contribution, the fitting parameter t and the Einstein frequency ν are not expected to be closely related. This function was shown to be a reasonable fit of the temperature dependence on elasticity for a variety of materials [80].

2.3.2 Landau Theory of Phase Transitions

Phase transitions are marked by a symmetry breaking between two distinct phases. To build a theoretical understanding of phase transitions, Landau postulated that the free-energy can be expanded in terms of an ordering parameter, η. The Landau expansion of a second-order phase transition is

$$F = F_0 + \frac{1}{2}\alpha(T - T_0)\eta^2 + \frac{1}{4}\beta\eta^4 \tag{2.51}$$

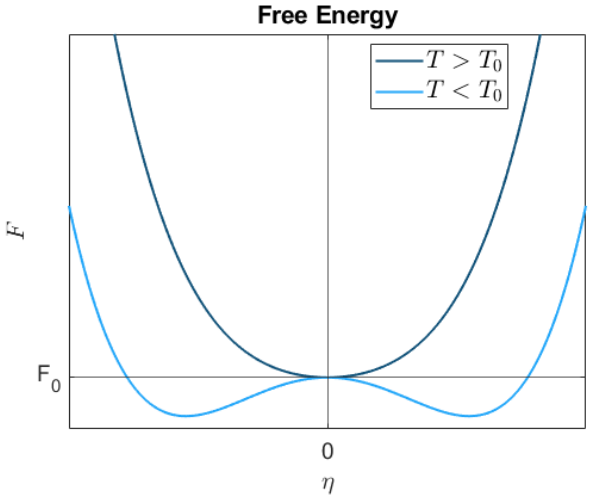

Figure 2.8: Free energy F versus order parameter η above and below a second order phase transition. Above the transition temperature, T_0, the free energy is minimized for $\eta = 0$. Below the transition, the free energy is minimized for a nonzero ordering parameter.

where F_0 is the background free energy, T_0 is the transition temperature, and α, and β are positive constants [81]. As plotted in Fig 2.8, when $T > T_0$, F is minimized by $\eta = 0$. When $T < T_0$, F is minimized for a nonzero ordering parameter, the magnitude of which will grow with decreasing temperature. Furthermore, below the transition, the minima in the free energy are degenerate such that the system must spontaneously select one minima.

The changes in elastic constants across the phase transition can be computed by minimizing F with respect to η and then applying Eqn 2.13, or they can be computed directly [82]:

$$c_{ij} = c^0_{ij} - \frac{Z_i Z_j}{Y} \qquad \text{with } Z_i = \frac{\partial^2 F}{\partial \eta \partial \epsilon_i} \text{ and } Y = \frac{\partial^2 F}{\partial \eta^2} \tag{2.52}$$

c^0_{ij} is the bare elastic constant, in the absence of any phase transition (i.e. the elasticity as expected from phonon anharmonicity). Z_i and Z_j will be nonzero if the free energy contains terms that couple the corresponding strains ϵ_i and ϵ_j to the ordering parameter η. It is insightful to examine how different types of coupling effect the elastic moduli [50, 82].

Linear η coupling with strain

For a linear coupling between the strain and the ordering parameter, both the strain and the ordering parameter must have the same symmetry, for example, in a structural transition. This coupling introduces the term:

$$F_c = -g\eta\epsilon_i \tag{2.53}$$

with coupling constant g. The free energy becomes

$$F = F_{el} - g\eta\epsilon_i + \alpha(T - T_0)\eta^2 + \frac{1}{2}\beta\eta^4 \tag{2.54}$$

where F_{el} is the elastic contribution to the free energy. With the help of Eqn 2.52, the elastic constants can be computed

$$\begin{aligned} c_{ij} &= c^0_{ij} \quad \text{if} \quad j \neq i \\ c_{ii} &= c^0_{ii} - \frac{g^2}{2\alpha(T - T_0) + 6\beta\eta_0^2} \end{aligned} \tag{2.55}$$

Here, η_0 is the equilibrium value from minimizing F. Above T_0, $\eta_0 = 0$ such that

$$c_{ii} = c^0_{ii} - \frac{g^2}{2\alpha(T - T_0)} \tag{2.56}$$

As the temperature approaches T_0, c_{ii} decreases. Because the elastic moduli cannot be negative, the phase transition will occur at temperature $T_c > T_0$, when $c_{ii} = 0$.

$$T_c = \frac{g^2}{2\alpha c^0_{ii}} + T_0 \tag{2.57}$$

Quadratic η coupling with strain

Ordering parameters that do not have the same symmetry as the lattice — such as for a superconducting or antiferromagnetic phase transition — cannot couple linearly with the strain. Parameters for these transitions can couple quadratically, introducing the coupling energy

$$F_c = -g\eta^2\epsilon_i \tag{2.58}$$

to the free energy

$$F = F_{el} + \left(\alpha(T - T_0) - g\epsilon_i\right)\eta^2 + \frac{1}{2}\beta\eta^4 \tag{2.59}$$

Again using Eqn 2.52, the modified elastic moduli become

$$\begin{aligned} c_{ij} &= c^0_{ij} \quad \text{if} \quad j \neq i \\ c_{ii} &= c^0_{ii} - \frac{2g^2\eta_0^2}{\alpha(T - T_0) + 3\beta\eta_0^2} \end{aligned} \tag{2.60}$$

Below T_0, minimizing Eqn 2.59 gives

$$\eta_0 = \sqrt{\frac{\alpha(T - T_0) + g\epsilon_i}{\beta}} \tag{2.61}$$

The elastic moduli are defined for zero strain. Substituting η_0 into 2.60 with $\epsilon_i = 0$ yields

$$c_{ii} = c^0_{ii}, \quad T > T_0 \tag{2.62}$$

$$c_{ii} = c^0_{ii} - \frac{g^2}{\beta}, \quad T < T_0 \tag{2.63}$$

Thus, when the ordering parameter is coupled quadratically to strain, then there will be a discontinuity in c_{ii} at T_0.

3 Focused Ion Beam

State-of-the-art lithographic techniques enable the fabrication of MEMS with nanoscale precision. This is thanks to the billions of euros for scientific funding and the decades of research that have gone into producing large, single-crystals of silicon and fine-tuning the fabrication parameters [2]. Unfortunately, lithographic processes are difficult to develop in new materials. Spin-coating, for example, requires flat, homogeneous surfaces for the resists to be even. The resist must also be chemically compatible with the material. Depositions and chemical etching are strongly dependent on the chemistry of the target. Samples of new materials may be microscopically small — far from the ~ 1 m wafers of silicon available today. Reproducing established lithographic processes on novel materials can therefore take years — and significant funding — to develop. Focused Ion Beams (FIBs) remove this barrier, enabling fast, high-precision rapid-prototyping of microstructures with few restrictions on the starting sample [83, 84]. The FIB's capability to selectively etch or deposit without the use of resists has found applications that include: 3D imaging and analysis [85], production of lamellae (micron-scale slices) for Transmission Electron Microscopy (TEM) [86] and electronic studies of quantum materials [32, 33]. Moreoever, FIBs are also used for defect engineering and ion implantation [87, 88].

The operating principles of a FIB are similar to that of a Scanning Electron Microscope (SEM) in concept. In an SEM, electrons are focused onto a spot on a sample, producing electrons from the incident beam that are elastically scattered away from the sample (called back-scattered electrons or BSE) and electrons that are ejected from the sample (secondary electrons or SE). The beam of electrons can be scanned across the surface while the BSE or SE are detected at each discrete point to generate an image. Because the wavelength of the incident electrons is shorter than that of visible light, SEM images have much greater resolution than possible in traditional optical microscopes (although, in practice, SEM resolution will be limited by lens aberrations, defects and interactions between the beam and the sample) [89]. Likewise, in a FIB, a beam of ions is focused onto a spot that can be scanned across the sample. As the ions are much more massive than electrons, momentum transfer between the impinging beam and atoms in the target produce secondary ions and neutral atoms, in addition to SE [90]. While

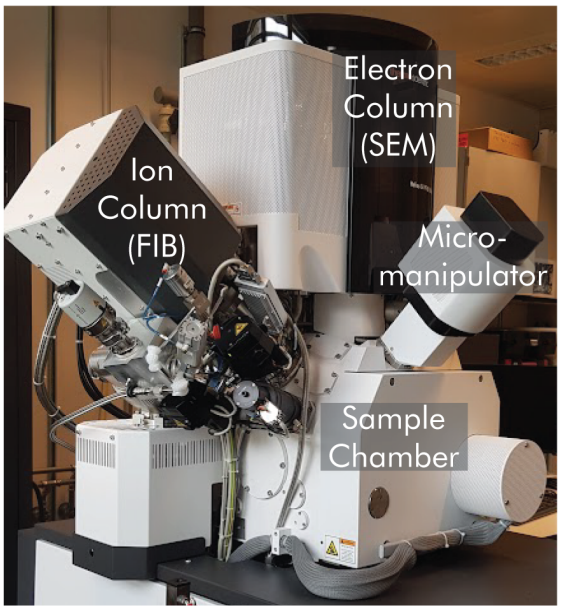

Figure 3.1: FEI Helios dual beam plasma FIB. The Scanning Electron Microscope (SEM) can be used for sample imaging. An in-situ micro-manipulator makes it possible to move microscopic samples.

the SE emitted can also be used to generate images, one main functionality of the FIB comes from the capability to remove material by repeatedly scanning the beam across a user-defined pattern. This enables one to carve complex geometries with length scales ranging from several hundred microns to 10 nm [91–93].

Many modern FIBs contain both ion and electron beams. The SEM and FIB are mounted at an angle to each other (Fig 3.1), making it easier to visualize 3D geometries thanks to the different perspectives of the two beams. Furthermore, both FIB and SEM can locally deposit material with the help of a Gas Injection System (GIS) that injects large, organic molecules which are absorbed onto the surface. The impinging beam breaks apart the molecules, causing lighter components to be sputtered away while heavy elements are deposited [94]. FIB induced deposition (FIBID) is multifunctional: the deposit can protect regions of the sample from ion-beam damage, provide a strong, mechanical weld, or act as an electrical contact [33].

The goal of this chapter is to briefly overview the operating principles of FIBs, provide general tips for etching and deposition processes and discuss the effects of beam interactions with the sample. The process flow of micro-cantilever fabrication is presented in detail in Chapter 4. For a handbook on scanning electron microscopy including in-depth technical explanations, the reader is recommended to [89, 95]. Excellent resources for micro- and nanofabrication FIB processes can be found in [83, 94, 96, 97] and FIB processing for electron-transport measurements in quantum materials are discussed in [32, 33, 98, 99].

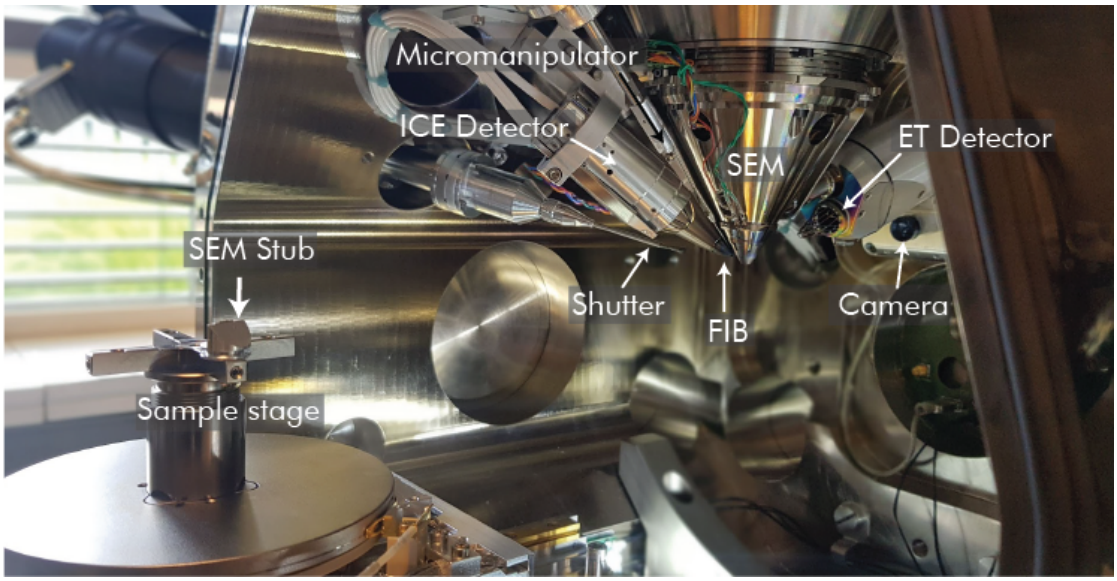

Figure 3.2: Inside of the sample chamber of a FEI Helios pFIB (Fig 3.1). With the door opened (as pictured) the stage is accessible to the user such that an SEM stub with the sample on top can be mounted onto the sample stage. When the door is closed, the sample can be positioned underneath the SEM. Various detectors in the chamber can be used for imaging with SE or BSE. While removing large amounts of material with the FIB, a retractable shutter can be inserted in front of the SEM to prevent removed material from contaminating the SEM. Finally an optical camera allows the user to monitor the position of the SEM stub, to prevent collisions with the SEM or FIB columns.

3.1 Operating Principles

The main components of a FIB system are the electron column, ion column, sample chamber and computer controls (Fig 3.1). The electron and ion columns each contain a source and a series of electrostatic lenses for focusing and scanning the beam. A series of detectors located in the sample chamber are used for detecting the SE and/or BSE emitted from the sample. The sample itself is mounted on a five-axis stage such that it can be tilted and rotated. Because the ion column is usually tilted at an angle of around 52° (54° in a Zeiss, 52° in FEI systems) from the electron column, the sample stage is perpendicular to the SEM at a 0° tilt and perpendicular to the FIB at a 52°. To prevent interactions between the ions and air particles, the system must be kept under high vacuum during operation.

Sample Chamber

Prior to FIBing, the sample is first mounted onto a small holder (called an SEM stub) that is screwed onto a piezoelectrically or mechanically driven stage that can be positioned with microscale precision. The tilt range of the stage is usually around $-10° \leq \theta \leq 60°$. If a different tilt angle is needed, angled SEM stubs allow for the sample to be mounted at a pre-tilt. As the

vacuum of the sample chamber must be ~ 10^{-6} mbar (or ~ 10^{-5} mbar during depositions), some systems use an exchange chamber for inserting and removing the sample, maintaining the vacuum of the main chamber. In the FEI Helios FIB, the sample is inserted by opening the main chamber, which must then be pumped down before use. Figure 3.2 shows the inside of the sample chamber with the door opened.

After pumping, the stage is moved such that the sample is visible in the SEM, and the height of stage is moved so that if the SEM image is centered around a feature, that feature remains at the center of the image at all tilt angles. This height is called the eucentric height. The stage must also be in the coincidence point, which is the height where the SEM and FIB beams coincide, and their images will both show the same part of the sample. The sample chamber also contains a camera, so the position of the sample with respect to the SEM and FIB columns can be monitored while the stage is moved. This is critical as, if the sample collides with one of the columns, this can damage the column. If the highest point on the stage is correctly at coincidence, then the stage can be safely moved without risk of hitting the columns.

For FIBID, a GIS with a retractable nozzle that can be brought close to the sample, is used for injecting the precursor gas. Many systems also contain a micromanipulator, enabling lamellae to be moved in-situ. Finally, the material that has been etched with the FIB can be redeposited elsewhere. Too much of this redeposited material on the opening of the SEM can contaminate the SEM. For this reason, some systems contain a shutter which can be brought in front of the SEM during etching to protect it.

Detectors

For SEM, electrons from the incident beam can penetrate deep into the sample, producing a chain reaction of collisions. The primary electrons (PE) inelastically scatter, transferring energy to knock electrons out of their atomic orbits. If these SE are close to the surface and have sufficiently high energy to overcome the potential surface barrier, then they can be scattered into the vacuum of the chamber. The PE can continue inelastically scattering until they loose energy and become trapped in the sample, or they can elastically scatter off of the large nuclei and be ejected from the substrate (BSE).

The image contrast of an SEM differs depending on the type of electron detected. Most BSE will retain at least ~ 50% of the energy of the primary electron beam (e.g. primary electrons may have 5-30 keV) [89]. Because of this high energy of the BSE, they can escape even from deep within the sample. Additionally, the fraction of incident electrons that leave the sample is dependent on the atomic number, Z. The stronger positive charge of nuclei for higher Z produce more BSE [89, 95]. In an inhomogeneous sample, regions consisting of atoms with a larger Z will result in a greater percentage of electrons that are backscattered and will appear brighter in the image in comparison to regions composed of elements with smaller Z, yielding a strong compositional contrast. SE, on the other hand, have much less energy (< 50 eV) than BSE and can only escape if they are generated near the surface. Furthermore, the emission of

SE is less sensitive to the atomic number of the atom. Therefore, SE have poorer compositional contrast but are better for imaging topography [89, 94]. Imaging can also be done by detecting SE emitted by interactions between the ion beam and the sample, although BSE are exclusive to SEM.

Sample chambers often contain several different types of detectors that can be used for SE or BSE. The type of the electron is distinguished by its energy level. Common detector types in an SEM include *Everhart-Thornley Detector* (ETD) which are located in the sample chamber (See Fig 3.2) and *Through-the-Lens* (TLD) located in the SEM lens. Both ETD and TLD mostly detect SE but are capable of measuring BSE as well [89]. The operating principles of these detectors is detailed in [89].

Finally, various techniques can be used for microchemical analysis. When SE are created by the electron beam, this also creates an electron-hole. A higher-energy electron may fill this hole, releasing the energy difference as an X-ray, with a wavelength characteristic of the element. Many FIB systems are equipped with a retractable X-ray detector. By measuring the energy of X-rays released at different positions, the elements in a sample can be mapped out. This technique is called Energy-Dispersive X-ray Spectroscopy (EDX or EDS) [89]. In addition to producing X-rays, energy resulting from the filling of an electron vacancy can be also emitted by the ejection of an outer-shell electron. Chemical analysis done by the detection of these Auger electrons is the principle of Auger Electron Spectroscopy (AES) or Scanning Auger Microscopy (SAM) [100]. The ion beam can also be used for chemical analysis: in Secondary Ion Mass Spectrometry (SIMS), secondary ions emmitted from interactions between the ion beam and the sample are detected to map the surface composition [101].

Electron and Ion Columns

Both the electron and ion columns consist primarily of a source, condenser lens, apertures and scanning and focusing lenses. A sketch of the ion column is shown in Fig 3.3 (a). The energy of the ions or electrons can be controlled by changing the accelerating voltage of the electrodes at the source. A condenser lens located below the source controls the spread of ions (electrons) and brings them into convergence. The beam then passes through an aperture which is a precisely drilled hole in a metallic sheet that prevents non-convergent ions (electrons) from reaching the sample. Different apertures can be used to select the total current flow. A series of electromagnetic scanning and focusing lenses focus the beam and scan it across the sample or the pattern [89, 94].

The ion used for the source greatly affects the interaction between the beam and the sample, and thus the performance of the FIB. Nearly 40% of the periodic table and many metal alloys have been successfully used as an ion source, although only a few are readily available commercially [90, 103]. The most common source type is the Liquid Metal Ion Source (LMIS) used in the popular gallium FIBs. In a LMIS, the metal is contained in a reservoir and heated to its melting temperature. The liquid metal can then flow along a tungsten needle that is

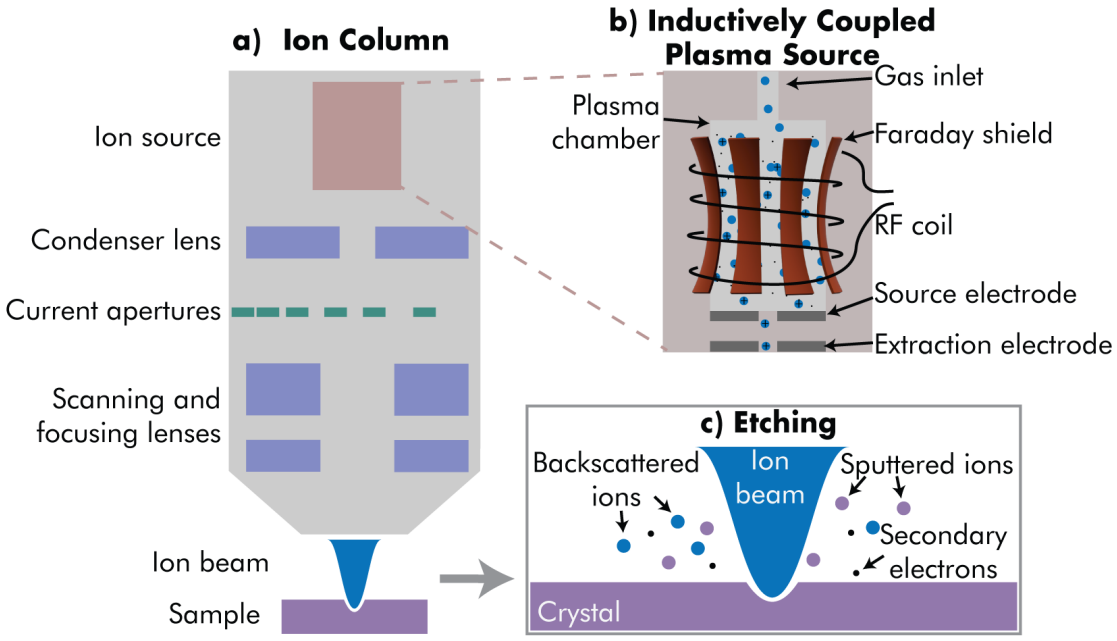

Figure 3.3: (a) Sketch of the main components of an Ion Column. (b) A Xenon FIB uses an inductively-coupled plasma source. Sketch based on [102]. (c) The incident beam on the sample etches into the material, producing backscattered ions, sputtered ions and atoms, and secondary electrons.

attached to the reservoir. The end of the needle has a sharp tip (radius $\sim 2-5\ \mu$m) located in an electric field formed by the extraction electrode. The combination of the electrostatic forces and the surface tension of the liquid causes the liquid metal on the needle to form a cone (called the Taylor cone) with end radius $\sim 1.5-3$ nm [104]. If the voltage on the extraction electrode is high enough, then ions will be emitted from the tip with a Gaussian-shaped distribution. Gallium is the preferred metal source because its melting point is near room temperature, allowing it to stay a liquid during operation without continuous heating. For non-gallium based LMIS, convection from continuously heating the metal source tarnishes the stability of the Taylor cone [103, 105].

One of the most important parameters for FIB processing is the spot size of the beam, which is dependent both on the current used and on the ion source. The beam diameter sets the imaging and patterning resolution. Fig 3.4 shows the spot size versus current for different sources. A gallium FIB at a low current ($\sim$ 1 pA) can have a beam spot size as small as $\sim$ 5 nm [90]. Above $\sim$ 10 nA, the beam shape becomes less sharp and more spread out, reducing the capacity of the beam to mill well-defined edges and, above $\sim$ 100 nA, the Taylor cone becomes unstable [102]. The etching rate is dependent on the current flow of ions to the sample and the target material. Consequently, higher currents are desirable for removing relatively large ($\geq 100\ \mu m^3$) volumes of material. Plasma-based FIBs (pFIBs) allow for etching with currents up to several μA. These FIBs use an Inductively Coupled Plasma (ICP) source in which the electrons in a reservoir of gas are excited by using a radio frequency (RF) current flowing in

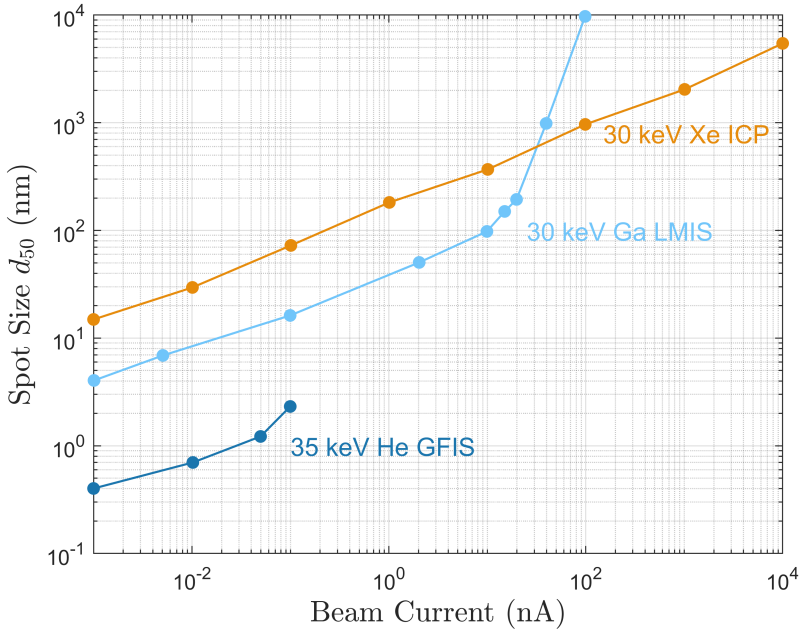

Figure 3.4: Spot sizes of He Gas Field Ion Source (GFIS), Ga Liquid Metal Ion Source (LMIS) and Xe Inductively Coupled Plasma Source (ICP) versus current. The spot size d_{50} is the diameter of the ion beam containing 50% of the ion current. Figure based on [90].

an antenna wrapped around the source chamber (Fig 3.3). The frequency of excitation is in between the plasma's electron resonance frequency and the ion resonance frequency, such that the electrons are heated to ionize the gas while the ions remain close to room temperature. A Faraday shield in between the RF coil and the chamber minimizes capacitive coupling between the coil and the gas while the inductive coupling is maintained. Ions are extracted from the plasma by maintaining a potential difference between a source and an extraction electrode [102]. The most popular gas for an ICP is xenon, although multi-ion source plasma FIBs that allow the user to easily switch between xenon, argon, oxygen and nitrogen have recently reached the market.

While Xe FIBs excel at high-currents, the shape of the beam has a longer tail than in the Gaussian-shaped gallium beams. This results in less-precision for fine structures. An even sharper and more-precise beam than that of a gallium FIB can be achieved using a helium or neon Gas Field Ion Source (GFIS). In a GFIS, a large electric field is used to ionize the neutral gas ions [102]. A He FIB can be used for currents in the range < 10 pA, with structures fabricated as small as 4 nm [91–93]. Helium and neon FIBs are often sold as a dual-beam system (sometimes called helium ion microscopes or HIMs), where the He column replaces the electron column used for imaging in LMIS and ICP FIBs. From Xe to He, FIB micro-structuring is therefore possible in a wide range of length scales from millimeter to nanometer.

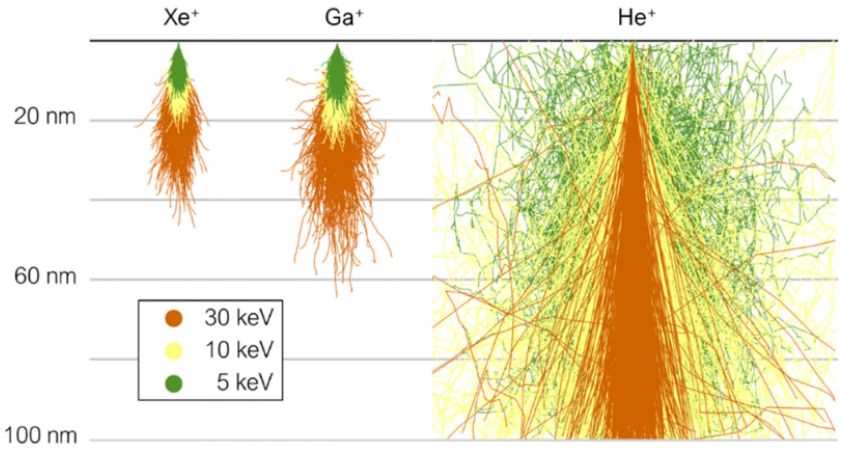

Figure 3.5: Stopping and Range of Ions in Matter (SRIM) simulations of Xe^+, Ga^+ and He^+ ions in silicon showing the interaction volume of the ion in the sample. Figure reproduced from [94].

Ion-Sample Interactions

The ion used for the FIB affects not only the size and shape of the beam, but also the interactions within the sample. Upon impact, ions will inelastically scatter with atoms in the substrate. Energy transferred to atoms near the surface can result in these atoms being sputtered out of the bulk, provided that the transferred energy is greater than the atom's binding energy and that the direction of the momentum transferred is out of the sample. These sputtered atoms may be pumped away by the vacuum system, or they can be redeposited on a nearby surface — this material is called *redeposition*. The sputter rate depends on the ion and the material and can even vary for different elements within a sample such that some elements can be sputtered from the surface more easily than others, changing the surface composition (*differential sputtering*) [35].

Atoms that are not close enough to the surface and that do not receive enough energy to be sputtered away can still be displaced from their original positions and collide with other nearby atoms. This chain reaction of collisions in the material is termed the *collision cascade* and will amorphize the impacted region of a crystalline sample. Both differential sputtering and amorphization can result in an outer crust that has very different properties from the bulk [35]. For example, this outer crust can be very insulating, making it difficult to establish electrical contacts with the bulk.

Furthermore, the ions will travel into the substrate until they are elastically scattered out (backscattering) or they have lost all of their energy and become implanted, which can effectively dope the material. Ion implantation is strongly dependent on the ion source used. One study used Atom Probe Tomography to compare the ion implantation of samples prepared with a multi-ion plasma FIB with N, O, Ar, and Xe. The ionic implantation within 100 nm from the surface was found to be lowest in Xe at $< 1\%$ and highest in N at $< 8\%$ [106]. Other

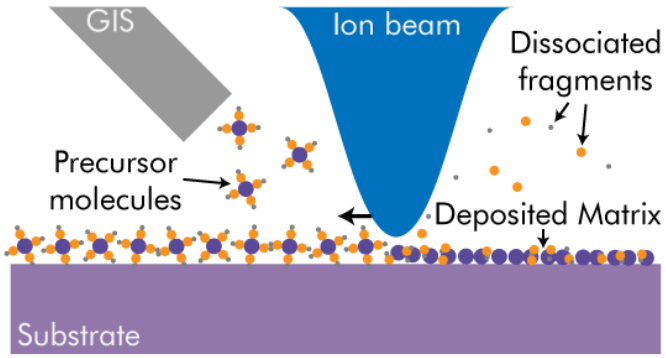

Figure 3.6: A sketch of the deposition process. The GIS needle is brought in near the substrate and a precursor gas is injected. These molecules are absorbed onto the surface and the FIB is used to break apart molecules locally, by scanning across the pattern.

studies comparing gallium and xenon implantation at grain boundaries found significant Ga-implantation but no significant Xe-implantation [107–110]. The differences in implantation concentrations is largely due to the size of the ion. Larger ions, such as Xe, do not penetrate as deeply into the sample and are therefore more likely to be backscattered out. This makes Xe a particularly attractive source when ion implantation needs to be avoided. A Xe pFIB was used for the work of this thesis.

At this point, it must be stressed that differential sputtering, amorphization and implantation are surface-effects and will be restricted to the distance traveled by the incident ions, while the bulk of the sample is preserved. The total volume of material that is affected by the incident beam is called the interaction volume, and is dependent on the ion size and the substrate. Figure 3.5 shows SRIM simulations of Xe^+, Ga^+ and He^+ ions at different voltages in silicon. For Xe and Ga FIBs, the damage layer is limited to the first < 60 nm of the milled surface. Increasing ion size or decreasing the excitation voltage will decrease the penetration depth and therefore also the thickness of the amorphization layer. The interaction volume is also dependent on the incident angle: ions will penetrate farthest into the substrate when the ion beam is normal to the substrate [89, 94].

Deposition

The deposition process is similar to etching but with the addition of a precursor gas. The retractable nozzle of the GIS is brought near the sample and a gas of precursor molecules is injected. Different precursors can be used, but the most common are for tungsten, carbon, and platinum depositions. The common precursor for W, for example, is $W(CO)_6$. As these molecules flow in, some will be adsorbed onto the surface of the sample, forming a monolayer (Fig 3.6) [94, 96, 111]. When the ion beam scans across the pattern, interactions between the beam and the substrate produce SE that can, in turn, interact with the monolayer and induce a decomposition of the molecule into volatile and non-volatile fragments. The volatile compo-

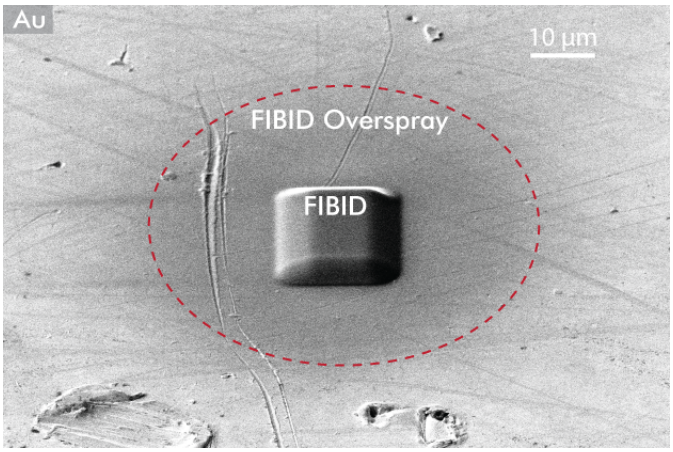

Figure 3.7: FIB Pt-deposition on a rough substrate. Surrounding the deposition is a dark halo of FIBID overspray.

nents dissociate and are pumped away by the vacuum while the non-volatile components are permanently deposited on the substrate [94]. In W deposition, the lighter CO are the volatile fragments. The decomposition of the precursor is never perfect, and the actual deposit will be a mixture of tungsten, carbon, oxygen and implantation from the ion source (negligible if Xe, significant for Ga). This material can therefore have physical and electrical properties that differ significantly from pure W [96, 112, 113]. Furthermore, the composition of the deposit can vary significantly depending on the deposition parameters. This complicates studies on the physical and electrical properties of FIBID as these properties can vary significantly depending on the growth parameters.

To deposit FIBID, one needs to carefully balance parameters such that the deposit grows efficiently and the ion beam does not begin to etch into the substrate. FIBID is limited either by the time it takes for the replenishment of the molecular monolayer (precursor-limited regime) or by the production of SEs (electron-limited regime). If the deposition is electron-limited, the monolayer is replenished faster than it can be decomposed, and the deposition will grow continuously. If the deposition is precursor-limited, the monolayer is not replenished fast enough, and the ion beam can begin to etch into the substrate [94]. A successful growth therefore requires sufficient time in between passes with the ion beam for the regeneration of the precursor.

Finally, some of the precursor gas is decomposed outside of the patterned area. Fig 3.7 shows a FIB deposit surrounded by a dark halo that is a thin layer of additional deposit. This deposit is sometimes referred to as *overspray* and arises from SE scattered far from the impinging beam site that induce the decomposition of the precursor molecules [94, 114].

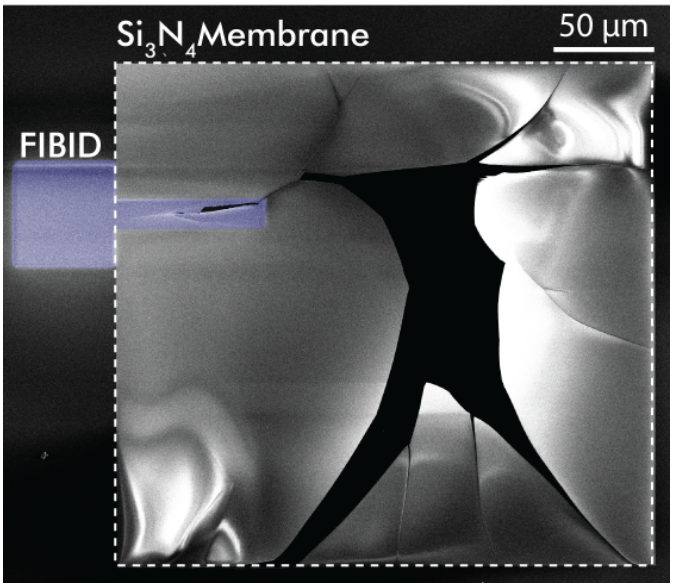

Figure 3.8: A 200 nm thick Si_3N_4 membrane that shattered during deposition due to charging effects.

3.2 FIB Processing

The etching and deposition capabilities of the FIB allow it to be used for micro-structuring complex devices. Etching away material enables the user to carve out 3D geometries and FIB deposition can be locally grown on the surface e.g. for mechanical or electrical connections. This process can be involved, and it requires careful planning and understanding of the FIB mechanisms before the sample ever enters the FIB. In addition to the ion, accelerating voltage, and current, the user can fine-tune many different parameters to optimize the fabrication and build a device with sharp, well-defined features. This section discusses in-detail these parameters before focusing specifically on a few key aspects exclusive to etching. It is also worthwhile to briefly consider the use of the micromanipulator. Specific values of parameters will be discussed in the context of the FEI Helios PFIB UXe (a xenon system) used for the work in this thesis. The concepts presented are universal for most FIBs, although specific settings may vary depending on the ion source and on the make and model of the system.

3.2.1 Charging and Heating

As micro-structuring a sample involves bombarding it with a flow of ions, charge can build up near the irradiated spot, particularly if the sample is poorly grounded or insulating. The accumulated charge causes the beam to deflect, resulting in an image drift [115–117]. Beam drift can be detrimental to etching and deposition processes as the position of the beam wanders outside of intended patterned area. In extreme cases, an excess of charge build-up can discharge, destroying the sample. Figure 3.8 shows a 200 nm thick Si_3N_4 semiconducting membrane in which charge accumulated during FIB deposition suddenly discharged, shattering

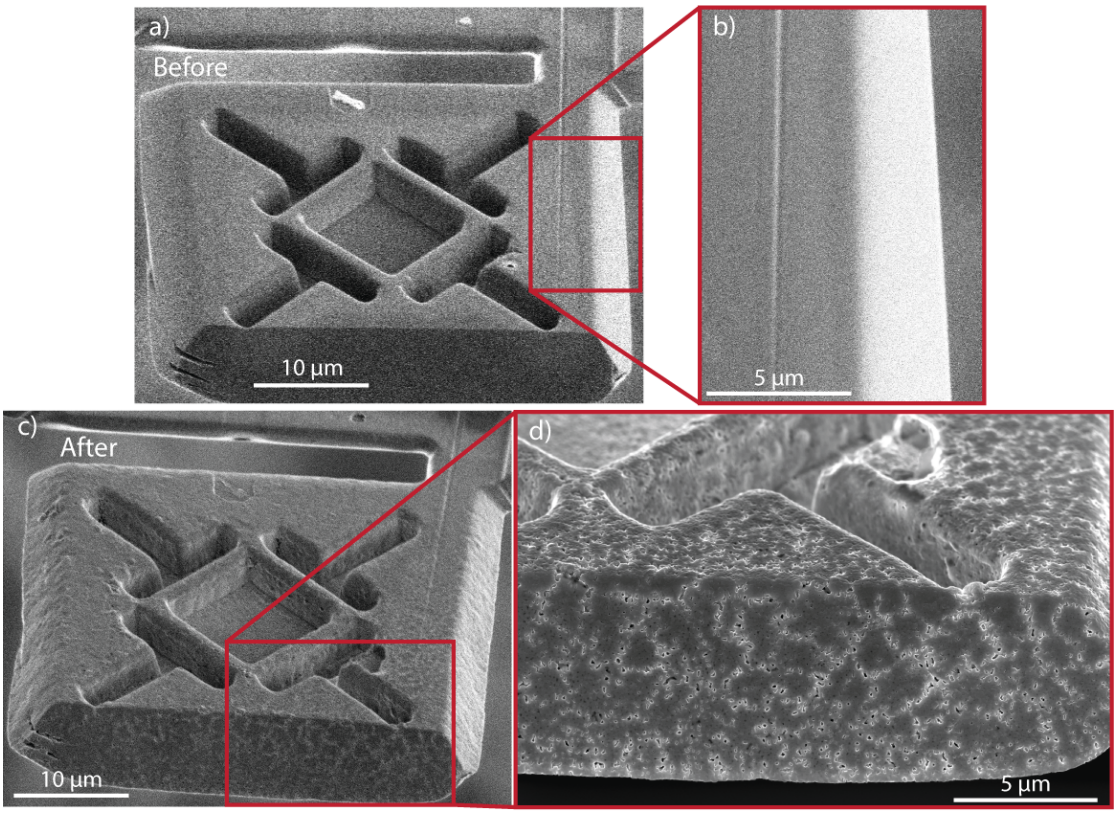

Figure 3.9: A solid, metallic crystal of SmFeAsO that deformed during FIB etching from sample heating, before (a-b) and after (c-d). Images (a) and (c) were taken within a minute of each other. In (d) the bright areas around the holes are regions where charge builds up, showing that they are much more insulating.

the membrane. The solution to this is to make sure that FIB samples are always well grounded. For good conductors, it is enough to glue the sample to the SEM stub with conductive paint (e.g. Silver Conductive Adhesive 503, #12686 from EMS). This paint can be easily removed with tweezers or solvent. In the example of the Si_3N_4 membrane, the membranes can be grounded by depositing 200 nm of gold on the surface and using the silver paint to electrically connect it to the SEM stub.

Moreover, the energy delivered to the sample during structuring can lead to significant heating. Naturally, the effect of this depends on the heat conduction of the sample and how sensitive it is to the heat. A particularly interesting example of heating deformation was seen in a single crystal of SmFeAsO that deformed from being solid and metallic in appearance to a sponge-like sample filled with holes ($\sim$ 100 nm) surrounded by insulating regions (Fig 3.9). The crystal was mounted on a thin glass capillary deposited with 200 nm gold, and therefore the heat had only a narrow pathway through which to dissipate. Overheating can be prevented by making sure that the etched region has a large thermal connection to the SEM stub and reducing the energy delivered to the sample per unit time.

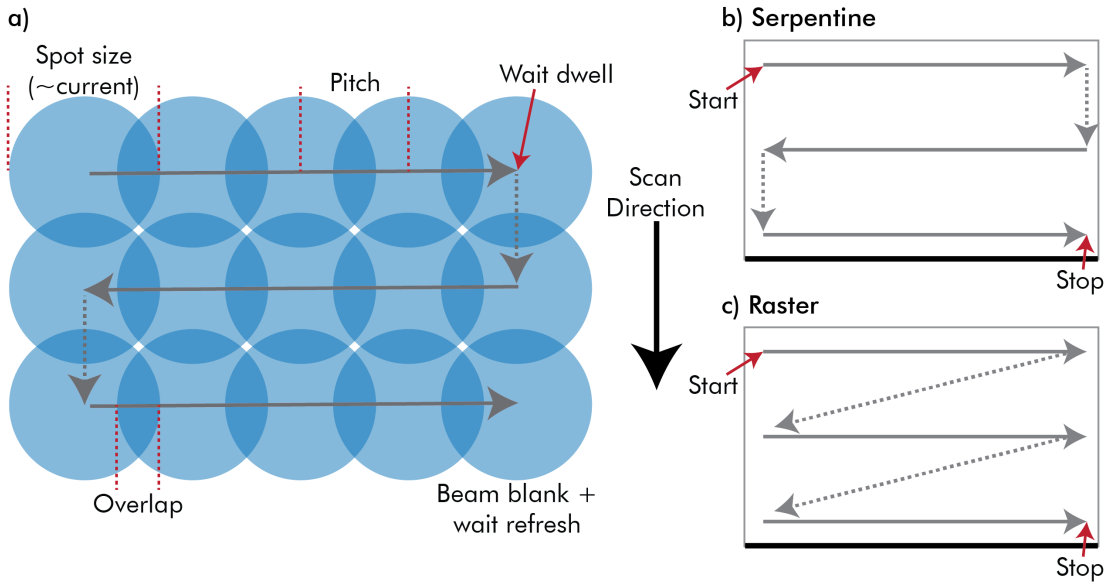

Figure 3.10: (a) In FIB processing, the ion beam is scanned across a user-defined pattern. The spot size of the beam is dependent on the current. The distance between each spot is the *pitch*. At each spot in the pattern, the beam will wait time t_{dwell}. After the last spot, the beam will blank and wait for a time t_{refresh} before repeating the pattern. (b) and (c) Different possibilities for scanning the beam across a rectangular pattern. The start and stop points for a single pass are marked. This pass will be repeated until the desired ion dose is reached.

3.2.2 Patterning and Scan Parameters

For both FIB etching and FIBID, the ion beam is scanned across different points in a pattern. Figure 3.10 (a) shows an example of how the beam will scan across a rectangular area. Each aspect from the accelerating voltage and current, the scanning parameters or the pattern to be scanned should be thoughtfully selected. A poor choice in parameters can result in, for example, the ion beam etching into the sample rather than depositing during FIBID. Generic parameter values for various FIB processes in the FEI Helios plasma FIB are shown in Table 3.1. More specific values for particular steps are discussed in Ch 4. These values should be tuned according to the material and application.

Beam Parameters

- **Acceleration voltage (kV):** the voltage used to accelerate ions through the column towards the sample. As shown in Fig 3.5, the acceleration voltage determines the depth of penetration of the ion in the sample. A higher acceleration voltage will therefore have a deeper layer of amorphization and ion implantation [106, 110, 118]. However, the imaging and milling resolution will be better at a higher acceleration voltage (e.g. 30 kV) because, at lower voltages (5 – 10 kV), the capacity of the ion optics to focus the beam is reduced [33].

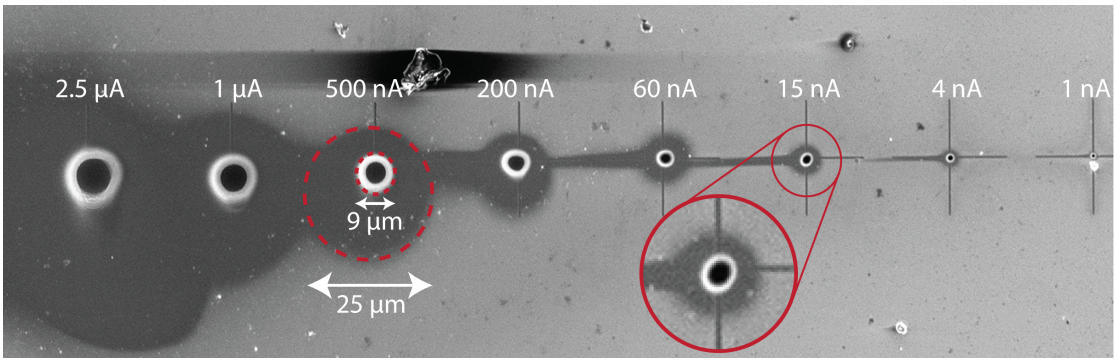

Figure 3.11: Spot test showing the etching of the ion beam on a single spot for different currents in the FEI Helios pFIB on silicon. Rounding of the etched walls can be seen by the white circles and damage from the long beam tail of the pFIB can be seen as the dark region surrounding the holes. Spot diameter and beam tail damage decrease for decreasing currents. Ideally, the spot should be perfectly circular. In this image, at 15 nA, the hole is slightly elongated, resulting from a slight astigmatism of the beam.

- **Ion beam current (pA-μA):** quantifies the flow of ions reaching the sample per unit of time and is selected by the diameter of the current aperture. Larger currents will therefore have a larger spot size, reducing the number of points in a pattern at which the beam must dwell (Fig 3.10) and, consequently, the amount of time needed to scan across the pattern. Both the spot size and the shape for any given current vary, depending on the alignment of the system. For precise fabrication, it is good practice to conduct a spot test, by milling a spot far away from the sample at the fabrication current. This allows one to check the shape of the beam, which should be circular, as well as the spot diameter, damage from the beam tail and rounding of the sidewalls that occurs from the Gaussian-like distribution of ions (Fig 3.11). The diameter should always be kept in mind during patterning: in Fig 3.11 at 500 nA, the spot diameter is 9 μm. If a pattern is drawn for etching, the actual etched area will extend ~ 4.5 μm outside of the drawn pattern with beam tail damage extending further.

  Additionally, the increase in beam diameter will increase the total power delivered to the sample but decrease the power density. Tuning the current can adjust the sample heating by reducing power delivered either to a spot or to the sample [33].

  Critically, for depositions, if the current is too high, then the production of SEs will be faster than the replenishment of the precursor monolayer, and the FIB will begin to etch rather than deposit [83, 94, 96].

Scanning Parameters

- **Dwell time t_{dwell} (ns-μm):** the amount of time the beam stays on a single spot before moving to the next. A short dwell time means that the etched area has a larger opening through which sputtered material can escape, reducing redeposition and improving the

	V (kV)	I (nA)	t_{dwell} (ns)	Overlap (%)	Blur (μm)	Gas Flow (%)
SEM Imaging	5-15	.8	25-2000	-	-	-
FIB Imaging	30	.03	25-2000	-	-	-
Etching	30	.1 - 2500	100	80	0	-
Deposition	12	.33- 20	50	-100 to 90	0-2.5	60-100

Table 3.1: Example parameters for various FIB processes done in an FEI Helios plasma FIB.

angle of the sidewall while a long dwell time can result in a narrow hole, increasing the percentage of sputtered atoms that will be redeposited inside the etched area [97, 119]. Successful depositions require short ($\sim 25-50$ nA) dwell times such that the precursor molecules have time to replenish. For etching processes, reducing dwell time can reduce heating as less energy will be delivered to a single spot per each scan.

- **Pitch and overlap (%):** The pitch is the distance between each spot while the overlap is the percentage of the spot size touching its neighbors. Setting one parameter will set the other.
- **Blur and defocus (μm):** To increase the size of the spot while decreasing the intensity, the beam can be defocused by setting either the blur or the defocus (these parameters are linked). Specifying the defocus defines the distance from the sample to the focal plane while specifying the blur sets the diameter of the defocused beam. Slightly defocusing the beam can increase the rate of deposition as the energy is dispersed, breaking apart the precursor molecules over a wider area without depleting the precursor too quickly in one concentrated spot. This widening of the effective spot size will, however, increase the generation of SE outside of the pattern, increasing the amount of overspray.
- **Refresh time t_{refresh} (ns-ms):** After finishing a scan, the FIB is blanked, such that the beam is deflected away from the sample. The system waits t_{refresh}, before repeating the scan. Critically for depositions, t_{refresh} must be large enough for the precursor to replenish. For etching a sample sensitive to over-heating, increasing t_{refresh} can allow more time for the heat to dissipate.
- **Gas flow (%):** (for depositions) sets the flow rate and type of the precursor gas injected into the chamber for FIBID. The precursor gas determines the composition of the FIBID.
- **Depth/height (μm) or dose (nC/μm):** The dose specifies the total ion current that should be delivered to a unit of area before the pattern is finished. In some systems (such as FEI) this is input as the z distance of the pattern to specify the final depth (for etching) or height (for deposition). As etching is dependent on the material parameters, this value is usually calibrated for etching in silicon and the actual final depth will vary depending on the etching rate of the sample. Likewise, deposition is dependent on the gas flow, pattern parameters and the substrate, and therefore actual height will vary.
- **Scanning direction:** indicates the direction that the beam is scanned through the pattern.

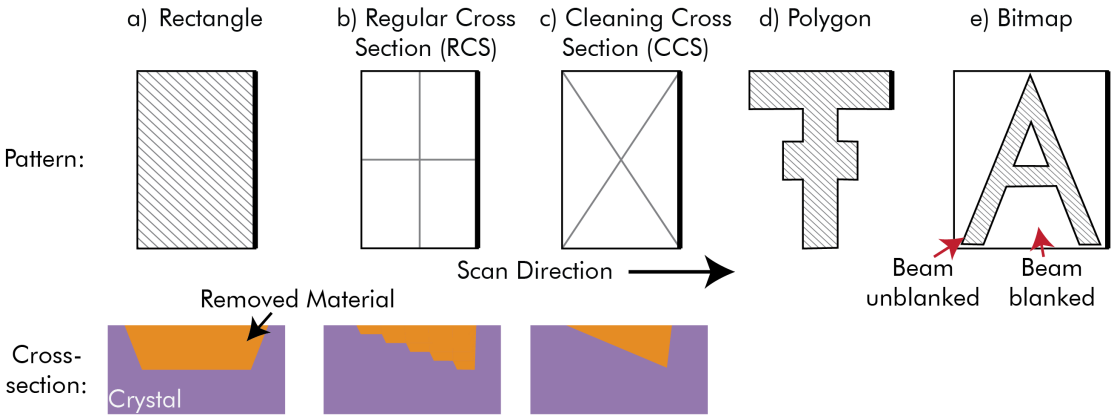

Figure 3.12: A few of the pattern types available on an FEI FIB. Top sketches shows pattern examples while the bottom sketches are the cross-section of the milled area. (a) In a Rectangle, a trench is milled out evenly. (b) An RCS mills out stepped trenches, removing less material than a Rectangle. (c) A CCS mills one line at a time to the full depth before moving onto the next line. Cutting a CCS results in sloped trench, due to redeposition. (d) An arbitrary polygon pattern can be drawn, for example, by merging rectangular patterns. A polygon will mill a trench evenly as in a rectangle. (e) Complicated images or structures can be cut by converting an image into a grayscale 24-bit bitmap pattern. The image contrast sets the FIB dosage at different pixels. For a simple letter with a solid background, the FIB beam is blanked while scanning across the background and unblanked on the letter. See Figure 3.14 for a more intricate bitmap.

Scanning Patterns

- **Spot:** The ion beam stays at a single point and is not scanned, mostly useful for testing the shape and size of the beam at different currents.

- **Line:** The beam moves across spots on a line, blanks for t_{refresh} and then repeats until the specified dose or depth has been reached.

- **Rectangle:** The beam scans across a rectangle, spending an even amount of time in each position to etch (or deposit) a flat rectangle (Fig 3.12 (a)). The most common methods for scanning across a rectangle are raster or serpentine (Fig 3.10 (b) and (c)). The scanning direction specifies the last line of the pattern, before the beam blanks, waits, and repeats. For a rectangular pattern, it is also possible to use a dynamic scanning direction in which the beam traverses the pattern in one direction, waits t_{refresh}, and then traverses the pattern in a different direction (e.g. dynamic top-to-bottom scans from top-to-bottom and then from bottom-to-top).

- **Regular Cross Section (RCS):** Overlaps rectangles with a set number of passes and scans through each of them, such that the region closest to the scan direction is scanned the most (Fig 3.12 (b)). This pattern is commonly used for digging out a lamella because it removes less material and is therefore faster than a Rectangle.

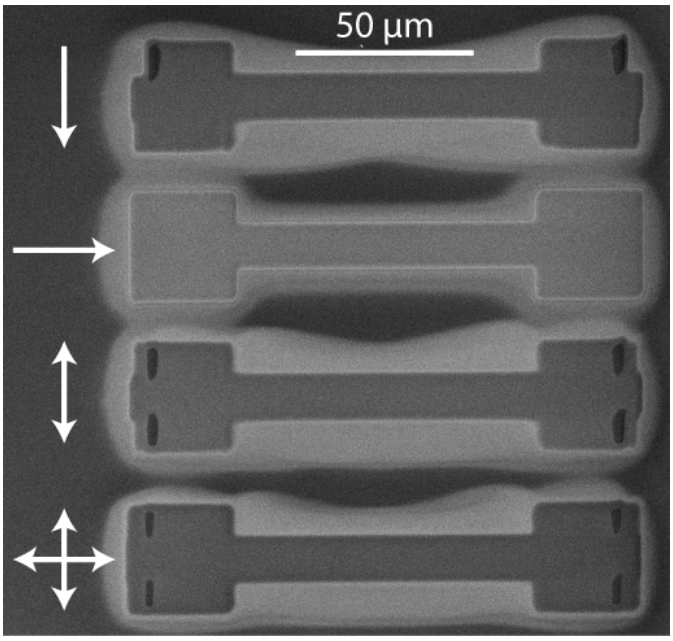

Figure 3.13: The path over which the beam in a polygon pattern is scanned is less straightforward than in a Rectangle. The result may be an inhomogeneous dose resulting in uneven etching. All four etched patterns used the exact same pattern and etching parameters — only the scan direction (as indicated by the arrows) was varied. In the bottom two patterns, dynamic top-to-bottom and dynamic all-directions were used. For a dynamic top-to-bottom scan, the beam scans top-to-bottom, waits t_{refresh}, and then scans from the bottom-to-top. For a dynamic all-directions scan, the pattern is scanned in each direction (top-to-bottom, bottom-to-top, left-to-right, and right-to-left) one after another until the dose is reached. Only the left-to-right scanning direction resulted in the desired uniform etch.

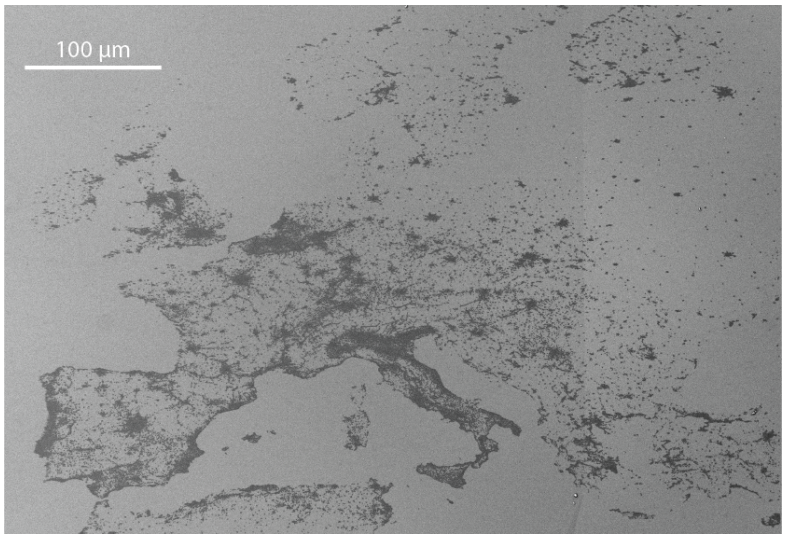

Figure 3.14: A satellite image at night shows the light pollution of Europe. This image was converted into a grayscale bitmap and etched into silicon using a bitmap pattern with a Zeiss Crossbeam 540 gallium FIB. In a bitmap pattern, the image contrast defines the dose delivered at different points across the pattern. Original satellite image taken by NASA [120, 121].

- **Cleaning Cross Section (CCS):** Scans across each line to the full dose before moving to the next line. If the pattern is drawn on a flat sample, redeposition from the later lines will fill up etched regions from earlier lines, resulting in a sloped trench (Fig 3.12 (c)). As the name implies, the CCS is mostly used for cleaning or polishing an edge at the last line of the pattern.

- **Polygon:** Overlapping rectangles are merged together which can, in principle, enable uniform dosage across an arbitrary shape (Fig 3.12 (d)). However, this is not always the case: while a rectangle has a well-defined geometric shape over which the beam can be guided in a simple path, delivering a homogeneous dose, polygons can be arbitrarily complex. The computer must decide upon a path for the beam to take (a mathematically challenging problem) and the result may not supply an even dose. This is demonstrated in Fig 3.13 in which a polygon pattern was etched using different scanning directions. Only the left-to-right scanning direction has achieved the desired uniformity for this pattern. In this direction, the path of the beam can simply be a serpentine or raster (Fig 3.10), as used for rectangular patterns. Therefore, if precision and uniformity are necessary, it is recommended to test different scan directions of a polygon before patterning on the sample.

- **Bitmap:** More complicated patterns are possible using a bitmap pattern (Fig 3.12 (d)). A grayscale, 24-bit bitmap image can be used to define the FIB dosage at different points using the contrast of the image. While this is most often used for cutting the name of a sample onto a substrate, intricate patterns can also be etched (Fig 3.14).

3.2.3 Etching

Etching into a material will not produce straight walls or sharp corners. The shape of the beam and its interactions with the sample will result in rounding and redeposition can build up around the etched trench. As shown in Fig 3.11, reducing the current reduces the beam tail and improves precision; although this increases fabrication time, and the rounding will only be reduced and not removed. Sidewall rounding can be removed with a few key tricks:

- Scan direction: for an RCS or CCS, the wall closest to the last line of the pattern will have less redeposition.
- Capping layer: a thick deposition on the surface can protect the top from beam tail damage. After structuring, this deposition can later be cut-off, resulting in a sharper corner and a flatter wall.
- Free-space structuring: a lamella can be cut out of the sample and then mounted onto a holder that allows the lamella to be polished or structured in free-space. Etched material can escape freely into the vacuum of the chamber, eliminating redeposition. This process is essential for FIB cantilever fabrication and is described in detail in 4.2.3.
- Polishing: sidewall rounding can be removed by careful polishing. Polishing in free-space rather than in a milled trench eliminates redeposition, making it possible to achieve parallel walls much more efficiently. This method, detailed in 4.2.4, involves using a CCS at a slight angle to correct for the beam shape and interactions.

Additionally, either an inhomogenous surface or a spatial variation of the sputter rate due to ion interactions in the sample can lead to the appearance of striations which resemble cloth curtains (Fig 3.15). This effect, called "curtaining", is strongly material dependent. Because the ion interactions depend on the ion, curtaining may also be dependent on the ion source [99]. Cutting off an inhomogenous surface and/or depositing a capping layer can help prevent curtaining. Curtaining can often be removed by polishing with a CCS. Another approach is to use a special rocking stage that rocks the sample in the ion beam to alternate the incident angle of ions [122].

Finally, one of the advantages of the FIB is the ability to select defect-free parts of a sample. While etching, defects such as holes, flux-inclusions, or cracks can be revealed (Fig 3.15). In the best case, these can be polished or cut off. In the worst case, if a defect runs through a critical part of a sample that cannot be cut off, it may be necessary to start over with the fabrication.

3.2.4 Micromanipulator

FIBs are often equipped with a micromanipulator needle that can be useful for transferring lamellae. After the shape of the lamella is cut out of the sample, leaving bridges to hold it in

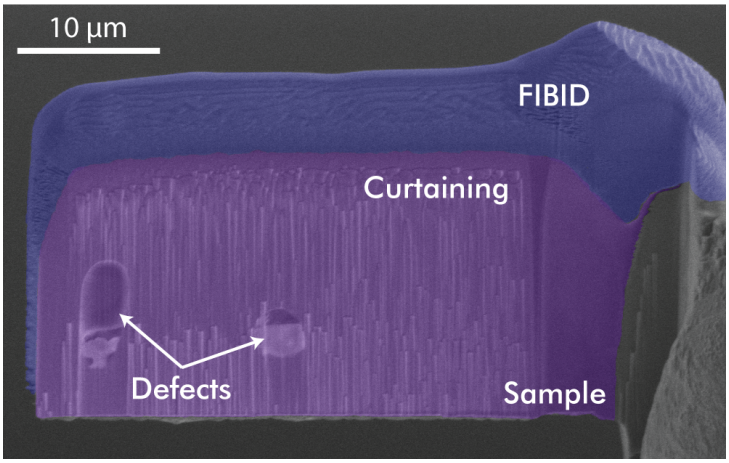

Figure 3.15: An SEM image showing a lamella with FIBID on the top. Curtaining is clearly visible as the striations on the side of the lamella. Both the curtaining and the defects that have been revealed during etching can be polished away.

place, the needle is welded to the lamella with FIBID. The bridges are cut, and the lamella can be extracted. For mounting, the needle is steered to press the lamella against the new mount. FIBID is used to weld the lamella to the mount and the needle is cut away. The micromanipulator is invaluable for cantilever fabrication and multiple transferring processes are discussed in Chapter 4.

For the work done in this thesis, an FEI EasyLift Micromanipulator was used. The EasyLift system allows the needle to be moved freely along x, y and z (where x and y are in the imaging plane of the SEM and z is parallel to the SEM — see Fig 4.7) and to be rotated along the axis of the needle. With this system, the stage cannot be moved once the manipulator is inserted near the sample. The needle has to be retracted and reinserted each time the stage is moved.

The tip of a new needle is usually ~ 500 nm; however, because a piece of the needle is cut after each transfer, the needle will become much thicker after use. A thick needle is hard to maneuver as it can scrape against sides of the sample or mount. Consequently, it is good practice to sharpen the needle for a tip ~ 1 μm in between each transfer. To sharpen the needle, the stage is moved such that the sample is far away from the ion column, this prevents redeposition from the W needle from being deposited on the surface of the sample as the needle is cut. The needle is inserted and rectangle or line patterns are drawn on either side at a slight angle from the axis of the manipulator, defining the needle point (Fig 3.16 (a)). These patterns can be run at high current to efficiently remove the excess material (i.e. 200 nA - 2.5 μA). The needle is then rotated 30°, the patterns are adjusted and the etch is repeated. This process is continued until the needle has been rotated 180° and a sharp point is defined (Fig 3.16 (b)). This sharpening process should only take a few minutes. If the needle has become so thick that it requires a long time, then it is more efficient to have the needle replaced.

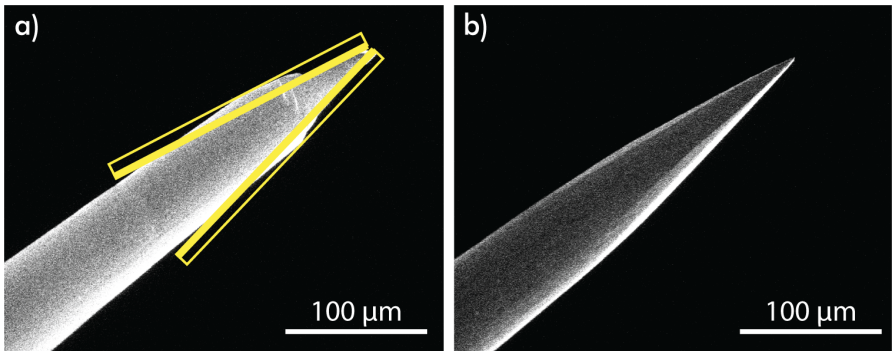

Figure 3.16: Sharpening the micromanipulator: (a) Patterns are drawn at a slight angle on either side of the needle. These patterns are run at high current to remove excess material. The manipulator is rotated and this process is repeated. (b) Sharpened needle.

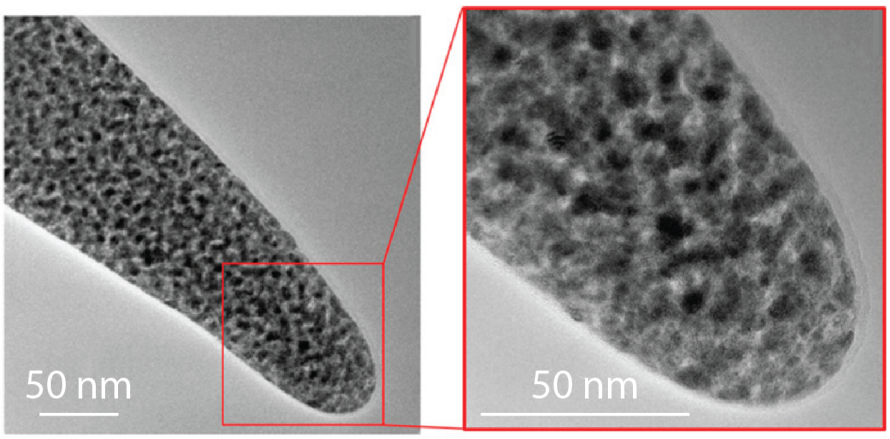

Figure 3.17: High-Resolution TEM image of a FIB deposited PtC nanotip showing the metalic nanograins in the carbonaceous matrix. The tip was deposited at 30 kV, 260 pA using Trimethyl(methylcyclopentadienyl)platinum(IV) (MeCpPtMe3) as a precursor gas. Figure reproduced from [123].

3.2.5 FIBID

It is worthwhile to return to the unique microstructure of depositions that arises due to the imperfect decomposition of the precursor molecules. As the precursor gas for W or Pt deposition is broken apart, some of the organic components will be pumped into the vacuum while some are deposited. TEM measurements of FIB deposits reveal metallic nanocrystals embedded in a carbonaceous matrix (Fig 3.17) [123]. The exact composition of the deposit varies depending on the growth parameters and the recorded physical properties can differ not only from their pure-metal constituent but also by changing growth parameters [94, 124]. Perhaps the most startling deviation of FIBID from pure metal was reported in 2004, when it was discovered that FIBID W is a superconductor with $T_c \sim 5$ K [112]. Single crystalline W, in contrast, is a superconductor with $T_c < 50$ mK [125].

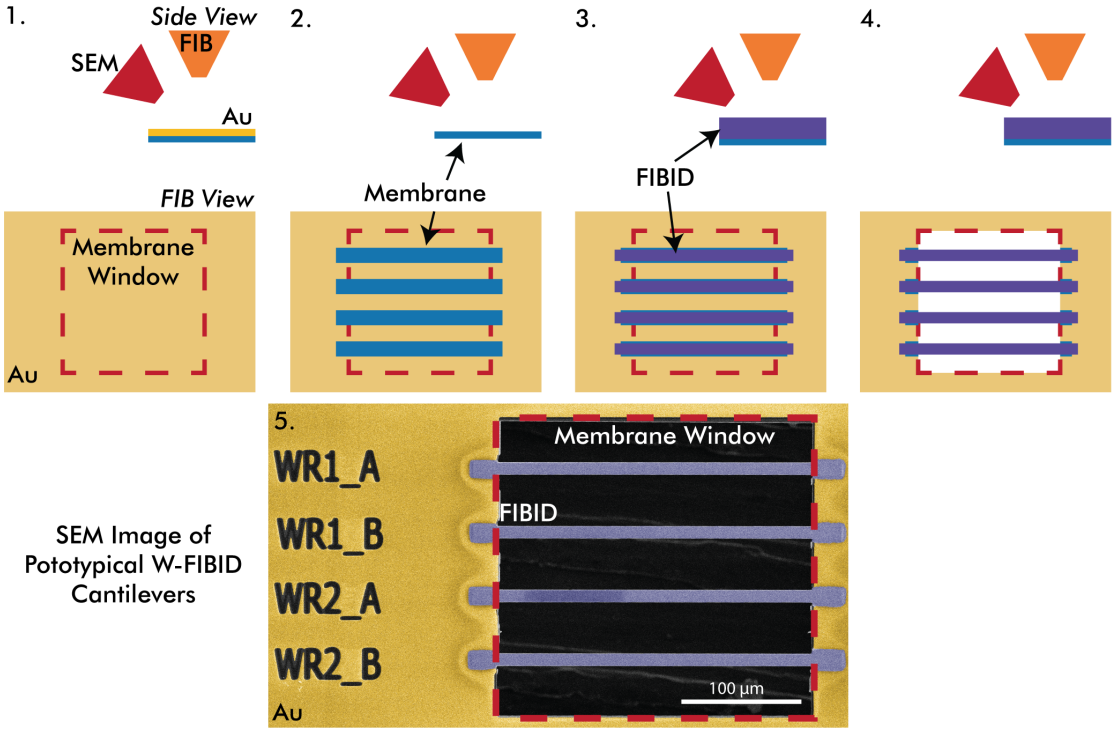

Figure 3.18: Top: Sketch for fabrication method of FIBID cantilevers by growing deposits on a 200 nm Si_3N_4 window. 1. The membrane is coated with gold to prevent charging (see Fig 3.8). 2. This gold can then be removed on the areas where the deposits will be grown. 3. FIBID are grown across the length of the membrane. 4. The rest of the membrane is cut, releasing the deposited cantilevers. Bottom: SEM image of prototype W FIBID cantilevers grown using this method.

In this thesis, FIBID is used to clamp FIB-fabricated cantilevers to the substrate and define the fixed boundary condition. To determine Young's modulus from the resonance frequency of the cantilever, a simple approach has been used in which one end of the cantilever is assumed to be perfectly rigid, rather than an imperfect clamp. The accuracy of this model for the absolute determination of Young's modulus is limited by neglecting the effect of the clamp. Furthermore, depositing the clamp also creates overspray on the cantilever which will shift the measured value of Young's modulus. While the thickness of the overspray and the dimensions of the clamp can be measured via SEM images, the elastic properties and density of the deposits are not known. Obtaining these values would improve the calculation of Young's modulus. Because of the many parameters that can be varied for FIBID, determining the elastic properties of FIB deposits requires a large number of measurements on many different samples. A review on ion beam and electron beam induced deposition by Utke et. al. examines the existing elasticity measurements on deposits, almost all of which are conducted on nanostructures grown with a gallium FIB [124]. A method for the growth of macroscale FIBID cantilevers for the study of deposits with varying parameters including different ion sources is proposed below and sketched in Fig 3.18.

1. **Gold coating of a thin membrane:** Depositions can be grown on top of a commercially-available thin Silicon Nitride membrane (200 μm thick frame, 200 nm thick membrane window, window size 250 μm from Spi supplies). To prevent charging of the semiconducting Si_3N_4 (Fig 3.8), the membrane is deposited with 200 nm of gold. The membrane chip is then mounted onto an SEM stub with SEM silver paint (e.g. Silver Conductive Adhesive 503, #12686 from EMS) touching the gold for grounding. With the gold deposition covering the membrane, the window cannot be distinguished from the rest of the chip while imaging with the FIB. This is also a problem when low voltages are used in the SEM, however, if an accelerating voltage of at least 15 kV is used, then the electrons penetrate far enough through the gold and membrane such that the covered window is visible and patterns in the FIB can be aligned.

2. **Gold removal:** The stage is tilted such that the membrane is normal to the ion beam (52° in the FEI Helios). With the ion beam at 12 kV and a current of 15-200 nA, the gold is removed only on the parts of the membrane where FIBID cantilevers will be deposited. The low voltage of 12 kV is used such that the ions do not penetrate as far into the membrane, damaging the thin membrane. The patterning should be watched carefully while the gold is etched. A change in contrast indicates that the gold has been removed and the patterning should be stopped, etching longer will etch through the membrane.

3. **Deposit cantilever:** Cantilevers of the desired growth parameters are deposited across the length of the membrane window.

4. **Cut membrane:** The membrane must be carefully cut through to release the cantilevers. To avoid removing the gold such that the membrane charges and shatters, this is best done using CCS to cut through the membrane, line-by-line.

5. **Label and image:** Bitmap patterns are used to label each cantilever with the deposit material, recipe name, and cantilever name. SEM images showing the geometry of each cantilever are taken.

If the resonance frequencies of the cantilevers are measured, Euler-Bernouli Beam Theory for a double-clamped beam (Eqn 2.38) can be applied to calculate the ratio E/ρ. For a deposit thickness much larger than the 200 nm membrane, then the effect of the membrane will be a small correction. This correction can be determined by measuring the resonance frequency of cantilevers cut from the membrane without depositions. Finally, determining E explicitly requires a separate measurement of the density. This can be done by using calibration cantilevers with a known resonance frequency and measuring the shift in resonance with a small deposit at the end of the cantilever. The mass of the deposit can be determined from the change in the resonance frequency.

4 FIB Fabrication of Resonant Cantilevers from Exotic Materials

At the heart of this project is the fabrication of cantilevers from novel materials. Because the frequency of a mechanical resonator is defined by the geometry, elastic tensor, and the orientation of the sample with respect to the lattice (Eqn 2.37), this technique emphasizes precise geometric control and well-oriented samples. Additionally, FIB cantilever fabrication truly excels in the flexibility of materials from which cantilevers can be cut. While this thesis examines cantilevers of the cuprates, iron-based superconductors and perovskite nickelates, FIB fabrication of devices for electrical transport has been successfully applied for many other correlated electron systems such as topological materials [35, 44] and heavy-fermions [37–39, 126].

The FIB's ability to selectively etch enables a three-dimensional geometric control by cutting the sample into the desired configuration with a 100 nm precision. FIBID is used throughout the process primarily as a weld to rigidly connect different components. An in-situ micromanipulator is also integral as, with it, the sample can be moved and positioned. The workflow for cantilever fabrication involves cutting the rough shape of a cantilever out of an oriented crystal. With the micromanipulator, the lamella is then extracted from the crystal and welded to a grid which makes it possible to cut and polish the lamella into its final shape. The micromanipulator is then used again to move the cantilever to the sample chip where one end is fixed into place using a layer of FIBID. The name of the cantilever can be cut into the substrate, SEM images taken to measure the final geometry of the cantilever and the sample is ready for resonance measurements.

At different steps, there exists the possibility for modification according to the needs of the experiment. The procedure presented here produces a simple cantilever beam, fixed on one end, predominantly from single crystals displaying intriguing quantum phenomena. This process, however, should be applicable for nearly all materials that can be etched with a FIB — although some may present additional challenges to overcome. Moreover, the 3D nature of this process enables the realization of more complicated geometries. Doubly-clamped cantilevers could be built, or deposition processes could be used to create multi-layered beams. The goal of the following sections is to provide a clear description of the steps that the interested reader

can follow and modify as needed.

Finally, as the main goal of FIB cantilever fabrication is to explore elasticity, it is worth mentioning that FIBs have previously been used to study elasticity in materials that are otherwise challenging to work with, for example, due small sample sizes. In micropillar compression, the FIB is used to etch pillars into a sample which can then be compressed while the deformation is measured to obtain the stress-strain curve. Unfortunately, surface amorphization from the FIB-fabrication can greatly increase the yield-strength of the pillars [127]. On the other hand, resonance measurements on FIB-fabricated cantilevers are conducted well into the material's elastic regime rather than at the high-strains of micropillar compression. Resonance frequencies of FIBed cantilevers are therefore sensitive primarily to the bulk of the sample, rather than to the ≈ 30 nm layer of surface amorphization. Furthermore, measurements of resonance frequencies are much more accurate than measurements of small deformations in hard materials. This improved accuracy is greatly needed for studying the small modifications to elasticity that can arise due to subtle electronic correlations.

4.1 Cantilever Design

Fabrication begins with the design of the cantilever and the substrate on which the sample is mounted. The cantilever geometry is chosen based on a few guiding principles:

1. Most essentially, the cantilevers should be designed such that the resonance frequency of interest is within the range of the interferometer used for measurements (cantilevers in this thesis were designed for a fundamental resonance $f_1 < 500$ kHz). For a simple, rectangular cantilever, EB Theory (2.2.1) can be used:

$$f_n = \frac{\alpha_n^2}{2\pi}\frac{T}{L^2}\sqrt{\frac{E}{12\rho}} \tag{2.37}$$

   where T, L, E and ρ are the thickness, length, Young's modulus and density of the cantilever and $\alpha_1 = 1.875$ for the fundamental resonance mode of single-clamped cantilever. If Young's modulus is not known, E is estimated based on similar materials (e.g. $E \approx 100$ GPa for the materials in this thesis). For EB theory to be accurate, $T << L$ (See Fig 2.5). For other cantilever geometries, Finite Element Analysis can be used to simulate the resonance frequencies and modes and design the geometry accordingly.

2. Obviously, the geometry must be cut from the available samples and the final cantilever cannot be larger. Furthermore, some length ($2-10$ μm) of the cantilever is cut off during the fabrication procedure and the final cantilever is firmly clamped on the substrate by covering $4-10$ μm with FIBID. Therefore, if the starting length of the crystal is 100 μm, then the maximum possible unclamped length of the final cantilever is 94 μm.

3. To measure the cantilever using an interferometer, the width should be wider than the

spot size of the lens (2 μm for the lens in this work). A wider cantilever is easier to align for measurements. The fabrication time also increases with the width.

4. A very thin cantilever is at risk of deforming due to heating during fabrication. While it is possible to thin a cantilever down to 500 nm, low currents ($I \approx .1$ nA) must be used to prevent excess heating. It is therefore easier and faster if $T \geq 1$ μm.

5. The error, σ_E, on the calculation of Young's modulus from EB theory is given by:

$$\frac{\sigma_E}{E} = 2\sqrt{\left(4\left(\frac{\sigma_L}{L}\right)^2 + \left(\frac{\sigma_T}{T}\right)^2 + \left(\frac{\sigma_f}{f}\right)^2\right)} \tag{2.39}$$

A typical cantilever has resonance frequency $f \approx 100$ kHz, $\sigma_f \approx 10$ Hz, length $L \approx 100$ μm, $\sigma_L \approx 1$ μm, and thickness $T \approx 1$ μm, $\sigma_T \approx .1$ μm. The error is therefore dominated by the first and second terms with the geometric uncertainties largely due to small variations in thickness across the length of the cantilever. Increasing T can reduce the error on the calculation of Young's modulus.

Following these guidelines, cantilevers during the course of this thesis were fabricated with dimensions $L = 17 - 100$ μm, $W = 6 - 12$ μm, and $T = .8 - 2$ μm.

4.1.1 The Substrate: Mounting Conditions

The substrate used for mounting the cantilever is critically important to the fabrication process as the cantilever must be well-coupled to the piezoelectric transducer used for vibrating the resonance modes. Most importantly, for a good mount, the sample must have well-defined boundary conditions: the cantilever should sit flat on the surface and be rigidly fixed on one end with minimal dissipation between the piezo and the sample. Furthermore, in the measurement set-up used, samples are aligned by taking images using a photo-diode to measure the intensity of reflected light at different positions — requiring high contrast between the light reflected on the cantilever and the background (5.4.1). Finally, the substrate should be of practical design for fabrication and handling.

Several methods were tested in order to determine the best cantilever mounting condition. Commercially-available membrane chips (e.g. Spi Supplies Silicon Nitride Membrane Window TEM Grids, 200 nm thick, 0.25 mm window) were found to be excellent substrates for mounting FIB cantilevers. These silicon chips have a window (aperture 100 μm – 1 mm) consisting of a thin (10 – 200 nm) silicon nitride membrane most often used as holders for Transmission Electron Microscopy (TEM) samples. Beneath the membrane is an inclined slope that results from the highly directional etchant used for fabrication. When the membranes are turned upside down, cantilevers can be mounted on the backside, on the edge of the slope. During measurements, incident laser light on the cantilever will be reflected directly back into the lens, while incident light on the steep slope will be reflected at an angle, away from the lens (Fig 4.1) providing excellent signal contrast for imaging.

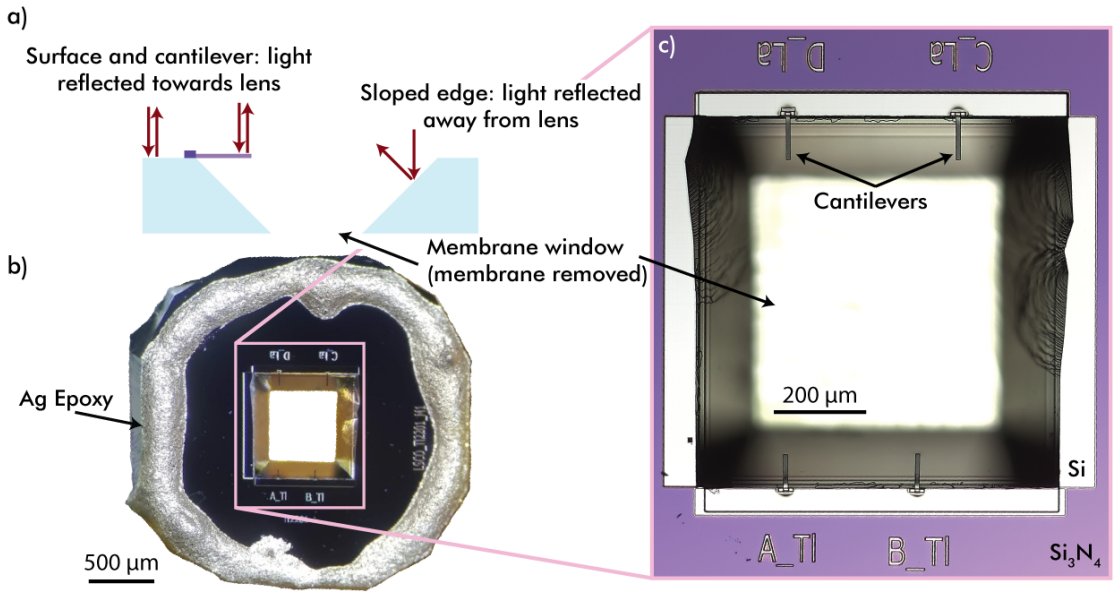

Figure 4.1: Method of mounting cantilevers onto the backside of a silicon chip fabricated with a thin membrane. The membrane is removed before mounting samples. (a) Incident light on the surface of the chip and on the cantilever is reflected back into the lens. Incident light on the sloped edge is angled away from the lens. By measuring the intensity of reflected light with a photodiode, the sample can be imaged and aligned. (b) A membrane chip. Silver Epoxy drawn as a ring on the edge before mounting samples acts to protect the cantilevers from any accidents during handling. (c) This chip has four cantilevers on the edge of the slope. The Si_3N_4 layer has been removed adjacent to the slope so that the cantilevers are mounted directly on the silicon.

Although the membrane itself is not used in this mounting method, thin shards from the membrane pose a risk to the cantilevers if it is accidentally broken at some point after fabrication. For this reason, the membrane should be gently removed before mounting any samples with a pair of tweezers or by brushing the top side of the chip on a rough piece of paper. For extra sample protection, a small ring of silver epoxy (e.g. Epo-Tek H20E) can be drawn around the edge of the chip preventing cantilevers from breaking off even if the chip is flipped upside down (Fig 4.1). Additionally, the bottom side of the chip also has a thin layer ($\approx$ 200 nm) of silicon nitride that can detach from the silicon during the process of cantilever mounting. To avoid this (and prevent charging of the cantilever as the silicon nitride layer is insulating), this layer should be removed with the FIB (with currents 200 nA – 2.5 μA) before mounting any cantilevers on the chip.

4.2 Fabrication Steps

An outline of the full fabrication process is given below and illustrated in Fig 4.2. The methods for large and small samples vary slightly and each are detailed in Sections 4.2.1 and 4.2.2, respectively. Sections 4.2.3-4.2.5 detail the remaining fabrication steps. Cantilevers were fabricated using an FEI Helios FIB with a Xenon-plasma source equipped with an EasyLift Micromanipulator that uses a Tungsten needle. The process can also be done using a FIB with a different ion source (i.e. Gallium) although the currents used for some steps may have to be modified depending on the capabilities of the system.

Cutting a Lamella from an Oriented Sample

1. **Orientation:** Because the dependence of Young's modulus on the elastic tensorial components results from the orientation of the cantilever (See Sec. 2.1.3), the first step is to determine the crystalline directions. Samples are oriented by Laue diffraction or by single crystal X-ray diffraction (XRD).

2. **Mounting for FIB:** The bulk crystal must be mounted for processing in the FIB, taking care that the orientation matrix obtained in step 1 can be referenced to either a face or a line on or near the crystal. To prevent sample charging, the crystal must also be well-grounded.

3. **Cutting a Lamella:** Inside of the FIB, the rough shape of the lamella is cut in the chosen orientation. One or two bridges are left to hold the sample in place.

Transferring the Lamella to a Grid

4. **Welding the Manipulator:** The micromanipulator is welded to one corner of the sample using FIBID.

5. **Lamella Extraction:** Bridges are cut and the micromanipulator with the sample can be

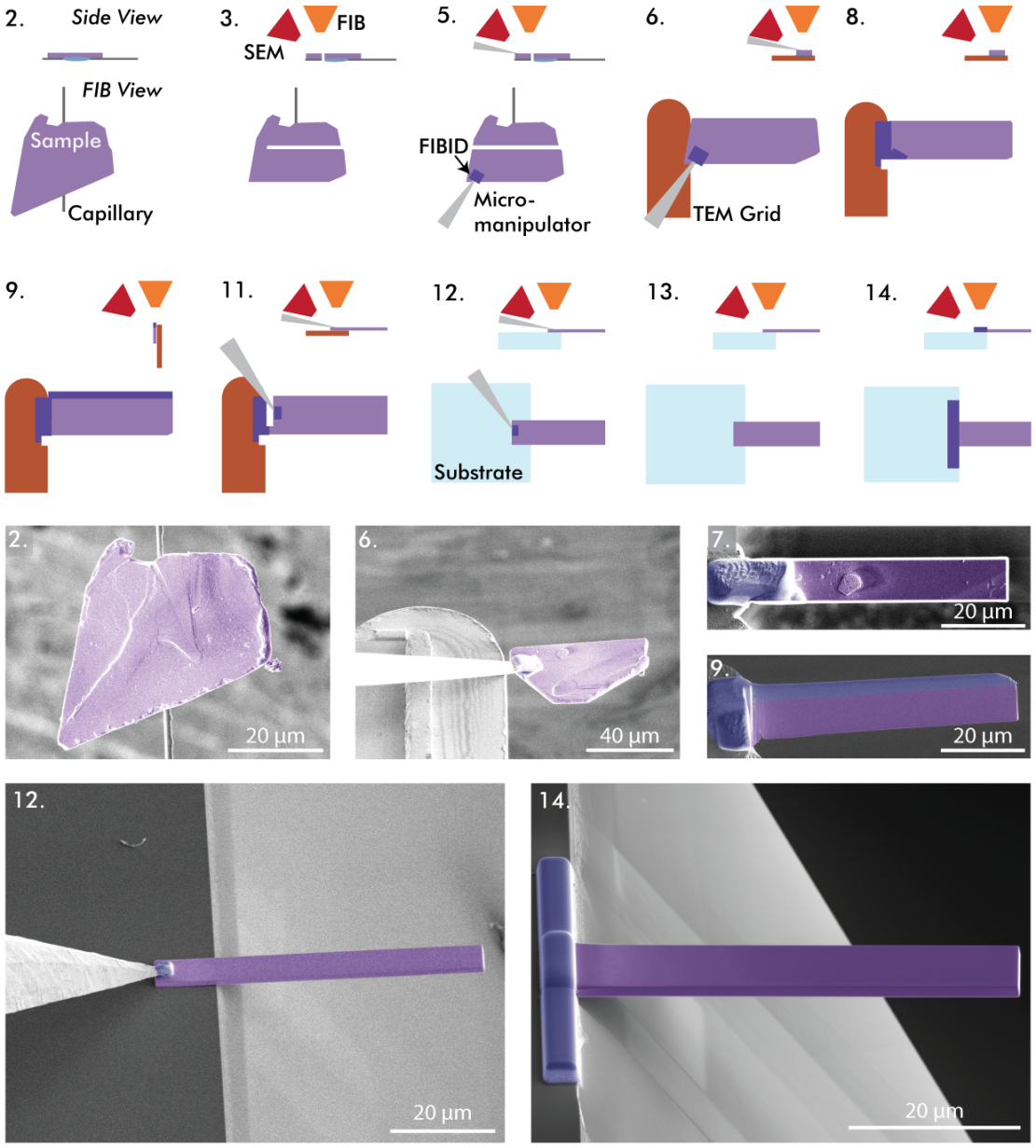

Figure 4.2: FIB process for cantilever fabrication from a microscale single crystal. Upper images show a side view and FIB view sketches of key steps. Lower images are SEM images of key steps. For XRD, the sample is mounted onto a thin glass capillary after which it is inserted into the FIB for fabrication. First, the micromanipulator can be welded to the sample using FIBID and a piece of the crystal can be cut off. This lamella is then mounted to a TEM grid, the manipulator is removed and the cantilever is polished. The manipulator is then used again to remove the sample from the TEM grid and mount it onto the substrate. FIB deposition finally fixes the boundary conditions of the sample.

safely extracted.

6. **Mounting to a Grid:** In order to ensure parallel sides from the cantilever, it must be polished and cut in free-space to prevent any redeposition from nearby surfaces. A commercially available TEM grid acts as a convenient holder for free-space polishing. Using the micromanipulator, the sample is pressed flat onto the TEM grid and FIBID is used to weld the sample to the grid.

7. **Removing the Manipulator** The micromanipulator is then cut free and extracted.

Polishing the Cantilever

8. **Rough cutting:** The lamella is cut rectangular, leaving ≈ .5 μm on the edges that can be polished off later.

9. **Fine Polishing:** The cantilever sides are polished such that they are parallel.

10. **Final Shaping:** Next, the final shape of the cantilever is cut, leaving a small bridge holding it to the grid.

Transferring and Mounting the Cantilever

11. **Cantilever Extraction:** The micromanipulator is welded to one end of the cantilever, the bridge is cut through and the manipulator is extracted.

12. **Mounting:** The cantilever is pressed flat onto the surface of the final sample chip. By cutting through the cantilever near the manipulator, redeposition welds the cantilever onto the substrate, the manipulator is detached and can be safely removed.

13. **FIBID Weld:** FIBID is used to weld the cantilever to the substrate, defining the boundary conditions of the clamped beam.

14. **Final Imaging:** The name of the sample can be cut into the substrate and final SEM pictures with the sample geometry are taken.

4.2.1 Cutting a Lamella from an Oriented Sample - Large Crystal

1. Orientation

For relatively large crystals, this can be done by Laue diffraction or XRD. For Laue, samples were mounted directly onto the sample holder and crystal faces were determined using a MutliWire Laue back-reflection diffractometer. For XRD, large samples can be mounted onto the end of an X-ray needle fixed to a magnetic foot. Well-defined edges of the sample can be used as references from which cantilevers along different orientations can be cut.

	Acceleration Voltage (kV)	Current (nA)
Deposit Capping layer	12	4-20
Cut Trenches	30	1000-2500
Rough Polish	30	60-200
Undercut	30	60-200

Table 4.1: Typical currents and voltages for cutting a lamella from a large sample in an FEI Helios PFIB.

2. Mounting for FIB

The sample can then be mounted onto an SEM stub with a small amount of conductive paint (i.e. Silver Conductive Adhesive 503, #12686 from EMS) to fix the sample and to electrically ground it.

In order for the final cantilever to have the desired orientation with respect to the crystalline lattice, the sample should be mounted such that the longest and shortest directions for the final cantilever are both parallel to the plane of the sample stage (perpendicular to the FIB column when the stage is tilted 52°). E.g. for an orthorhombic sample, if the length, L, should be in the [100] crystallographic direction, and the thickness, T, should be in the [001] direction, then the bulk crystal should be mounted such that [010] is perpendicular to the stage (parallel to the FIB at 52° tilt) (See Fig 4.3).

3. Cutting a Lamella

The process for cutting the lamella from the large crystal is illustrated in Fig 4.3. Typical currents and voltage values for each step are detailed in Table 4.1.

(i) **Deposit Capping Layer:** A capping layer from FIBID (usually Pt, although W and C can also be used) is used to protect the lamella from the beam tail thereby improving the parallelity of the cantilever sides. Additionally, the homogeneity of the deposit can reduce the effects of curtaining if the sample surface or composition is inhomogeneous. First, the sample is tilted such that the surface is normal to the FIB (52°). An even section of the surface — free from cracks or defects — is selected. For a final cantilever with dimensions 1 μm × 10 μm × 100 μm, the capping layer should be around 9 μm wide, 130 μm long and $3-5$ μm thick. Due to the long beam tail of the pFIB, a thicker capping layer is needed than for gallium FIBs. It is important that the capping layer and the cut lamella are longer than the final desired length of the cantilever, as the transferring process reduces the length and some of the cantilever will be covered with deposit while mounting. Furthermore, the starting lamella should be thicker than the final cantilever, as this thickness will be carefully polished down to create parallel surfaces.

(ii) **Cut Trenches:** Before digging out the lamella, the width and shape of the beam should

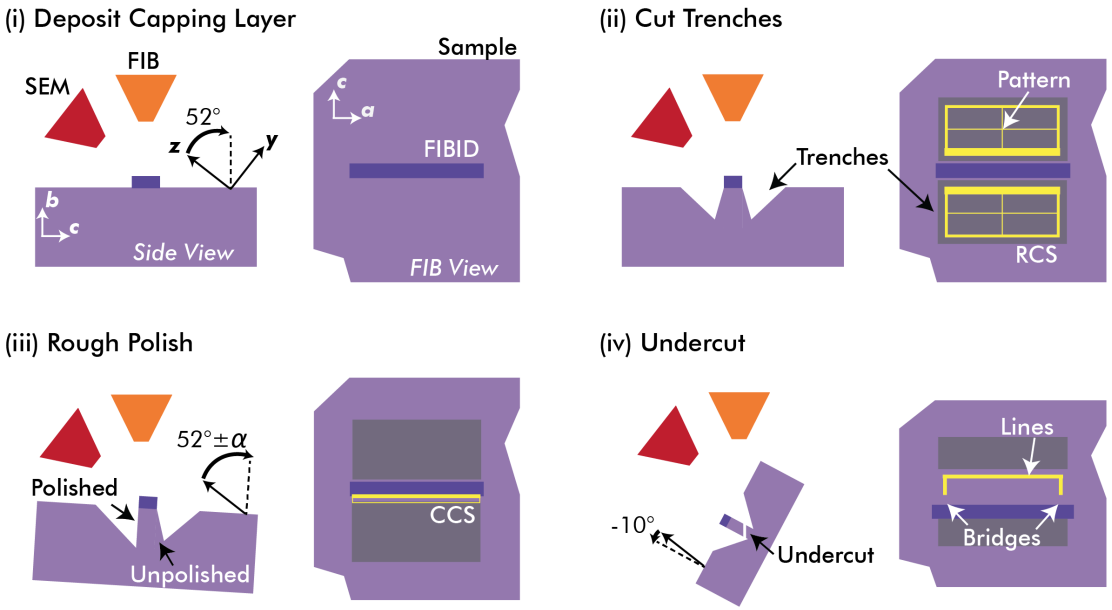

Figure 4.3: Steps for cutting a lamella out of a large sample. In this example, the length of the final cantilever will be along $\vec{a}$, the width along $\vec{b}$ and the thickness along $\vec{c}$. In the FEI Helios FIB, the sample stage is perpendicular to the SEM at 0° and perpendicular to the FIB at 52°. This latter stage tilt is assumed throughout this chapter unless otherwise specified. (i) A capping layer is deposited on a clean section of the crystal. (ii) Trenches are cut using a Regular Cross Section (RCS) to dig out the lamella. Patterns for cutting are shown in yellow and the removed area in grey. Trench cutting is usually done at very high currents, when the diameter of the beam is large and the cut area will be much larger than the pattern. The patterns should therefore be spaced appropriately far apart such that the lamella is not too thin. (iii) After cutting, the sides of the lamella are not parallel — the angle, $\alpha \approx 1.5° \pm 1°$, of the sides is dependent on the material and the FIBing current. The stage is tilted to $52° + \alpha$ and the sides are polished using a Cleaning Cross Section (CCS). The sample can then be tilted to $52° - \alpha$ and the other side polished. (iv) The stage is tilted such that one side of the lamella is visible in the FIB. Line patterns are drawn to cut the rectangular shape of the lamella, leaving bridges on either side to hold the lamella until it is transferred.

be considered. The beam shape will vary depending on the currents used and on the alignment of the system. It is therefore good practice to preform a spot test on an unused section of the sample at the cutting current to measure the diameter of the beam prior to patterning. For the trenches, two Regular Cross Sections (RCS) should be drawn such that the direction of patterning is in the direction of the deposit. The distance between the RCS should be the sum of the desired thickness of the initial lamella ($\approx 9\ \mu$m), the diameter of the beam, and $\sim 4-5\ \mu$m for rough polishing. For example, for a cutting current of 2.5 μA and a silicon cantilever 1 μm × 10 μm × 100 μm, a typical trench size 125 μm long, 40 μm wide and 35 μm deep with 25 μm in between patterns.

(iii) **Rough Polish:** After cutting the trenches, the sides of the lamella will be sloped due to the profile of the beam tail. Furthermore, redeposition that occurs while cutting or polishing the lamella while it is in the trench makes it very difficult and time-consuming to achieve perfectly parallel sides of the cantilever. It is for this reason that the sample will be extracted and polished on a freestanding grid in future steps. However, the very steep sides of the lamella after the initial cut prevent the lamella from being mounted flat onto the grid. To reduce this steepness, a quick 'rough polish' is done. The angle, α, of the sloped walls is dependent both on how the ion beam interacts with the material and on the beam current used. α should therefore be determined for each current used for polishing. To determine α, the beam current is set to the desired polishing current. With the stage tilted to 52°, both sloped sides of the lamella should be visible in the FIB image. The stage is then tilted a small angle $52^\circ + \alpha$ where $\alpha \approx 1^\circ$ and a CCS is used to remove excess material, with scanning direction of the CCS towards the lamella. The stage is then tilted back to 52°. If the sloped walls of the polished side are still visible, then α is increased a small amount ($\approx .5^\circ$) and the polishing procedure repeated until the sloped wall of the sample is no longer visible at 52°. The stage can then be tilted to $52^\circ - \alpha$ and a CCS used to polish the opposite wall.

(iv) **Undercut:** Before removing the sample, the shape of the lamella must be cut free, leaving behind a bridge on either side to hold the lamella until the transfer. The stage is tilted to expose one side of the sample to the FIB as much as possible (-10° in the FEI Helios, making the incident angle of the FIB on the lamella side 62°). Line patterns are then cut to define the shape of the lamella.

4.2.2 Cutting a Lamella from an Oriented Sample - Microscale Crystal

1. Orientation

When the starting crystal is small ($\lessapprox 500\ \mu$m), it becomes difficult to mount directly onto an X-ray needle and crystal edges often cannot be resolved in the camera of many XRD systems, making it impossible to use sample edges as a reference for orientation. Furthermore, there is a high risk of losing the sample while transferring it from the X-ray needle to an SEM stub. In order to overcome these challenges, a method was developed that involves mounting

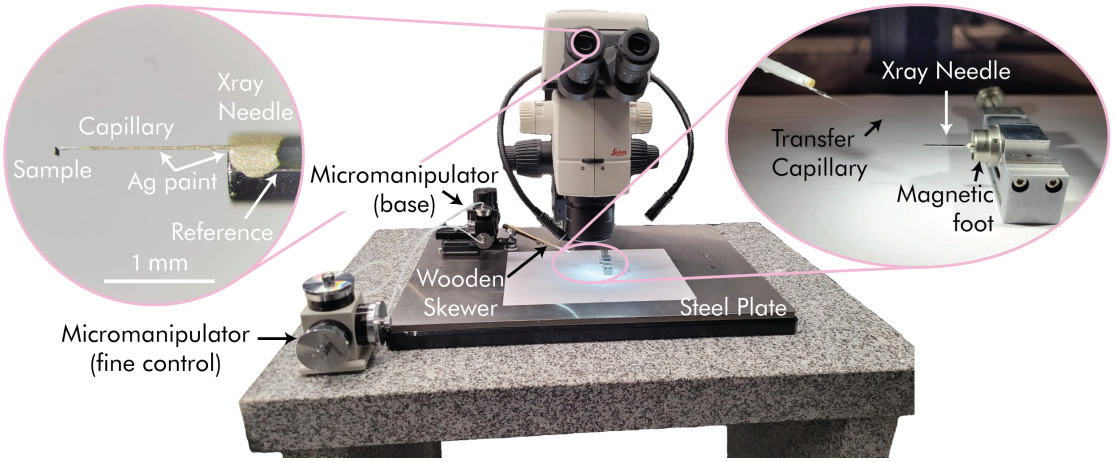

Figure 4.4: Microscope setup for mounting a microscopic sample onto an X-ray needle. A glass capillary for transferring the sample is attached to a wooden skewer steered by a micromanipulator. The sample is mounted onto the end of a capillary glued to the X-ray needle.

selected crystals onto a thin glass capillary glued to the end of an X-ray needle (Fig 4.4). After orientation, a specially designed XRD SEM stub allows for the needle to be inserted into the FIB without the need to transfer the sample.

First, under a microscope, a single crystal is selected from the growth batch. Cleanly defined edges with no polycrystalline growths or residual flux distinguish good samples. For extraction and transfer, a three-axis hydraulic micromanipulator (Narishige Model MHW-3) is used. This manipulator consists of two components: a base — upon which a wooden skewer with a transfer tip can be fixed — and a fine control. The base contains coarse positioning knobs and a magnetic foot, allowing it to be rigidly fixed to a stainless steel plate on the microscope. The fine control is connected by hydraulic tubing and can be removed from the table, decoupling the user from the transfer tip and thereby minimizing vibrations. It was found that a thin glass capillary, made by pulling a glass tube through a small flame, was the best transfer tip for the materials studied in this thesis ($10-200$ μm in longest dimension) as the sample could be seen through the transparent capillary and the diameter of the tip can be controlled by the user. In the best case, the tip is smaller than the sample but thick enough to be self-supporting ($10-50$ μm). Usually, the sample can be lifted through electrostatic forces by simply touching the sample with the transfer capillary, although multiple attempts and patience may be necessary. For the stubborn sample, a tiny amount of vacuum grease on the tip may be helpful.

Once the sample is lifted on the transfer capillary, it is ready for mounting on the prepared needle. To prep the needle in advance: the FIB is used at high currents (2.5 μA) to cut a straight line at the top of the needle that is parallel to the length. This line will later be used as a reference to orient the sample when it is placed into the FIB and therefore should be large enough to be visible in the X-ray camera ($\approx$ 500 μm long, 1 μm deep). The needle can then be fixed onto the magnetic foot using a conductive glue (Dupont 4929N or H20E).

Next, a glass capillary is glued (using Araldite Rapid two-component epoxy) onto the needle near the reference line. Ideally, the capillary should be thick enough to support the sample but not larger than the crystal. When in doubt, it is better to err on the side of too large as surplus material can be cut away in the FIB. Very thin capillaries (diameter $\approx 1\ \mu$m), have been observed to vibrate and move in the FIB, making it very difficult to extract a cantilever and impossible to orient. Furthermore, a long, thin connection provides only a narrow thermal pathway, increasing the risk of overheating while FIBing. A diameter of $5-10\ \mu$m maintains stability but does not introduce an excess of material that will later need to be removed.

To mount the crystal: the coarse positioning knobs of the micromanipulator are used to drive the transfer capillary with the sample near to, but above, the free end of the needle capillary. A third glass capillary can then be used to draw by hand a droplet of two-component epoxy (Araldite Rapid) smaller than the sample at the end of the needle capillary. Finally, the micromanipulator is used to bring the sample to touch the glue droplet, pulling the sample onto the needle capillary. In the best case the sample should touch the capillary at one end, like a flag on a flagpost. The transfer capillary can be removed and the sample is ready for X-ray.

Samples were X-rayed at room temperature in a Supernova diffractometer (Oxford Diffraction). This system has the option to use either copper or molybdenum as a source. For this work, molybdenum was used as the X-rays have a shorter wavelength and penetrate deeper into the sample. In the XRD system after the sample has been X-rayed, the position of the X-ray needle is adjusted such that the FIB-cut reference line is visible in the X-ray camera. The needle is then rotated and images are taken every 1°. The crystalline axes can be overlaid on these images to find the polar (φ) and azimuthal (θ) angles of the axes with respect to the reference line. With θ and φ found for each axis, these values can be used to determine the tilt and rotation angles of the FIB stage that are needed to cut the cantilever along the desired orientation.

2. Mounting for the FIB

In order to electrically ground the sample, silver paint (Dupont 4929N) can be carefully drawn with an additional glass capillary from the X-ray needle to the sample capillary, near the crystal (Fig 4.4).

The set-up can be placed into the FIB without the need for remounting by using an SEM stub (built in-house) with a magnetic base for the magnetic foot. This XRD SEM stub allows for the sample to be rotated freely along the axis of the X-ray needle (Fig 4.5).

Inside of the FIB, the crystal on the XRD SEM stub can be brought into the eucentric height; however, because the base of the SEM stub and the magnetic foot are much higher than the sample, extreme caution is vital when moving the stage, so as to avoid hitting the optics with the SEM stub. Small increments should be used whenever tilting or rotating the stage, and

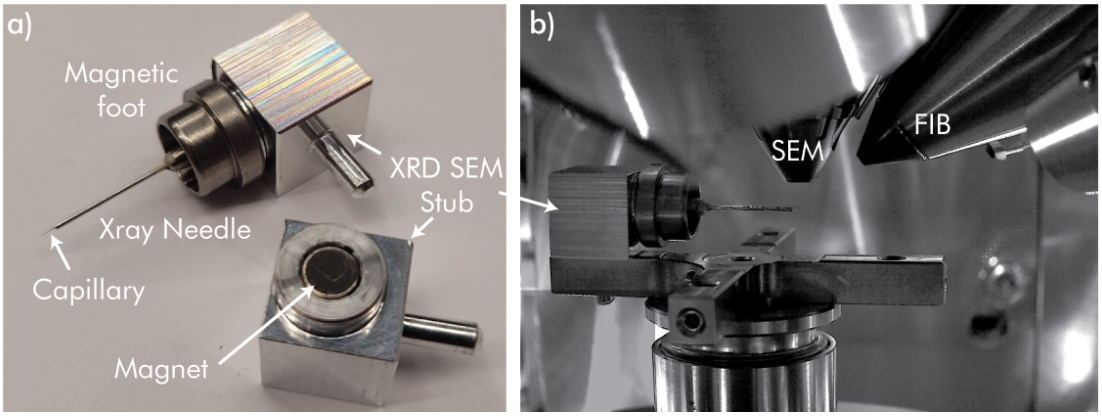

Figure 4.5: (a) SEM stub built in-house for mounting XRD needles. The magnetic foot with the X-ray needle can snap easily on and off of the XRD SEM stub and be rotated as needed thanks to a magnet epoxied into the stub. The glass capillary on which the sample is mounted is glued onto the end of the X-ray needle. (b) XRD needle in FIB. Because of the height of the XRD SEM stub's base, extra care while moving the stage is required to prevent the stub from hitting the SEM and FIB columns.

the user should continuously watch the position of the stub with respect to the optics while moving.

3. Cutting a Lamella

If the smallest dimension of the sample is $> 10\ \mu$m, then lamellae can be cut and fabricated using the cutting procedure described in Section 4.2.1. Thin, platelet-like samples, however, require a slightly different approach (Fig 4.6).

(i) **Grounding Deposition:** Electrical connection between the sample and the silver paint is established in the FIB with a thin layer of platinum deposition (≈ 10 nm, at 12 kV and $7.5-20\ \mu$A).

(ii) **Cut Capillary:** If the glass capillary is very thick under the sample, then the XRD needle should be turned such that the normal of the platelet is perpendicular to the FIB column (at 52° tilt). The excess capillary near the sample can be removed using a rectangular pattern, leaving behind a capillary thickness of 5-10 μm for stability. These capillaries have been observed to melt and deform in the FIB if the current is too high, but this can be circumvented by cutting the capillary with a current ≤ 60 nA. If needed, the refresh rate of the pattern can also be increased to allow more time for heat to dissipate in between scans.

(iii) **Cut Lamella:** Once the excess capillary is removed, then the XRD needle can be turned such that the platelet normal is parallel to the FIB column. The rough shape of the

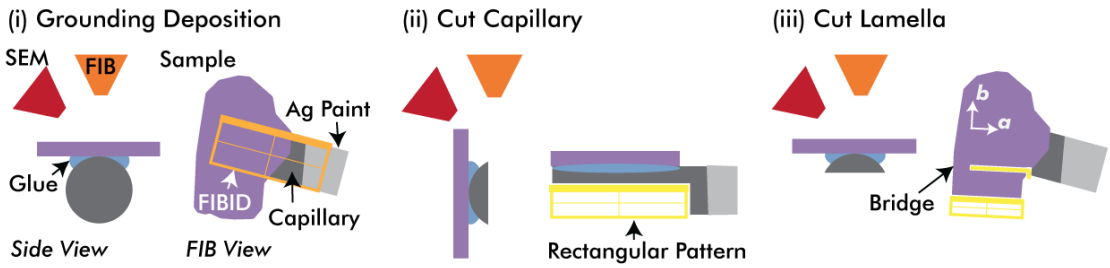

Figure 4.6: Steps for cutting a lamella out of a platelet sample. In this example, the length of the final cantilever will be along $\vec{a}$, the width along $\vec{b}$ and the thickness along $\vec{c}$. (i) A thin ($\approx$ 10 nm) layer of Pt is deposited from the sample to the silver paint to electrically ground the sample. (ii) If the capillary is too thick, a rectangular pattern is used to thin it down such a lamella can be cut from the platelet. (iii) The shape of the lamella is cut out, leaving a bridge connecting it to the rest of the sample.

lamella can be cut (30 kV, 4-60 nA), leaving a thick bridge ($\approx 5\,\mu$m) connecting it to the rest of the sample.

4.2.3 Transferring the Lamella to a Grid

Steps for transferring the lamella from the bulk crystal to the TEM grid are the same regardless of the size and shape of the starting sample; however, the orientation of the lamella will be different. An example of a platelet bulk crystal is shown in Fig 4.2 (3-8) while the transfer from a non-platelet crystal is shown in Fig 4.8. For the platelet crystal, the sample should be oriented such that the FIB is perpendicular to the lamella plane. For the non-platelet crystal, the FIB should be parallel to the width of the lamella.

4. Welding the Manipulator

To prevent the manipulator from colliding with the sample when it is inserted, the sample must be at (or below) eucentric height. The micromanipulator can then be inserted and carefully brought near the surface of the lamella. The micromanipulator needle must be sharp enough to not collide with anything on the surface of the sample. If the needle is not sharp, sharpen it first at a location far away from the sample (See 3.2.4) before moving the stage back to the sample and re-inserting the needle. The needle must be resharpened in between each transfer such that the tip is around $1-2\,\mu$m.

While driving the needle, the position must be carefully watched by alternating imaging between the FIB and the SEM. Because many images need to be taken, it is important that a low current is used in the FIB (30 kV with 30 pA) to prevent damage to the sample. The resolution and dwell time of both the SEM and FIB should be low — such that the position of the needle with respect to the sample is clear but the motion of the needle can be watched in real time ($25\,\text{ns} \leq t_{\text{dwell}} \leq 100\,\text{ns}$). In the EasyLift, the x and y motion are in the imaging plane

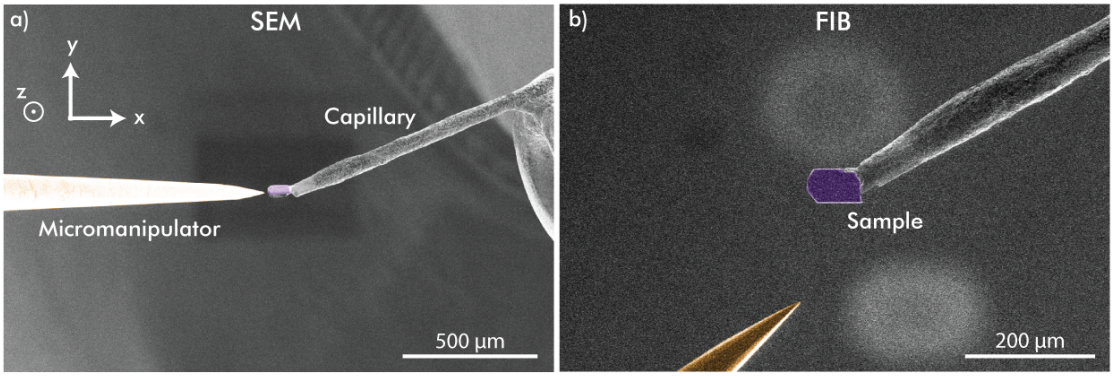

Figure 4.7: SEM (a) and FIB (b) views of a sample on a capillary with the EasyLift Micromanipulator. Motion in the SEM image corresponds to motion along x and y while the z-axis is parallel to the electron beam.

of the SEM while the z-axis is parallel to the SEM (Fig 4.7). For this coordinate system, it is therefore best practice to drive the x and y motion while imaging in the SEM and the z motion while imaging with the FIB. To transfer, the micromanipulator should be fixed to one corner of the sample. First, the needle should be driven near, but not on, the sample in both the SEM and FIB images.

For non-platelet crystals, it is easiest to fix the needle onto the upper-left corner (Fig 4.8). While the manipulator is still above the sample in z (below in the FIB image), the needle can be driven to the target position in x and y. While imaging in the FIB, the needle can be brought down in z. It may be necessary to occasionally stop and adjust the position of the tip along x and y in the SEM. When the needle makes contact with the sample, it will slide along the surface. This can be seen through motion along x in the FIB or SEM.

For platelet crystals, it is easiest to fix the needle onto the lower-left corner. The needle can be brought above the target position in the SEM image when the tip is just off of the sample in the z-axis (just below the sample as seen in the FIB). The needle can be brought down in z while imaging in the FIB, until it is positioned just above the target. Switching back to the SEM, the needle can slowly lowered in y. The image should be switched frequently back to the FIB: if the tip of the needle passes below the target in the FIB image, then the needle should be lowered again in z to bring the tip above the target. It may be necessary to switch between adjusting y with the SEM and adjusting z with the FIB several times before reaching the target. Contact between the needle and the sample can be seen by watching the shadow of the needle in the SEM. Depending on the stiffness of the capillary, the needle may also start to push the sample down or begin to slide on the surface.

The force applied by the micromanipulator on the sample should be minimal to prevent damage or breakage. Once contact is observed, the user should immediately stop lowering the needle. It may be helpful to move the needle a small amount above the sample in the opposite direction and then slowly bring it down again until it just makes contact.

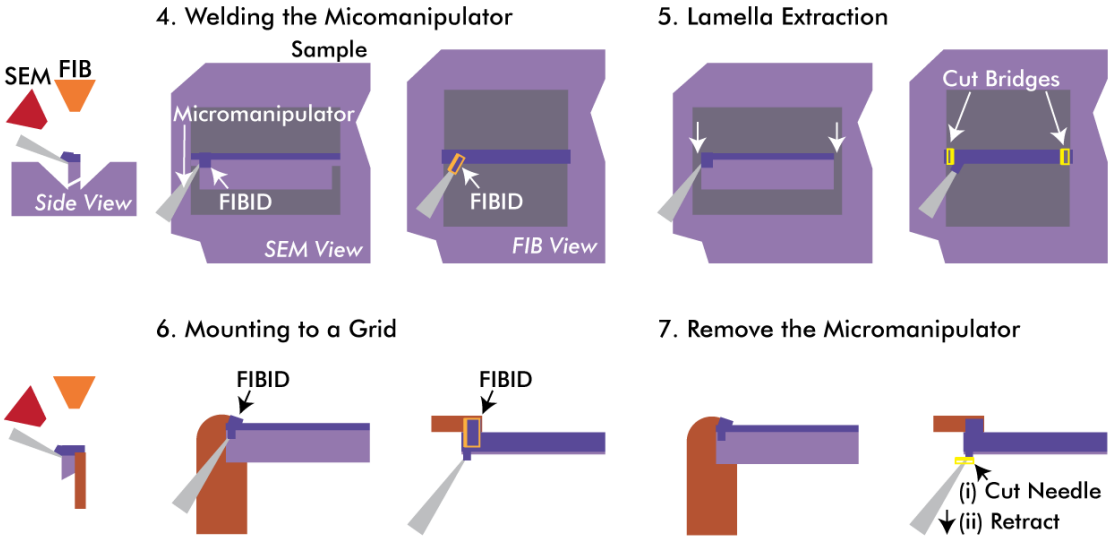

Figure 4.8: Steps for transferring a lamella from a non-platelet crystals to a TEM grid. These steps are the same as for a platelet crystal (Fig 4.2), only the angles of the lamella and TEM grid differ. (4) The micromanipulator is welded to the lamella using FIBID. (5) The bridges are cut and the lamella can be removed from the sample. (6) The lamella is welded to the TEM grid. (7) The micromanipulator is cut off and removed.

Voltage (kV)	Current (nA)	Pt gas	C gas	Dwell time (ns)	Overlap	Blur (um)
12	2.5-7.5	100%	1%	50	-100%	2.5

Table 4.2: Typical deposition parameters for platinum welding used for connecting the sample to the micromanipulator and the TEM grid.

To weld the needle to the lamella, a deposit should be done overlapping both the needle and the sample by a couple of microns on either side. The deposit should be as wide as the tip of the needle and around 2 μm thick. Platinum is deposited using the parameters shown in Table 4.2. After depositing, the needle should not be moved until the sample is cut free.

5. Lamella Extraction

Lamella bridge(s) can be cut using rectangular or line patterns at 30 kV, 15 nA. The sample should be regularly imaged while cutting, as once cut free, the needle may push the sample into the cutting beam. Once it appears that the bridge(s) are cut through, the lamella should be moved slowly to make sure that there are no remaining connections to the bulk that need to be cut. If the lamella is free, then it can be steered out of the trench (non-platelet crystal) by alternating between moving up in y while imaging with the SEM and moving up z while imaging in the FIB. For a platelet crystal, the lamella can simply be moved up in z away from the bulk. Once the sample is clearly free and there are no obstacles in the path of the micromanipulator, the needle with the sample can be extracted. It is critical that the sample is

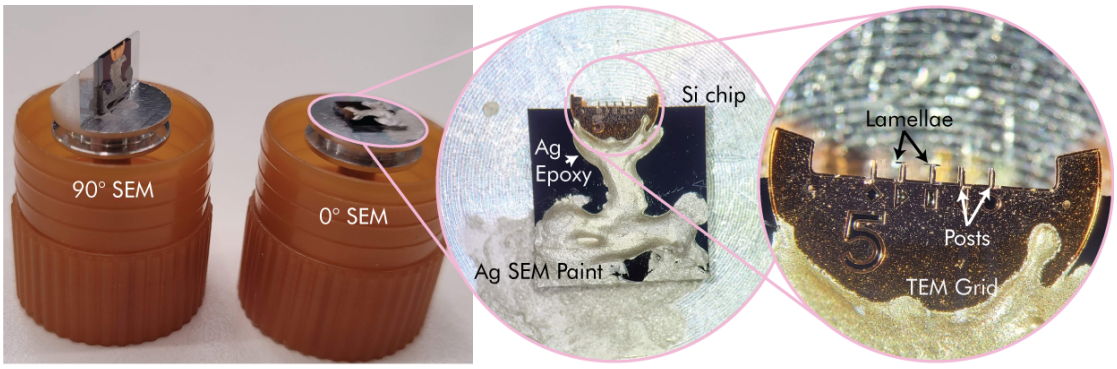

Figure 4.9: TEM grids are glued with silver epoxy onto a silicon chips to allow for easier handling. The chips are mounted onto angled or flat SEM stubs for FIBing using silver paint. This silver paint connects the silver epoxy to the SEM stub, grounding the sample and can be easily removed with a pair of tweezers such that the grids can be remounted. The grid posts allow for free-space polishing and cutting of lamellae welded to the posts.

safely above the trench for the non-platelet crystal as extracting the needle too early can result in the lamella being ripped off.

6. Mounting to a Grid

By polishing the cantilever in free-space, redeposition from nearby surfaces is eliminated, enabling a much higher geometric precision then would otherwise be possible for a lamella in a bulk crystal. Furthermore, with the lamella on a grid, is possible to tilt and rotate to more orientations. Commercially available copper EM-Tec FIB lift out grids (TEM grids) with five posts have been found to work as convenient lamellae holders. These thin grids will need to be mounted at 90° and 0° tilt angles (with respect to the sample stage) at different fabrication steps. To reduce the risk of breaking the cantilever while remounting, the TEM grid is glued (with H20E silver glue from Epo-Tek) to a silicon-on-insulator chip (4 mm × 4 mm). The chip can then be mounted to a standard flat SEM stub for a 0° tilt or on the 90° side of a 45/90 degree angled standard profile SEM pin stub with silver conductive paint (Silver Conductive Adhesive 503). While mounting, it is important that the silver paint acts as an electrical path between the silver glue on the TEM grid to the SEM stub, such that the sample is grounded (Fig 4.9).

The angle of the TEM grid should be parallel to the angle of the lamella on the micromanipulator. For lamella extracted from non-platelet crystals, the TEM grid should be mounted on a 90° SEM stub while for lamella from platelet samples (Fig 4.8, step 6), the TEM grid should be mounted at 0° (Fig 4.2, step 6).

In the ideal situation, the lamella will be mounted perfectly parallel to the TEM grid (Fig 4.10 (a)). However, while extracting the lamella from the sample, it can become slightly tilted (Fig 4.10 (b)). To prevent the lamella from being mounted at an angle, the stage is then tilted until

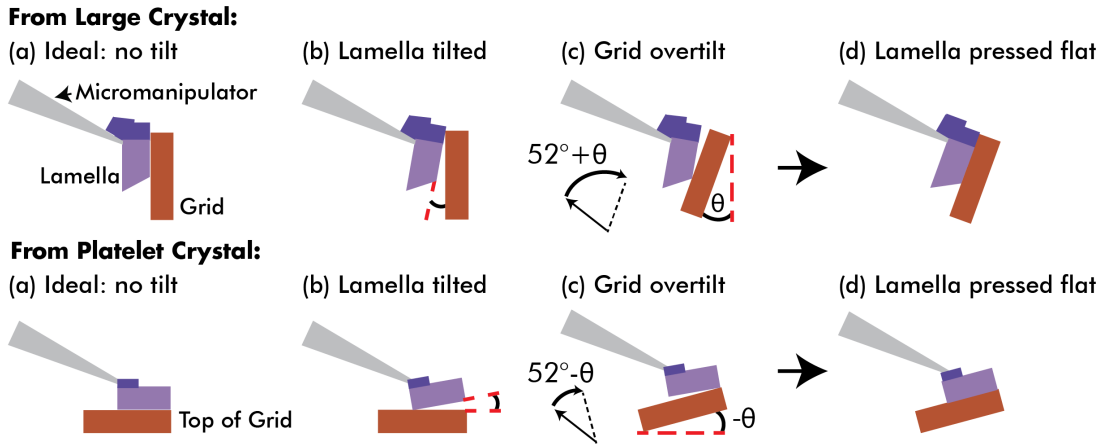

Figure 4.10: Mounting of a lamella on a TEM grid (Side view). The orientation of the lamella is after extraction from a non-platelet crystal (top) or from a platelet crystal (bottom). (a) Ideal situation: no tilt between the lamella and the gird. (b) Lamella pre-tilt prevents it from being mounted flat onto the gird. (c) The TEM grid is tilted more than the lamella. Note that the direction of the tilt is towards the corner of the lamella without the micromanipulator (positive tilt for a lamella extracted from a large crystal, negative for a lamella extracted from a platelet). (d) Pressing the lamella against the TEM flattens it, eliminating the offset. Caution is required here: if the angle between the lamella and grid in (c) is too large, then pressing it flat can cause the lamella to break off and be lost.

the TEM grid is angled $1-2^\circ$ in the same direction (Fig 4.10 (c)). In this configuration, when the lamella is pressed against the grid, the grid flattens it, resulting in no tilt between the grid and lamella. However, if the grid is tilted too far, pressing the lamella down can cause it to break off and be lost. Therefore, since the offset tilt of the lamella is unknown, it is safest to start with the stage tilted perpendicular to the FIB (52° in the FEI Helios) and adjust the tilt incrementally.

The FIB is focused on the top of one of the grid posts and this position is set to be the eucentric position. The micromanipulator with the lamella is inserted and driven near the post in z. While imaging with the SEM, the sample is moved to the target position along x and y. Mounting is easiest if the side of the lamella with the needle is the side fixed to the grid (Fig 4.8 step 6); otherwise, pressing the sample against the grid can cause it to break off, if not done extremely carefully. Along the y-axis, the top of the lamella should be slightly below the top of the TEM post and, along x, the post and sample should overlap at least a couple of microns. Once in the target position in x and y, imaging is switched to the FIB and the needle can be driven down in z while stopping occasionally to adjust the position in the SEM. If the grid is over-tilted with respect to the lamella, then the lamella should be pressed flat against the post. Otherwise, the sample should be extracted, the stage tilted $1-2^\circ$, and the process of positioning the lamella repeated until the lamella is flush with the grid.

The sample is then welded to the grid using the Pt deposition parameters of Table 4.2. The

	Current (nA)
Imaging for Transfers	.03
Bridge Cut	15
Manipulator Cut	15
Rough Cutting	4
Fine Polishing	.1-4
Final Shaping	.1-1
Final Bridge Cut	1
CCS Redeposition Weld	1

Table 4.3: Typical current parameters for mounting and polishing a lamella. For all values, an accelerating voltage of 30 kV is used.

deposition pattern should should be $\approx 3-5$ μm wide, overlap the lamella and the TEM grid by several microns and be $2-3$ μm thick. If there is a large (≈ 2 μm) height difference between the two surfaces to be connected, then it is advisable to first grow a deposit with thickness equal to the height difference only on the lower surface — leaving ≈ 1 μm space between the pattern and the edge of the higher surface. When the deposit is flush with the higher surface, a second deposit connects the surfaces. This provides a more solid connection between the two surfaces: attempting to grow FIBID directly across two surfaces with a large height difference can result in a self-shadowing effect known as terrace formation. As deposition grows on the higher surface, terraces extrude outward, blocking the growth of deposition below. These terraces will continue to grow as the deposition grows and can result in a large crack in the deposit [33].

7. Removing the Manipulator

The micromanipulator can be cut through by drawing a rectangular pattern on the needle, near to the lamella. Here, it is important to leave a small space between the pattern and the lamella to avoid the beam tail cutting into the lamella. When the needle is cut through, it is withdrawn from the lamella and extracted.

4.2.4 Cantilever Polishing

8. Rough Cutting

At this step the lamella will not be a perfect rectangular prism. If the lamella was dug out of a trench, then the sample will have a slope on the bottom edge from the angle of the undercut. There can also be the leftover micromanipulator and uneven edges from where the bridge(s) were cut. As fine polishing will be done at low currents, any excess material only prolongs the polishing time and should be removed now. The sample should be mounted at 0° and tilted perpendicular to the FIB and the edges of the cantilever cut, leaving .5 μm on each edge larger than the final size (Fig 4.11 step 8). If, however, the material is likely to have large defects (flux

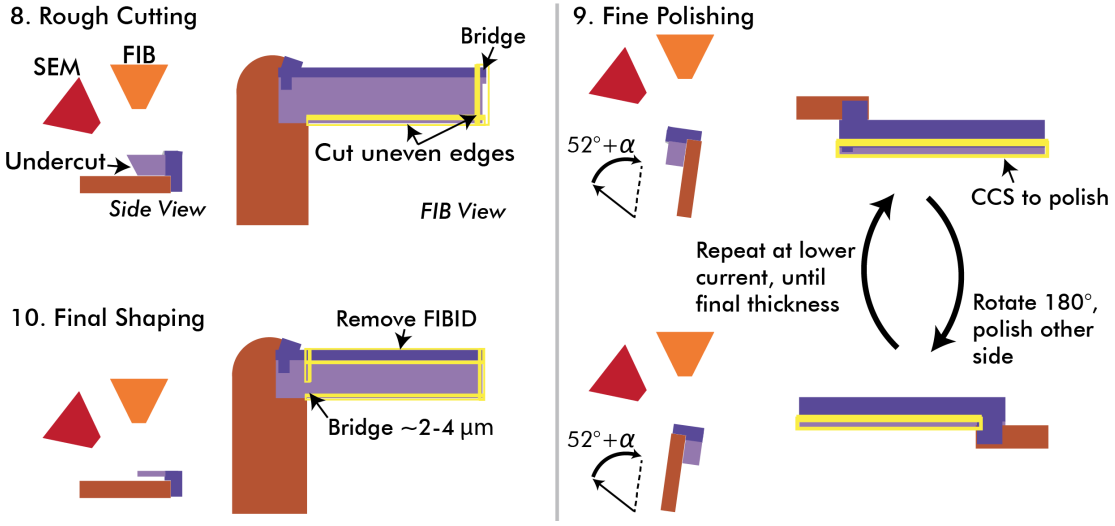

Figure 4.11: Steps for polishing the lamella into the final cantilever shape. (8) To save time on polishing, uneven edges of the cantilever are cut off, leaving the shape of the final cantilever + ≈ .5 μm on the edges. (9) With the TEM grid mounted on the 90° stub, the sample is tilted to 52° + α where $\alpha \approx 1.5° \pm 1°$ is dependent on the interaction of the beam with the material. The exposed side of the lamella is polished using a cleaning cross section, then the sample is rotated 180° and the other side is polished. The parallelity of the sides can be checked by rotating −90° and imaging with the free edge of the cantilever with the SEM. α is adjusted as necessary. This process is repeated at progressively lower currents until the desired thickness of the cantilever is achieved. (10) Mounted again to the 0° stub, the final shape of the cantilever is cut with rectangular patterns in parallel. A bridge is left to hold the cantilever to the TEM grid. In this case it is important to consider where the micromanipulator will be located while transferring so as to not cover the bridge with the needle which would make it impossible to cut through with the FIB. For the mounting condition pictured, the bridge is in the lower left-hand corner of the cantilever.

in the crystal or holes), then it can be good to leave more space, such that if a defect is revealed during polishing, if possible, the edge with the defect can be cut off in the last step.

9. Fine Polishing

After remounting the TEM grid to 90°, the lamella is ready for polishing. If there is not already a protective capping layer on the top, this can be grown ≈ 2 μm thick using the deposition parameters of Table 4.2.

Next, it is necessary to determine the polishing angle of the sample, $\alpha \approx 1.5° \pm 1°$ using the same method described in 4.2.1 on one side of the lamella. After α is known, the stage is tilted to 52° + α and a CCS pattern is drawn over the visible side, with the final line closest to the center of the lamella and a depth at least equal to the width of the sample. Running the full CCS at low currents is sluggish and ineffective because there is less material to remove further

away from the lamella and the beam may spend excess time scanning on lines where there is no material to remove. A more efficient approach involves monitoring the polishing process to move the active FIBing line to positions where it will be most efficient at removing material. First, the CCS is started and the active line is moved near the last line of the pattern, on the side of the lamella. While the FIB is scanning across this line, the sample is imaged frequently with the SEM. A line of contrast should appear. As the ion beam is scanned across the active line, the contrast line will move down the lamella and the contrast will become stronger. Eventually, this contrast line will develop into a local minimum at the position of the active line. At this point, progression of the line down the lamella will slow as the sputtered atoms become stuck in the dip and are unable to escape. The goal is to move the active FIBing line backwards, towards the beginning of the CCS when the contrast line is dark and clearly visible but before the local minimum forms. By moving the active line backwards 1-3 lines (better to take small steps for higher currents and larger steps at lower currents), it is pushed to the bottom of the lamella and this material is removed. The active FIBing line is then brought again up to the top of the lamella, and the process of waiting for a clear contrast line to appear and then following it downward is repeated until the active FIBing line can be kept on the final line of the CCS without any lines ever appearing. This process of active polishing greatly reduces polishing time, particularly at low currents, as the beam is always focused on the region where it can most effectively remove material.

To achieve precise sides of the cantilever, final polishing must be done at low currents ($.1 - .33$ nA). Because this process can be extremely slow, the polishing begins at a higher current ($\approx 1 - 4$ nA). After one side is polished, the stage is rotated 180° and the other side is polished at the same current. The parallelity of the lamella can then be checked by rotating 90°, such that the free edge of the cantilever can be imaged with the SEM. If needed, α can be corrected. The stage is rotated back to one side and the process is repeated at subsequently lower currents until the desired thinness of the sample is reached (Fig 4.11 step 9). At each step, the width of the CCS depends on the starting thickness, goal thickness, and the width of the beam. For each polishing current, it is good practice to perform a spot test off of the sample to measure the beam diameter and check the astigmatism.

Progressively decreasing the polishing current is especially crucial for samples with poor heat conduction. Because one end of the lamella is fixed to the copper grid which acts as a large, cold thermal bath and one end is in free space, a thin lamella ($< 1.5\ \mu$m) can develop a large thermal gradient. Strain from this gradient can cause the sample to bow into the beam. If this occurs, the crystal lattice is deformed and the lamella is useless for resonating cantilever studies. Low currents, short dwell times and long refresh times reduce the sample heating.

10. Final Shaping

With the TEM grid mounted on a flat SEM stub and the FIB perpendicular, the deposition layer is removed and the cantilever is cut into the final shape, leaving a bridge holding it to the post (Fig 4.11 step 10). To keep sharp, well-defined edges, this is done with rectangular

Voltage (kV)	Current (nA)	Pt gas	C gas	Dwell time (ns)	Overlap	Blur (μm)
12	.33-1	100%	1%	50	90%	0

Table 4.4: Deposition parameters for welding the micromanipulator to a cantilever before mounting it on a substrate and for welding the cantilever to the substrate. These parameters result in a slower deposit rate than the parameters listed in Table 4.2 but produce less overspray.

patterns in parallel at low currents.

4.2.5 Transferring and Mounting the Cantilever

11. Cantilever Extraction

The stage is rotated such that the fixed end of the cantilever is closest to the SEM. Extracting the cantilever from this orientation makes it possible for the cantilever to be mounted flat against the surface of the substrate in Step 12 by tilting the stage analogous to Step 6. Because the scan direction of the SEM is now perpendicular to the length of the cantilever, a weaker magnification is needed to view the full cantilever. Rather, it can be helpful to rotate the scan direction by 90°, such that the length of the cantilever is parallel to the length of the screen (Fig 4.12 Step 11).

(i) Using the same method detailed in Step 4, the micromanipulator is brought to the surface of the cantilever, on the end closest to the SEM. The manipulator is welded to the cantilever using the parameters listed in Table 4.4 with a deposition thickness of ≈ 1 μm. These parameters result in less overspray than Table 4.2, reducing the effect of a deposited overspray contributing to the elastic stiffness.

(ii) A rectangular pattern is used to cut the bridge. As this end will be removed after welding the cantilever to the substrate, a slightly higher current can be used than for cutting the final shape ($\approx 1nA$). The cantilever can then be safely extracted and the stage moved to the substrate.

12. Mounting

In the final mounting procedure, it is paramount that the cantilever is flush to the surface of the substrate and the length of the cantilever should be perpendicular to the edge of the substrate. If the cantilever mount is uneven, this introduces uncertainty in the boundary conditions that reduce the precision in the determination of the elastic components. This process can be time-consuming, as it may be necessary to position the sample, remove, adjust the stage and reposition several times but the result is the worthwhile flatly mounted cantilever (Fig 4.12 Step 12).

(i) With the stage initially tilted perpendicular to the FIB, the cantilever is inserted and

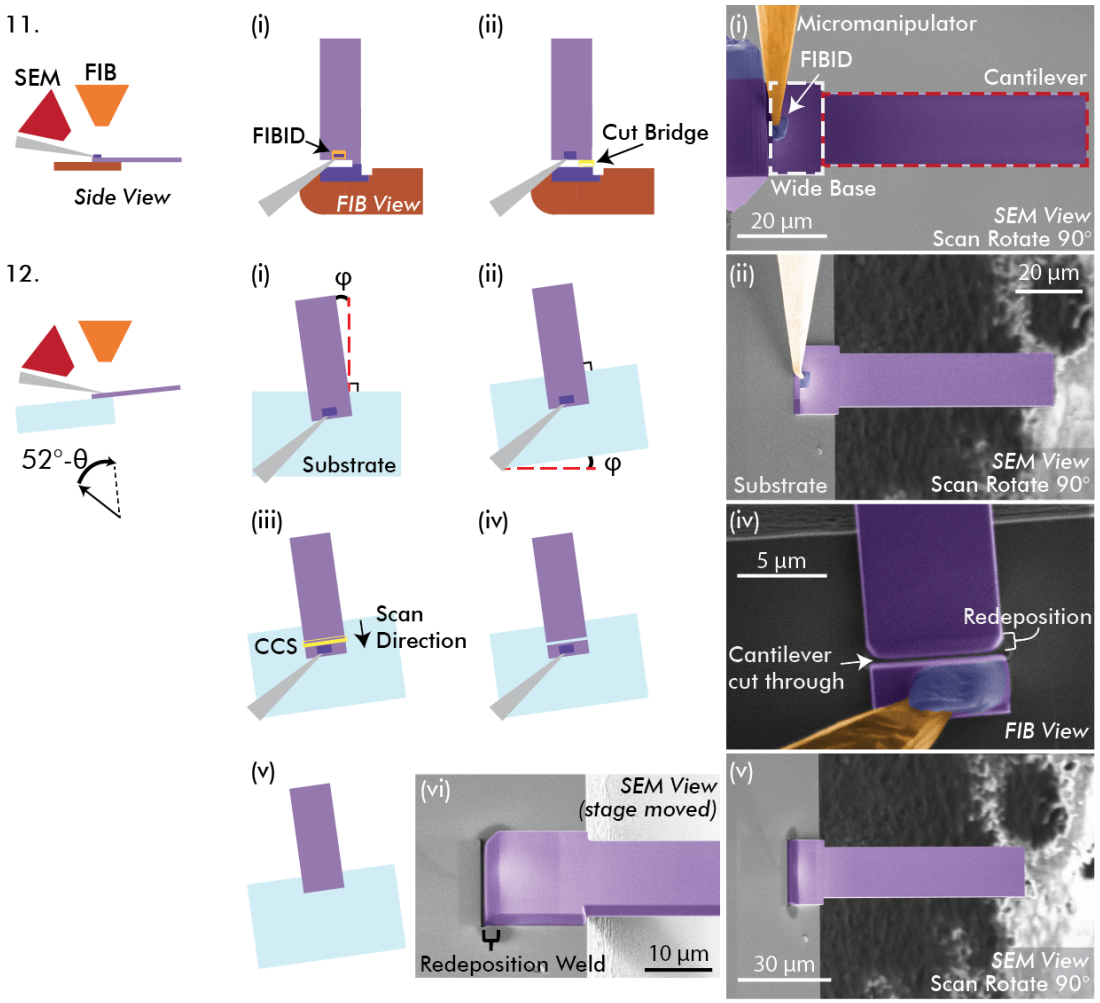

Figure 4.12: Steps for mounting a cantilever onto the final substrate (Section 4.2.5). SEM or FIB images at key stages are shown on the right. Except for Step 12(iv), SEM images are shown of a special, wide-based cantilever. Step 12(iv) is the FIB view of a standard cantilever. 11. With the stage rotated such that the fixed end of the cantilever is closest to the SEM, (i) the micromanipulator is welded onto the nearest end and (ii) the bridge is cut through. At this orientation, it can be helpful for imaging to rotate the scan direction of the SEM by 90°. This scan direction is better suited to the rectangular shape of the image. In these images, the position of the SEM column is towards the left, and not the bottom, as for 0° scan rotation. 12(i) As shown in Fig 4.10, the substrate is given a small tilt and the cantilever is pressed flat onto the surface. After pressing flat, the sample may be rotated an angle φ with respect to the substrate. (ii) By removing the cantilever, rotating the stage φ, reinserting the manipulator and pressing the cantilever flat to the surface, it can be mounted with length perpendicular to the edge of the substrate. (iii) A CCS pattern is drawn on the end of the cantilever. The scan direction is towards the needle; while cutting through the cantilever, redeposition connects the cantilever with the substrate. This serves the dual purpose of cutting free the manipulator and welding the cantilever to the substrate. (iv) Before moving the needle, an image must be taken with the FIB to verify that the cantilever has been cut through. (v) The needle is extracted. (vi) The cantilever is flush to the surface and welded in place.

driven near the target position, such that the sample is well above the edge of the substrate in y. While imaging with the FIB, the manipulator can be brought down, just below the target position in z. Switching back to the SEM, the cantilever is lowered in y until it touches the surface. It may be necessary to stop and adjust the z-position of the needle in the FIB. If the free end of the cantilever begins to move before the welded end touches the surface, then there is already a positive angle between the substrate and the cantilever such that continuing to lower in y will press the cantilever flat. If, however, the free end does not move before the welded end touches, the sample will be mounted at an angle. The needle should be extracted, the stage tilted $\approx -2^\circ$, and the process repeated until the cantilever can be pressed flat.

(ii) Depending on the tilt and rotation of the cantilever on the needle, pressing the sample flat may yield a small in-plane rotation. The angle of this rotation can be measured by imaging in the FIB. The sample can be extracted, the stage rotated accordingly and the cantilever remounted.

(iii) The steps of removing the micromanipulator and welding the cantilever to the substrate are done concurrently: it was found that the redeposition produced from a CCS with scan direction away from the cantilever acts as a strong weld while simultaneously cutting free the manipulator. The CCS must be at least as wide as the sample as well as thick and deep enough to adequately cut through the sample. For a 1 μm thick cantilever, a CCS about 1.5 μm thick and 1.5 μm deep will usually weld the cantilever and release the needle, although these parameters may need to be adjusted depending on the etching rate of the material. The CCS should also be placed before the FIB deposit, as otherwise this will increase the thickness of the material to be cut.

(iv) After the running CCS and before moving the needle, it is necessary to first image with the FIB to make sure that the cantilever has been cut through (Fig 4.2 12.(iv)). If the CCS did not cut through the sample, then the cantilever is weakly welded to the substrate and still weakly connected to the needle. Moving the needle will break one or both of these joints, often resulting in the loss of the sample. In this case a line cut or a second, thinner CCS should be first run to cut off the manipulator.

(v) The micromanipulator can be lifted off and extracted. The redeposition weld has been shown to be sufficiently strong such that the stage can be moved, the chamber vented, or the cantilever vibrated on resonance without damaging the weld.

13. FIBID Weld

To fix the boundary condition of the cantilever, FIBID is grown on the base, rigidly clamping the base to the substrate (Fig 4.13). The stage is tilted back to perpendicular to the FIB and FIBID is grown on either side of the cantilever, with each deposition $5-15$ μm wide and ≈ 1 μm away from the cantilever and thickness equal to the cantilever thickness. FIBID can then be deposited over the side deposits and the cantilever base $1-2$ μm thick. As overspray during

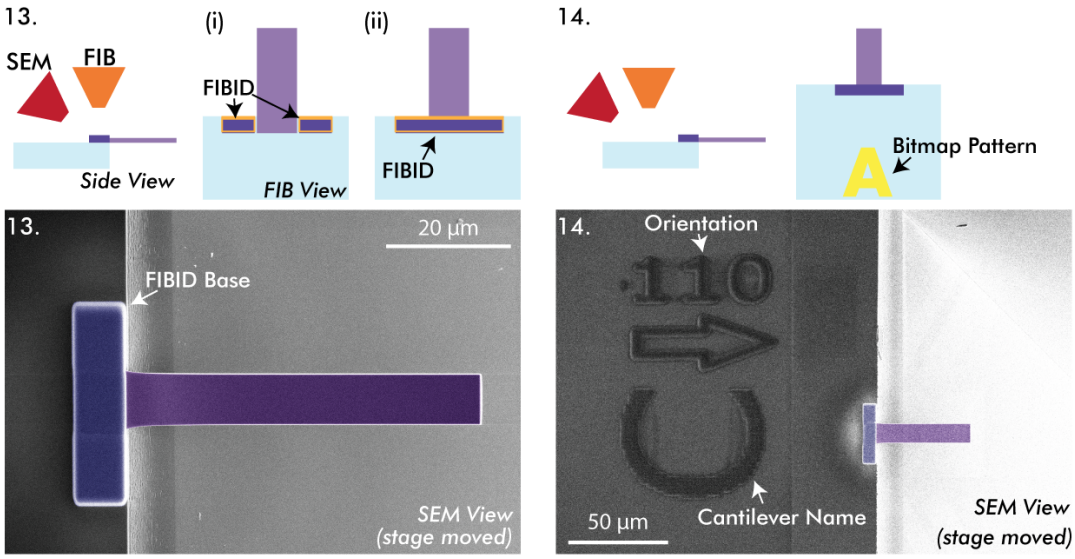

Figure 4.13: 13.(i) FIBID is grown on either side of the cantilever such that the top of the deposition is flush with the top of the cantilever. (ii) FIBID is grown over the side deposits and the cantilever, forming the fixed boundary condition of the sample. 14. Bitmap patterns are used to cut the name of the substrate, the name of the cantilever, and any other identifying information onto the substrate. The SEM image shows a cantilever "C" with the length cut along the 110 direction. The cantilever material (SmFeAsO undoped) and the name of the chip (SmFeAs(O,F)_M3) are also cut on the substrate (not pictured).

the deposition introduces uncertainty in the sample geometry and increases the effective stiffness, the deposition parameters are chosen to reduce overspray (Table 4.4).

This step of the final FIBID weld increases the quality factor of the cantilever in comparison to a cantilever welded in place using only the redeposition of the CCS. In addition, the small gap in between the cantilever and the substrate can act as a crack in the system. While welding the cantilever with FIBID, injected gas can flow into this crack and these molecules broken apart by secondary electrons produced from the FIB scanning across the top surface. This effectively fills the gap. Cantilevers with the additional FIBID weld therefore have more well-defined boundary conditions. The CCS weld is nevertheless a useful step before the FIBID is added: FIB deposition can grow unevenly if parts of the deposit are shadowed from the gas injection nozzle. Removing the micromanipulator reduces shadowing. Without the micromanipulator, the stage can then also be rotated if needed to prevent parts of the cantilever from shadowing the deposit.

14. Final Imaging

As the chips can hold several cantilevers, bitmap patterns are used to cut names of the chip and cantilevers into the substrate. The substrates used for this project consist of a thin layer of Si_3N_4 on Si. By cutting the labels deep enough to remove the Si_3N_4, the resulting optical

contrast makes them easily readable with an optical microscope. SEM images of the top and edges of the sample are taken such that the geometry can be determined and the effective Young's modulus extracted from the resonance frequency.

5 Micro-Resonator Measurement Methods

Exploring phase transitions in quantum materials requires measurements conducted as a function of the relevant parameters such as temperature and magnetic field. While resonance modes of microscale cantilevers can be easily measured at room temperature using commercially-available desktop vibrometers, tracking small changes in resonance frequency down to the low temperatures at which most quantum phenomena arise is non-trivial. In this thesis, an interferometer is used as a sensitive non-contact instrument to detect displacement or velocity of the resonating cantilevers. To explore the magnetic field dependence, the measurement is done with the sample in the bore of a magnet, which adds a tight spatial constraint. These measurements necessitated a novel design for resonance experiments in high magnetic fields and low temperatures.

Schematics of the experimental set-up can be seen in Fig 5.1. For magnetic field and temperature control, a probe was designed for measurements in a Variable Temperature Insert (VTI) inside of a 16 T magnet. The VTI allows the temperature to be swept and stabilized in the range 2-300 K. On the probe, FIB-fabricated cantilevers are mounted onto a piezoelectric transducer. Piezoelectrics (or piezos) are materials with a unique coupling of electric polarization and strain such that applying an electric field results in the compression or expansion of the crystal (and vice versa) [128, 129]. By applying a voltage across electrical contacts located on opposite sides of the piezoelectric, the cantilever can be mechanically excited with a tunable magnitude and frequency. Motion of the cantilever is detected using an interferometer focused on the free-end. By sweeping the drive frequency and tracking the amplitude, the resonance spectrum can therefore be obtained.

To increase sensitivity by rejecting signals with frequency different than the drive frequency, a Lock-in Amplifier (LIA) is implemented. The output (i.e. the reference) of the LIA was used to drive the vibrations of the piezo while the optical signal from the interferometer was converted to a voltage input in the LIA. The experimental set-up can therefore be considered in four main components: micro-resonator probe, magnet and VTI for temperature and field control, equipment for excitation and readout, and measurement software.

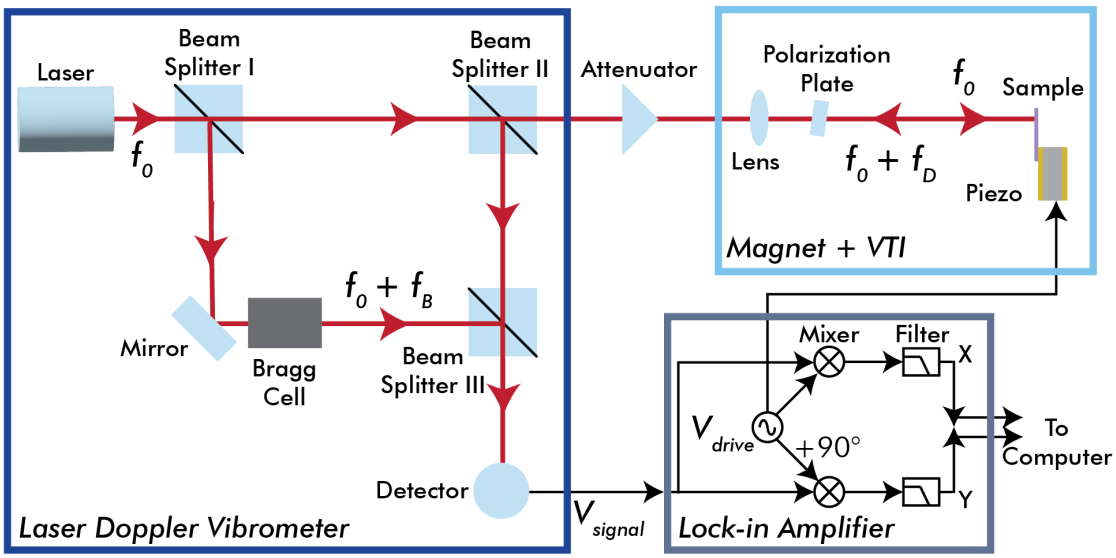

Figure 5.1: Experimental schematics: the optical path of the laser is indicated in red, while electrical signals are shown in black. Cantilevers are mechanically excited by applying a voltage difference (V_{drive}) on opposite sides of a piezoelectric. Motion of the cantilever is detected using an interferometer — specifically a Laser Doppler Vibrometer. Because of the Doppler effect, the motion of the cantilever shifts the frequency of the laser, f_0, by the Doppler frequency, f_D. The vibrometer used for this research converts the velocity computed from f_D into a voltage, V_{signal}, which is fed into a Lock-in Amplifier. By multiplying V_{signal} by V_{drive}, the LIA detects the component of V_{signal} with the same frequency as V_{drive}.

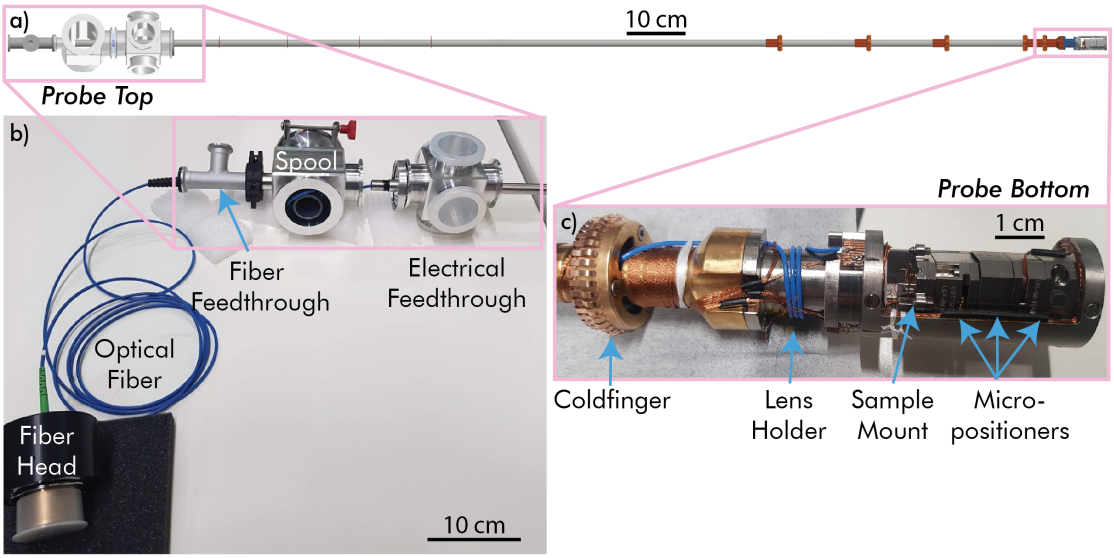

Figure 5.2: (a) Sketch of the Micro-Resonator probe designed for optical measurements of resonating FIB-fabricated cantilevers down to low temperatures (~ 2 K) and in high magnetic fields (16 T). (b) The top of the probe provides the optical and electrical connections between the vacuum of the measurement chamber and the atmosphere of the laboratory. Electrical wires on the probe were soldered onto sockets on the electrical feedthrough (wires and sockets not pictured). An optical fiber carries laser light between the interferometer and the sample. The Fiber Feedthrough was built by epoxying the fiber into a KF-16T piece and extra fiber length is stored in the fiber spool. The fiber runs through the center of the probe to the base (c) where a lens focuses the light onto the sample. A stack of three piezoelectric micro-positioners (Attocube ANPz51 RES and 2 orthogonally-mounted ANPx51 RES) make it possible to align the cantilevers in-situ and conduct spatial scans to map out the resonance modes. The sample is mounted on top of the micro-positioners using a sample mount consisting of a base screwed onto the top micro-positioner and a removable platform (not pictured, see Fig 5.4 and Fig 5.5). Coldfingers near the base of the probe are designed to provide thermal contact with the chamber and improve temperature control.

5.1 Micro-Resonator Probe

Measurements that are conducted in high magnetic fields require a probe — a long rod that holds the sample inside the magnet's field center and consists of all necessary electrical and optical components for measurements (Fig 5.2 (a)). In order to study the resonance frequency of FIB-fabricated cantilevers, a probe was constructed with the key features:

- Optical fiber and lens for transmitting and focusing the interferometric laser
- Piezoelectric micro-positioners to align cantilevers in-situ and conduct spatial scans
- Sample platform with a piezoelectric transducer for mechanical excitation
- Heater and thermometers for fine temperature control

This probe was designed to fit inside the VTI of a 16 T magnet with a tight spatial constraint of 26 mm diameter but can be easily adapted for measurements in other systems with a larger inner diameter.

5.1.1 Probe Base

The base of the probe consists primarily of the fiber lens, a polarization plate, the sample platform and three piezoelectric micro-positioners (Fig 5.2 (c)). The fiber is connected to the lens inside of a lens holder, which holds the lens such that the focal point is in the center of the magnetic field of the 16 T magnet. A polarization plate directly in front of the lens reduces the effect of noise in the fiber by polarizing transmitted light. The chip with FIB-fabricated cantilevers is glued onto the piezoelectric transducer with GE varnish that can be removed with a small amount of solvent. The transducer is mounted onto a sample mount consisting of removable sample platform and a base screwed onto the micro-positioners. As the temperature changes, different thermal expansion or contraction of different materials can cause the sample to drift around, out of the focus position of the lens. To prevent this, the lens holder, sample mount, micro-positioners and screws were all made out of titanium.

Lens

An Attocube D12/F2.8 lens with an FC/PC fiber connector was used for focusing the laser light onto the sample. This lens has a high angular tolerance, making it possible to measure samples that are mounted at a slight tilt. At the focal length of 2.8 mm, the spot size of the lens is 2 μm, defining the spatial resolution. The lens is fitted inside of a lens holder (Fig 5.3 (a)) screwed onto the probe.

Polarization Plate

Back-reflections can be generated from imperfections in the optical path, such as vibrations or thermal gradients. These back-reflections interfere with the signal, generating noise. This noise can be reduced by polarizing the light in between the sample and the lens, rejecting the signal of the unpolarized light. This is accomplished by placing a quarter-wave plate which polarizes transmitted light by 45°, directly in front of the lens. The laser beam passes through the polarization plate twice: first on the way to the sample and again after it is reflected back to the lens, resulting in a total polarization of 90°. The polarization plate was epoxied onto a holder designed to fit around the lens holder. The plate holder can be rotated around the lens to maximize the signal before being fixed into place with grub screws (Fig 5.3). Furthermore, back-coupling between the plate and the lens can introduce noise. For this reason, the plate is angled at an 8° tilt to the lens. This is a standard angle used in optics that causes light reflected off of the plate to be angled away, reducing back-coupling.

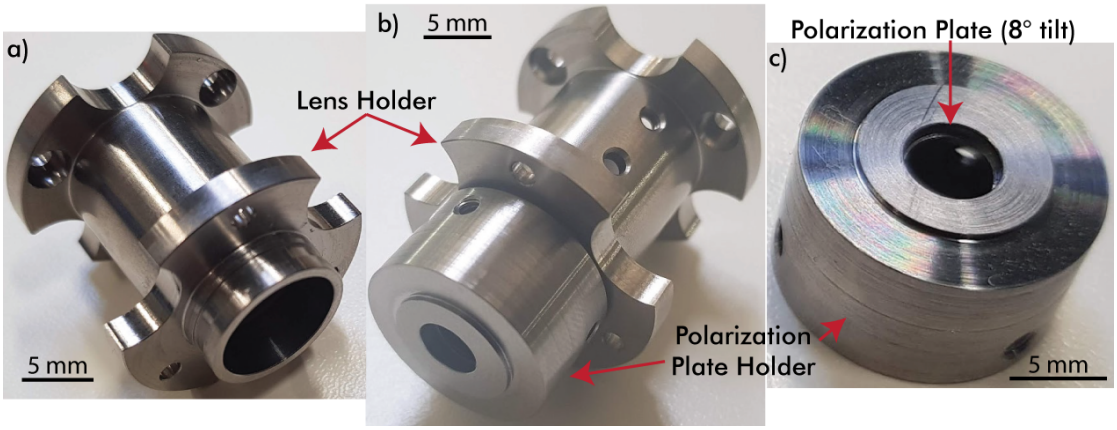

Figure 5.3: Lens holder (a) and polarization plate holder (c): The polarization plate holder fits over the base of the lens holder where it can be rotated during testing to optimize the signal and then be fixed into place with grub screws. The polarization plate sits at an 8° tilt to minimize back-reflection.

Sample Mount

For designing the sample mount, two separate guiding design principles are in contradiction to each other. First, optical experiments require a high degree of tunability to optimize the optical paths. A misaligned sample will reflect the laser light at an angle. If this angle is greater than the tolerance angle of the lens ($\pm 7°$ for the lens used), then the reflected signal light will miss the lens. On the other hand, resonance measurements require a flat spectrum within the bandwidth of interest. If mechanical resonance modes of the stage are near in frequency to the resonance modes of the measured cantilever, these background modes can appear in the spectrum, making it difficult to distinguish the resonance of the cantilever. An adjustable mount that allows the angle of the sample to be finely-tuned will not be rigid and may have a noisy spectrum. To determine the best sample mounting condition, two separate mounts were designed: an adjustable stage and a rigid stage. After testing both approaches, it was found that cantilevers fabricated following the procedure detailed in Ch 4 were always mounted sufficiently flat such that no fine-tuning of the angle was necessary. The adjustable stage also had significantly more mechanical noise; therefore, the rigid stage is a better design for these experiments.

The design of the adjustable stage was inspired by kinematic mirror mounts used in optical experiments to finely tune angles. Kinematic mounts use three screws with balls at the heads that can freely rotate. Springs located in between the screws pull the two sides of the mount together while the screws push them apart. If the screws are mounted on orthogonal axes, tightening or loosening one of the screws will rotate the platform. The rounded heads of the screws sit inside grooves specifically designed to constrain all six degrees of freedom (Fig 5.4 (a)). The screw at the origin rests inside of a cone which, combined with the downward force of the springs, fixes the system from translations along the x, y and z axes. The second screw

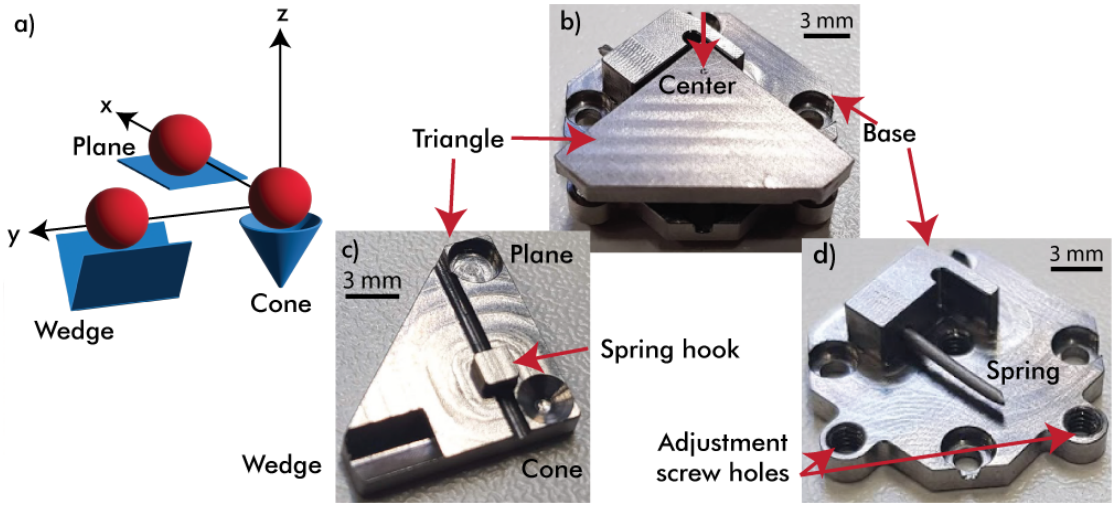

Figure 5.4: Adjustable sample stage design: (a) Principles of a six contact point mount: consider an object held into place with three screws with rounded heads such that the screws can slide freely along a plane. To fully constrain (but not over-constrain) the system, six contact points are needed. One screws fits into a cone, restraining translational motion along x, y and z. The second screw fits into a wedge, preventing rotation along y and z. The final screw sits on a plane, eliminating rotations about x. High-precision kinematic mounts, such as those used for aligning lenses for optical measurements, use this design for a reproducible fine-angular control [130–132]. (b) Triangular sample holder (c) based on these kinematic principles and base (d). The base contains a straight wire spring which slides into a hook cut in the triangle. This spring applies a downward force on the triangle while adjustment screws with rounded heads are used to adjust the tilt. The screw heads fit into a six-point constraint system identical to (a). Note that in (c) the triangle is flipped upside down.

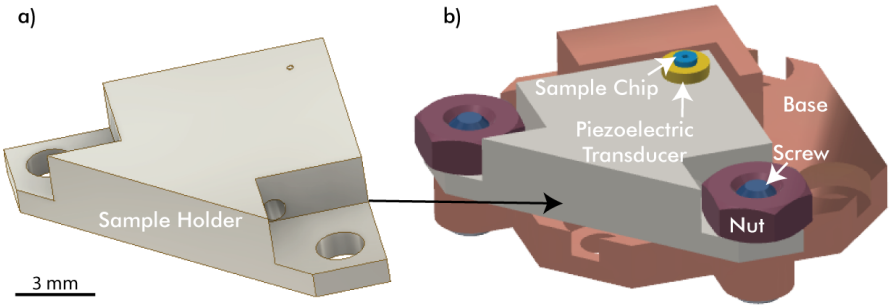

Figure 5.5: Rigid stage: (a) A second, stationary design of the sample platform is firmly fixed into place by bolts (b). This design uses the same base as in Fig 5.4 but the adjusting screws with rounded heads are substituted by standard screws and two nuts fix the platform.

fits inside of a wedge which prevents rotations along y and z. This wedge must be pointed towards the center screw, otherwise the system is over-constrained. The final screw only needs one point of contact (a flat plane) to fully constrain the system by preventing rotations about x. This system provides the stability, adjustability and reproducibility necessary in sensitive optical measurements [130–132].

This system of constraints was adopted for the design of a sample mount consisting of an angle-adjustment triangle and a base (Fig 5.4 (b-d)). Titanium grub screws were rounded at the end to allow for the screws to slide along the surface. The angle can be tuned by adjusting the wedge and plane screws while the center screw, over which the cantilever is mounted, is stationary. A simple straight-wire spring — inspired by the straight springs used in woodwind instruments — provides the downward force to hold the triangle into place, allowing the triangle to be easily slid on and off of the base for sample mounting. This straight-wire spring has the additional advantage of taking up minimal space: size constraints of the VTI restrict the sample holder (base and triangle) to be no more than a few millimeters tall. Traditional, coiled springs added a minimum of three millimeters to the total design.

The rigid stage is mounted using the same base, making it possible to easily change between the two platforms. A hole for the spring allows the stage to be slid on the base and held into place. To firmly fix the stage, two nuts are screwed on, clamping the stage on the base (Fig 5.5). Measured resonance spectra of both stages are shown in Fig 5.6. The spectrum of the rigid stage is significantly quieter.

Micro-positioners

To move the samples in-situ for alignment and spatial scans, the sample stage is mounted onto a stack of three piezoelectric micropositioners (Attocube ANPz51 RES and two ANPx51 RES mounted orthogonally). These positioners allow for sub-micron position control over a 3 mm (or 2.5 mm for the ANPz51) travel range. A resistive encoder is used to read-out the position.

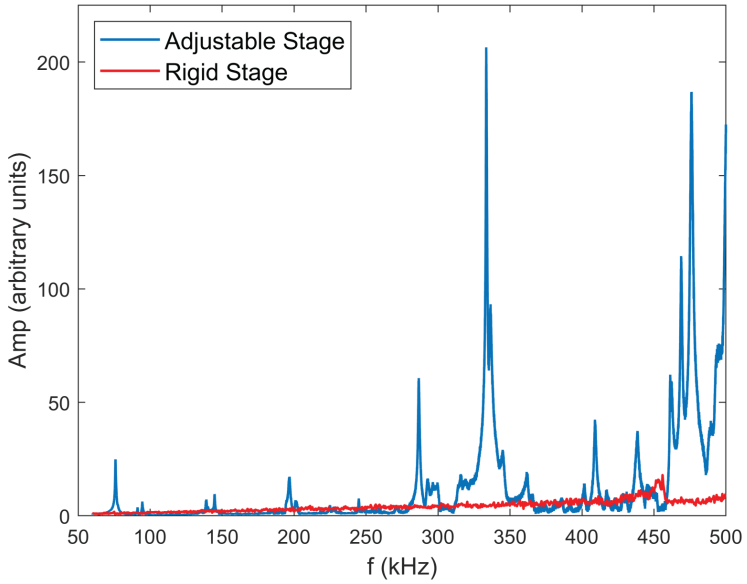

Figure 5.6: Measured resonance spectra of the rigid and adjustable sample stages. These spectra have been normalized to the amplitude of the stage at a constant frequency outside of the plotted range measured simultaneously with the spectra measurements. This step (described in 5.4.2) removes noise that was present in the interferrometric set-up used. The exact resonance modes can vary depending on how tightly the stages are mounted and the temperature.

5.1.2 Fine-Temperature Control

While the VTI uses helium gas, a heater and a thermometer to control the temperature of the sample chamber across a wide temperature range, this method alone is not sufficient for temperature stability near the sample. A few key components on the probe itself allow for a finer temperature control. For reducing radiation from the top of the probe, copper-on-PCB baffles were soldered onto the upper-half of the probe. Copper pieces were designed to establish thermal contact between the probe and the walls of the VTI. These so-called 'coldfingers' were soldered onto the lower-half of the probe and contain removable copper springs to press against the VTI inner wall. Unfortunately, the top of the VTI has a bottleneck (not shown in the manual) that did not allow for the coldfingers with the springs to fit into the chamber. The springs were therefore removed, although new springs can be added for measurements in a system with a wider inner chamber. Because, without the copper springs, there is no direct thermal contact between the VTI and the probe, a low pressure (.5-1 mbar) of helium exchange gas is needed to reach base temperature (2 K). Damping from gas in the chamber shifts the measured resonance frequency, f_{meas} from the real, intrinsic frequency of the cantilever, f_0, by [133]

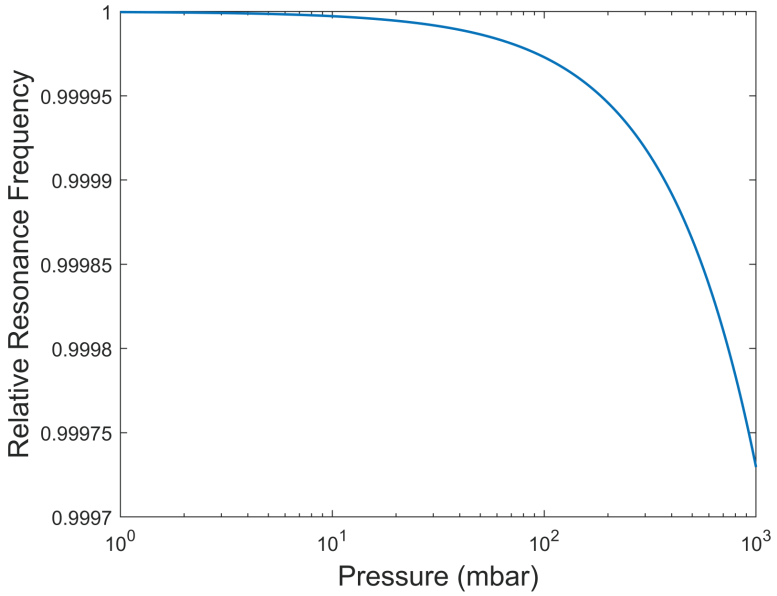

Figure 5.7: Relative resonance frequency for a silicon cantilever with density $\rho = 2330$ kgm^{-3}, width $w = 10$ μm, and thickness $t = 1$ μm in a chamber of helium gas at $T = 300$ K.

$$\frac{f_{\text{meas}}}{f_0} = \frac{1}{\sqrt{\left(1 + \frac{\pi MPw}{4RT\rho t}\right)}} \tag{5.1}$$

with $M = 4.003 \times 10^{-3}$ kg/mol the molar mass of the helium gas in the sample chamber, $R = 8.314$ J mol^{-1}K^{-1} the universal gas constant, P the chamber pressure, and T the temperature. w, t, and ρ are the width, thickness and density of the cantilever, respectively. For a silicon cantilever with $\rho = 2330$ kg m^{-3} and typical dimensions $w = 10$ μm, $t = 1$ μm, the pressure dependence of the relative frequency at $T = 300$ K is plotted in Fig 5.7. At 1 mbar, $f_{\text{meas}} = .99999973 f_0$. Thus the effect from the damping due to this small pressure of helium gas can be neglected.

Cernox CX1030 and CX1050 thermometers were mounted onto the colderfinger nearest to the base and on the base plate of the sample mount to measure the temperature of the probe and the sample, respectively. Six 100 Ω resistors were configured into three parallel branches of two resistors each, on the outside of the lens holder. These resistors act as a heater to set the temperature of the probe thermometer.

5.1.3 Probe Top

The top of the probe is used to pass the optical and electrical signals from the vacuum of the VTI to the atmospheric pressure of the laboratory (Fig 5.2 (b)). These connections must be vacuum-tight while preserving the quality of the signal. To transfer electrical signals, a KF-40 6-cross was specially designed and built in-house to be lightweight and compact. Internal wires were soldered on plugs that can be connected and disconnected with ease.

Transmitting the optical signals from vacuum to atmosphere requires careful consideration. An early design for this experiment consisted of two separate optical fibers: one connected to an interferometer on the outside of the probe and the other fixed on the probe and connected to the lens. Optical signals were transmitted across a vacuum feedthrough to which both fibers were connected. The inclusion of this feedthrough added two unnecessary connections — each of which can significantly increase noise as back-reflections are generated at each optical interface. To eliminate these optical connections by using a single optical fiber from the interferometer to the lens, a special vacuum feedthrough for the fiber was built. The fiber cladding was stripped in a length ~ 6 cm near the center of the fiber. This stripped region was epoxied into opposite branches of KF16-T piece. The center branch of the T-piece was left without epoxy, such that this branch could be used to continuously pump on the feedthrough if the epoxied sides were not leaktight. Even without continuous pumping, this fiber feedthrough is vacuum tight down to 10^{-6} mbar.

The length of the fiber on the probe-side of the feedthrough is equal to the probe length + ~ 10 cm, with the additional length to allow for future modifications of the probe. This extra length is stored inside the fiber "spool": a component with two KF-50 connections to allow access to the fiber, and KF-16 and KF-40 connections to connect with the optical and electrical feedthroughs. Just below the spool, the fiber is fed into the middle of the stainless steel tube that forms the body of the probe.

5.2 Temperature and Field Control

For initial tests of the probe and samples, preliminary measurements were done in a vacuum-tight tube. For sweeping temperature, the tube (pumped down to $< 1e-4$ mbar) was placed in a dewar of liquid nitrogen. This rudimentary method allows for slow cooling of the sample down to 80 K.

Measurements with a temperature range down to 2 K and in high magnetic field were conducted in the VTI of a 16 T Cryomagnetic magnet (Fig 5.8). The magnet itself is a solenoid wound with superconducting Nb/Ti filament that sits at the bottom of a dewar of liquid helium. The magnetic field can be driven by applying a current through two current leads into the solenoid. This method is energy-intensive and heat from the current leads results in significant helium boil-off. Alternatively, a superconducting switch in between the leads allows the magnet to be used in an energy-conservative persistent mode. The superconducting

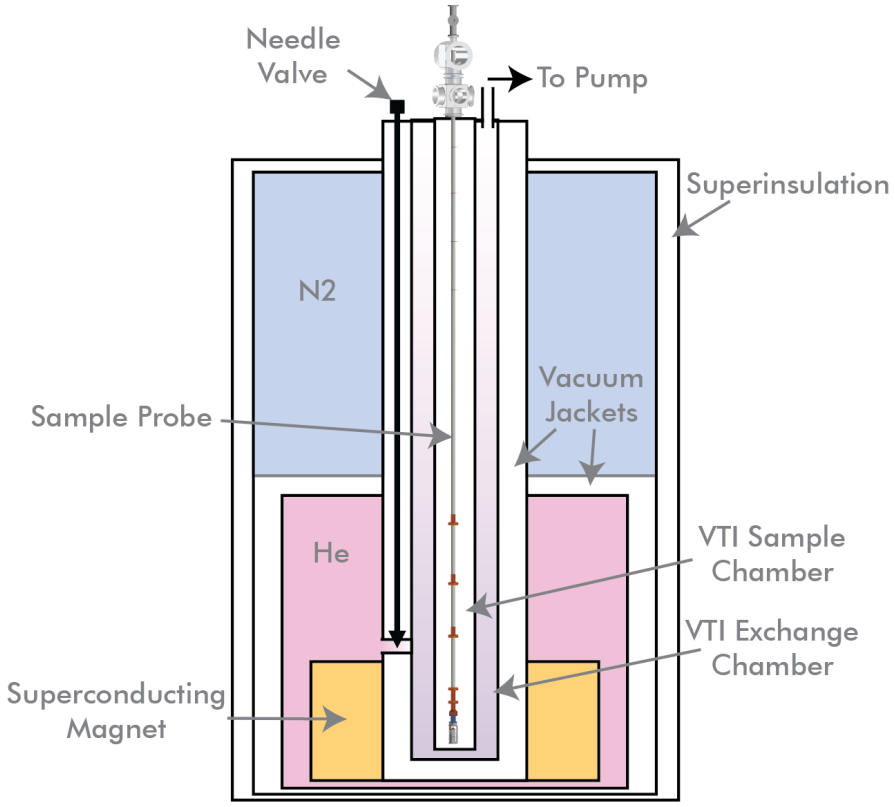

Figure 5.8: Sketch of the magnet and Variable Temperature Insert (VTI). The superconducting magnet is kept cool by liquid helium. To reduce helium boil-off, the system is thermally isolated from the laboratory with vacuum jackets, a tank of liquid nitrogen, and a special type of insulation called superinsulation. The sample itself must be held in the center of the magnetic field on a measurement probe. The VTI sample chamber is cooled by a flow of helium inside of the VTI exchange chamber. A needle valve in between the helium reservoir and the exchange chamber makes it possible for the user to regulate this helium flow.

switch is heated to a normal-state while the current in the leads is swept to the desired field. Once the field is stabilized, the heater is turned off, closing the superconducting loop and trapping the magnetic flux. The current in the leads can then be safely brought to zero, while the field inside is stable. When the magnetic field must be changed, the current in the leads must first be increased to equal the current of the magnet. The superconducting switch can then be heated and the magnetic field adjusted.

The VTI inside the magnet bore uses a method of helium exchange gas to allow for precise temperature control. Fundamentally, the VTI consists of an exchange chamber and a sample chamber. The measurement probe is placed inside of the sample chamber and measurements can be done under high vacuum or with a constant low-pressure of helium exchange gas to improve temperature exchange between the probe and the inner-walls of the chamber. A needle valve between the exchange chamber and the helium reservoir of the magnet allows for a small and controlled amount of helium to flow into the exchange chamber. A second valve, located at the top of the VTI, leads to a pump used to continuously pump on the exchange chamber. Finally, a heater and a thermometer are used to set and read the temperature of the exchange gas. By controlling the flow of helium gas and the voltage of the heater, the temperature of the VTI can be regulated.

5.3 Excitation and Readout

The mechanical excitation of the cantilever at different frequencies was conducted by using a LIA to apply a voltage V_{drive} across electrodes on the piezoelectric transducer. Cantilever deflection was measured with a Laser Doppler Vibrometer (LDV) — a type of interferometer that uses the Doppler shift to determine target velocity. The LDV converts the optical signal into an electronic one (V_{signal}) which was fed into the input of the LIA. The LIA computes the resulting amplitude and phase of the signal at the drive frequency and this information is sent to the computer. The critical optical and electrical schematics are sketched in Fig 5.1.

5.3.1 Laser Doppler Vibrometer

In an LDV (Fig 5.1), a laser beam with initial frequency of f_0 is split into two branches with one beam acting as the reference and the other aimed toward the target. When the target beam is reflected off of a moving target's surface, the Doppler effect causes the frequency of the light to be shifted by the Doppler frequency f_D, where f_D is proportional to the velocity of the target v:

$$\textbf{Doppler effect:} \quad f_D = 2\frac{v}{\lambda} \tag{5.2}$$

with λ is the wavelength of the light. The interference between the target and the reference

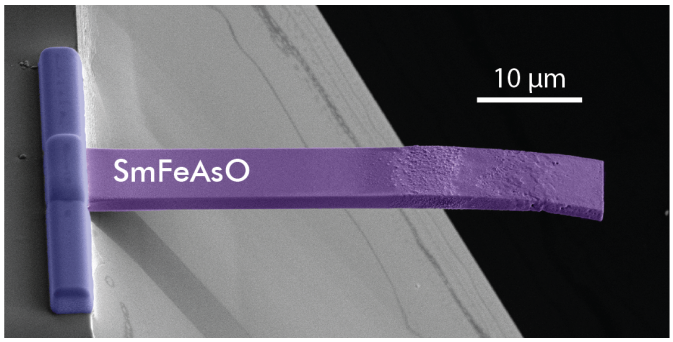

Figure 5.9: SEM image of a SmFeAsO cantilever damaged from laser heating during measurement.

beams allows for the determination of $|f_D|$ such that the speed can be computed. In order to ascertain the target's direction, a Bragg cell is added to the reference branch of the interferometer to shift the reference frequency by a known frequency, f_B, before the target and reference beams are recombined [134].

For experiments in this thesis, an OptoMET LDV Nova-Series Basis was used. This vibrometer is equipped with an infrared measurement laser with λ = 1550 nm and an output power of < 10 mW. The system is equipped with a velocity decoder designed for frequencies up to 500 kHz with a resolution of .1 μm s$^{-1}/\sqrt{\text{Hz}}$, although some resonance modes could be detected up to 2000 kHz. This frequency determines the resonance modes that can be measured. The capabilities of this technique could therefore be expanded by using a vibrometer with a larger frequency range.

Finally, it is necessary to consider the effect of the laser on the sample. During early tests, some cantilevers became damaged due to heating from the laser. This was marked by a change in the resonance frequency and can be seen in SEM images of the sample. Fig 5.9 shows a SmFeAsO cantilever after measurement. Structural damage is visibly concentrated near the free-end. Damaging during measurement was also observed as changes in the optical and electrical properties of nickelate cantilevers, although this phenomenon is more scientifically interesting and its discussion has been saved for 9.2.

Two solutions were found to prevent laser heating: (1) the sample can be measured far out of focus, decreasing the power per unit area or (2) the power of the laser can be reduced by the addition of an optical attenuator. The first solution has the disadvantages of losing spatial resolution and reducing the signal intensity. In the second, an optical attenuator with FC/APC connection was added in between the LDV and the sample probe, attenuating the laser in both directions. Thus the signal intensity is significantly reduced, although the spatial resolution is preserved. The efficacy of these solutions are illustrated in Fig 5.10. The resonance frequency of an undamaged sample of SmFeAsO was measured at different focal points and with different attenuator strengths. Due to the softening of the elastic constants with increasing temperature, laser heating on the sample can be seen as a downward shift of the resonance

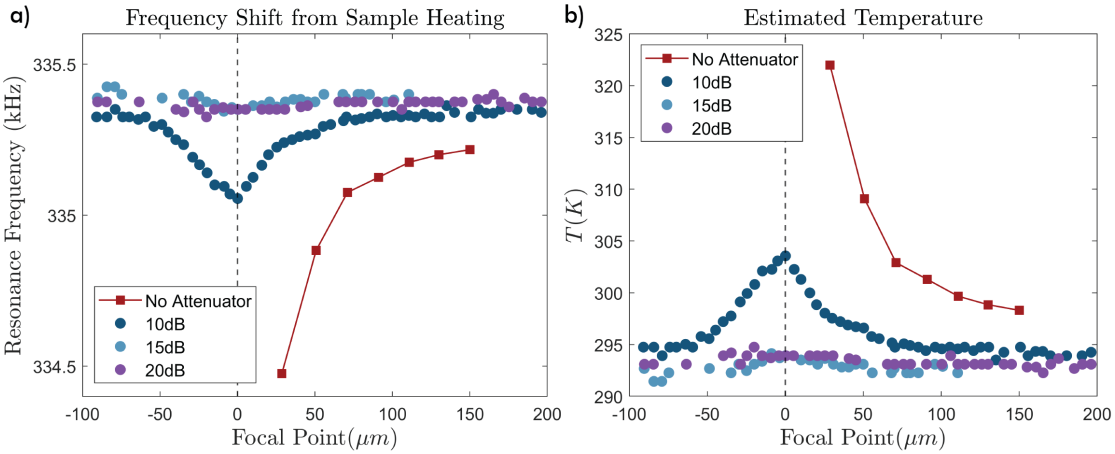

Figure 5.10: (a) Laser heating decreases the resonance frequency of the cantilever. This was used to determine the heating effects by adjusting the focal point (where 0 μm corresponds to the cantilever in-focus) and with different laser attenuators. (b) Based on the temperature dependence of the elastic constants (Eqn 2.48) and frequency versus temperature measurements on this cantilever, the resonance frequencies of (a) can be used to estimate the temperature of the cantilever. This test was done under vacuum, at room temperature.

frequency (Fig 5.10 (a)). When the focus point is far from the sample, or with a sufficiently strong attenuation, then no frequency shift from laser heating can be seen. Based on the temperature dependence of the elastic constants (Eqn 2.48) and from resonance frequency versus temperature measurements on this sample (Fig 6.5), the temperature of the cantilever can be approximated (Fig 5.10 (b)). This calculation assumes a uniform temperature and, as such, should be considered only as a rough estimate of the average cantilever temperature and will underestimate the temperature near the laser.

To prevent sample damage as seen in Fig 5.9, the sample was not measured in focus without an attenuator. No shift in the resonance frequency when the cantilever is in focus was seen with 15 dB and 20 dB optical attenuators. I.e. no significant laser heating is apparent when the laser power is tuned from < 10 mW to < .32 mW. Later measurements were therefore done using a 15 dB or 20 dB attenuator with the cantilever in focus. A better solution to this problem would be to tune the laser power directly, rather than adding an attenuator that will attenuate the incoming signal as well as the outgoing laser. This was not possible for the vibrometer used in this thesis but is worth keeping in mind if the reader is interested in purchasing an interferometer for micro-cantilevers.

5.3.2 Lock-in Amplifier

LIAs are powerful devices for isolating a periodic signal in the presence of a noisy background by making use of the orthogonality of sines. The raw input signal, V_{signal}, is multiplied by the reference, V_{ref} (in this case the driving voltage, V_{drive}) and the reference phase shifted

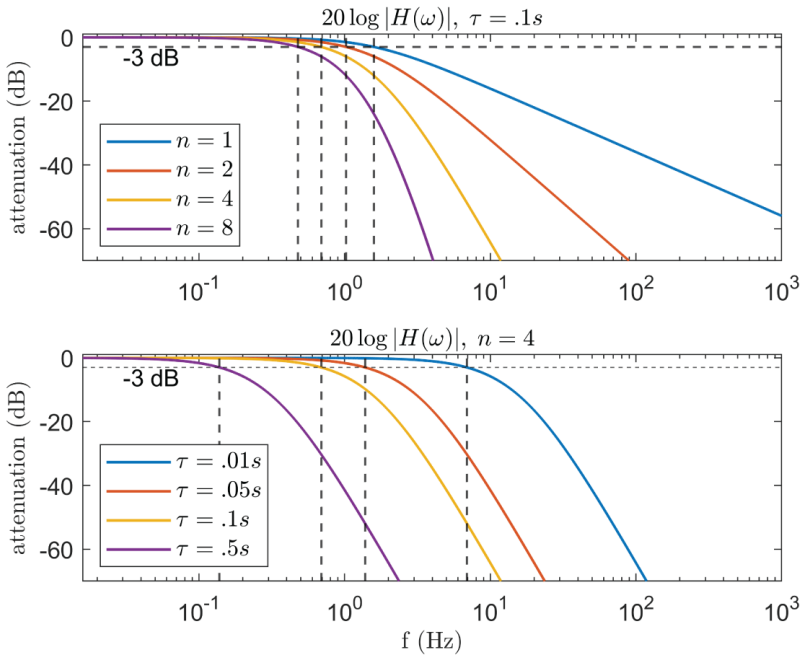

Figure 5.11: Bode plots for n RC filters. The top graph shows different filtering orders with the same time constant $\tau = .1$ s while the bottom graph shows different time constants for the order $n = 4$. The cut-off frequencies, defined as the frequency at which the signal amplitude is reduced by -3 dB, are indicated for each plot as vertical dotted lines.

by 90°. If V_{ref} is a pure sinusoidal function with frequency f_{ref}, these operations convert the components of V_{signal} with $f = f_{\text{ref}}$ from AC to DC. A low-pass filter then isolates the X and Y components within a small bandwidth around f_{ref}. X and Y can then be converted to the amplitude, R, and phase, θ. The conversion of the raw input signal, V_{signal}, into X and Y or R and θ is conducted within one demodulator. Many LIAs contain multiple demodulators, allowing for the measurement of several different signals.

Furthermore, the frequency resolution will be defined by the low-pass filter. As an ideal filter, with perfect transmission for all frequencies within the bandwidth and zero transmission outside of the bandwidth, is impossible to realize, it is useful to consider the shape of the low-pass filter. The transfer function of the n low-pass RC filters used can be approximated by

$$H_n(\omega) = \left(\frac{1}{1 + i\omega\tau}\right)^n \tag{5.3}$$

where $\tau = RC$ is the time constant. The Bode plots (defined as $20\log|H(\omega)|$) for different filtering orders, n and for different time constants shown in Fig 5.11 shows the frequency attenuation. The cut-off frequency is defined as the frequency at which the signal power is reduced by half, or -3 dB. Increasing the filter order increases the steepness of the roll-off

above the cut-off frequency, thereby better approximating an ideal filter. The cut-off frequency can also be decreased by increasing the time-constant. Therefore, both the frequency order and the time constant should be considered to determine the frequency resolution [135].

A Zurich Instruments HF2LI 50 MHz was used for measurements in this thesis. This lock-in amplifier has the capacity to supply two output voltages ($V^{1,2}_{\text{drive}}$) and read in two signal inputs ($V^{1,2}_{\text{signal}}$). Moreover, it has six demodulators, e.g. it can be configured to demodulate $V^{1,2}_{\text{signal}}$ at $f^{1,2}_{\text{drive}}$ and at the higher harmonics $2f^{1,2}_{\text{drive}}$ and $3f^{1,2}_{\text{drive}}$.

5.4 Principles of Measurement Software

5.4.1 Aligning the Cantilever

The small inner chamber of the VTI creates one of the pressing challenges of this technique: within the restricted dimensions of the micro-resonator probe, it was not possible to fit a camera for in-situ imaging to align the sample. Furthermore, the short focal length of the lens and limited visibility of the sample stage means that a cantilever cannot reliably be aligned ex-situ, e.g. with the help of a microscope and a targeting laser. Consequently, the vibrometer and micro-positioners must be used for imaging by moving from position to position in a arduous pixel-by-pixel fashion. As the goal of this thesis is ultimately to explore scientific questions and not to build a camera, this alignment process was optimized to locate and focus on a $\sim 10 \times 100$ μm cantilever.

The first question to approach is how to collect the data at each pixel. The main functionality of the LDV is as a velocity detector, which, without prior knowledge of the cantilever resonance mode, cannot be used to distinguish the cantilever from its background. The LDV is also equipped with a displacement decoder; however, this decoder is designed to be sensitive across a continuously varying displacement (e.g. sinusoidal motion at a point) rather than to detect large and sudden jumps like a profilometer. Early attempts used this decoder, but significant height steps resulted in incorrect distance measurements such that an accurate image could not be obtained. Fortunately, the vibrometer also contains a photodiode to detect the signal intensity. If a brightly reflecting cantilever is appropriately mounted over a dark background, cantilevers can be focused and imaged by plotting the signal intensity versus position.

Aligning the cantilever therefore begins in fabrication, with an apt choice of mounting conditions. Mounting cantilevers over the sloped trench on the bottom side of a Si_3Ni_4 membrane chip was found to produce excellent signal contrast while protecting the cantilever from damage (See 4.1.1). For a cantilever mounted on the edge of a chip (for example, most commercially available cantilevers), good contrast can be obtained by mounting the sample over a background covered with a carbon paint or lubricant (Bonderite L-GP 156 Acheson). On the sample platform, the cantilevers should be mounted over the center of the platform (directly over the center screw) which was marked with a drill tip on both the rigid and adjustable sample stages

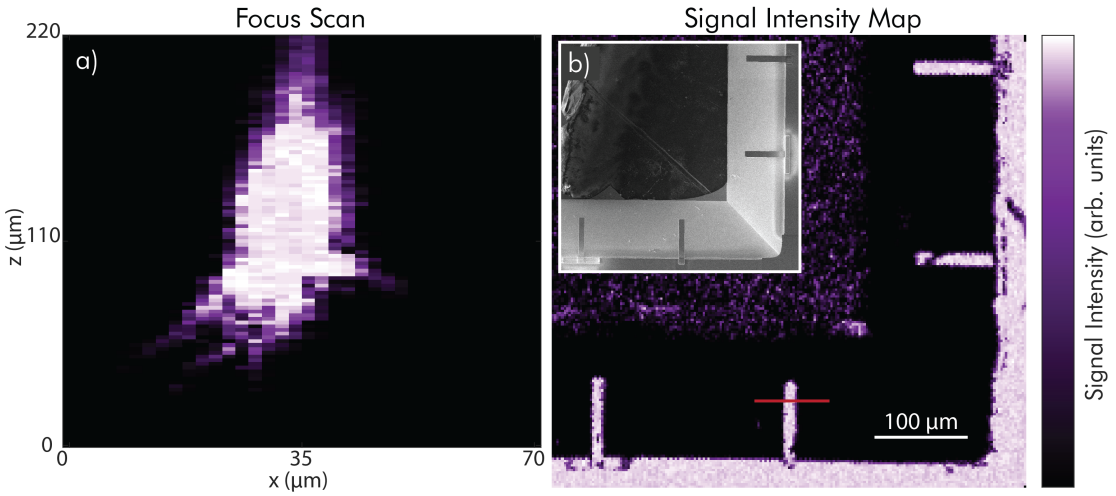

Figure 5.12: Reflected signal intensity measured over xz (a) or xy (b), where z is parallel to the incident laser beam. (a) Typical scan used to focus the sample. A rough imaging is conducted to first locate the sample, then a line in the xy-plane that crosses over the width of the cantilever is selected. The signal intensity along this line is measured as a function of z. There is a region in z where the width of the area showing non-zero signal intensity is nearly constant. This indicates the focal region — in this graph the focus point is around $z = 110$ μm. (b) An in-focus signal intensity map of a chip containing four cantilevers. The inset shows an SEM image of the same cantilevers. The red line indicates the line across which (a) was taken to focus the samples. The angled mirror surface of the membrane trenches beneath the cantilevers have zero signal intensity, making the samples easy to distinguish.

(Figures 5.4 (b) and 5.5). This point is the center of range for the micro-positioners.

To image the cantilever on the micro-resonator probe, an imaging software was written that can scan across x, y and z corresponding to the directions of the micro-positioners with z normal to the sample plane. In principle, this software can be used to scan across all three dimensions but, in practice for the sake of time, the scan is only ever run across one or two dimensions, tracing a serpentine scan pattern in 2D. At each data point, the signal level (output from the vibrometer as a dimensionless integer) and measured positions are saved to a data file. The signal intensities can be interpolated as a function of position and plotted as an image. The collection of data at each pixel takes ≈ 1 s, where the time is largely dependent on the distance the micro-positioners travel in between pixels as most of the time is spent in moving. For example, to scan a typical area of 1.5 mm $\times$ 1.5 mm with a step size of 5 μm to detect a 10 μm wide cantilever, 90,000 pixels are needed. For 1 s per pixel, the total scan time is 25 hours. If the sample is slightly out of focus, then the cantilever may not even be visible in this image. To align cantilevers more efficiently, the following steps are used:

1. **Rough focusing:** With the x and y micro-positioners located in the center of their range, the z micro-positioner is moved with large steps to find the position in z at which the signal intensity is maximum. The idea is to focus the chip well enough that the top of

the chip will have high signal intensity.

2. **Large step imaging:** With z set to the rough focal point determined in Step 1, the scan software is used to scan over a large range of x and y, using the relatively large step size of 50-100 μm. From this rough image, the low-intensity square of the trench should be visible. If it is not visible, it may be necessary to repeat Step 1 at a different position.

3. **Locate cantilever:** The scanning range is decreased to scan only over the trench where the cantilever is positioned with a small enough step size to resolve the cantilever (2.5-10 μm).

4. **Focus cantilever:** A line in the xy-plane that crosses over the width of the cantilever is selected and scanned as a function of z. From the resulting signal intensity plot (Fig 5.12 (a)), the focus point can be extracted.

5. **Fine imaging:** At the focus point, the cantilever can be imaged with a small step size ($2.5-5$ μm). Fig 5.12 (b) shows a fine-image taken in-focus of four cantilevers. In general, it is only necessary to conduct the fine image around a small area for each cantilever individually.

Once the image is obtained, the stage can be moved such that the laser is focused near the free-end of the sample and the resonance can be measured by sweeping the driving frequency. The scanning software used for imaging can also optionally read in the velocity with a constant drive frequency or conduct resonance frequency scans at each data point. The former option is useful to spatially map out the resonance mode (see Fig 6.2) while the later option can be useful to check for problems such as the position-dependent shift in resonance frequency that arises from heating as shown in Fig 5.10.

5.4.2 Tracking Changes in Resonance

With the laser focused on the free-end of the cantilever, the resonance spectrum can be obtained by mechanically exciting the piezoelectric transducer at different frequencies and plotting the resulting velocity or displacement amplitude versus frequency. Once the full spectrum is obtained, finer sweeps can be done in a smaller range across the resonance mode(s). To track the change in the resonance vs temperature, these resonance sweeps can be run continuously while the temperature is swept. The amplitude of the cantilever, R, as a function of the driven frequency, f, follows the form of a Lorentzian:

$$R(f) = \frac{A_0}{\sqrt{(2\pi)^2(f-f_0)^2 + (\Gamma/2)^2}} \tag{5.4}$$

Where Γ is the linewidth. Eqn 5.4 can be fit to the frequency sweep to determine the resonance frequency f_0. The Q-factor, Q, can be calculated from

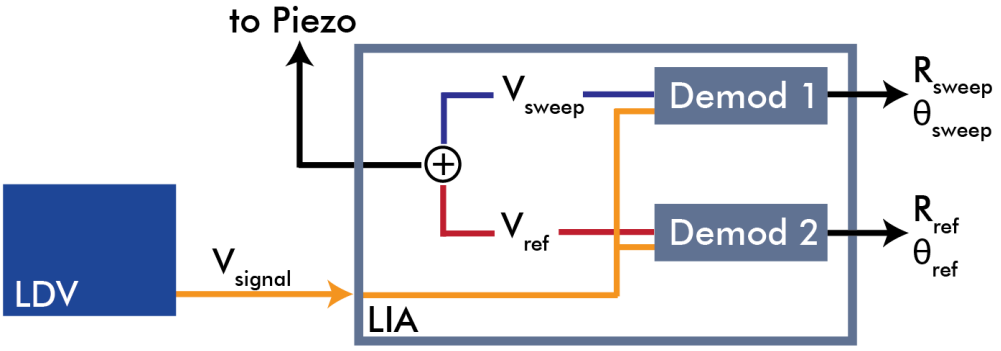

Figure 5.13: Sketch of the measurement scheme to detect slow fluctuations. The piezoelectric transducer is driven by V_{sweep}, with a frequency sweep across the cantilever resonance, and V_{ref}, with a constant frequency outside of the swept frequencies. Two demodulators are used to demodulate V_{signal} by V_{sweep} and V_{ref}.

$$Q = \frac{f_0}{FWHM} \tag{5.5}$$

where FWHM is the full width of the resonance peak at half the maximum. By saving the full frequency sweep data and conducting the fit during post-processing, one can check that the fit procedure is performed properly and look for anomalies in the shape of the resonance mode — such as excessive noise, resonance peaks that arise from the background or possible non-linearities.

Signal Fluctuations

Unfortunately, the addition of the attenuator causes a critical problem: V_{signal} fluctuates over a long period of several seconds causing the resonance spectrum to show additional peaks that are not reproducible. The exact origin of this is unknown, although without the attenuator, these slow fluctuations do not appear. This could be due to back-reflections from the attenuator, or a result of the significant reduction in signal intensity. The time period of fluctuations is too long to effectively average over. Each point in the > 100 pt frequency sweep would need to be measured for several seconds, increasing the time to obtain a single data point in $f_0(T)$ by an order of magnitude. No method was found to eliminate these fluctuations with the vibrometer used for this thesis, although this may not be a problem in a system in which the laser power can be tuned directly. Without a viable solution, early experiments suffer from significant noise, reducing accuracy in the determination of f_0 and Q. To remove exceptionally noisy sweeps from these early experiments, resonance frequency data from the raw frequency sweeps that meet the below criteria are excluded from the final results:

$$\frac{\max(R - R_{\text{fit}})}{\max(R)} > \text{cutoff} \tag{5.6}$$

Where R_{fit} is the fit of the raw data, R, to Eqn 5.4 and a cutoff of .2 was used. This effectively removes sweeps which show multiple large peaks arising from these fluctuations as it was not possible to distinguish between these noisy peaks and the real resonance mode.

However, it was later discovered that, while the fluctuations could not be removed from the optical set-up, they could be distinctly measured and separated from the raw signal in postprocessing — substantially reducing noise and improving resolution of $f_0(T)$. A sketch of the measurement scheme to detect these slow fluctuations in the velocity channel is provided in Fig 5.13. The LIA is used to supply two voltages, V_{sweep} and V_{ref}. The frequency of V_{sweep} is swept to obtain the resonance spectrum while the frequency of V_{ref} is a constant outside the range of f_{sweep}. The piezoelectric transducer is driven by the sum of these voltages:

$$V_{\text{drive}} = V_{\text{sweep}} + V_{\text{ref}} \tag{5.7}$$

Two of the LIA's six demodulators are used to demodulate V_{signal} with V_{sweep} and V_{ref} to obtain (R_{sweep}, θ_{sweep}) and (R_{ref}, θ_{ref}), respectively. Two of the remaining demodulators can be configured in the same manner for the displacement channel of the LDV while the last two demodulators can be used for higher harmonics. The raw amplitude, R_{sweep}, and background fluctuations, R_{ref}, of an example resonance sweep of a cantilever as measured through the velocity channel are plotted in Fig 5.14. In the top graph, the resonance visible in R_{sweep} is clearly distorted. The middle graph shows R_{ref} which, in the absence of fluctuations, should be constant. In the bottom graph, dividing R_{sweep} by R_{ref} removes the distortions, revealing a well-defined resonance peak.

As this process relies on measuring the response of the cantilever far off of resonance, R_{ref} will naturally have a much smaller signal-to-noise ratio than R_{sweep}. In order to maximize the signal-to-noise ratio of R_{ref}, the amplitude of V_{ref} is much larger than the amplitude of V_{sweep} needed to excite the cantilever into resonance. For example, in a typical measurement, $|V_{\text{ref}}| = 9V$ and $|V_{\text{sweep}}| = .1V$.

Background Modes

The body of the micro-resonator probe and its components (e.g. the sample stage) have mechanical resonance modes that compose a background resonance spectrum. These background resonances can pose a significant problem when they near and sometimes cross over the cantilever resonance, making it difficult to distinguish the cantilever resonance frequency.

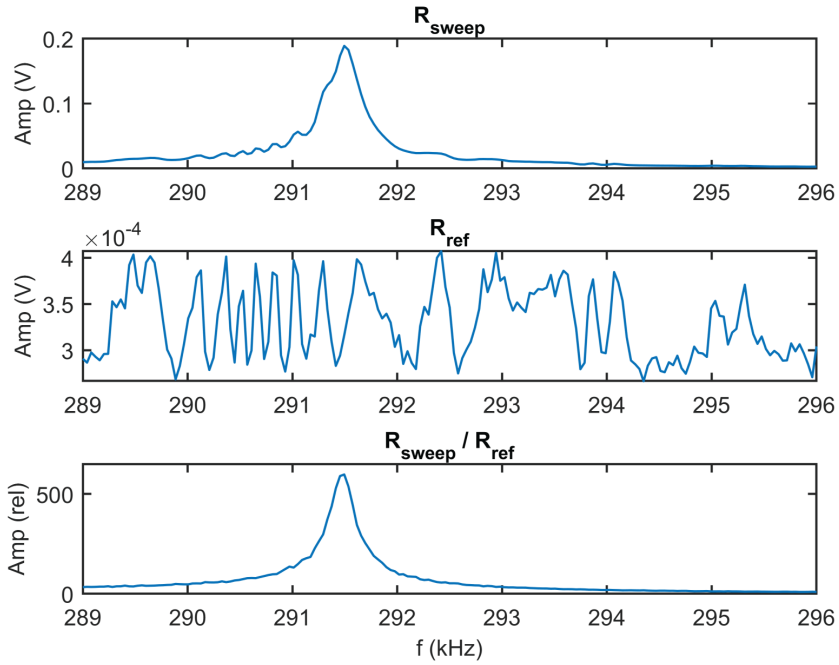

Figure 5.14: Top: the raw signal of a cantilever resonance that is distorted by long-period fluctuations. Middle: by measuring the cantilever at a constant frequency outside of the sweeping range, the fluctuations can be isolated. Bottom: Dividing R_{sweep} by R_{ref} removes the distortions of the resonance.

Fig 5.15 shows an example frequency sweep conducted across the fundamental resonance of a cantilever with clearly visible background resonance modes. Using the reference signal obtained as described in 5.4.2, the amplitude of the cantilever is calculated as:

$$R_{\text{cant}} = \frac{R_{\text{sweep}}^{\text{cant}}}{R_{\text{ref}}^{\text{cant}}} \tag{5.8}$$

By conducting an identical sweep with the laser focused on the sample chip, the background spectrum can be obtained:

$$R_{\text{bkg}} = \frac{R_{\text{sweep}}^{\text{bkg}}}{R_{\text{ref}}^{\text{bkg}}} \tag{5.9}$$

From these measurements, the pure cantilever amplitude can be computed:

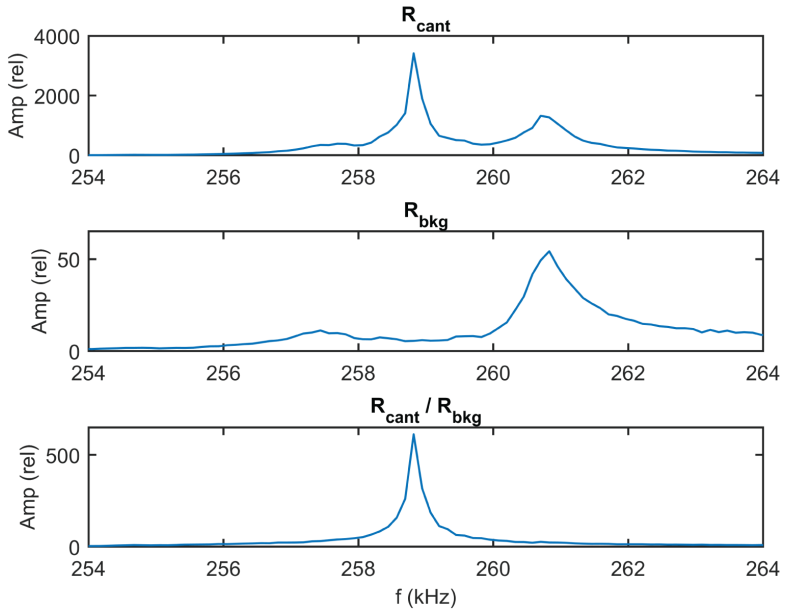

Figure 5.15: Top: Example of a resonance sweep across the fundamental resonance mode of a cantilever. Middle: background resonance spectrum as measured on the sample chip, near the base of the cantilever. Note the much smaller amplitude of the background peaks on the sample chip versus on the cantilever. Bottom: By dividing the cantilever amplitude by the background amplitude, the pure cantilever resonance can be extracted.

$$R = \frac{R_{\text{cant}}}{R_{\text{bkg}}} \tag{5.10}$$

Background resonance modes can vary in temperature and sometimes also with the position of the sample stage or the micro-positioners. In order to remove the background throughout a temperature or field sweep, a sweep is first conducted on the cantilever, the stage is moved such that the laser is focused on the sample chip, near the base of the cantilever, the measurement is repeated and the stage is moved back to the cantilever (Fig 5.16). This process runs continuously as the temperature is swept.

Automating repeated stage movement during temperature scans is tricky: the position readout of the micro-positioners is temperature dependent, with a particularly steep slope at very low temperatures (< 10 K). This T-dependence varies for each micro-positioner and for their position as well. Calibrating the position encoders is therefore a very involved process. Unfortunately, even a small misalignment of the laser position can cause it to wander off of the cantilever, losing subsequent data. A work-around for the encoders' T-dependence involves moving the sample stage relative to the current position. Before beginning the measurement, the stage is moved such that the laser is focused on the free-end of the cantilever ($\vec{r}_{\text{cant}}$) and the user defines a vector $\vec{r}$ in between the cantilever and background positions.

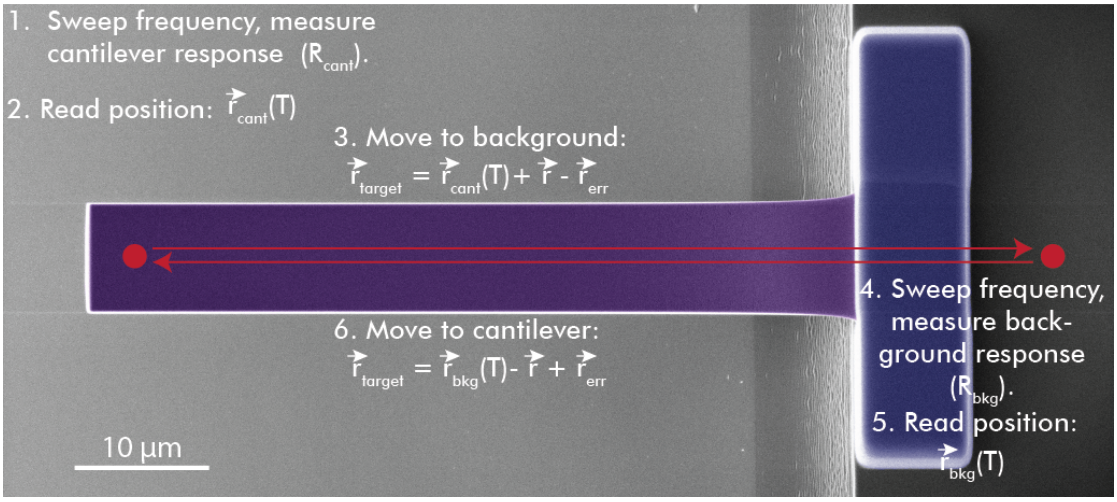

Figure 5.16: During a temperature sweep, background resonance modes can be removed from the cantilever spectrum by moving the stage to the sample chip near the base of the cantilever and measuring them explicitly after each sweep on the cantilever. Because the position readout of the micro-positioners is temperature dependent, this process is best done by moving the stage to an initial starting position on the cantilever (R_{cant}) and defining a vector $\vec{r}$ to which the stage should move for the background spectrum.

When the measurement starts, a frequency sweep is conducted to measure R_{cant}. After the sweep ends, the current position on the cantilever, $\vec{r}_{\text{cant}}(T)$, is read and the stage is moved to $\vec{r}_{\text{target}} = \vec{r}_{\text{cant}}(T) + \vec{r} - \vec{r}_{\text{err}}$ where $\vec{r}_{\text{err}} = \vec{r}_{\text{target}} - \vec{r}_{\text{position}}$ is the error from the previous move ($\vec{r}_{\text{err}} = 0$ initially and $\vec{r}_{\text{position}}$ is the actual position). The frequency sweep on the background is conducted to obtain R_{bkg}, after which the current position on the background is measured again $\vec{r}_{\text{bkg}}(T)$. The stage is then moved to $\vec{r}_{\text{cant}}(T) - \vec{r} + \vec{r}_{\text{err}}$ and the process is repeated. By re-measuring the position after each scan, this algorithm corrects for changes in the position readout that are due to temperature changes. Unfortunately, the full process is time-costly. Measuring background resonance modes more than doubles the amount of time it takes to obtain a single data point and is therefore only used when background modes interfere with the cantilever mode.

Phase Locked Loop

Rather than conducting frequency sweeps at each temperature, a more efficient method of tracking the resonance frequency can be done using a Phase Locked Loop (PLL) which uses a feedback loop to lock onto the phase at resonance and track changes in the phase. However, the background spectrum can shift the phase of the cantilever resonance, making it difficult to accurately track. Some desktop vibrometers have the capacity to measure a sample and background point concurrently. This process would be technically challenging to implement for temperature and field measurements, but would eliminate the need to move the stage for background measurements, thus making it easier to extract the pure resonance of the

cantilever or track resonance using a PLL. Furthermore, for the purpose of establishing this technique, it was often helpful to examine the full raw data to fully understand the resonance and look for problems. Nevertheless, implementing a PLL in the future could greatly increase frequency and temperature resolution.

6 Evaluation of FIB Cantilevers

The current capabilities of this technique were established beginning with the FIB-fabrication of cantilevers from silicon, a cubic material whose room-temperature elastic properties have been exquisitely well-studied [66, 67]. Starting with a material with a known elastic tensor enables an evaluation of the accuracy of the technique and highlights areas for improvement. From FIB fabricated cantilevers of Si, the anisotropic Young's modulus along the [110] direction, E_{110}, was determined to within 7-12% of the expected value based on [67]. Based on geometric uncertainties and deviations from a perfectly rectangular cantilever, the error on Young's modulus was 19%. Improvements in the fabrication process that decrease geometric variations were able to reduce the calculated error on Young's modulus for materials presented later in this thesis to 8-12%.

Once the fabrication and measurement processes have been successfully demonstrated on Si, the focus is shifted to a material known to exhibit interesting electronic correlations but whose measurements are limited by the fact that single crystals only exist on a sub-100 μm length scale. SmFeAsO undergoes both a magnetic and tetragonal-to-orthorhombic structural transition at $T_s \approx 130$ K [136–140] and is regrettably under-explored due to its challenging size. FIB-fabricated micro-cantilevers are thus an ideal tool to probe its intriguing properties. Cantilevers cut in the [100] direction of SmFeAsO follow the stiffening expected from phonon anharmonicity at high temperatures and show a clear jump at T_s. These measurements demonstrate the capacity of this technique to explore phase transitions in quantum materials.

6.1 FIB-Fabricated Cantilevers of a Known Material: Silicon

The FIB fabrication process detailed in Ch 4 was used for two Si cantilevers with the longest and shortest dimensions along the [110] and [001] axes, respectively. The final current used for polishing and structuring sets the geometric precision and was 1 nA for both cantilevers — higher precision can be achieved with $I = .1 - .33$ nA. These cantilevers were welded to the sample chip using W FIBID — deposition parameters are summarized in Table 6.2. The sample chip was then mounted onto the micro-resonator probe in a vacuum tight tube continuously

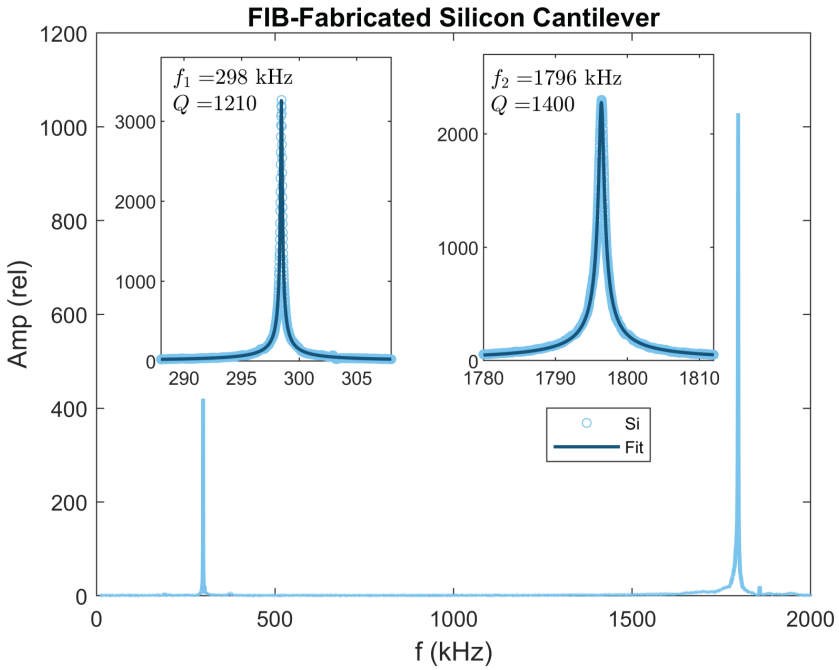

Figure 6.1: The measured resonance spectrum of a FIB-fabricated Si Cantilever. The insets show frequency sweeps around each resonance mode fit to Eqn 5.4 to extract the resonance frequency and Q-factor.

	Voltage (kV)	**Current (nA)**	**Dwell time (ns)**	**Overlap (%)**	**Blur (μm)**
Sample A	30	4	40	-100	0
Sample B	12	7.5	50	90	0

Table 6.1: Deposition parameters used for the base weld of the FIB-fabricated Si cantilevers.

pumped to $<1e^{-4}$ mbar and measurements were conducted at room-temperature. For these initial tests, the laser was focused onto the free-end of the cantilever without attenuation. No evidence of sample deformation due to laser heating was seen in either SEM images or in the quality-factor of the resonators. This is not surprising given silicon's relatively high melting temperature (T_m = 1414 °C). Nevertheless, laser heating is likely to have shifted the measured resonance frequencies downwards from the expected room-temperature value [141].

The resonance spectrum of a FIB-fabricated Si cantilever is shown in Fig 6.1. The insets show finer-frequency scans conducted around each measured resonance. The resonance frequency, f_n, and Q-factor, Q, are determined by fitting the fine-scans to Eqn 5.4. One advantage of this technique is that the laser can be scanned across the surface on resonance to map out the motion of the cantilever. This enables one to determine the resonance mode, as well as to check for problems such as uneven mounting conditions. Fig 6.2 shows spatial scans of f_1 and f_2 on resonance.

From the fundamental resonance frequencies, E_{110} can be calculated using Eqn 2.41 with

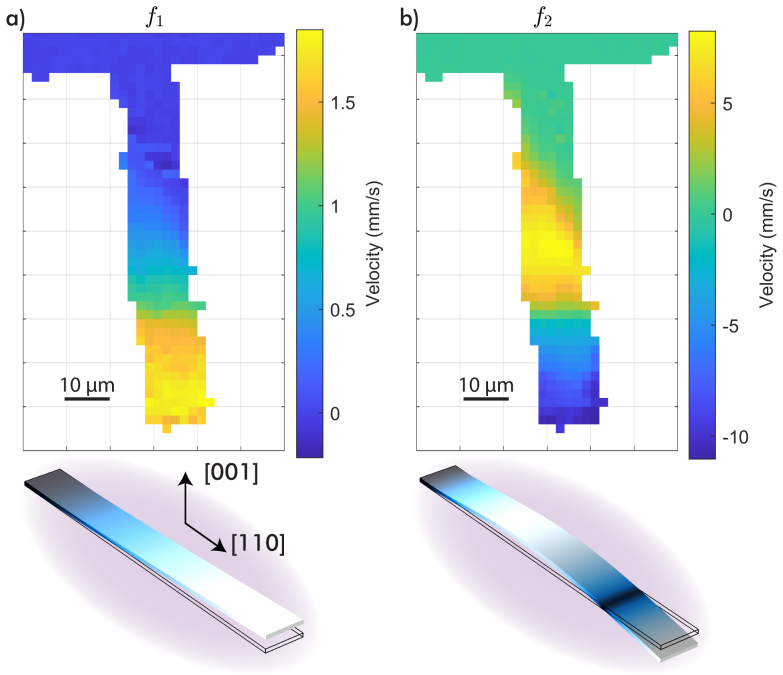

Figure 6.2: (Top) Spatial scans of resonances f_1 (a) and f_2 (b) shown in Fig 6.1. (Bottom) Simulated resonance modes to show the cantilever motion.

the error calculated from Eqn 2.42. Geometric factors of the cantilevers have been measured from SEM images. E_{110} and σ_E are 157.4 ± 30 GPa and 150.0 ± 28 GPa. These results are summarized in Table 6.2. Young's modulus can be compared to the expected values from elasticity measurements of silicon in literature. The room temperature elastic components as measured from Pulse-echo ultrasound (PE) measurements are summarized in Table 2.1 [67]. From Eqn 2.22, E_{110} of a cubic sample is

$$\frac{1}{E_{\mathbf{110}}} = \frac{1}{4}(2s_{11} + 2s_{12} + s_{44}) = \frac{1}{4}\left[\frac{1}{c_{44}} + \frac{1}{c_{11}/2 + c_{12}/2 - c_{12}^2/c_{11}}\right] \tag{6.1}$$

such that Young's modulus is E_{110} = 168.9 GPa. The expected value from PE is therefore within the error bar of Young's modulus from the FIB-fabricated cantilevers. Considering the possibility of laser heating, E_{110} softens with increasing temperature. From room temperature to the melting point at ~ 1400 °C, E_{110} decreases by ~ 21 GPa [141]. If the unattenuated laser was heating the sample, then the effect would have been to shift the measured value of E_{110} down by up to a few GPa. Correcting for laser heating would shift the measured E_{110} up towards the value calculated from [67], which will therefore still be within the error.

Results from the FIBed cantilevers can also be compared to a similar experiment in which silicon cantilevers were fabricated via lithographic processes. For a cantilever with the same

	E_{110} **(GPa)**	σ_E **(GPa)**	σ_E/E_{110} **(%)**
Pulse-echo	168.9	-	-
Lithographic Fabrication	170.1	3.2	1.9
FIB Fabrication (Sample A)	157.4	30	19
FIB Fabrication (Sample B)	150.0	28	19

Table 6.2: Values of E_{110} of silicon. The PE value of E_{110} is computed from Eqn 6.1 using the elastic tensor reported in [67]. Lithographically fabricated silicon cantilevers were measured in [66]. The expected value of E_{110} from PE falls within the error of the measured E_{110} from the FIB-fabricated cantilevers of this work.

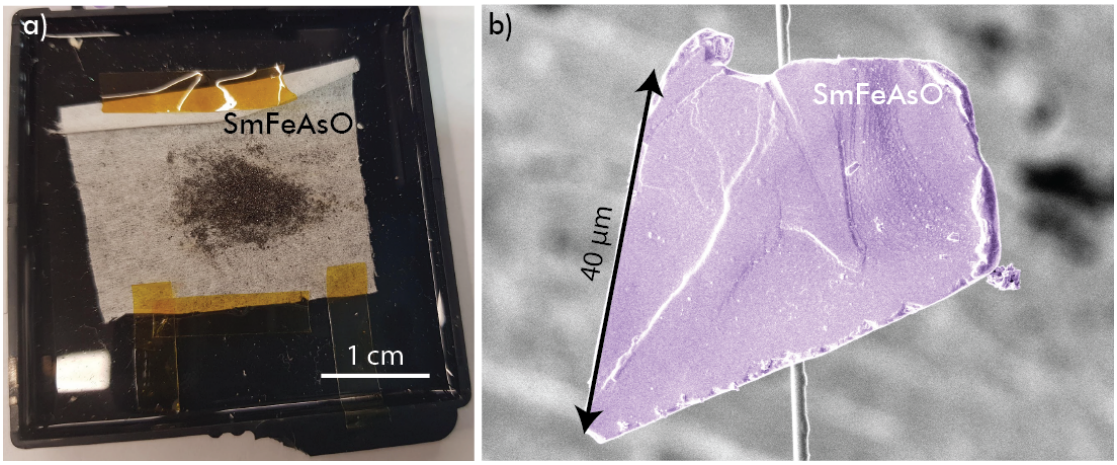

Figure 6.3: (a) Without magnification, single crystals of SmFeAsO appear as a pile of dust. (b) SEM image of a typical crystal.

orientation as those studied in this thesis, $E_{110} = 170.1 \pm 3.2$ GPa [66]. When massive, high-quality single crystals are available, PE measurements will be more accurate than resonance modes of lithographically fabricated cantilevers in determining elastic constants. This is due to the sensitivity of resonance modes to the geometry of the sample. For example, a 5% variation in measured elastic moduli was found for silicon cantilevers with different resonator geometries [142]. FIB-fabrication can be considered as a viable alternative for elasticity measurements in materials for which lithographic processes and PE are not available.

6.2 Phase Transition in a Quantum Material: SmFeAsO

When viewed without a microscope, single crystals of SmFeAsO could be confused for a pile of dust (Fig 6.3 (a)). With length scales ~ 40 μm, measurements that can be conducted to explore their properties and the rise of high-temperature unconventional superconductivity upon flouride-doping are limited. Interest in REFeAs(O,F) (RE = rare-earths) was one of the main drives motivating the application of FIB-fabrication for quantum materials. More than a decade ago, FIB deposition and etching enabled researchers to explore the electronic transport

Figure 6.4: SEM image of a FIB-fabricated cantilever of SmFeAsO.

Sample	T **(K)**	E_{100} **(GPa)**	σ_E **(GPa)**	σ_E/E_{100} **(%)**
A	290	93.6	10.3	11
B	230	86.2	13.4	16
C	290	109.4	11.5	11

Table 6.3: E_{100} and error, σ_E, of SmFeAsO cantilevers.

properties of the microscopic high-T_c pnictides [30–33]. FIBed micro-cantilevers now enable the exploration of the elastic properties. The elasticity of SmFeAs(O,F) is fascinating enough to merit it own chapter (Ch 7), while here it demonstrates the potential of FIBed cantilevers for the study of quantum materials.

SmFeAsO cantilevers were fabricated using the process flow outlined in Ch 4. To measure E_{100}, the length of the cantilever was directed along [100] (Fig 6.4). Measurements were conducted on the micro-resonator probe inside the VTI of a 16 T magnet for temperature control. To prevent heating from the laser on the sample, a 15 dB attenuator was used. The fundamental resonance frequency was found by sweeping the excitation frequency and fitting the resulting amplitude versus frequency curve to Eqn 5.4. Young's modulus is computed from Eqn 2.41. The addition of the attenuator to the optical path reduces the signal quality and results in long-period amplitude fluctuations. Studies on the [100] cantilevers were done prior to the addition of the second driving amplitude at a constant frequency which makes it possible to measure and remove these fluctuations (5.4.2). The additional noise in the frequency sweeps results in noise in f_0 vs T (and thus also in E_{100} vs T). For exceptionally noisy sweeps, it was not possible to obtain f_0, resulting in gaps in the temperature scans. Furthermore, because of the noise, it was not possible to reliably obtain the Q-factor. Nonetheless, these measurements on SmFeAsO [100] cantilevers provide insight into the elastic properties and the effect of the magnetic and structural phase transition.

Results of E_{100} are summarized in Table 6.3. At T = 290 K, two samples (A and C) were measured to have E_{100} of 93.6 GPa and 109.4 GPa with an error of 11%. Sample B (not measured up to 290 K) was measured at 230 K to have E_{100} = 86.2 GPa with an error of 16%. Temperature-dependent measurements of E_{100} from cantilever A are shown in Fig 6.5 (top). Arrows indicate

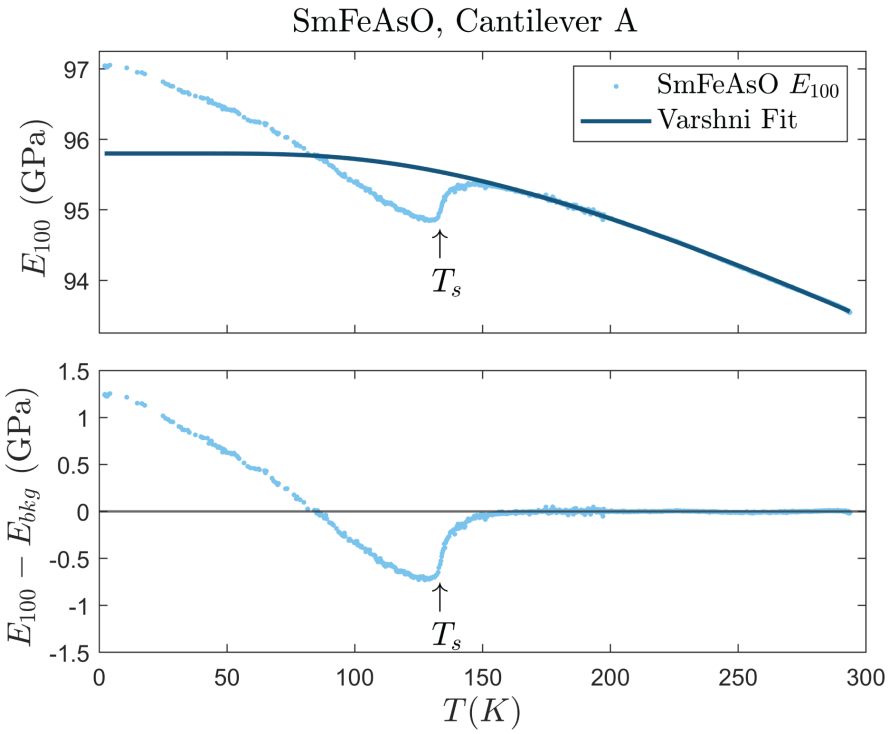

Figure 6.5: E_{100} versus temperature (top) fit to Varshni's equation for the phonon contribution (Eqn 2.48). The phonon contribution was subtracted from the raw data (bottom). Arrows indicate the structural phase transition (T_s) as determined by synchotron XRD in [136].

the tetragonal-to-orthorhombic structural phase transition, T_s [136, 139, 140]. Above T_s, the stiffening in E_{100} corresponds with expected stiffening from the phonon contribution and can be fit to

$$\textbf{Varshni fit}: \quad E = E^0 - \frac{s}{e^{t/T} - 1} \tag{2.48}$$

with fitting parameters E^0 = 95.8 GPa, s = 9.2 GPa and t = 479 K. In Fig 6.5 (bottom) this background was subtracted from the raw data to show the contribution to Young's modulus from the magnetic and structural transition. At $T \approx T_S$, E_{100} shows a clear discontinuity with a magnitude of $-.7$ GPa or $\sim .7\%$. Below the transition, E_{100} stiffens.

These results can be compared to elasticity measurements conducted on another family of the pnictides, $BaFe_2As_2$. Like SmFeAsO, the undoped parent compound has a structural and magnetic phase transition that is suppressed upon doping. In three-point bending measurements on $BaFe_2As_2$, E_{100} shows a sharp drop at T_s = 135 K. In contrast to the stiffening shown in Fig 6.5, E_{100} is relatively constant in temperature below T_s [143]. The temperature independence below T_s is attributed to the formation of multiple domains at the structural

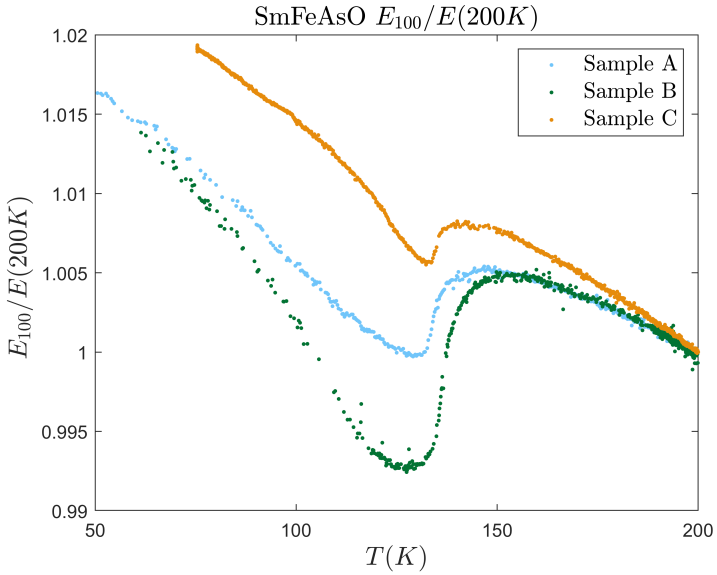

Figure 6.6: E_{100} of three different SmFeAsO cantilevers normalized to $T = 200$ K. Differences between the cantilevers can be seen above and below the phase transition as well as in the shape of the transition. This is most likely due to compositional variations between the samples.

transition and the reported Young's modulus therefore does not likely correspond to Young's modulus of a monodomain sample.

In pulsed-echo ultrasound measurements, softening is observed at T_s in the c_{11}, c_{33}, $c_E = \frac{1}{2}(c_{11} - c_{12})$, and c_{44} components. Below the structural and magnetic phase transition, these components stiffen. Above T_s, c_{44} and c_{66} also soften before the transition [144, 145]. From Young's modulus for a tetragonal crystal (Eqn 2.28), $E_{100} = E_{100}(c_{11}, c_{12}, c_{13})$ and therefore the anomaly observed at T_s in E_{100} SmFeAsO, corresponds to a dip in one or more of these components. While more measurements are needed to work out the exact elastic moduli, results on E_{100} are consistent with the measurements in literature of $BaFe_2As_2$. These measurements on SmFeAsO FIBed cantilevers exhibit the potential of FIB micro-cantilever fabrication as a novel method of probing elasticity across phase transitions in quantum materials.

It should be noted that significant variation in the samples were observed, despite consistent fabrication methods. This can be seen in the large high-temperature variance of E_{100} given in Table 6.3, as well as in the temperature scans of all three cantilevers (Fig 6.6). The shape and magnitude of the transition, and the slope of E_{100} varies depending on the sample. This is most likely due to compositional differences between the samples. Cutting into the crystals with the FIB often revealed large defects such as vacancies or flux-inclusions. FIB fabrication allows the user to choose crystals without deformation and polish off visible defects; however, some defects may still remain hidden in the sample. Furthermore, there may be variations in the amount of oxygen in the samples that arise during the growth of these crystals. Re-

moving oxygen will effectively electron-dope the crystal and shift the transition downwards. Finally, a slight misalignment can result in a softening of E_{100} (See Ch 7); the accuracy of this technique may benefit from an additional XRD step on the final cantilever to determine any misalignment.

7 Electronic Nematicity in SmFeAs(O,F)

The 2008 discovery of superconductivity with $T_c = 26$ K in fluorine-doped LaFeAsO piqued the interest of the scientific community [12]. The race began to unearth new iron-based superconductors (FeSC) and delve into their complex phase diagrams in which superconductivity arises (usually) in close proximity to a magnetically-ordered state. Among the newly found superconductors was fluorine-doped SmFeAsO which, to this day, maintains its status of the highest-T_c of the bulk FeSC ($T_c \approx 55$ K), surpassed only by monolayer films of FeSe ($T_c \approx 65$ K) [146, 147]. Despite the noteworthy T_c, the experimental challenges of working with the microscale crystals have limited research on SmFeAs(O,F) in favor of larger FeSC such as the popular $BaFe_2As_2$.

Studies on doped $BaFe_2As_2$ revealed an interesting phenomenon: a large electronic anisotropy that precedes or accompanies the magnetic ordering [22, 23]. This breaking of the rotational symmetry was dubbed "electronic nematicity" and begs the question of the nature of the relationship between nematicity and superconductivity [148–151]. A complete picture of their correlation benefits from the exploration of nematic fluctuations in FeSC with different max T_c. Nematicity has been observed in many other FeSC, including Fe(Se,S) [24, 28], $Ca(Fe,Co)_2As_2$ [152], and LaFeAs(O,F) [153, 154], yet the small sizes of single crystals of SmFeAs(O,F) has so far precluded their study. One method of measuring nematic susceptibility is through elasticity studies which have revealed a strong electron-lattice coupling and a giant, anomalous softening of the shear component, c_{66}, anticipating the nematic transition in $(Ba,K)Fe_2As_2$ and $Ba(Fe,Co)_2As_2$ [1, 29] and in FeSe [28]. With FIB-fabrication of cantilevers, the elastic properties of microscopic crystals of SmFeAs(O,F) — in particular the existence and intensity of nematic fluctuations — can now be investigated.

The resonance frequency of an undoped SmFeAsO [110] cantilever reveals a giant softening of c_{66} from room temperature down to a structural and magnetic phase transition. This softening is a clear indication of electronic nematic fluctuations. In doped $SmFeAsO_{1-x}F_y$ cantilevers with $T_c \approx 49$ K, the softening of c_{66} is greatly diminished, following a trend that was observed in cobalt or potassium-doped $BaFe_2As_2$ [1, 27, 29]. Interestingly, despite the higher T_c, both the nematic susceptibility and the energy of the electron-lattice coupling are weaker

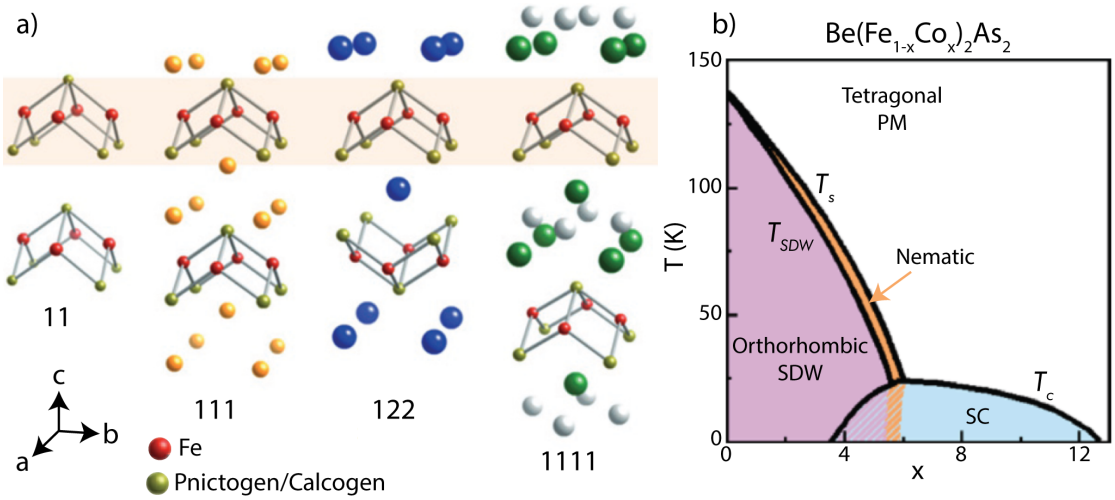

Figure 7.1: (a) Different structures of the iron-based superconductors, named after their elemental ratios. A common ingredient among all structures are the iron layers (highlighted in orange) consisting of Fe and a pnictogen or a chalcogen. Iron ions are shown in red with the pnictogen or chalcogen shown in gold. Other colors indicate the atoms separating the iron layers. Figure reproduced from [13]. (b) Phase diagram of $Ba(Fe_{1-x},Co_x)_2As_2$, showing superconductivity (SC), a magnetically-ordered Spin Density Wave (SDW) state, and electronic nematicity. Figure adapted from [155].

in SmFeAsO, possibly indicating a negative correlation between nematicity and T_c. Finally, the superconducting state of $SmFeAsO_{1-x}F_y$ is investigated in fields up to 10 T.

7.1 Background - the Iron-Based Superconductors

The FeSC are comprised of different 'families' all sharing a common layered structure with planes consisting of Fe and P or As (iron pnictides) or Fe and S, Se or Te (iron chalcogenides). Structures are often referred to by their elemental quantities, e.g. $BaFe_2As_2$ and SmFeAsO are members of the 122 and 1111 structures, respectively. The most common structures are shown in Fig 7.1 (a). The Fe layers can be stacked directly on top of each other or can be separated with other elements in between. Properties of the FeSC can be tuned by doping either the in-plane or out-of-plane components to donate holes or electrons to the Fe layers or with isovalent doping to apply chemical pressure [13, 156].

In some families, the undoped parent compound is superconducting (e.g. FeSe [28]) while in others, the parent has a magnetically-ordered state that is suppressed with doping, giving rise to a superconducting dome with a doping-dependent critical temperature, T_c. Fig 7.1 (b) shows the doping-dependent phase diagram of one such family, $Ba(Fe_{1-x}Co_x)_2As_2$. The exploration of these complex phase diagrams yields insight into the electronic correlations that give rise to superconductivity. The proximity (and, in some cases, coexistence) of the ordered magnetic state and superconductivity indicates that spin fluctuations are a likely

pairing mechanism for the coupling of electrons [13, 21, 156–160].

The magnetic state consists of iron atoms ordered antiferromagnetically along one chain of nearest neighbors and ferromagnetically arranged along the opposite direction [161–164]. This Spin Density Wave (SDW) transition occurs either below [165, 166], or concurrent with [167], a tetragonal-to-orthorhombic structural transition ($T_{SDW} \leq T_s$). In $BaFe_2As_2$, for example, $T_s = T_{SDW}$ in the parent compound and upon hole-doping but electron-doping leads to a splitting of the two phase transitions such that $T_{SDW} < T_s$ [148]. Notably, the lattice distortion at T_s is small, on the order of a few tenths of a percent, but is accompanied by a comparatively large resistivity anisotropy [22]. This property led to the assertion that the structural distortion is not driven by phonons — as is typical for a structural transition — but rather by electronic interactions, e.g. either spin or orbital ordering. To distinguish the state where the underlying crystal symmetry is broken fundamentally by the electrons, the term "nematic" was borrowed from the field of liquid crystals, in which the shape of the molecules break the rotational symmetry but not the translational symmetry. In the electronic nematic state, electronic interactions break the rotational symmetry of the lattice while preserving the translational symmetry, differentiating the *a* and *b* axes.

While superconductivity in the FeSC is likely mediated by spin fluctuations [168], the prevalence of nematicity alludes to the possibility of nematic fluctuations working in collaboration with other attractive interactions (i.e. spin fluctuations) to enhance T_c [150, 155, 169–173]. This is highlighted by the fact that the nematic transition temperature extrapolates to zero as the doping concentration is tuned to max T_c [155]. Nematic fluctuations around this region of the phase diagram are evidence of a nematic quantum critical point, a second-order phase transition that occurs at zero temperature and can facilitate superconductivity [27, 174, 175]. On the other hand, below T_c, superconductivity has been observed to suppress nematicity, indicating a competitive relationship [26, 176, 177]. These features, combined with the fundamental question of the driving mechanism of nematicity, have motivated extensive studies of nematic behavior, particularly in FeSe and $BaFe_2As_2$.

In the nematic state, the sample can become "twinned", e.g. multiple domains form with orientations along different axes. This can complicate measurements of nematicity. For example, domain averaging prevents the measurement of resistivity anisotropy in a sample with many domains. Coupling between the lattice and nematicity allow for this issue to be solved with the application of uniaxial stress [22] or strain to detwin the sample. With the application of strain, the nematic suscepitiblity above T_s has been explored via resistivity anisotropy in $Ba(Fe_{1-x},Co_x)_2As_2$ [23], $FeSe_{1-x}S_x$ [24], and $LaFe_{1-x}Co_xAs$ [154]. Furthermore, lattice coupling also makes it possible to probe electronic nematicity via elasticity.

7.1.1 Observations of Nematicity via Elastic Measurements

In the FeSC, electronic nematicity is coupled bilinearly to the lattice, with ϵ_6 the relevant strain component [28]. The relevant elastic constant is therefore the shear component, c_{66} (Hooke's

law Eqn 2.11). From Landau theory (2.3.2), the free energy can be written:

$$F = F_0 + \frac{1}{2}c_{66,0}\epsilon_6^2 - \lambda\epsilon_6\varphi + \frac{1}{2}(\chi_\varphi)^{-1}\varphi^2 + \frac{\beta}{4}\varphi^4 \tag{7.1}$$

c_{66}^0, is the elastic component in the absence of coupling, such that the second term is the bare elastic energy. The bilinear coupling is given by $-\lambda\epsilon_6\varphi$ with coupling constant, λ, and ordering parameter, φ. The last two terms are the Landau expansion with nematic susceptibility, χ_φ. Nematicity has been observed to follow a Curie-Weiss type behavior [27]. In this case, the nematic susceptibility can be written:

$$\chi_\varphi = \frac{1}{\alpha(T - T_0)} \tag{7.2}$$

With the help of Eqn 2.52, the shear component in the presence of coupling can be determined from Eqn 7.1:

$$c_{66} = c_{66}^0 - \frac{\lambda^2}{(\chi_\varphi)^{-1} + 3B\varphi^2} \tag{7.3}$$

As the temperature approaches T_0, c_{66} is expected to soften. Because the elastic components cannot be negative, the transition occurs at the modified temperature, T_s, when $c_{66} = 0$.

$$T_s = T_0 + \frac{\lambda^2}{\alpha c_{66}^0} \tag{7.4}$$

In the mean-field case, the temperature dependence of c_{66} can be written [27, 178]

$$c_{66} = c_{66}^0\left(\frac{T - T_s}{T - T_0}\right), \quad T > T_s \tag{7.5}$$

$$c_{66} = c_{66}^0\left(\frac{2(T_s - T)}{3T_s - T_0 - 2T}\right), \quad T < T_s \tag{7.6}$$

Re-writing in terms of the Curie constant, $\lambda^2/\alpha c_{66}^0 = T_s - T_0$:

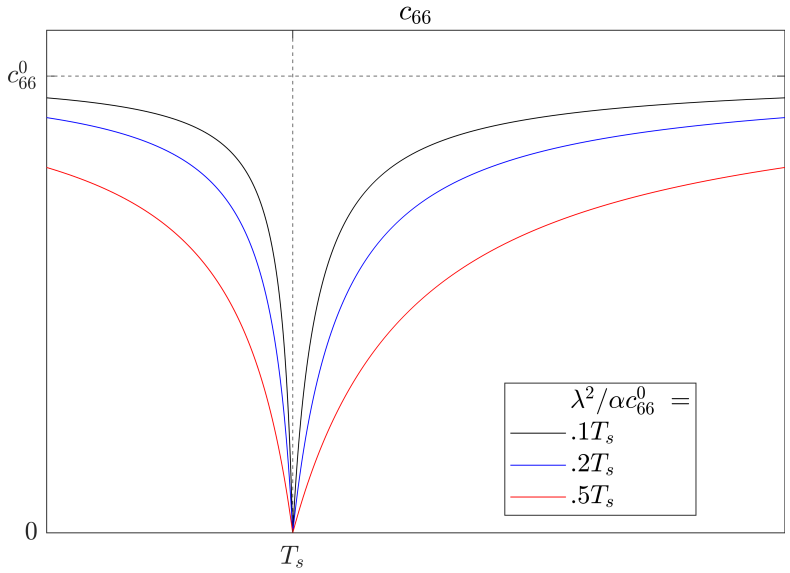

Figure 7.2: Expected temperature dependence of c_{66} for bilinear coupling, calculated from Eqns 7.8 and 7.7. The Curie constant, $\lambda^2/\alpha c_{66}^0 = T_s - T_0$, sets the steepness of the curve.

$$c_{66} = c_{66}^0\left(\frac{T - T_s}{T - T_s + \lambda^2/\alpha c_{66}^0}\right), \quad T > T_s \tag{7.7}$$

$$c_{66} = c_{66}^0\left(\frac{2(T_s - T)}{2T_s - 2T + \lambda^2/\alpha c_{66}^0}\right), \quad T < T_s \tag{7.8}$$

Temperature dependence of c_{66} for different values of $\lambda^2/\alpha c_{66}^0$ are plotted in Fig 7.2. Above the transition, $\varphi = 0$, and the nematic susceptibility can be solved for:

$$\frac{\lambda^2}{c_{66}^0}\chi_\varphi = 1 - \frac{c_{66}}{c_{66}^0} \tag{7.9}$$

Eqn 7.9 shows that the nematic susceptibility can be probed directly from measurements of c_{66}. Indeed, in PE studies on $Ba(Fe_{1-x}Co_x)_2As_2$, c_{66} shows a large anomalous softening in the parent compound that is reduced with increasing electron doping [29, 179]. PE allows for the elastic components to be measured individually. Alternatively, c_{66} can be explored by measuring Young's modulus along the appropriate direction. Young's moduli along [100] and [110] are:

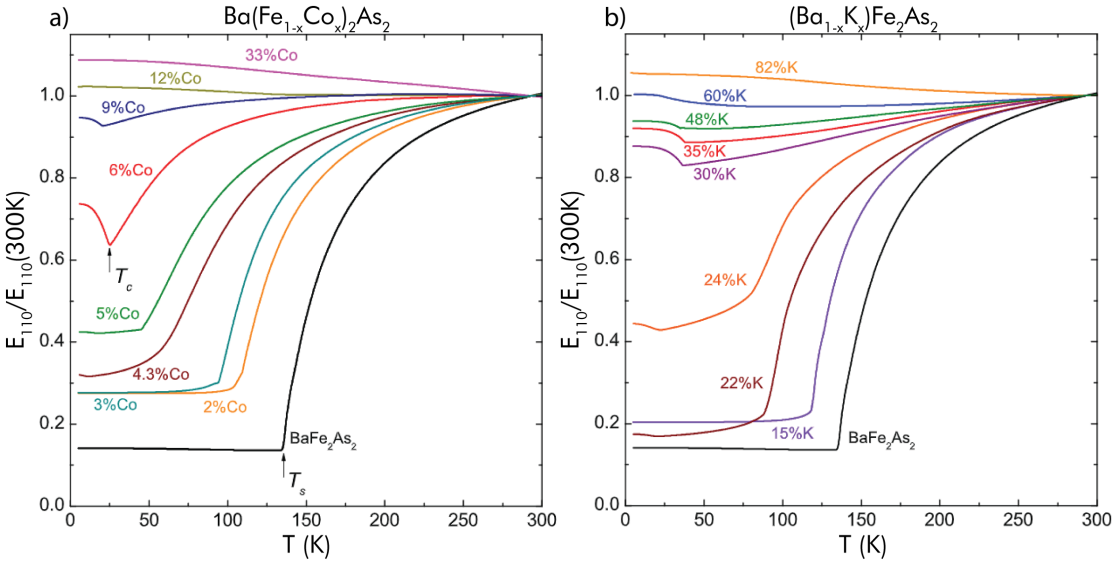

Figure 7.3: Normalized E_{110} for different doping concentrations of $Ba(Fe,Co)_2As_2$ (a) and $(Ba,K)Fe_2As_2$ (b) as measured by three-point bending in [1]. When c_{66} is small, E_{110} is dominated by c_{66}. Anticipating the nematic transition, T_s, c_{66} shows a large anomalous softening that is reduced with increasing hole or electron doping. Figure reproduced from [27].

$$\frac{1}{E_{\mathbf{100}}} = \frac{c_{13}^2 - c_{11}c_{33}}{(c_{11}-c_{12})(2c_{13}^2 - c_{11}c_{33} - c_{12}c_{33})} \tag{2.28}$$

$$\frac{1}{E_{\mathbf{110}}} = \frac{1}{4}\left[\frac{1}{c_{66}} + \frac{1}{c_{11}/2 + c_{12}/2 - c_{13}^2/c_{33}}\right] \tag{2.29}$$

While E_{100} is independent of c_{66}, if $c_{66} << c_{11}/2 + c_{12}/2 - c_{13}^2/c_{33}$, then c_{66} will dominate E_{110}. Because c_{66} should approach 0 as $T \to T_s$, near the phase transition, one can approximate

$$\frac{c_{66}}{c_{66}^0} \approx \frac{E_{110}}{E_{110}^0} \tag{7.10}$$

and the nematic susceptibility can be calculated directly from the Young's modulus

$$\frac{\lambda^2}{c_{66}^0}\chi_\varphi \approx 1 - \frac{E_{110}}{E_{110}^0} \tag{7.11}$$

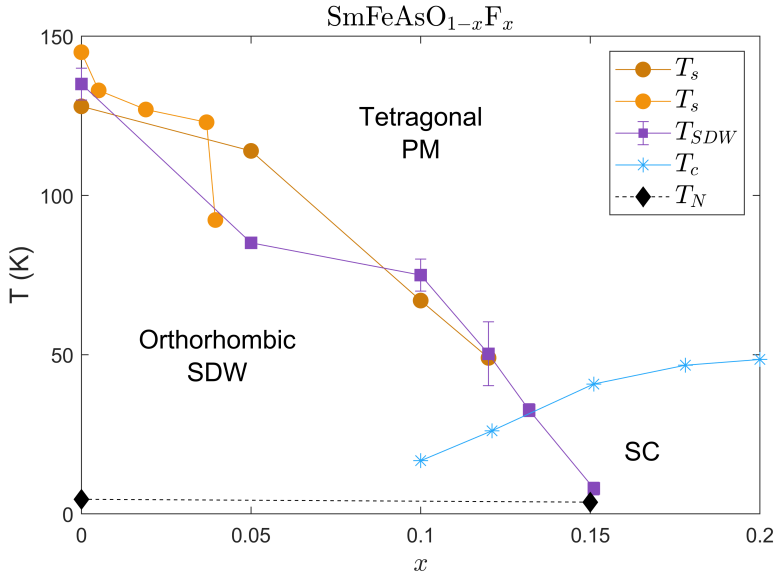

Figure 7.4: Phase diagram of $SmFeAsO_{1-x}F_x$. Dark and light orange circles mark the structural phase transition, T_s, as measured by XRD in [136] and [138], respectively. Purple squares indicate the spin-density wave, T_{SDW}, measured by μSR in [140]. Blue asterisks showing the superconducting transition temperature are from magnetization measurements in [181] and black diamonds show the antiferromagnetic ordering of the Sm^{3+} ions, T_N, as indicated by anomalies in the specific heat measured in [182].

This approach is used by Böhmer et. al. to study the nematic susceptibility in $Ba(Fe_{1-x}Co_x)_2As_2$ and $(Ba_{1-x}K_x)Fe_2As_2$ [1] and in FeSe [180] using a method called three-point bending in which the deformation of samples are measured with a capacitance dilatometer. Samples for these experiments were cut to have dimensions $length \times width \times thickness \approx 3 \times 1 \times 0.1$ mm^3. E_{110} of $Ba(Fe_{1-x}Co_x)_2As_2$ matches well with c_{66} measured by PE, demonstrating that the approximation of Eqn 7.10 is valid [27, 29]. In Fig 7.3, E_{110} for electron and hole-doped $BaFe_2As_2$ are plotted. The parent compound shows large softening by more than 80% from room temperature to the structural phase transition. This softening is reduced with increasing doping. Electronic nematic fluctuations are apparent with both hole and electron doping. At 33% Co doping, well beyond the superconducting dome, E_{110} follows the expected data from phonon anharmonicity, with no apparent nematic effect. c_{66} does not reach 0 at the structural phase transition in $BaFe_2As_2$ and the reasons for this are unclear.

PE was not able to measure below T_s due to the dissipation that occurs at domain walls [29]. In the three-point bending measurements, E_{110} is nearly temperature independent when $T < T_s$ but the authors note that this is most likely due to the multiple-domain formation and not a measure of a single-domain [27].

Sample	E_{110} (GPa)	σ_E (GPa)	σ_E/E_{110} (%)
A (doped)	116.9	10.4	9
B (doped)	117.9	9	8
C (parent)	101.2	11.6	11

Table 7.1: E_{110} of SmFeAs(O,F) cantilevers as measured at T = 300 K. E_{100} for the parent compound is given in Table 6.3.

7.2 Elasticity of SmFeAs(O,F)

Under F-doping, SmFeAsO has one of the highest superconducting transition temperatures of the FeSCs, with a max reported $T_c \sim 55$ K [146]. Its phase diagram, shown in Fig 7.4, resembles that of $BaFe_2As_2$, with an orthorhombic and SDW state that is suppressed with increasing doping, giving rise to the superconducting dome. Whether or not $T_s = T_{SDW}$ remains an open question. SmFeAsO undergoes a second magnetic transition with the antiferromagnetic ordering of the Sm^{3+} ions at $T_N \sim 5$ K [182]. During the course of this thesis, the elastic properties of the parent compound SmFeAsO and doped $SmFeAsO_{1-x}F_y$ were explored via FIB-fabricated micro-cantilevers.

7.2.1 Method

Single crystals of SmFeAs(O,F) (doped and parent) were grown by Zhigadlo et. al. using the methodology described in [14]. This process requires a NaCl/KCl flux with a pressure of 30 kbar and a maximum temperature of 1350-1450 °C. Because the crystals have a low solubility in NaCL/KCl flux, single crystals are small — on the order of $50-100$ μm for the parent and doped compounds. Dissociation of oxygen during growth can result in a fluorine-to-oxygen substitution that is not one-to-one such that the true chemical formula of the doped compound is $SmFeAsO_{1-x}F_y$, with x not necessarily equal to y. The transition temperature of the doped compounds measured and grown in [14] was found to vary with $T_c \sim 45-53$ K owing to variations in doping. Both fluorine substitution and oxygen removal effectively electron-dope the system.

Cantilevers were fabricated using the FIB-fabrication process outlined in Ch 4 with thicknesses 1-1.5 μm, width 7-10 μm, and length 31-60 μm. To probe E_{100} and E_{110} of the parent compounds, cantilevers were cut in the ab plane with longest axis along [100] and [110], respectively. In the doped compound, E_{110} is measured with [110] cantilevers. Measurements were conducted on the Micro-resonator probe described in Ch 5 inside the VTI of a 16 T magnet for temperature and magnetic-field control with pressure pumped to ~ 1 mbar. A 15 dB attenuator was used to reduce the power of the laser and prevent sample heating (5.3.1). At each temperature or field, the mechanical excitation frequency was swept across the fundamental resonance mode and Eqn 5.4 fit to the response to compute the resonance frequency, f_0, and Q-factor. Young's modulus was calculated with Eqn 2.41 from f_0, the geometry of cantilever, and the density, $\rho = 7.45$ Mg·m^{-3} [183]. E_{110} for the parent and doped cantilevers

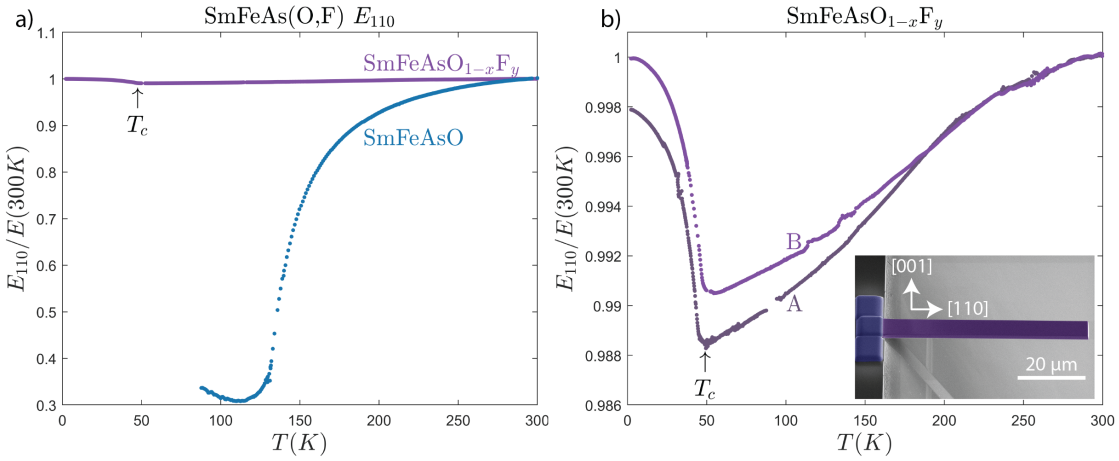

Figure 7.5: Normalized Young's modulus of [110] cantilevers for doped+parent (a) and only doped (b) samples. Inset of (b) is an SEM image of a SmFeAsO$_{1-x}$F$_y$ cantilever. E_{110} of the parent compound softens by nearly 70%. Upon Fluorine doping, this softening is reduced to ~ 1%. The doped cantilevers have $T_c \approx 49$ K. Cantilevers A and B show good agreement with each other, although differences in slope may be due to small angular misalignment.

are summarized in Table 7.1 and E_{100} of the parent are shown in Table 6.3.

The addition of the attenuator reduces the quality of the signal and results in long-period noise that would require a very long time constant to average out. In the [110] cantilevers, this source of noise was removed in post-processing by exciting the cantilever with a constant frequency, outside of the range of the sweeping frequency. The amplitude of the cantilever at both frequencies is measured concurrently, and the amplitude at the swept frequency is normalized by the amplitude at the constant frequency (See 5.4.2). The [100] cantilevers were measured prior to the use of the constant drive frequency, such that the long-period noise is not removed. This results in additional noise in f_0, E_{100} and Q-factor vs T.

7.2.2 Electronic Nematicity

Young's modulus for the [110] cantilevers are presented in Fig 7.5. The parent compound shows large softening by nearly 70% from room temperature down to the structural phase transition. In the doped cantilevers, this softening is reduced to ~ 1% (Fig 7.5 (b)) down to the superconducting transition ($T_c \approx 49$ K). Against the expectation shown in Fig 7.2, Young's modulus does not go to zero at T_s. This was also observed in $BaFe_2As_2$ and FeSe [27]. With the approximations $E_{110} \approx c_{66}$ and $E^0_{110} \approx c^0_{66}$, Eqn 7.7 can be fit to the parent compound to extract $e^0_{110} = 108$ GPa, $T_s = 125.9$ K and $\lambda^2/\alpha c^0_{66} = T_s - T_0 = 11.6$ K, where e^0_{110} is a temperature-independent Young's modulus (in the absence of both nematicity and phonon stiffening).

With Eqn 7.11, the nematic susceptibility can be calculated from E_{110} and E^0_{110}. As it is not possible to measure Young's modulus in the absence of nematic effects (E^0_{110}), Böhmer et. al. assume that the temperature dependence of E^0_{110} is independent of doping. At 33% Co-

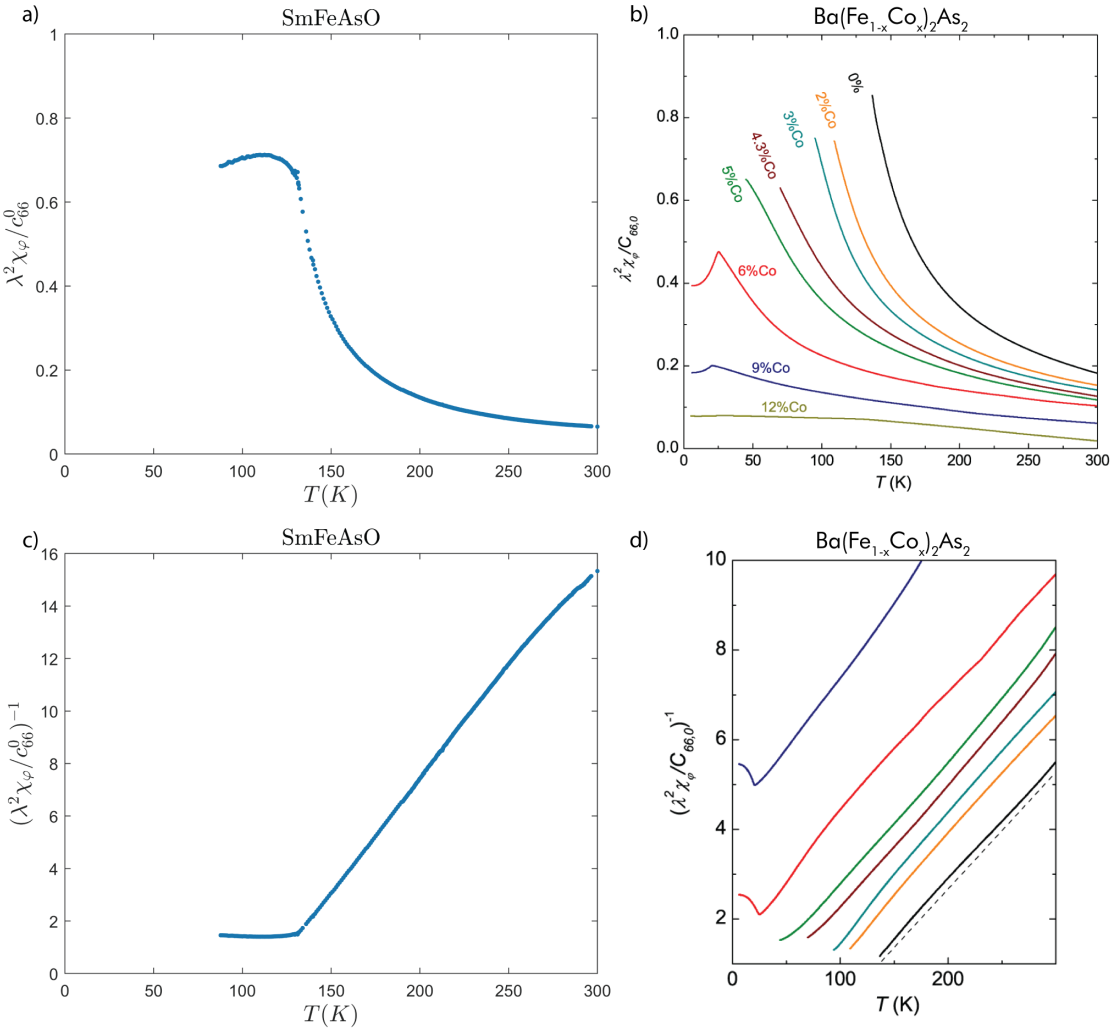

Figure 7.6: Nematic susceptibility, χ_φ, in units of λ^2/c_{66}^0 (a,b) and inverse nematic susceptibility (c,d) of SmFeAsO (a,c - this work) and $Ba(Fe_{1-x}Co_x)_2As_2$ (b,d - Figures reproduced from [27]). The inverse susceptibility, $(\lambda^2\chi_\varphi/c_{66}^0)^{-1}$ follows a Curie-Weiss-like temperature dependence.

doping, $Ba(Fe_{1-x}Co_x)_2As_2$ is overdoped and follows the stiffening expected from phonon anharmonicity with no indication of nematicity. The authors therefore used the temperature dependence at this doping concentration to approximate E^0_{110} [1, 143]. Overdoped samples of SmFeAs(O,F) do not exist; however, χ_φ can be estimated for the parent compound by approximating E^0_{110} to be independent of temperature:

$$E^0_{110}(T) \approx e^0_{110} \tag{7.12}$$

The nematic susceptibility, in units of λ^2/c^0_{66} of SmFeAsO is then calculated with Eqn 7.11 and plotted in Fig 7.6 (a). For comparison, χ_φ of $Ba(Fe_{1-x}Co_x)_2As_2$ from [1, 27] is shown in Fig 7.6 (b). The linearity of the inverse, $(\chi_\varphi)^{-1}$, is reminiscent of the inverse of the magnetic susceptibility of the Curie-Weiss law (Fig 7.6 (d)).

These results demonstrate the presence of nematicity in SmFeAs(O,F). The susceptibility of the parent compound is, however, notably smaller than in $BaFe_2As_2$. Furthermore, the Curie constant, $\lambda^2/\alpha c^0_{66} = T_s - T_0$, is the characteristic energy of the electron-lattice coupling. In Co and K-doped $BaFe_2As_2$, $\lambda^2/\alpha c^0_{66} \approx 30-40$ K [1] while in SmFeAsO, $\lambda^2/\alpha c^0_{66} \approx 11.6$ K. This result is significant because, while the max T_c of SmFeAs(O,F) is higher ($T_c \approx 55$ K) than in $(Ba_{1-x}K_x)Fe_2As_2$ ($T_c \approx 38$ K) and the structural transitions of the parent compounds occur at comparable temperatures, nematicity is notably weaker in SmFeAs(O,F). This indicates that nematicity competes with superconductivity, against predictions that nematic fluctuations work to enhance T_c [150, 169–171].

7.2.3 Domain Formation and the Structural Transition

At high temperature, the behavior of E_{110} of the parent fits very well with the prediction shown in Fig 7.2. Near T_s, E_{110} slowly curves upward rather than continuing to decrease. This is likely due to the formation of nematic domains. In E_{100} which shows no softening from nematicity, the structural transition is a sharp dip after which E_{100} continues to stiffen (Fig 7.7 (a)). Additionally, at high temperatures, all [110] cantilevers have a comparable Q-factor that increases slightly with decreasing temperature. Around $T \approx 170$ K, the Q-factor of the parent compound begins to slowly decay. Below $T \approx 90$ K, the cantilever becomes too dissipative for resonance measurements. In contrast, the Q-factor of the doped cantilevers continue to increase until $T \approx 10-30$ K (7.7 (b)). It is interesting that the decay in Q of the parent compound begins far above the structural transition and thus before the expected formation of the domains.

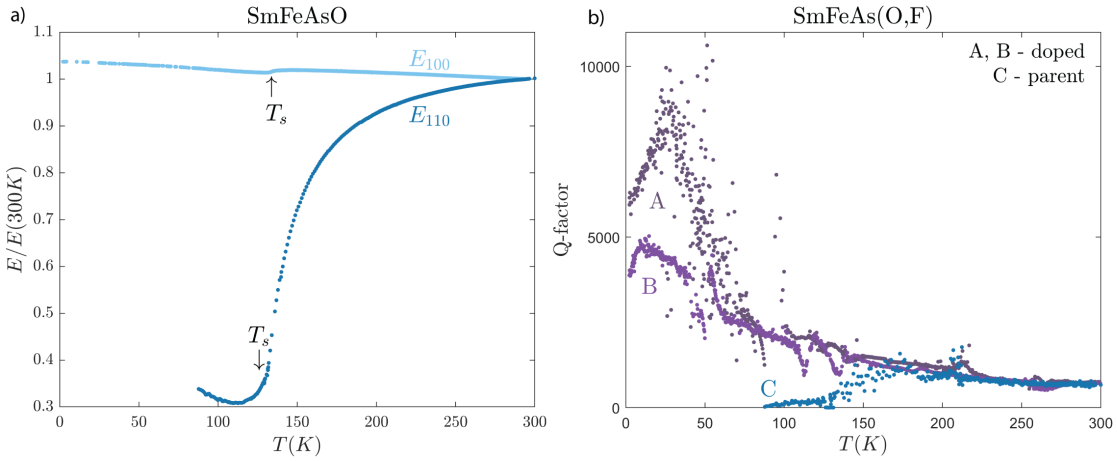

Figure 7.7: (a) E_{100} and E_{110} in SmFeAsO. Arrows mark T_s from the minimum of E_{100} (T_s = 130 K) and from fitting Eqn 7.7 to E_{110} (T_s = 125.9 K). (b) Q-factor for doped and parent [110] cantilevers. The Q-factor for the parent cantilever decays to zero while the Q-factor for the doped cantilevers increases.

7.2.4 Magnetic Field Measurements

Measurements on a doped cantilever were done with the field parallel to [001] (normal to the plane of the cantilever, Fig 7.8 (c)). E_{110} and the Q-factor versus temperature at different fields are shown in 7.8 (a) and (b), respectively. As expected for a superconducting transition, increasing the field decreases T_c. Interestingly, when B = 5 T or 10 T at $T \approx 37$ K or 31 K the Q-factor quickly decays to zero and the resonance could not be measured below this point. One possible explanation for this phenomenon is dissipation from the vortex-lattice. In a type-II superconductor, when fields are applied above H_{c1}, the magnetic field can penetrate through the sample in normal-state vortices. With sufficiently low magnetic fields, these vortices are pinned in place forming a glass-type lattice. Increasing the field will increase the number of vortices, eventually reaching a saturation point where the vortices become depinned and can move like a liquid. The vortex phase diagram showing the vortex-glass melting line and upper critical field, H_{c2}, on $SmFeAsO_{.8}F_{.2}$ from [184] is shown in Fig 7.8 (c). The decay of the Q-factor is likely due to the vortex-glass to vortex-liquid melting point. In the vortex-liquid state, strain gradients of the vibrating cantilever can move the depinned vortices freely. Below the melting point, these strain gradients can push the vortices from one pinning site to another in an energy-dissipative process, resulting in a rapid decay of the Q-factor. AC-susceptibility measurements on $SmFeAsO_{.8}F_{.2}$ ($T_c \approx 52$ K) revealed a vortex-lattice melting point of $T_m \approx 35$ K at 5 T [184]. This value is comparable to the temperature of the Q-factor decay ($T \approx 37$ K) at 5 T in the doped cantilevers, supporting this hypothesis.

Interestingly, RUS measurements on $Ba(Fe_{.957}Co_{.043})_2As_2$ note a spike in dissipation (Q^{-1}) at the vortex-glass melting point. Below T_m, the resonance frequency increases by ~ 28% in a 10 T field [185]. No resonance was detected below T_m in $SmFeAsO_{1-x}F_y$; however, it is possible that the frequency increased beyond the measured range. More measurements are necessary

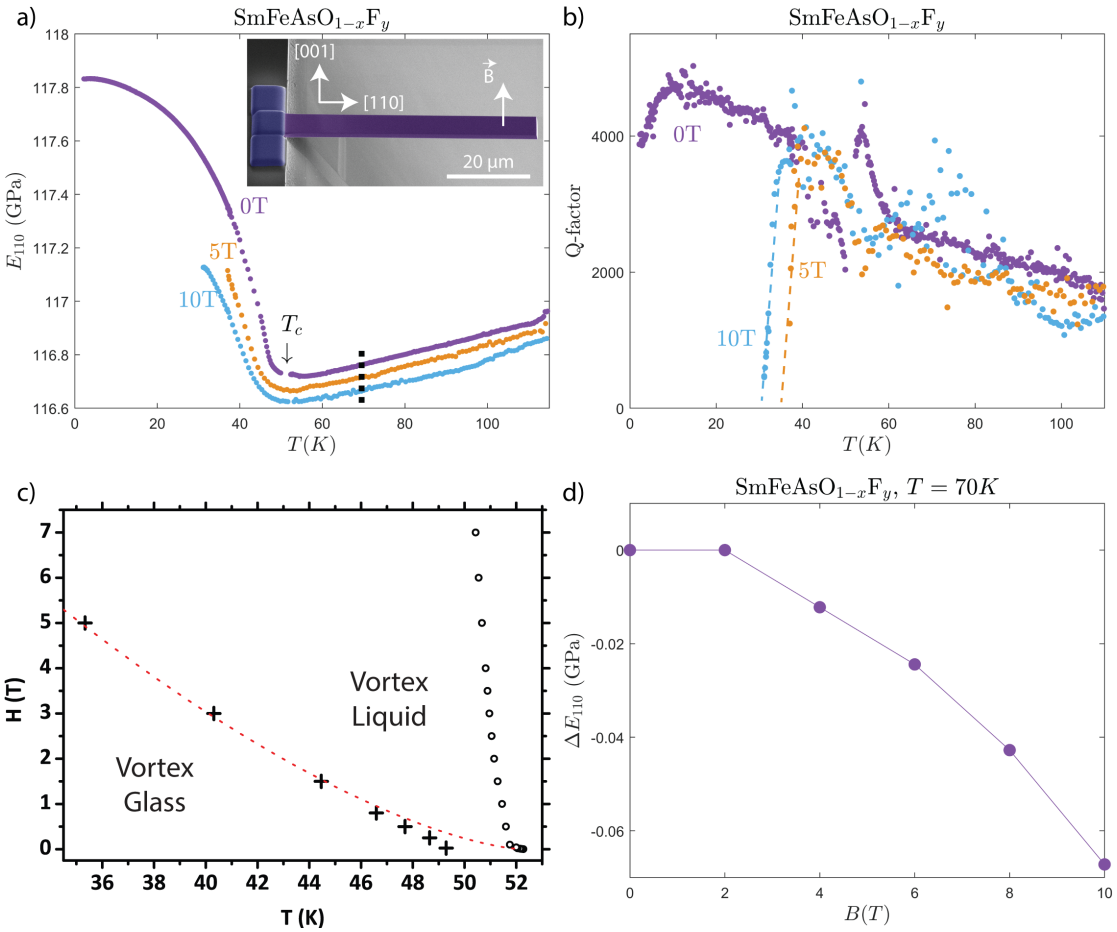

Figure 7.8: Magnetic field studies of a $SmFeAsO_{1-x}F_y$. (a) E_{110} vs. T at different field strengths — these curves are not offset. Inset SEM image shows the cantilever with field applied perpendicular to the sample. (b) Q-factor of the measurements in (a). The anomaly at 40-60 K in the 0 T curve is a result of background peak in the spectrum and is not reproducible. At 5 T and 10 T, the Q-factor rapidly drops to zero, below which no resonance was measured, dotted lines have been added as a guide to the eye. The decrease in the Q-factor in magnetic field below T_c may be due to dissipation from normal state vortices. At 0 T, the Q-factor begins to decrease around 10 K. (c) Vortex phase diagram as measured by AC-susceptibility measurements on $SmFeAsO_{.8}F_{.2}$. Plus symbols mark the Vortex-glass melting point while the circles mark the upper critical field, H_{c2}. Figure adapted from [184]. (d) Field sweep at constant $T > T_c$. The temperature of the field scan is marked by the black dotted line in (a). $\Delta E_{110} = E_{110}(B) - E_{110}(0)$ decreases parabolically with increasing field.

to see whether or not the resonance returns at lower temperatures.

Furthermore, a second feature is notable in Fig 7.8 (a): even above T_c, the application of a magnetic field shifts E_{110} downwards significantly. Measurements of E_{110} vs field at constant temperature $T > T_c$ show a parabolic softening with increasing field (Fig 7.8 (d)). It is unclear how the field-dependence will evolve at increasing temperatures. In the field-dependent RUS study of $Ba(Fe_{.957}Co_{.043})_2As_2$ in [185], no significant shift in the frequency above T_c is reported. An understanding of this phenomenon therefore calls for further exploration.

8 Cuprates

Since the 1911 discovery of superconductivity in mercury by Kammerlingh Onnes, the field has experienced its fair share of notable achievements. Arguably one of the most pivotal was the observation of superconductivity in a copper oxide (cuprate). In 1986, La-Ba-Cu-O was reported to have a critical temperature of $T_c \approx 30$ K [186], a significant improvement over the $T_c = 23$ K record held by Nb_3Ge [187]. Later studies have pushed T_c as high as 135 K and the cuprates still hold the record of the highest T_c at atmospheric pressure to this day [188]. In each family, the parent compound is an antiferromagnet (AFM) and an insulator driven by spin-interactions. Electron or hole doping suppresses the AFM state, eventually giving rise to unconventional superconductivity. Understanding these strange superconductors requires examining the correlated electron states that surround superconductivity.

In fact, the phase diagrams of the cuprates are richly complex (see Fig 8.1). In addition to AFM, both spin (SDW) and charge density waves (CDW) have been observed in close proximity to or overlapping with superconductivity [189–194]. Furthermore, a partial gap akin to the energy gap present in superconductors begins to open at temperatures, T^*, above T_c. This region is referred to as the pseudogap and it remains controversial whether or not T^* is the transition temperature of a distinct thermodynamic phase [187, 195, 196]. The pseudogap can be detected via many different experimental methods such as NMR, STM or ARPES [197–202]. However, a distinct phase transition has not been reported in thermodynamic probes such as specific heat [203], with the exception of one RUS study that showed a change in slope of resonance frequency vs T at T^* in $YBa_2Cu_3O_{6+x}$ (YBCO) [47]. This result has yet to be seen in other cuprate families and its interpretation has been disputed [204]. Thus ultrasound studies are vital to delineate the cuprate phase diagram.

Cantilevers were fabricated from two cuprate families: $Tl_2Ba_2CuO_{6+x}$ (Tl2201) and $La_{2-x}Sr_xCuO_4$ (LSCO). Tl2201 samples deformed at some point during measurement — the cause of this is not fully understood. A [100] cantilever of LSCO did not show the same effect and the resonance modes could be studied. LSCO has a high-temperature tetragonal-to-orthorhombic phase transition that is clearly seen by a 17% decrease of Young's modulus. A second phase transition that corresponds to superconductivity shows only a .09% change in Young's modulus. No clear

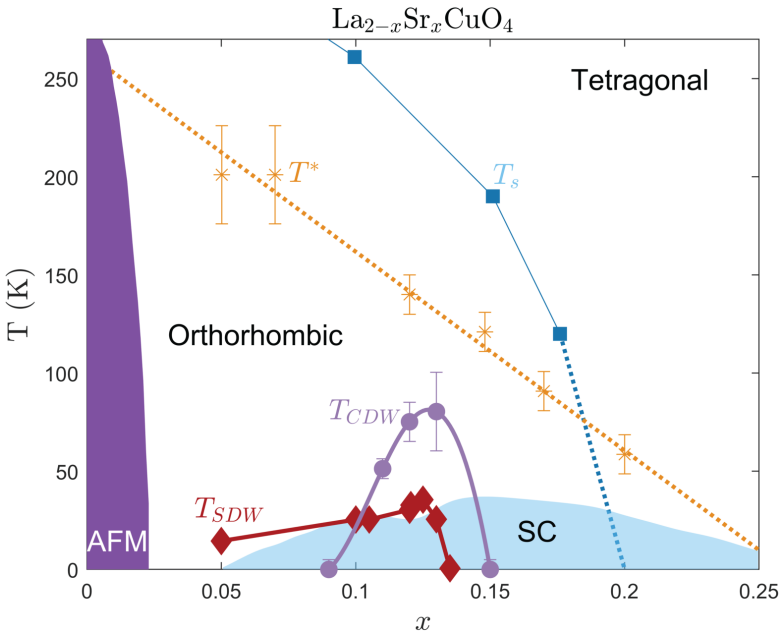

Figure 8.1: LSCO phase diagram. Tetragonal to orthorhombic structural phase transition (T_s) from XRD in [205]. CDW as measured in [206] and SDW from [207–212]. The pseudogap, T^* is determined by Nernst measurements in [213]. AFM and superconductivity based on [206].

evidence of the SDW, CDW or a phase transition at T^* were observed.

8.1 Structure and Methods

The cuprates have a layered perovskite crystal structure (Fig 8.2) characterized by their copper-oxide planes. Crystals are either tetragonal or orthorhombic in symmetry. Doping is often done by annealing to remove O^{-2} or by substitution of interstitial ions, donating charge carriers to the planes. Superconductivity can be induced by both hole and electron doping [214, 215]. Both the Tl2201 and LSCO samples examined here are hole-doped.

Cantilevers were fabricated using the process given in Ch 4. The cuprates have a high oxygen mobility. This can be a problem for structuring samples as heating from the ion beam in the vacuum chamber of the FIB can anneal the sample, removing oxygen and thus changing the sample doping. Doping concentration of LSCO is therefore estimated based on the temperature of the measured phase transitions. Samples were cut from the *ab* plane with the length of the cantilever parallel to [100]. With Eqn 2.41, E_{100} can then be determined from measurements of the fundamental resonance frequency using $\rho = 6.34\ \mathrm{Mg \cdot m^{-3}}$ [217]. Cantilever dimensions were $1 - 1.3\ \mu\mathrm{m} \times 10\ \mu\mathrm{m} \times 74 - 96\ \mu\mathrm{m}$. Measurements were conducted on the micro-resonator probe inside the VTI of a 16 T magnet with the pressure pumped to ~ 1 mbar. Laser power was reduced with a 15 dB attenuator at all times to prevent sample heating. The full experimental method is described in Ch 5.

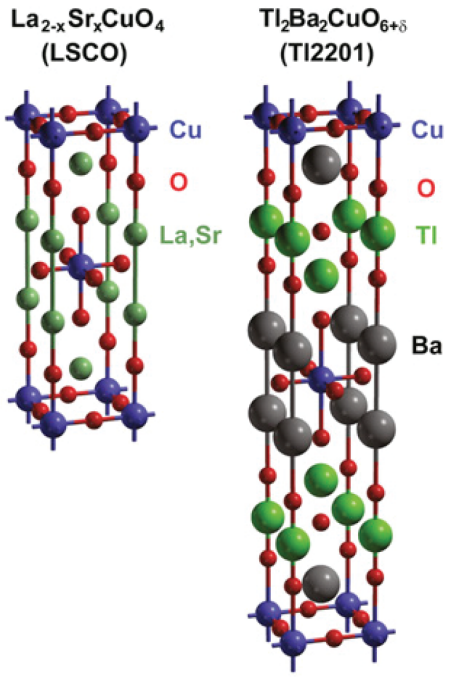

Figure 8.2: Layered Perovskite crystal structures of LSCO and TL2201. Figure reproduced from [216]

8.2 What happened to Tl2201?

Immediately post-fabrication, cantilevers of Tl2201 appeared pristine. After exposure to air, small spots appeared on the surface, near the base, possibly a reaction between Tl2201, air and the FIB deposition. After measurement, both cantilevers were deformed, showing large "splatter-like" marks near the base and an inhomogenous surface (Fig 8.3). Both cantilevers had a relatively poor Q-factor of ~ 100 (in comparison to the $Q \sim 1000$ of other FIBed cantilevers) and the resonance frequency versus temperature showed no signs of any transitions. There was no sudden or gradual change in frequency at constant temperature that would signal a change in the sample. This suggests that the transformation occurred at the beginning of measurements, either during imaging or during initial frequency sweeps to find the resonance.

While a large thermal gradient across the sample generated by laser heating cannot be excluded as a possible cause, a 15 dB attenuator was used throughout imaging and measurement to reduce the laser power to < .32 mW. This attenuator was shown to prevent heating in SmFeAsO cantilevers of a similar size (5.3.1). Furthermore, it does not appear that the free-end melted while the base is preserved as is expected for a large thermal gradient and seen in the melted SmFeAsO Fig 5.9. One possibility is that the oxygen removed from FIBing created an insulating crust through which the FIB deposit is not able to provide a good thermal contact to the bulk. This could result in the full cantilever becoming thermally isolated such that even the reduced laser power results in significant heating. One possible avenue to prevent this is to anneal the

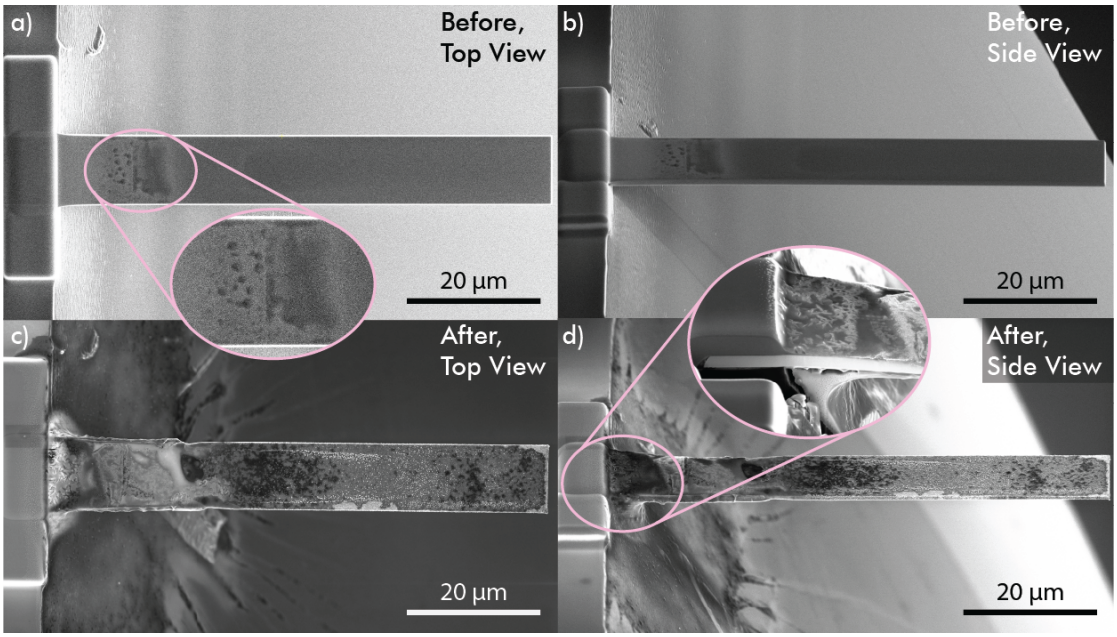

Figure 8.3: SEM images of a Tl2201 cantilever before (a,b) and after (c,d) measurement. Images before measurement show dark spots near the base of the cantilever that only appeared after fabrication and exposure to air (inset of (a)). After measurement, the cantilever appears completely destroyed with a large "splatter" near the base. These results were seen in both measured samples. Inset of (d) was taken after cutting cross sections to reveal the inside of the sample. A lighter, homogeneous region is surrounded by a darker crust.

sample in an oxygen-rich environment to restore oxygen in the outer layer immediately after fabrication (or after welding the cantilever to the chip with redeposition but before depositing the FIBID base). The reaction of TL2201 cantilevers demonstrates that there is still much to learn about ion interactions with complex materials.

8.3 LSCO

LSCO cantilevers showed no strange reactions and were not damaged during measurements. Young's modulus along [100], E_{100}, for LSCO is summarized in Table 8.1. The full temperature dependence is plotted in Fig 8.4. A large high-temperature jump corresponds to the tetragonal-to-orthorhombic phase transition. From the transition temperature, $T_s \approx 216$ K, the effective doping concentration of this cantilever after FIBing can be approximated to be $x \approx .13$.

For $T > T_s$, E corresponds to E_{100}. Below T_s, Young's modulus is reported as E due to the possible formation of domains and the unknown orientation of the cantilever in the orthorhombic state. Across the structural transition, Young's modulus changes significantly with $\Delta E \approx 14.1$ GPa. This can be compared to ultrasound studies in $La_{2-x}Sr_xCuO_4$ with $x = .09, .14, .19$ which report a large decrease in c_{66} and c_{11} at T_s [218]. From Eqn 2.28:

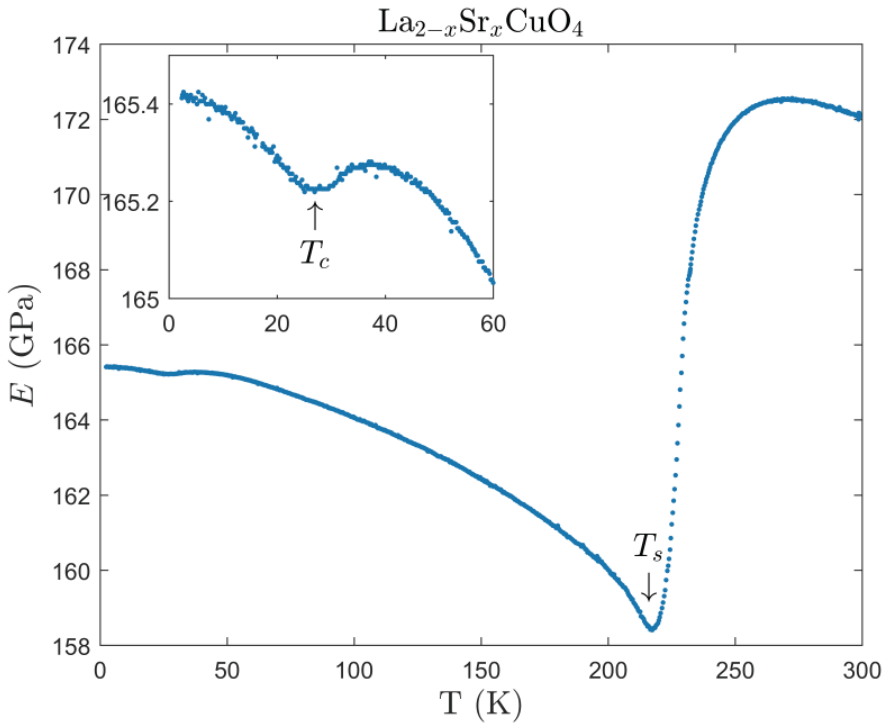

Figure 8.4: Temperature dependence of Young's modulus of a LSCO cantilever. The temperature of the phase transitions indicates that the effective doping is $x \approx .13$. The inset shows a smaller transition at low temperatures. Based on the suppression of this transition in magnetic field (Fig 8.5), this is the superconducting transition. Arrows indicate the structural transition, T_s, and T_c.

E_{110} **(GPa)**	σ_E **(GPa)**	σ_E/E_{110} **(%)**
172.1	31.9	19

Table 8.1: E_{100} of a $La_{2-x}Sr_xCuO_4$ cantilever measured at room temperature. Based on the temperatures of the structural and superconducting phase transitions, $x \approx .13$.

$$\frac{1}{E_{\mathbf{100}}} = s_{11} = \frac{c_{13}^2 - c_{11}c_{33}}{(c_{11}-c_{12})(2c_{13}^2 - c_{11}c_{33} - c_{12}c_{33})} \tag{2.28}$$

E_{100} is independent of c_{66}. The softening of E is therefore likely an indication of a jump in c_{11}. For $x = .14$, $\Delta c_{11} \approx 9\%$ across T_s [218], comparable to the $\Delta E \approx 8\%$ measured for this $x \approx .13$ cantilever.

At low temperatures, the superconducting transition is visible. Fig 8.5 shows the low temperature region at 0 T and 10 T with the magnetic field applied perpendicular to the cantilever (eg parallel to [001]). T_c is suppressed with field, demonstrating that this is the superconducting transition and not T_{CDW} or T_{SDW}. The shift in T_c at 10 T ($\Delta T = 10$ K) is comparable to the

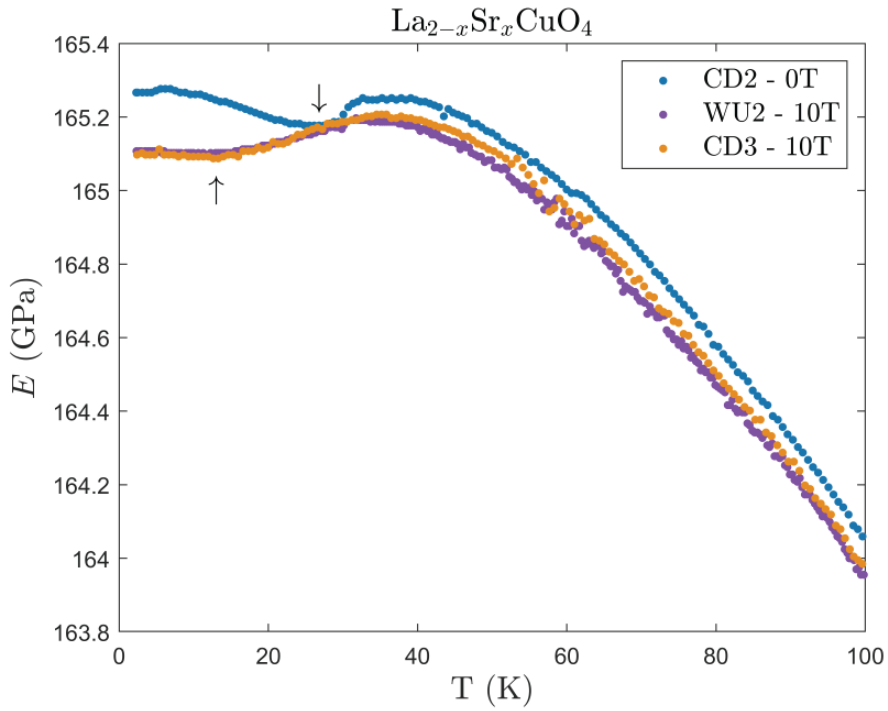

Figure 8.5: Cool down (CD) or warm up (WU) of E vs T at 0 T and 10 T. The applied magnetic field is perpendicular to the cantilever (parallel to [001]). Arrows indicate the local minima.

reported values of T_c at 0 T and 10 T for x = .15, .8 where ΔT = 7 K, 10 K, respectively [219, 220].

Furthermore, the jump in the elastic moduli at a second-order phase transition can be related to a corresponding jump in the specific heat using the Ehrenfest relations [45, 143]. The derivative in the transition temperature with respect to the uniaxial pressure, p_i ($i = a, b, c$), can be calculated from the discontinuity in Young's modulus, ΔE:

$$\frac{dT_c}{dp_i} = -\frac{\Delta E}{E^2 \Delta \alpha_i} \tag{8.1}$$

where $\Delta\alpha_i$ is the discontinuity at the phase transition in the thermal-expansion coefficient, α_i. The pressure dependence of T_c can also be computed from the jump in the specific heat, ΔC_p, using the Ehrenfest relation:

$$\frac{dT_c}{dp_i} = V_m \frac{\Delta \alpha_i}{\Delta C_p / T_c} \tag{8.2}$$

with the molar volume, V_m. For a sample with doping concentration $x = .1$, the specific heat

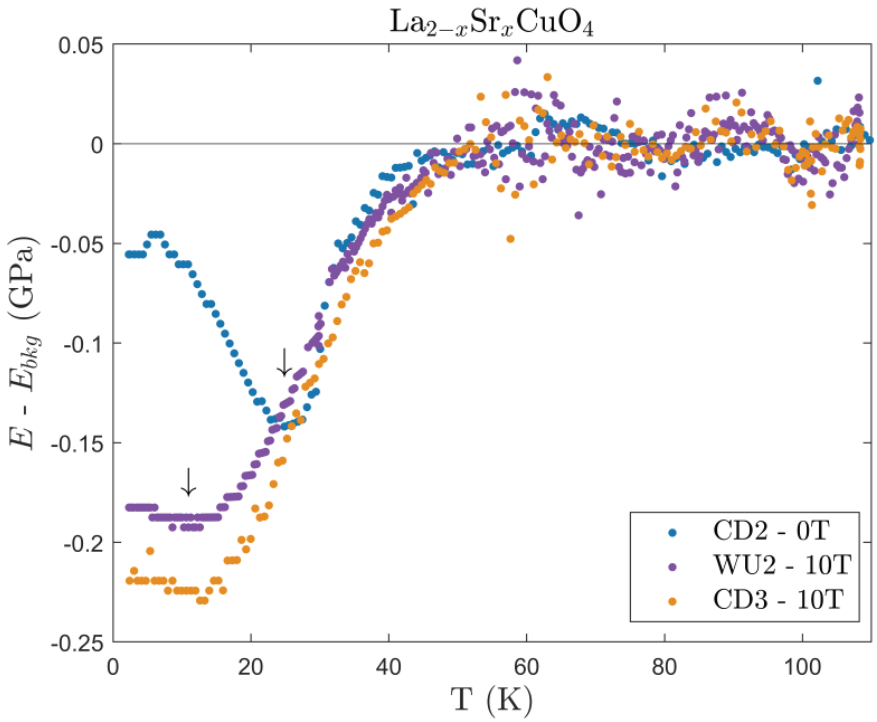

Figure 8.6: Young's modulus with the background subtracted. Arrows mark the minimum indicating T_c.

discontinuity was reported to be $\Delta C_p/T_c = 2.5$ mJ/mol K^2 [221] with $\Delta\alpha_a = 3.1\times10^{-7}$ K^{-1} [222]. From Eqn 8.2, $dT_c/dp_a = 7$ K/GPa. The jump, ΔE, can be examined by subtracting the background from E. In Fig 8.5, Varshni's equation (Eqn 2.48) was fit to E from 50-100 K and subtracted. Using $\Delta E = 0.14$ GPa and $E = 165.3$ GPa in Eqn 8.1, $dT_c/dp_a = 16.5$ K/GPa. The discrepancy in the pressure dependence of T_c may be a result of the different doping concentrations as well as a different jump in the thermal expansion in the multi-domain cantilever.

Additionally, the superconducting transition is much broader than has been previously reported for LSCO [218, 223, 224]. This may be an indication of laser heating — perhaps the measurement should have been done with a stronger laser attenuator. Laser heating may be present in LSCO when it was not seen in SmFeAsO due to oxygen reduction in the amorphous FIBed layer resulting in a weaker thermal link between the cantilever and the FIBID and sample chip. Hence, the best practice for this technique is to test the sample for laser heating (as shown in Fig 5.10) at the beginning of measurements.

Finally, it should be noted that no other anomalies corresponding to T_{SDW}, T_{CDW} or T^* were observed during this work. More experiments on cantilevers with different doping concentrations and with different orientations would be beneficial to look for signatures at these temperatures.

9 The Rare-Earth Nickelates

Originally grown as polycrystals in 1971 by Demazeau [225], the perovskite nickelates ($RNiO_3$, R = Rare Earth) were largely ignored for nearly twenty years due to their challenging fabrication. Discovery of high-temperature superconductivity in the cuprates — which also belong to the perovskite structure — combined with improvements in nickelate synthesis, eventually led to their renewed interest in 1989 [226]. The perovskite nickelates have an AFM ground state with a unique $\uparrow\uparrow\downarrow\downarrow$ spin-order. At high temperatures, they undergo a sharp, metal-to-insulator (MI) transition [227, 228]. These features, in addition to the structural similarity to the cuprates, have made them interesting subjects of scientific exploration. In 2019, superconductivity was discovered in doped compounds of the infinite-layer nickelates ($RNiO_2$) [84, 229–231]. Furthermore, the electronic and magnetic properties of the perovskite nickelates are alluring for technological applications including solar cells [232], solid-state batteries [233], memory devices [234], and artificial intelligence [234].

Owing to fabrication challenges, research in the rare-earth perovskite nickelates has been chiefly restricted to epitaxially-grown thin-films and polycrystals. The Ni^{3+} oxidation state of $RNiO_3$ requires high oxygen pressures for bulk crystals, whereas thin films can be easily grown at low pressures [227]. While thin-film measurements are extensive and have provided insight into many nickelate phenomena [227, 235, 236], lattice mismatch, strain and size effects from film thickness can cause properties of thin-films to deviate from those observed in the bulk, thereby necessitating research on single crystals.

Single crystals were recently grown for R = Nd, Sm, Gd, Dy, Y, Ho, Er and Lu in a unique synthesis process developed by Klein et al. Nanocrystalline precursors of R_2O_3 and NiO were mixed in stoichiometric amounts and dissolved in 65-75% aqueous HNO_3. Water and nitric acid were removed, the resulting powder annealed in oxygen and then mixed with a LiCL/KCl flux. This mixture was heated under 2000 bar of oxygen gas pressure at 850 °C for 12 hours in a reactor with a temperature gradient ~ 100 °C. The resulting micro-crystals show good agreement with their polycrystalline counterparts (Fig 9.1), an indication of their high-quality [237]. However, with a maximum length of $\approx 75\ \mu$m, bulk techniques that can be used for their study are limited. Here, FIB micro-machining may be a gateway to exploration on the

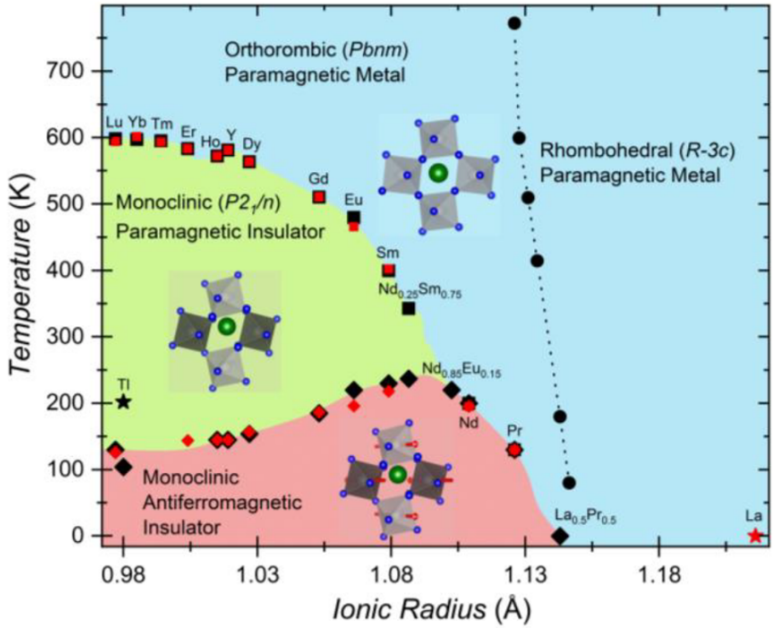

Figure 9.1: Phase diagram of the perovskite nickelates as a function of ionic radius. As shown in Fig 9.2, increasing the ionic radius stabilizes the metallic state. Red squares and rhombuses indicate T_{MI} and T_N respectively, from the single crystals synthesized in [237]. Black markers show the values for bulk polycrystals reported in [225, 238–250]. Figure reproduced from [237].

single crystalline nickelates. Unfortunately, FIBing the nickelates leads to oxygen removal on the FIBed surface, resulting in an insulating crust enclosing the device and making it difficult to form electrical contacts. Initial attempts to establish ohmic contacts have thusfar been unsuccessful; although it may still be possible with the appropriate choice of deposition, annealing, and/or etching parameters. FIB cantilevers, on the other hand, have the advantage of not relying on electrical contacts and are capable of probing the material properties, so long as the bulk is preserved.

Furthermore, the nickelates undergo a structural transition which may be particularly interesting to explore via elasticity. Fig 9.1 shows the phase diagram, in which the ground state can be tuned from an AFM insulator to a paramagnetic (PM) metal by changing the radius of the rare-earth. The structure of the perovskite nickelates is that of a single rare-earth ion surrounded by oxygen octahedra, each with a nickel at its core (See sketches in Fig 9.1). The oxygen octahedra stacked on top of each other are buckled with an angle that can be straightened by increasing the radius of the rare-earth and, in doing so, increasing the overlap of the oxygen orbitals (Fig 9.2 (a)). Thus, the metallic state can be stabilized by increasing the ionic radius. Within the metallic state, crystals are orthorhombic and paramagnetic. At the MI transition temperature (T_{MI}), an angle of $\approx .1°$ from 90° opens up between the a and c axes, changing the crystal structure to monoclinic. Concurrently, the nickel site differentiates into two: with short ($Ni^{3+\delta}$) and long ($Ni^{3-\delta}$) bonds with the oxygen — thereby doubling the unit cell [251–255]. This phenomenon is commonly referred to as the "breathing distortion".

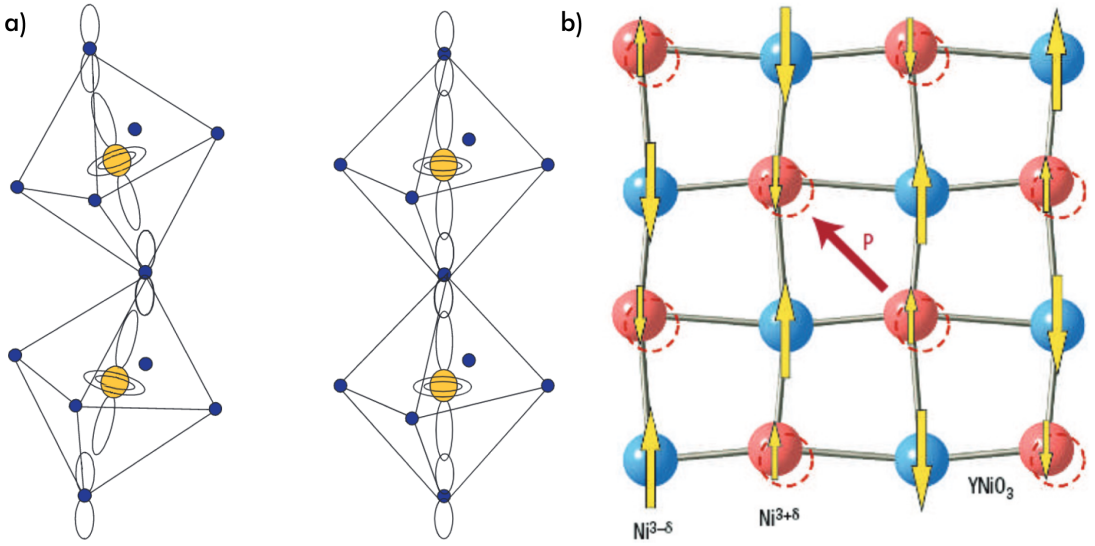

Figure 9.2: (a) NiO_6 octahedra with nickel and oxygen shown in yellow and blue, respectively. The buckling angle of the octahedra is straightened by increasing the size of the rare-earth that they surround. This increases the overlap between the oxygen orbitals and stabilizes the metallic state. Figure adapted from [227]. (b) The AFM phase has a ↑↑↓↓ spin configuration. Combined with the differentiation of the nickel sites into $Ni^{3-\delta}$ and $Ni^{3+\delta}$, this is predicted to produce a net polarization. Figure reproduced from [257].

For R = Nd and Pr, the MI and PM to AFM transition occur concurrently, while for the smaller rare-earths, the MI transition occurs at much higher temperatures [227, 228, 237, 256].

In the ground state AFM phase, the combination of the charge ordering and the ↑↑↓↓ spin ordering is predicted to lead to a net polarization [51, 257–262]. Materials with a coupled magnetic ordering and ferroelectricity, called multiferroics, have potential for the design of multifunctional devices in which the charges can be controlled via applied magnetic field and the spins controlled via applied voltages [257]. Recently, Ardizzone et al. reported evidence for multiferroicity based on Raman spectroscopy on single crystals of $RNiO_3$ (R =Y, Er, Ho, Dy, Sm, Nd) grown with the novel fabrication process of Klein et al. [237, 256]. Elasticity measurements may yield further insight into the role of the lattice distortion in this polarization.

As elasticity on the single crystals of rare-earth nickelates could not be previously studied due to their small size, FIB-fabrication was used to make cantilevers of $YNiO_3$. Two interesting phenomena were observed in these samples. The first is that laser-heating on $YNiO_3$ cantilevers under vacuum generates a thermal gradient across the length of the sample, annealing the end of the cantilever. The result is an $\approx 1\%$ increase in E_{001}, a change in the optical reflectivity and an apparent stark increase in resistivity (as seen in SEM images). These results are reminiscent of thin-film experiments on $NdNiO_3$, $SmNiO_3$, and $LaNiO_3$ which have revealed a reversible increase in the resistivity up to seven orders of magnitude, and an increase in the optical transparency, by electron-doping from removing oxygen [52, 263–267]. These doped electrons

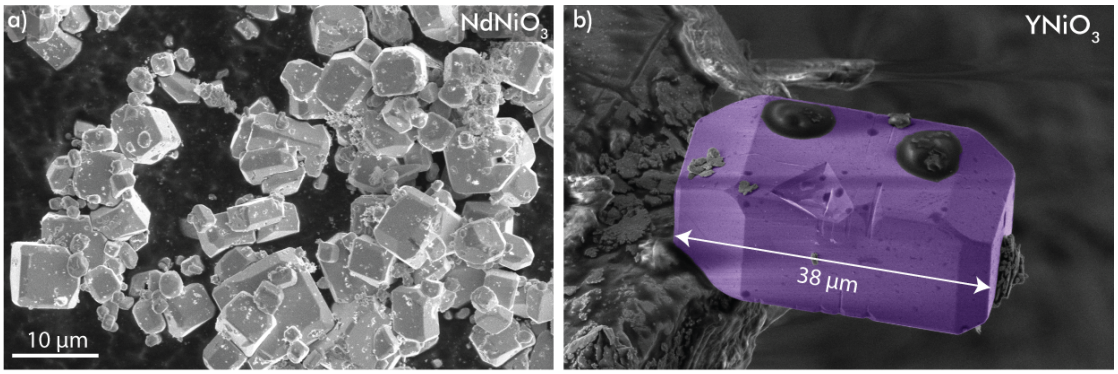

Figure 9.3: SEM images of single crystalline $NdNiO_3$ (a) and $YNiO_3$ (b) with purple added to distinguish the crystal. Magnification is the same in both images. Samples were fabricated by [237].

localize on the nickel sites, changing the oxidation from Ni^{3+} to Ni^{2+}, resulting in the observed increased resistivity [268].

Second, with the laser power attenuated to prevent oxygen dissociation, an $YNiO_3$ cantilever was cooled through the AFM transition (T_N). Above the AFM transition, the stiffening of E_{001} can well be described by phonon anharmonicity. At T_N, E_{001} dips by ≈ .2%, then continues stiffening with an increased slope down to 100 K. This phase transition is sharp and gives an indication on the coupling between the lattice and the AFM ordering parameter.

9.1 Method

Single crystals of rare-earth nickelates were grown by Klein et al. using their fabrication process [237]. SEM images of $NdNiO_3$ and $YNiO_3$ are shown in Fig 9.3. Before fabricating cantilevers, it is necessary to first consider the geometry of the sample and the frequency range for measurement. The vibrometer used for measurements in this thesis has a decoder for frequency measurements up to 500 kHz, although it was possible to detect resonances at higher frequencies (up to 2 MHz). For this reason, cantilevers were designed such that the fundamental resonance mode, $f_0 \leq$500 kHz. From Euler-Bernouli Beam theory (Eqn 2.37), $f_n \sim T/L^2$, where L is the length and T is the thickness. Because of the short length scales of $NdNiO_3$, the final length of the cantilever would be $L \sim 10$ μm and would need to have $T \approx 2$ nm for $f_0 \leq 500$ kHz or $T \approx 10$ nm for $f_0 \leq 2$ MHz. This is too thin for FIB cantilever fabrication as the smallest structures that can be fabricated are > 100 nm. Elastic properties of $NdNiO_3$ can still be studied by using a different cantilever design, for example, a thin cantilever with a large mass at the end. Fig 9.4 shows Finite Element Analysis simulations of one such cantilever. Assuming Young's modulus $E \approx 130$ GPa (based on the measured value for $YNiO_3$) and with density of $NdNiO_3$, $\rho = 7550$ kg/m^3 [225] the fundamental resonance frequency of this cantilever is $f_0 \sim 1200$ kHz, within the measurable range of the vibrometer used in this thesis.

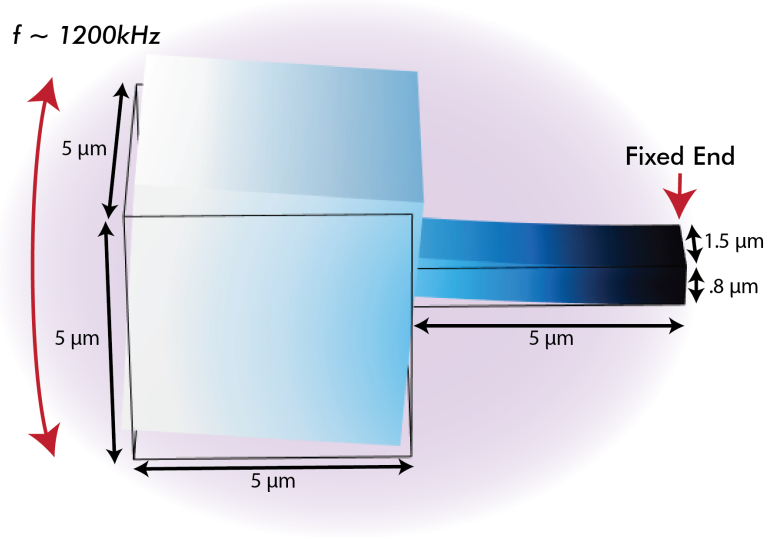

Figure 9.4: Comsol Multiphysics Finite Element Analysis simulation of a cantilever with a large mass at the end. Different geometries such as these can enable elasticity studies on samples such as $NdNiO_3$, which are too short for measurements on a rectangular beam. Cantilever frequency is estimated by assuming a Young's modulus approximate to Young's modulus measured for $YNiO_3$, $E \approx 130$ GPa, with density for $NdNiO_3$, $\rho = 7550$ kg/m^3 [225].

For this study, cantilevers were fabricated from $YNiO_3$ due to the larger sizes of the crystals (longest axis $\sim 30-50$ μm). The fabrication process described in Chapter 4 was used for [001] cantilevers to probe E_{001}. Measurements were done on the micro-resonator probe (Chapter 5) in a vacuum tight tube pumped continuously to $< 1e^{-4}$ mbar. From the resonance frequency and the geometry of the sample measured with SEM images, Young's modulus was calculated with Eqn 2.41. Using Eqn 2.42 with the thickness variation along the beam taken to be the error σ_T, the error on the Young's Modulus was calculated to be 20%. For sweeping temperature, the vacuum tube was placed in a dewar of liquid nitrogen while measurements were run continuously.

9.2 Laser Annealing of Cantilevers

Measuring $YNiO_3$ cantilevers under vacuum at room temperature with the laser at full power (<10 mW, $\lambda = 1550$ nm) was found to change the electrical and optical properties of the samples. Images taken on $YNiO_3$ cantilevers (A and B) before measuring with the interferometer appear uniformly dark across the surface of the samples (Fig 9.5). After measuring, both cantilevers show bright regions on the half nearest to the free end, while the fixed end is unchanged. SEM images can be an indication of a material's resistivity due to charging effects. While scanning the electron beam across an insulator, the injected primary electrons build-up. This charge accumulation creates a strong electric field that is repulsive for the generated secondary electrons (SE), increasing the percentage of SE that escape the sample and can be measured

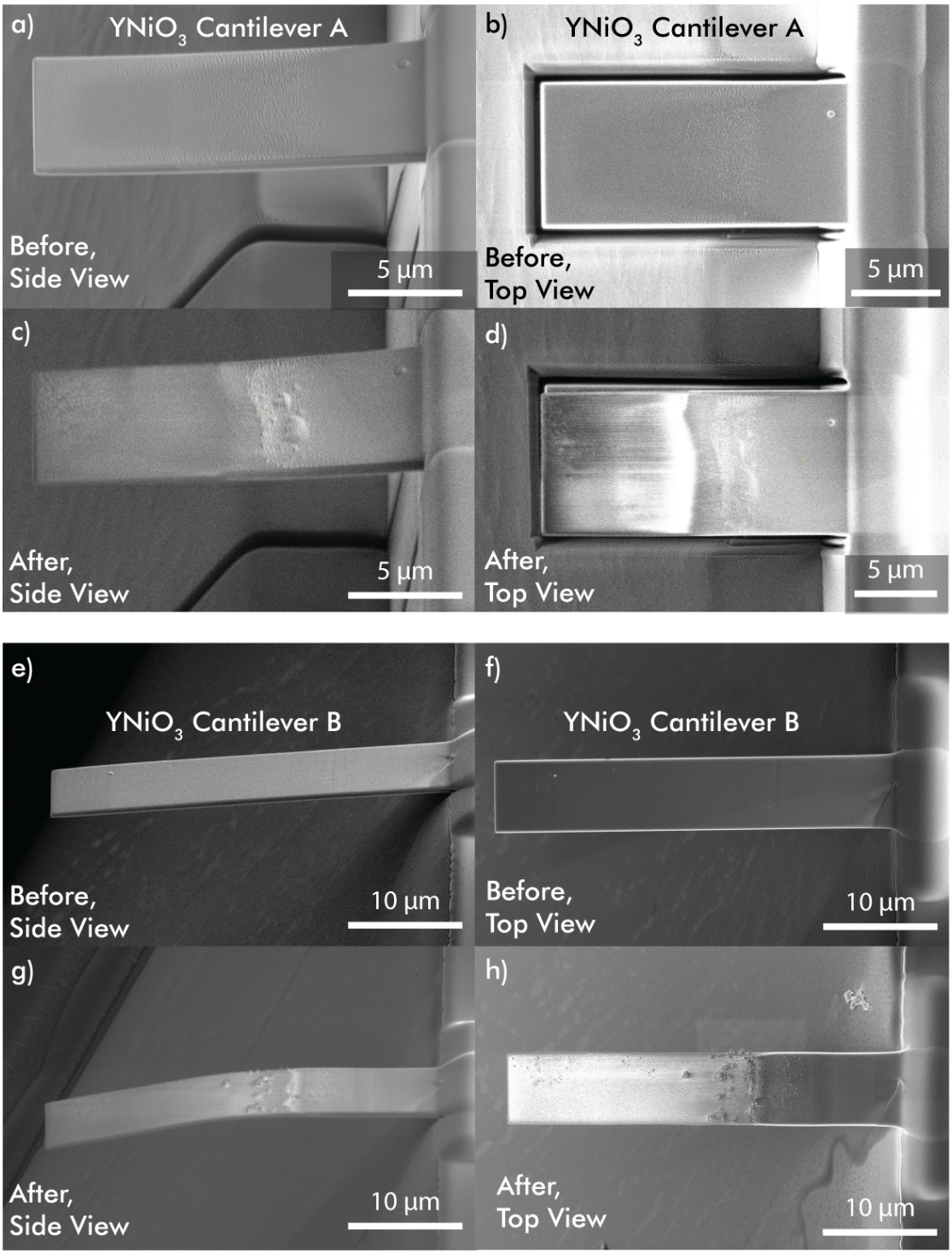

Figure 9.5: SEM images of $YNiO_3$ cantilevers A (a-d) and B (e-h). Images were taken before laser anneal (a-b, e-f) and after (c-d, g-h). Before annealing, cantilevers appear uniformly dark, indicating that the sample is well-grounded. After annealing, images taken from the top view show a bright region, corresponding to build-up of electrical charge. The side view of Cantilever B shows that the sample has bent.

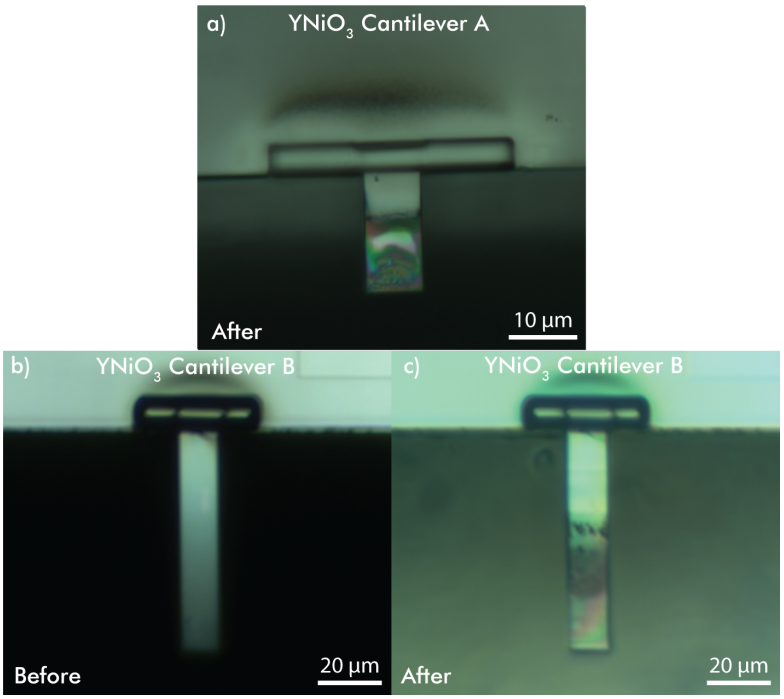

Figure 9.6: Optical images of the cantilevers A and B. (a) Cantilever A, image taken after measurement. No image was taken before. (b-c) Cantilever B before (b) and after (c) measurement.

by the detector. Insulating regions will therefore appear very bright when imaged by SE [95]. The SEM images of Fig 9.5 were taken by detecting SE. The light-colored areas in the $YNiO_3$ samples are therefore regions with high resistivity where the charge cannot dissipate. From the side views (stage tilted to 52°), a bend near the middle of sample B can be seen showing a significant structural distortion.

These changes are visible also in the optical images (Fig 9.6). The colorful regions of cantilevers A and B after measurement is in stark contrast to the metallic appearance near the cantilever bases and the full length of B before measurement.

Finally, an increase in elastic stiffness can be observed during measurements. Figure 9.7 shows the relative frequency, f/f_0, for two samples measured without attenuating the laser (Cantilever B, laser power < 10 mW) and with a 20 dB attenuator (Cantilever C, laser power <.1 mW). Over a period of 18 hours, the resonance frequency of the sample measured with laser attenuation increases, corresponding with an increase in Young's modulus by ~ 1%. There was no significant change in the frequency measured with the 20 dB attenuation. SEM images of the cantilever measured with attenuation showed no sign of structural deformation or charging, confirming that the observed phenomenon is caused by the laser.

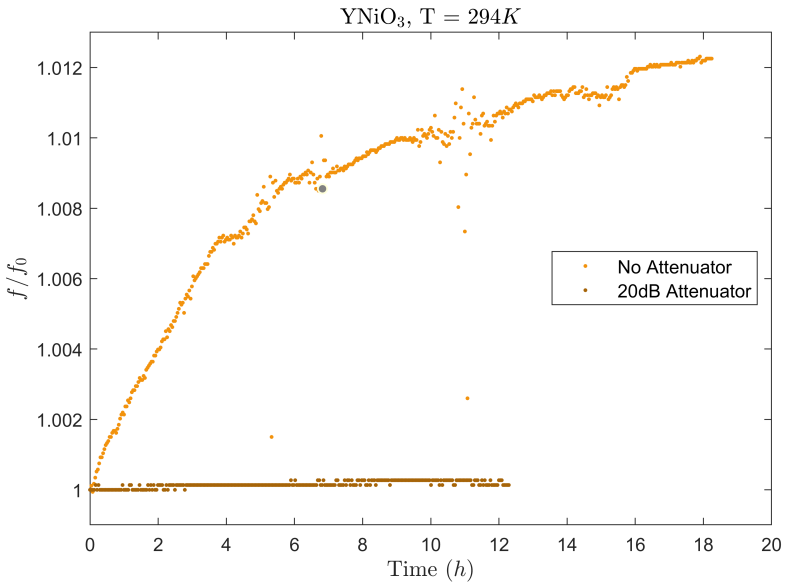

Figure 9.7: Change in frequency, f / f_0, (where f_0 is the frequency at Time = 0) of two cantilevers during measurements versus time. The stiffness of the cantilever measured without an attenuator (laser power < 10 mW) increases ~ 1% over a period of 18 hours. The cantilever measured with a 20 dB attenuator (laser power <.1 mW) shows no significant change in frequency beyond what can be expected from thermal fluctuations.

9.2.1 Electron Doping of Nickelates

The effect of the laser on the $YNiO_3$ cantilever can be better understood in light of the research on oxygen deficiencies in thin films and powders of other nickelates. When oxygen deficiencies are created, such as by annealing samples in a low-oxygen environment, the system is doped with electrons. In thin films of $NdNiO_3$, $SmNiO_3$ and $LaNiO_3$, this leads to an increase in resistivity by several orders of magnitude, and an increase in the optical transmission [52, 263–265, 269]. This process has been shown to be reversible; oxygen ions removed by annealing in vacuum can be reinserted by annealing in oxygen, resulting in electrical and optical properties similar to the samples as-grown [52, 265, 269]. In $LaNiO_3$ powder, oxygen reduction was found to also result in structural changes [270].

An excellent explanation for the observed decrease in conductivity, structural distortions and increase in transparency was provided by Kotiuga et al. When an oxygen vacancy is created, the added electron localizes on a nickel site, converting the Ni^{3+} into Ni^{2+}. A combination of crystal field splitting, and electron-electron correlations opens up a large, on-site gap thereby increasing resistivity and transparency. This process was determined via first-principles density functional theory and the reduction in the nickel valence state has been confirmed by synchrotron photoemission spectroscopy [268].

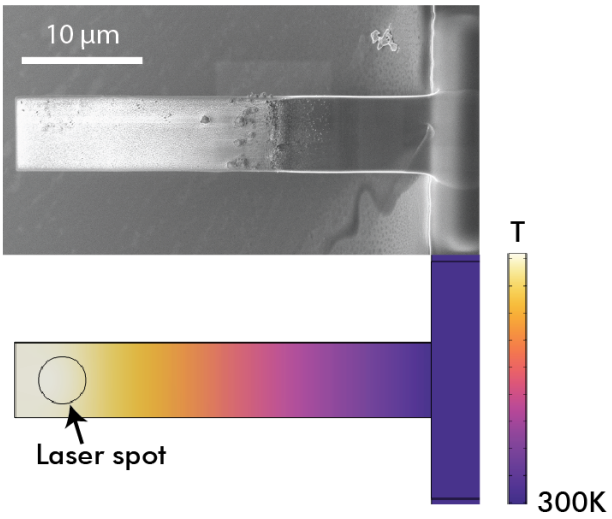

Figure 9.8: (Top) Cantilever B after measurement (Fig 9.5 (h)). (Bottom) Finite Element Analysis simulations were done in Comsol Multiphysics to simulate the heat gradient across a sample of the same dimensions. On the sample chip, far away from the cantilever, the temperature was set to room temperature. As the laser absorption and heat conductivity are unknown, it is not possible to accurately calculate the temperature on the sample. With the laser focused on the free-end, the heat must flow through the length of the sample to the base. This generates a gradient such that oxygen vacancies are created only on the free end while the base is relatively unchanged.

9.2.2 Discussion

Considering that this phenomenon has been observed in $NdNiO_3$, $SmNiO_3$ and $LaNiO_3$, it is reasonable that the same process is at work in $YNiO_3$ as well. In the case of the cantilevers, heating from the laser focused on the free-end can dissipate only by radiation or by conduction through the length of the cantilever (Fig 9.8). Finite Element Analysis simulations were done to model the heat gradient, using the Heat Transfer physics package in Comsol multiphysics. Constant heat was input at the laser spot on the surface of the cantilever while the temperature on the sample chip far away from the sample was set to room temperature. Laser heating generates a thermal gradient across the length. As the measurements are conducted in vacuum, oxygen vacancies are created on one end of the sample, increasing the resistivity, transparency and elastic stiffness, while the colder, fixed-end is preserved. This process may be at least somewhat reversible by annealing the sample in oxygen; although the structural deformation most likely cannot be reversed.

These experiments have demonstrated three main findings: (1) Band gap opening from electron-doping in $RNiO_3$ exists in R = Y, in addition to the previously demonstrated R = Nd, Sm and La. (2) Oxygen reduction in the nickelates can be done selectively via laser-annealing. (3) This phenomenon exists also in the relatively bulk cantilever (thickness $\sim 1\ \mu$m). Thin films have been studied with a thickness of only ~ 60 nm [268].

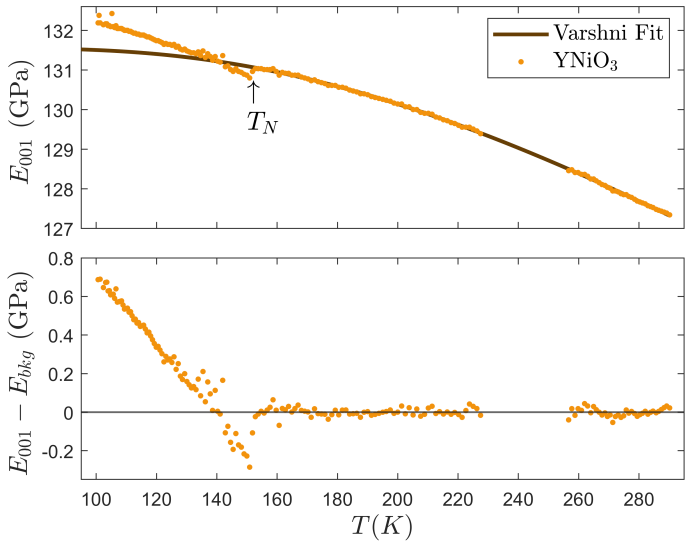

Figure 9.9: E_{001} versus temperature (top). In between 225 K and 255 K, a technical error resulted in the data in this temperature range to be lost. The data was fit to Varshni's equation for the phonon contribution (Eqn 2.48) in the temperature range 160-300 K. The phonon background was subtracted to show the contribution from the phase transition (bottom). A discontinuity in E_{001} is clearly visible at $T_N = 151$ K.

9.3 Elastic Response to the Magnetic Transition

The resonance frequency of cantilever C — which was only measured with an attenuated laser and showed no signs of oxygen dissociation — was tracked as a function of temperature. Measurements of E_{001} are shown in Fig 9.9 (top). A discontinuity at 151 K corresponds with T_N. Above T_N, the stiffening in E_{001} fits well with the expected stiffening from the phonon contribution (Eqn 2.48) with fitting parameters $t = 660$ K, $E^0 = 131.6$ GPa, $s = 37$ GPa. This background was subtracted from the raw data to show the contribution to Young's modulus from the phase transition in Fig 9.9 (bottom). The magnitude of the discontinuity is $-.28$ GPa or $\sim .2\%$

Below $T_{MI} = T_S = 580$ K, $YNiO_3$ is monoclinic. A monoclinic symmetry has 13 independent elastic constants (Eqn 2.17) and $E_{001} = s_{33}^{-1}$ is dependent on 11 of them, excluding only c_{44} and c_{55}. Therefore it is not currently possible to determine the exact elastic moduli that couple with the ordering parameter, η. The shape of the anomaly can be an indicator of how the ordering parameter couples with the lattice (See 2.3.2). A linear coupling between strain and η ($F_c = -g\eta\epsilon_i$) predicts a softening in the relevant elastic modulus above the transition while a quadratic-in-ordering parameter coupling ($F_c = -g\eta^2\epsilon$) predicts no change above the phase transition and a discontinuity at the phase transition. As the stiffening of E_{001} above T_N behaves as expected from the phonon contribution without softening but shows a discontinuity at T_N, this indicates that the coupling between the ordering parameter and the

strain is non-linear. More measurements on higher order modes and of samples with different geometries would help elucidate both the relevant strain components and their coupling to the ordering parameter. Furthermore, in $YNiO_3$, the MI transition occurs far above the magnetic transition while in $NdNiO_3$, $T_{MI} = T_N$. It would therefore be fascinating to study this transition in both compounds.

10 Outlook

Cantilevers of silicon, nickelates, cuprates and pnictides show the promising capabilities of this technique both as a method of determining the elastic properties and exploring phase transitions in quantum materials. In particular, both SmFeAs(O,F) and $YNiO_3$ are materials for which measurements are limited and the elastic tensor was previously inaccessible. With this technique, Young's modulus can be computed within a <10% error that comes mostly from geometric factors. One of the main sources of uncertainty is the FIB deposit that fixes the cantilever. The microstructure of the deposit can vary greatly depending on the deposition parameters. Using the process described in 3.2.5, FIBID cantilevers can be grown such that the elastic properties and their dependence on the growth parameters can be explored. With this, the cantilever and its deposited base can be simulated using FEA, also taking into consideration any geometric variance (i.e. in the thickness) along the length of the sample. This would reduce the uncertainty and allow for an even more accurate calculation of the elastic properties. Furthermore, tuning the deposition may reduce dissipation at the base, increasing Q-factors of FIB-fabricated cantilevers from quantum materials. By studying cantilevers of the deposits, methods to increase the hardness and decrease dissipation, for example by annealing or with different deposition parameters, can be found.

Measurements on FIB cantilevers reveal a giant softening of E_{110} in SmFeAs(O,F) that is reduced with doping and follows remarkably well from elasticity measurements in other pnictides [27]. As this softening is present only in E_{110} and not in E_{100}, it can be attributed to a softening of the shear component relevant for nematicity, c_{66}. Interestingly, the weaker Curie constant in SmFeAsO compared to $BaFe_2As_2$ may be indicative of a competitive nature between nematicity and superconductivity. Still, these results raise more questions deserving of further investigation. The decline of the Q-factor in the doped compound in magnetic field is noteworthy. While the dissipation of a resonator can spike at the vortex-glass melting point, this should be further explored to study the coupling between the vortices and the lattice and to see if the resonance returns at lower temperatures. Additionally, the shift in E_{110} above T_c with magnetic field is also curious. Does E_{110} in different fields later reconvene at higher temperatures?

In the cuprates, the temperature dependence of Young's modulus in LSCO shows good agreement with the results reported in literature from PE. Neither PE nor the FIB cantilever showed anomalies at T_{SDW}, T_{CDW} and T^*, hence, these results do not support the RUS observation of the pseudogap in YBCO [47]. Cantilevers of Tl2201 reacted during the measurement so it was not possible to study their elasticity. This may be due to the removal of oxygen in the cuprates that occurs from heating during FIBing. Annealing the cantilevers in oxygen before measurement is one possible avenue to solve this problem. Different ion sources may also change the composition of the crust; for example, the oxygen removal in the outer crust may be reduced by using an oxygen FIB. The Tl2201 cantilevers show that there is still much to be learned about the interaction of the ion beams with these complex materials.

In $YNiO_3$, the increase in resistivity with laser annealing is the first observation of this phenomenon in this compound and follows from previous results in thin films of other nickelates [268]. Thermal gradients generated by heating with a controlled laser source may also prove useful in other applications of microstructured quantum materials. For example, laser heating could be used to anneal a sample through a phase transition to control domain patterns. On the flip side, laser heating will likely prevent the optical-readout technique from being successfully adapted for measurements at lower temperatures such as the millikelvin temperatures achieved in a dilution refrigerator. However, a different detection method could be used for resonance measurements, such as capacitive or SQUID-based readouts [271].

In the non-annealed $YNiO_3$ sample, the discontinuity at T_N in E_{001} is sharp. Much more can be learned about this transition by studying other orientations and other nickelates. Single crystals of $NdNiO_3$ are significantly smaller than $YNiO_3$, and $YNiO_3$ crystals are shorter along [100] and [010] than along [001]. These short length scales limit the length of cantilevers that can be fabricated. Because a simple rectangular cantilever has resonance frequency $f_0 \sim T/L^2$, a shorter cantilever will have a higher fundamental resonance frequency. This technique would benefit greatly from a vibrometer with a wider frequency range, enabling studies of smaller cantilevers and higher resonance modes. Another fruitful approach is to build non-rectangular cantilevers to adjust the resonance frequency.

In MEMS devices, complex cantilevers are designed according to their functionality. Piezoelectrics, for example, are constructed into resonators used for RF communications, sensors, and energy harvesters and their geometries are chosen based on the target frequency and application [272]. Similar approaches can be taken for resonators of quantum materials, thanks to the flexibility of the FIB-cantilever fabrication process. Throughout the course of this thesis, cantilevers have been fabricated with a simple rectangular geometry, but much more intricate geometries are possible. Resonators can be designed in which the resonance mode is directly coupled to the interesting physics of the material, or to tune the frequency spectrum. Fig 10.1 (a) shows a silicon cantilever mounted directly over a FIB-cut trench into a piezoelectric transducer. This cantilever has a thinned down neck which shifts the fundamental resonance frequency downward. The resonance frequency can be shifted even further by increasing the mass at the end of the sample, for example, by leaving a thicker block (FEA simulations shown

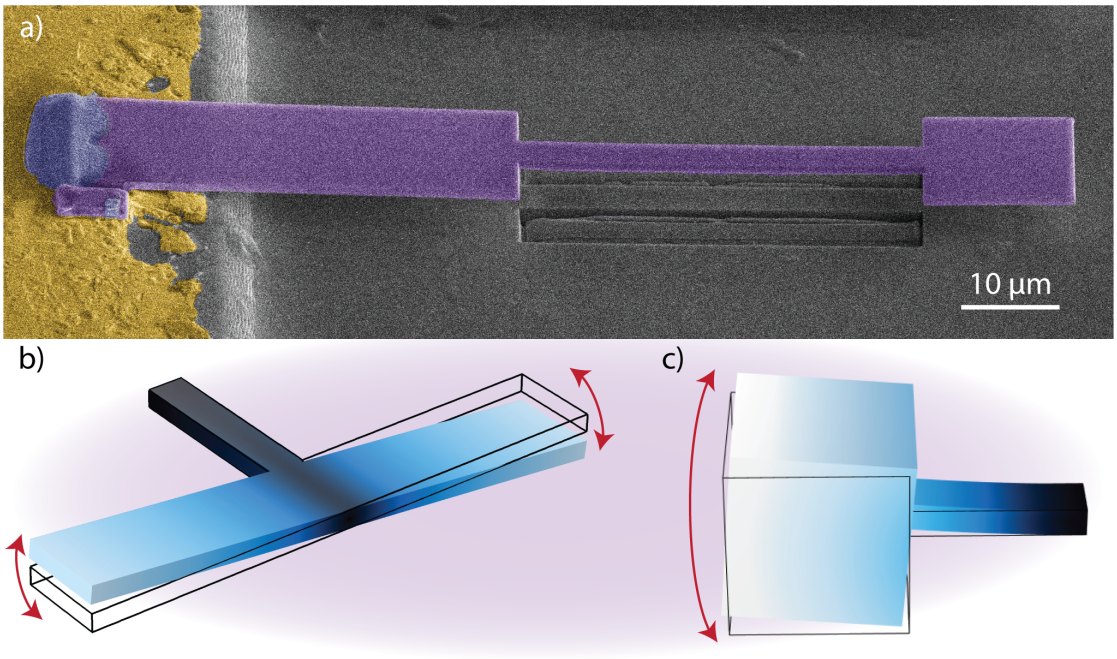

Figure 10.1: (a) SEM image of a cantilever with a thinned neck. (b) FEA simulations of a T-beam. (c) FEA simulations of a cantilever with a large mass. The designs of (a) and (c) shift the fundamental flexural resonance mode downwards, in comparison to the simple rectangular cantilever. Cantilevers can also be designed to favor other resonance modes. For example, the fundamental resonance mode of the T-beam (b) is torsional.

in Fig 10.1 (c)) or by adding a FIB deposition at the end. This can be useful to study samples with short ($\sim 10\,\mu$m) length scales such as the nickelates. Cantilever geometries can also be tuned to favor other resonance modes. For instance, the T-beam geometry of 10.1 (b) has a torsional mode as its fundamental resonance.

This thesis is only the beginning of this technique, and much more remains to be explored. So far, the focus has been on measuring previously inaccessible microscopic samples, and this technique can be instrumental in studies of elasticity and phase transitions on novel materials. Yet the possibilities of size effects and non-linearities may make this a powerful technique even on samples such as the cuprates, for which large, clean single crystals already exist. RUS, PE and bending techniques probe a bulk sample and often cannot be used to extract elastic information below a phase transition due to the formation of domains unless the sample is detwinned. This will also be the case in FIB-fabricated cantilevers, unless the length scale of the domains is comparable to, or larger than, the size of the cantilever. In these cases, it may also be possible to control the domain structure, for example, with different geometries of the cantilever and by resonating with different driving amplitudes through the phase transition. Perhaps strain gradients of the cantilever can be sufficient to self-detwin. Furthermore, measurements so far have been conducted on cantilevers resonating within a linear regime. MEMS cantilevers excited at high drive levels can show interesting non-linear

effects, such as bifurcations of the resonance [273]. What non-linear effects might exist in cantilevers of various quantum materials? Even as this thesis must come to an end, I hope that the technique of FIB-Fabricated cantilevers is just beginning a rich scientific career such that these and other questions can be addressed.

Publications

Evgeny Mikheev, Tino Zimmerling, **Amelia Estry**, Philip JW Moll, and David Goldhaber-Gordon
Ionic Liquid Gating of $SrTiO_3$ Lamellas fabricated with a Focused Ion Beam
Nano Letters **22** (10), 3872-2878 (2022).

Jonas Diaz, Carsten Putzke, Xiangwei Huang, **Amelia Estry**, James G Analytis, Daniel Sabsovich, Adolfo G Grushin, Roni Ilan, and Philip JW Moll
Bending strain in 3D topological semi-metals
Journal of Physics D: Applied Physics **55** (8), 084001 (2021).

Kyungchan Lee, Daixiang Mou, Na Hyun Jo, Yun Wu, Benjamin Schrunk, John M Wilde, Andreas Kreyssig, **Amelia Estry**, Sergey L Bud'ko, Manh Cuong Nguyen, Lin-Lin Wang, Cai-Zhuang Wang, Kai-Ming Ho, Paul C Canfield and Adam Kaminski
Evidence for a large Rashba splitting in $PtPb_4$ from angle-resolved photoemission spectroscopy
Physical Review B **103**, 085125 (2021).

Chunyu Guo, A Alexandradinata, Carsten Putzke, **Amelia Estry**, Teng Tu, Nitesh Kumar, Feng-Ren Fan, Shengnan Zhang, Quansheng Wu, Oleg V Yazyev, Kent R Shirer, Maja D Bachmann, Hailin Peng, Eric D Bauer, Filip Ronning, Yan Sun, Chandra Shekhar, Claudia Felser and Philip JW Moll
Temperature dependence of quantum oscillations from non-parabolic dispersions
Nature Communications **12** 6213 (2021).

Kimberly A Modic, Maja D Bachmann, BJ Ramshaw, F Arnold, KR Shirer, **Amelia Estry**, JB Betts, Nirmal J Ghimire, ED Bauer, Marcus Schmidt, Michael Baenitz, E Svanidze, Ross D McDonald, Arkady Shekhter and Philip JW Moll
Resonant torsion magnetometry in anisotropic quantum materials
Nature Communications **9** 3975 (2018).

Bibliography

[1] A. E. Böhmer, P. Burger, F. Hardy, T. Wolf, P. Schweiss, R. Fromknecht, M. Reinecker, W. Schranz, and C. Meingast, Physical Review Letters **112**, 047001 (2014).

[2] R. Uecker, Journal of Crystal Growth **401**, 7 (2013).

[3] J. F. Annett, *Superconductivity, superfluids and condensates* (Oxford University Press, 2007).

[4] M. R. Norman, Superconductivity **332**, 196 (2011).

[5] D. J. Scalapino, Reviews of Modern Physics **84**, 1383 (2012).

[6] G. R. Stewart, Advances in Physics **66**, 75 (2017).

[7] D. N. Basov and A. V. Chubukov, Nature Physics **7**, 272 (2011).

[8] Y. Terao, O. Ozaki, C. Ichihara, S. Kawashima, T. Hase, H. Kitaguchi, S.-I. Kobayashi, K.-I. Sato, I. Nakajima, N. Oonishi, M. Poole, K. Takeda, S.-I. Urayama, and H. Fukuyama, IEEE Transactions on Applied Superconductivity **23**, 4400904 (2013).

[9] B. J. Parkinson, R. Slade, M. J. D. Mallett, and V. Chamritski, IEEE Transactions on Applied Superconductivity **23**, 10.1109/TASC.2012.2235893 (2013).

[10] H. W. Weijers, W. D. Markiewicz, A. V. Gavrilin, A. J. Voran, Y. L. Viouchkov, S. R. Gundlach, P. D. Noyes, D. V. Abraimov, H. Bai, S. T. Hannahs, and T. P. Murphy, IEEE Transactions on Applied Superconductivity **26**, 10.1109/TASC.2016.2517022 (2016).

[11] F. Schmidt, J. Maguire, T. Welsh, and S. Bratt, Physics Procedia **36**, 1137 (2012).

[12] Y. Kamihara, T. Watanabe, M. Hirano, and H. Hosono, Journal of the American Chemical Society **130**, 3296 (2008).

[13] J. Paglione and R. L. Greene, Nature Physics 2010 6:9 **6**, 645 (2010).

[14] N. D. Zhigadlo, S. Katrych, Z. Bukowski, S. Weyeneth, R. Puzniak, and J. Karpinski, Journal of Physics Condensed Matter **20**, 342202 (2008).

[15] N. D. Zhigadlo, S. Weyeneth, S. Katrych, P. J. Moll, K. Rogacki, S. Bosma, R. Puzniak, J. Karpinski, and B. Batlogg, Physical Review B - Condensed Matter and Materials Physics **86**, 214509 (2012).

[16] R. S. Meena, V. R. Rao, H. Kishan, and V. P. S. Awana, IOP Conf. Series: Materials Science and Engineering **171**, 10.1088/1757-899X/171/1/012153 (2017).

[17] Y. J. Cui, Y. L. Chen, C. H. Cheng, Y. Yang, Y. Zhang, and Y. Zhao, Journal of Superconductivity and Novel Magnetism **23**, 625 (2010).

[18] C. Wang, L. Li, S. Chi, Z. Zhu, Z. Ren, Y. Li, Y. Wang, X. Lin, Y. Luo, S. Jiang, X. Xu, G. Cao, and Z. Xu, Europhysics Letters **83**, 67006 (2008).

[19] H. Hosono, A. Yamamoto, H. Hiramatsu, and Y. Ma, Materials Today **21**, 278 (2018).

[20] H. Q. Yuan, J. Singleton, F. F. Balakirev, S. A. Baily, G. F. Chen, J. L. Luo, and N. L. Wang, Nature Letters **457**, 565 (2009).

[21] T. Shibauchi, A. Carrington, and Y. Matsuda, Annual Review Condensed Matter Physics **5**, 113 (2014).

[22] J. H. Chu, J. G. Analytis, K. D. Greve, P. L. McMahon, Z. Islam, Y. Yamamoto, and I. R. Fisher, Science **329**, 824 (2010).

[23] J. H. Chu, H. H. Kuo, J. G. Analytis, and I. R. Fisher, Science **337**, 710 (2012).

[24] S. Hosoi, K. Matsuura, K. Ishida, H. Wang, Y. Mizukami, T. Watashige, S. Kasahara, Y. Matsuda, and T. Shibauchi, Proceedings of the National Academy of Sciences **113**, 8139 (2016).

[25] E. Fradkin, S. A. Kivelson, M. J. Lawler, J. P. Eisenstein, and A. P. Mackenzie, Annual Review of Condensed Matter Physics **1**, 153 (2010).

[26] R. M. Fernandes, L. H. Vanbebber, S. Bhattacharya, P. Chandra, V. Keppens, D. Mandrus, M. A. McGuire, B. C. Sales, A. S. Sefat, and J. Schmalian, Physical Review Letters **105**, 157003 (2010).

[27] A. E. Böhmer and C. Meingast, Comptes Rendus Physique **17**, 90 (2016).

[28] A. Böhmer and A. Kreisel, Journal of Physics: Condensed Matter **30**, 023001 (2018).

[29] M. Yoshizawa, S. Simayi, K. Sakano, Y. Nakanishi, K. Kihou, C. H. Lee, A. Iyo, H. Eisaki, M. Nakajima, and S. I. Uchida, Solid State Communications **152**, 680 (2012).

[30] J. Jaroszynski, F. Hunte, L. Balicas, Y. J. Jo, I. Raičević, A. Gurevich, D. C. Larbalestier, F. F. Balakirev, L. Fang, P. Cheng, Y. Jia, and H. H. Wen, Physical Review B **78**, 174523 (2008).

[31] P. J. Moll, R. Puzniak, F. Balakirev, K. Rogacki, J. Karpinski, N. D. Zhigadlo, and B. Batlogg, Nature Materials **9**, 628 (2010).

[32] P. J. Moll, "The role of anisotropy in iron-pnictides addressed by focused ion beam sample fabrication" (ETH Zurich, 2012).

[33] P. J. W. Moll, Annual Review of Condensed Matter Physics **9**, 147 (2018).

[34] X. Cai, Y. A. Ying, N. E. Staley, Y. Xin, D. Fobes, T. J. Liu, Z. Q. Mao, and Y. Liu, Physical Review B **87**, 81104(R) (2013).

[35] M. D. Bachmann, N. Nair, F. Flicker, R. Ilan, T. Meng, N. J. Ghimire, E. D. Bauer, F. Ronning, J. G. Analytis, and P. J. Moll, Science Advances **3**, 10.1126/SCIADV.1602983 (2017).

[36] X. Huang, C. Putzke, C. Guo, J. Diaz, M. König, H. Borrmann, N. L. Nair, J. G. Analytis, and P. J. W. Moll, npj Quantum Materials **5**, 12 (2020).

[37] P. J. Moll, B. Zeng, L. Balicas, S. Galeski, F. F. Balakirev, E. D. Bauer, and F. Ronning, Nature Communications 2015 6:1 **6**, 1 (2015).

[38] P. J. Moll, T. Helm, S. S. Zhang, C. D. Batista, N. Harrison, R. D. McDonald, L. E. Winter, B. J. Ramshaw, M. K. Chan, F. F. Balakirev, B. Batlogg, E. D. Bauer, and F. Ronning, npj Quantum Materials 2017 2:1 **2**, 1 (2017).

[39] M. R. V. Delft, M. D. Bachmann, C. Putzke, C. Guo, J. A. Straquadine, E. D. Bauer, F. Ronning, and P. J. Moll, Applied Physics Letters **120**, 092601 (2022).

[40] C. Guo, C. Putzke, S. Konyzheva, X. Huang, M. Gutierrez-Amigo, I. Errea, D. Chen, M. G. Vergniory, C. Felser, M. H. Fischer, T. Neupert, and P. J. W. Moll, Nature **611**, 461 (2022).

[41] C. Putzke, M. D. Bachmann, P. McGuinness, E. Zhakina, V. Sunko, M. Konczykowski, T. Oka, R. Moessner, A. Stern, M. König, S. Khim, A. P. Mackenzie, and P. J. Moll, Science **368**, 1234 (2020).

[42] P. H. McGuinness, E. Zhakina, M. König, M. D. Bachmann, C. Putzke, P. J. Moll, S. Khim, and A. P. Mackenzie, Proceedings of the National Academy of Sciences of the United States of America **118**, e2113185118 (2021).

[43] X. Huang, C. Guo, C. Putzke, Y. Sun, M. G. Vergniory, I. Errea, M. Gutierrez-Amigo, D. Chen, C. Felser, and P. J. W. Moll, arXiv, 10.1103/PhysRevB.106.064510 (2022).

[44] J. Diaz, C. Putzke, X. Huang, A. Estry, J. G. Analytis, D. Sabsovich, A. G. Grushin, R. Ilan, and P. J. W. Moll, Journal of Physics D **55**, 7 (2022).

[45] S. Ghosh, M. Matty, R. Baumbach, E. D. Bauer, K. A. Modic, A. Shekhter, J. A. Mydosh, E. A. Kim, and B. J. Ramshaw, Science Advances **6**, 10.1126/SCIADV.AAZ4074 (2020).

[46] S. Ghosh, A. Shekhter, F. Jerzembeck, N. Kikugawa, D. A. Sokolov, M. Brando, A. P. Mackenzie, C. W. Hicks, and B. J. Ramshaw, Nature Physics **17**, 199 (2020).

[47] A. Shekhter, B. J. Ramshaw, R. Liang, W. N. Hardy, D. A. Bonn, F. F. Balakirev, R. D. McDonald, J. B. Betts, S. C. Riggs, and A. Migliori, Nature **498**, 75 (2013).

[48] B. J. Ramshaw, A. Shekhter, R. D. McDonald, J. B. Betts, J. N. Mitchell, P. H. Tobash, C. H. Mielke, E. D. Bauer, and A. Migliori, Proceedings of the National Academy of Sciences of the United States of America **112**, 3285 (2015).

[49] A. Migliori and J. L. Sarrao, *Resonant ultrasound spectroscopy: applications to physics, materials measurements and nondestructive evaluation* (Wiley-Interscience, 1997).

[50] B. Lüthi, *Physical acoustics in the solid state*, Vol. 148 (Springer, 2005).

[51] J. V. D. Brink and D. I. Khomskii, Journal of Physics: Condensed Matter **20**, 434217 (2008).

[52] L. Wang, S. Dash, L. Chang, L. You, Y. Feng, X. He, K.-j. Jin, Y. Zhou, H. G. Ong, P. Ren, S. Wang, L. Chen, and J. Wang, ACS Applied Materials and Interfaces **8**, 9769 (2016).

[53] L. J. Bond, Nondestructive Evaluation of Materials **17**, 155 (2018).

[54] G. Jaeger, Archive for History of Exact Sciences **53**, 51 (1998).

[55] T. Sauer, European Physical Journal Special Topics **226**, 539 (2017).

[56] W. H. Keesom and W. de Haas, Verhandlingen der Koninklijke Akademie van Wetenschappen Amsterdam **34** (1932).

[57] P. Vannucci, *Anisotropic elasticity* (Springer, 2018).

[58] L. D. Landau and E. M. Lifshitz, *Theory of elasticity*, 3rd ed. (Red Educational and Professional Publishing, 1986).

[59] A. Cazzani and M. Rovati, International Journal of Solids and Structures **42**, 5057 (2005).

[60] T. C. T. Ting, Journal of Mechanics and Computation **21**, 249 (2005).

[61] S. M. Han, H. Benaroya, and T. Wei, Journal of Sound and Vibration **225**, 935 (1999).

[62] O. Bauchau and J. Craig, *Structural analysis with applications to aerospace structures*, Vol. 163 (2009), pp. 173–211.

[63] N. F. van Rensburg and A. J. van der Merwe, Wave Motion **44**, 58 (2006).

[64] F. A. Khasawneh and D. Segalman, Applied Acoustics **151**, 215 (2019).

[65] J. H. Kang, Journal of Sound and Vibration **333**, 3332 (2014).

[66] E. J. Boyd and D. Uttamchandani, Journal of Microelectromechanical Systems **21**, 243 (2012).

[67] J. J. Hall, Physical Review **161**, 756 (1967).

[68] *What is fea | finite element analysis? documentation | simscale*, (2021) https://www.simscale.com/docs/simwiki/fea-finite-element-analysis/what-is-fea-finite-element-analysis/.

[69] G. Giraldo, *Fea for beginners – finite element analysis | simscale*, (2020) https://www.simscale.com/blog/fea-for-beginners/.

[70] *Comprehensive introduction to physics, pdes, and numerical modeling*, (2019) https://www.comsol.com/multiphysics/introduction-to-physics-pdes-and-numerical-modeling.

[71] *The finite element method (fem)*, (Mar. 2019) https://www.comsol.com/multiphysics/finite-element-method?parent=physics-pdes-numerical-042-62.

[72] S. P. Chaphalkar, S. N. Khetre, and A. M. Meshram, American Journal of Engineering Research (AJER) **4**, 178 (2015).

[73] A. Dutt, SSRG International Journal of Mechanical Engineering **2**, 8 (2015).

[74] *Structural mechanics module user's guide* (Comsol Multiphysics, 2017).

[75] *What is structural mechanics? - an introductory guide*, (Apr. 2018) https://www.comsol.com/multiphysics/introduction-to-structural-mechanics.

[76] W. M. Visscher, A. Migliori, T. M. Bell, and R. A. Reinert, The Journal of the Acoustical Society of America **90**, 2154 (1991).

[77] B. Ramshaw, "Shubnikov-de haas measurements and the spin magnetic moment of $yba_2cu_3o_{\{}6.59\}$" (The University of British Columbia, July 2012).

[78] G. Leibfried and W. Ludwig, Solid State Physics - Advances in Research and Applications **12**, 275 (1961).

[79] B. T. Bernstein, Physical Review **132**, 50 (1963).

[80] Y. P. Varshni, Physical Review B **2**, 3952 (1970).

[81] L. D. Landau and E. M. Lifshitz, *Statistical physics*, 3rd ed., Vol. 1 (Pergamon Press, 1980).

[82] S. Ghosh, "Resonant ultrasound investigations of correlated electron systems" (Cornell University, 2022).

[83] I. Utke, S. Moshkalev, and P. Russell, *Nanofabrication using focused ion and electron beams: principles and applications* (Oxford University Press, 2012).

[84] P. Li, S. Chen, H. Dai, Z. Yang, Z. Chen, Y. Wang, Y. Chen, W. Peng, W. Shan, and H. Duan, Nanoscale **13**, 1529 (2021).

[85] L. Gu, N. Wang, X. Tang, and H. G. Changela, Scanning **2020**, 8406917 (2020).

[86] L. A. Giannuzzi and F. A. Stevie, Micron **30**, 197 (1999).

[87] F. I. Allen, Beilstein Journal of Nanotechnology **12**, 633 (2021).

[88] M. Schleberger and J. Kotakoski, Materials **11**, 1885 (2018).

[89] A. Ul-Hamid, *A beginners' guide to scanning electron microscopy* (2018).

[90] N. Bassim, K. Scott, and L. A. Giannuzzi, MRS Bulletin **39**, 317 (2014).

[91] M. C. Lemme, D. C. Bell, J. R. Williams, L. A. Stern, B. W. Baugher, P. Jarillo-Herrero, and C. M. Marcus, ACS Nano **3**, 2674 (2009).

[92] V. Sidorkin, E. V. Veldhoven, E. V. D. Drift, P. Alkemade, H. Salemink, and D. Maas, JVST B: Microelectronics and Nanometer Structures **27**, 18 (2009).

[93] J. Yang, D. C. Ferranti, L. A. Stern, C. A. Sanford, J. Huang, Z. Ren, L.-C. Qin, and A. R. Hall, Nanotechnology **22**, 285310 (2011).

[94] J. M. D. Teresa, *Nanofabrication: nanolithography techniques and their applications*, edited by J. M. D. Teresa (2020).

[95] J. I. Goldstein, D. E. Newbury, J. R. Michael, N. W. M. Ritchie, J. Henry, J. Scott, and D. C. Joy, *Scanning electron microscopy and x-ray microanalysis*, 4th ed. (Springer, 2018).

[96] I. Utke, P. Hoffmann, and J. Melngailis, Journal of Vacuum Science and Technology B **26**, 1197 (2008).

[97] C.-S. Kim, S.-H. Ahn, and D.-Y. Jang, Vacuum **86**, 1014 (2012).

[98] M. Bachmann, "Manipulating anisotropic transport and superconductivity by focused ion beam microstructuring" (University of St Andrews, 2019).

[99] X. Huang, "Anisotropic and nonlinear transport in microstructured 3d topological semimetals" (Ecole Polytechnique Fédérale de Lausanne, 2022).

[100] S. N. Raman, F. Paul, J. S. Hammond, K. D. Bomben, and D. F. Paul, Microscopy Today **19**, 12 (2011).

[101] E. R. A. van Hove, D. F. Smith, and R. M. Heeren, Journal of Chromatography A **1217**, 3946 (2010).

[102] N. S. Smith, J. A. Notte, and A. V. Steele, MRS Bulletin **39**, 329 (2014).

[103] L. Bischoff, P. Mazarov, L. Bruchhaus, and J. Gierak, Applied Physics Reviews **3**, 021101 (2016).

[104] R. G. Forbes, Vacuum **48**, 85 (1997).

[105] L. Giannuzzi and F. A. Stevie, *Introduction to focused ion beams: instrumentation, theory, techniques and practice* (2005).

[106] K. Eder, V. Bhatia, J. Qu, B. V. Leer, M. Dutka, and J. M. Cairney, Ultramicroscopy **228**, 113334 (2021).

[107] B. Gault, A. J. Breen, Y. Chang, J. He, E. A. Jägle, P. Kontis, P. Kürnsteiner, A. K. D. Silva, S. K. Makineni, I. Mouton, Z. Peng, D. Ponge, T. Schwarz, L. T. Stephenson, A. Szczepaniak, H. Zhao, and D. Raabe, Journal of Materials Research, 10.1557/jmr.2018.375 (2018).

[108] R. Estivill, G. Audoit, J.-P. Barnes, A. Grenier, and D. Blavette, Microscopy and Microanalysis **22**, 576 (2016).

[109] K. Fisher and E. Marquis, Microscopy and Microanalysis **22**, 692 (2016).

[110] X. Zhong, C. A. Wade, P. J. Withers, X. Zhou, C. Cai, S. J. Haigh, and M. G. Burke, Journal of Microscopy **282**, 101 (2021).

[111] R. Córdoba, P. Orús, S. Strohauer, T. E. Torres, and J. M. D. Teresa, Scientific Reports **9**, 14076 (2019).

[112] E. S. Sadki, S. Ooi, and K. Hirata, Applied Physics Letters **85**, 6206 (2004).

[113] S. Smith, A. J. Walton, S. Bond, A. W. S. Ross, J. Tom, M. Stevenson, and A. M. Gundlach, IEEE Transactiosn on Semiconductor Manufacturing **16**, 199 (2003).

[114] G. Arnold, R. Timilsina, J. Fowlkes, A. Orthacker, G. Kothleitner, P. D. Rack, and H. Plank, ACS Publications **6**, 7380 (2014).

[115] D. J. Stokes, T. Vystavel, and F. Morrissey, Journal of Physics D: Applied Physics **40**, 874 (2007).

[116] M. Touzin, D. Goeuriot, C. Guerret-Piécourt, D. Juvé, D. Tréheux, and H.-J. Fitting, Jounal of Applied Physics **99**, 114110 (2006).

[117] A. A. Bizyukov, O. I. Girka, E. V. Romashchenko, K. N. Sereda, and N. N. Yunakov, ВАНТ **83**, 204 (2013).

[118] Y. Yabuuchi, S. Tametou, T. Okano, S. Inazato, S. Sadayama, Y. Yamamoto, K. Iwasaki, and Y. Sugiyama, Journal of Electron Microscopy **53**, 471 (2004).

[119] W. Li, R. Minev, S. Dimov, and G. Lalev, Applied Surface Science **253**, 5404 (2007).

[120] M. O. Román, Z. Wang, Q. Sun, V. Kalb, S. D. Miller, A. Molthan, L. Schultz, J. Bell, E. C. Stokes, B. Pandey, K. C. Seto, D. Hall, T. Oda, R. E. Wolfe, G. Lin, N. Golpayegani, S. Devadiga, C. Davidson, S. Sarkar, C. Praderas, J. Schmaltz, R. Boller, J. Stevens, O. M. R. González, E. Padilla, J. Alonso, Y. Detrés, R. Armstrong, I. Miranda, Y. Conte, N. Marrero, K. MacManus, T. Esch, and E. J. Masuoka, Remote Sensing of Environment **210**, 113 (2017).

[121] M. Carlowicz, *Night light maps open up new applications*, (2017) https://earthobservatory.nasa.gov/images/90008/night-light-maps-open-up-new-applications.

[122] A. Denisyuk, T. Hrní, J. V. Oboa, M. Petrenec, J. Michalika, T. Hrnčíř, J. V. Oboňa, and J. Michalička, Microscopy and Microanalysis **23**, 484 (2017).

[123] M. Haub, T. Günther, M. Bogner, and A. Zimmermann, Applied Sciences **11**, 11793 (2021).

[124] I. Utke, J. Michler, R. Winkler, and H. Plank, Micromachines **11**, 397 (2020).

[125] J. Gibson and R. A. Hein, Physical Review Letters **12**, 688 (1964).

[126] M. D. Bachmann, G. M. Ferguson, F. Theuss, T. Meng, C. Putzke, T. Helm, K. R. Shirer, Y. S. Li, K. A. Modic, M. Nicklas, M. König, D. Low, S. Ghosh, A. P. Mackenzie, F. Arnold, E. Hassinger, R. D. McDonald, L. E. Winter, E. D. Bauer, F. Ronning, B. J. Ramshaw, K. C. Nowack, and P. J. Moll, Science **366**, 221 (2019).

[127] S. Shim, H. Bei, M. K. Miller, G. M. Pharr, and E. P. George, Acta Materialia **57**, 503 (2009).

[128] D. Damjanovic, *The science of hysteresis*, edited by I. Mayergoyz and G. Bertotti, Vol. 3 (Academic, 2005), pp. 337–465.

[129] J. F. Tressler, S. Alkoy, and R. E. Newnham, Journal of Electroceramics **2** (1998).

[130] *A closer look at kinematic movement*, https://www.edmundoptics.com/knowledge-center/application-notes/optomechanics/a-closer-look-at-kinematic-movement/.

[131] R. Campbell, *The principle of kinematic constraint - practical precision*, (Feb. 2016) https://practicalprecision.com/kinematic-constraint/.

[132] *Optical mirror mount technology guide*, https://www.newport.com/n/optical-mirror-mount-technology-guide.

[133] R. Sandberg, W. Svendsen, K. Molhave, and A. Boisen, 10.1088/0960-1317/15/8/011 (2005).

[134] S. J. Rothberg, M. S. Allen, P. Castellini, D. D. Maio, J. J. Dirckx, D. J. Ewins, B. J. Halkon, P. Muyshondt, N. Paone, T. Ryan, H. Steger, E. P. Tomasini, S. Vanlanduit, and J. F. Vignola, Optics and Lasers in Engineering **99**, 11 (2017).

[135] *Principles of lock-in detection and the state of the art* (Zurich Instruments - White Paper, 2016).

[136] S. Margadonna, Y. Takabayashi, M. T. Mcdonald, M. Brunelli, G. Wu, R. H. Liu, X. H. Chen, and K. Prassides, Physical Review B **79**, 014503 (2009).

[137] A. Martinelli, A. Palenzona, M. Tropeano, M. Putti, C. Ferdeghini, G. Profeta, and E. Emerich, Physical Review Letters **106**, 227001 (2011).

[138] Y. Kamihara, T. Nomura, M. Hirano, J. E. Kim, K. Kato, M. Takata, Y. Kobayashi, S. Kitao, S. Higashitaniguchi, Y. Yoda, M. Seto, and H. Hosono, New Journal of Physics **12**, 033005 (2010).

[139] M. R. Cimberle, F. Canepa, M. Ferretti, A. Martinelli, A. Palenzona, A. S. Siri, C. Tarantini, M. Tropeano, and C. Ferdeghini, Journal of Magnetism and Magnetic Materials **321**, 3024 (2009).

[140] A. J. Drew, C. Niedermayer, P. J. Baker, F. L. Pratt, S. J. Blundell, T. Lancaster, R. H. Liu, G. Wu, X. H. Chen, I. Watanabe, V. K. Malik, A. Dubroka, M. Rössle, K. W. Kim, C. Baines, and C. Bernhard, Nature Materials 2009 8:4 **8**, 310 (2009).

[141] J. Vanhellemont, A. K. Swarnakar, and O. V. D. Biest, ECS Transactions **64**, 283 (2014).

[142] E. J. Ng, V. A. Hong, Y. Yang, C. H. Ahn, C. L. Everhart, and T. W. Kenny, Journal of Microelectromechanical Systems **24**, 730 (2015).

[143] A. E. Böhmer, "Competing phases in iron-based superconductors studied by high-resolution thermal-expansion and shear-modulus measurements" (Karlsruhe Institute of Technology, 2014).

[144] S. Simayi, K. Sakano, H. Takezawa, M. Nakamura, Y. Nakanishi, K. Kihou, M. Nakajima, C. H. Lee, A. Iyo, H. Eisaki, S. I. Uchida, and M. Yoshizawa, Journal of the Physical Society of Japan **82**, 10.7566/JPSJ.82.114604 (2013).

[145] C. Fujii, S. Simayi, K. Sakano, C. Sasaki, M. Nakamura, Y. Nakanishi, K. Kihou, M. Nakajima, C. H. Lee, A. Iyo, H. Eisaki, S. I. Uchida, and M. Yoshizawa, Journal of the Physical Society of Japan **87**, 074710 (2018).

[146] Z. A. Ren, W. Lu, J. Yang, W. Yi, X. L. Shen, Z. C. Li, G. C. Che, X. L. Dong, L. L. Sun, F. Zhou, and Z. X. Zhao, Chinese Physics Letters **25**, 2215 (2008).

[147] S. He, J. He, W. Zhang, L. Zhao, D. Liu, X. Liu, D. Mou, Y.-B. Ou, Q.-Y. Wang, Z. Li, L. Wang, Y. Peng, Y. Liu, C. Chen, L. Yu, G. Liu, X. Dong, J. Zhang, C. Chen, Z. Xu, X. Chen, X. Ma, Q. Xue, and X. J. Zhou, Nature Materials **12**, 605 (2013).

[148] R. M. Fernandes, A. V. Chubukov, and J. Schmalian, Nature Physics **10**, 97 (2014).

[149] J. Hu and C. Xu, Physica C: Superconductivity and its Applications **481**, 215 (2012).

[150] X. Chen, S. Maiti, R. M. Fernandes, and P. J. Hirschfeld, Physical Review B **102**, 184512 (2020).

[151] R. M. Fernandes, A. E. Böhmer, C. Meingast, and J. Schmalian, Physical Review Letters **111**, 137001 (2013).

[152] T.-M. Chuang, M. P. Allan, J. Lee, Y. Xie, N. Ni, S. L. Bud'ko, G. S. Boebinger, P. C. Canfield, and J. C. Davis, Science **327**, 181 (2010).

[153] C. Hess, H. Grafe, A. Kondrat, G. Lang, F. Hammerath, L. Wang, R. Klingeler, G. Behr, and B. Büchner, physica status solidi (b) **254**, 1600214 (2016).

[154] X. Hong, F. Caglieris, R. Kappenberger, S. Wurmehl, S. Aswartham, F. Scaravaggi, P. Lepucki, A. U. Wolter, H. J. Grafe, B. Büchner, and C. Hess, Physical Review Letters **125**, 067001 (2020).

[155] A. E. Böhmer, J.-H. Chu, S. Lederer, and M. Yi, Nature Physics **18**, 1412 (2022).

[156] Q. Si, R. Yu, and E. Abrahams, Nature Reviews Materials 2016 1:4 **1**, 1 (2016).

[157] H.-H. Wen and S. Li, Annual Review of Condensed Matter Physics **2**, 121 (2011).

[158] C. Putzke, "Fermi surface and quantum critical phenomena of high-temperature superconductors" (University of Bristol, July 2014).

[159] P. Carretta and G. Prando, La Rivista del Nuovo Cimento **43**, 1 (2020).

[160] R. M. Fernandes, A. I. Coldea, H. Ding, I. R. Fisher, P. J. Hirschfeld, and G. Kotliar, Nature **601**, 35 (2022).

[161] M. Rotter, M. Tegel, D. Johrendt, I. Schellenberg, W. Hermes, and R. Pöttgen, Physical Review B **78**, 020503 (2008).

[162] D. K. Pratt, M. G. Kim, A. Kreyssig, Y. B. Lee, G. S. Tucker, A. Thaler, W. Tian, J. L. Zarestky, S. L. Bud'ko, P. C. Canfield, B. N. Harmon, A. I. Goldman, and R. J. Mcqueeney, Physical Review Letters **106**, 257001 (2011).

[163] P. Cai, X. Zhou, W. Ruan, A. Wang, X. Chen, D.-H. Lee, and Y. Wang, Nature Communications **4**, 1596 (2013).

[164] T. Mertelj, P. Kusar, V. V. Kabanov, L. Stojchevska, N. D. Zhigadlo, S. Katrych, Z. Bukowski, J. Karpinski, S. Weyeneth, and D. Mihailovic, Physical Review B **81**, 224504 (2010).

[165] S. Avci, O. Chmaissem, D. Y. Chung, S. Rosenkranz, E. A. Goremychkin, J. P. Castellan, I. S. Todorov, J. A. Schlueter, H. Claus, A. Daoud-Aladine, D. D. Khalyavin, M. G. Kanatzidis, and R. Osborn, Physical Review B **85**, 184507 (2012).

[166] A. Thaler, N. Ni, A. Kracher, J. Q. Yan, S. L. Bud'ko, and P. C. Canfield, Physical Review B **82**, 014534 (2010).

[167] N. Ni, A. Thaler, A. Kracher, J. Q. Yan, S. L. Bud'ko, and P. C. Canfield, Physical Review B **80**, 024511 (2009).

[168] I. I. Mazin and J. Schmalian, Physica C: Superconductivity and its Applications **469**, 614 (2009).

[169] S. Acharya, D. Pashov, and M. V. Schilfgaarde, Physical Review B **105**, 144507 (2022).

[170] S. Lederer, Y. Schattner, E. Berg, and S. A. Kivelson, Physical Review Letters **114**, 097001 (2015).

[171] S. Lederer, Y. Schattner, E. Berg, and S. A. Kivelson, PNAS **114**, 4905 (2017).

[172] D. Labat and I. Paul, Physical Review B **96**, 195146 (2017).

[173] H. Yamase and R. Zeyher, Physical Review B **88**, 180502 (2013).

[174] K. Ishida, Y. Onishi, M. Tsujii, K. Mukasa, M. Qiu, M. Saito, Y. Sugimura, K. Matsuura, Y. Mizukami, K. Hashimoto, and T. Shibauchi, PNAS **119**, 10.1073/PNAS.2110501119 (2022).

[175] T. Worasaran, M. S. Ikeda, J. C. Palmstrom, J. A. W. Straquadine, S. A. Kivelson, and I. R. Fisher, Science **372**, 973 (2021).

[176] S. Nandi, M. G. Kim, A. Kreyssig, R. M. Fernandes, D. K. Pratt, A. Thaler, N. Ni, S. L. Bud'ko, P. C. Canfield, J. Schmalian, R. J. Mcqueeney, and A. I. Goldman, Physical Review Letters **104**, 057006 (2010).

[177] E.-G. Moon and S. Sachdev, Physical Review B **85**, 184511 (2012).

[178] J. P. Benoit, J. Berger, M. Krauzman, and J. L. Godet, J. Phsique **47**, 815 (1986).

[179] M. Yoshizawa, D. Kimura, T. Chiba, S. Simayi, Y. Nakanishi, K. Kihou, C. H. Lee, A. Iyo, H. Eisaki, M. Nakajima, and S. I. Uchida, Journal of the Physical Society of Japan **81**, 024604 (2012).

[180] A. E. Böhmer, T. Arai, F. Hardy, T. Hattori, T. Iye, T. Wolf, H. V. Löhneysen, K. Ishida, and C. Meingast, Physical Review Letters **114**, 027001 (2015).

[181] Y. Takabayashi, M. T. Mcdonald, D. Papanikolaou, S. Margadonna, G. Wu, R. H. Liu, X. H. Chen, and K. Prassides, Journal of American Chemical Society **130**, 9242 (2008).

[182] L. Ding, C. He, J. K. Dong, T. Wu, R. H. Liu, X. H. Chen, and S. Y. Li, Physical Review B **77**, 180510 (2008).

[183] *Smfeaso rt crystal structure*, (2016) https://materials.springer.com/isp/crystallographic/docs/sd_1723370.

[184] G. Prando, P. Carretta, R. D. Renzi, S. Sanna, A. Palenzona, M. Putti, and M. Tropeano, Physical Review B - Condensed Matter and Materials Physics **83**, 174514 (2011).

[185] D. M. Evans, J. A. Schiemer, T. Wolf, P. Adelmann, A. E. Böhmer, C. Meingast, S. E. Dutton, P. Mukherjee, Y.-t. Hsu, and M. A. Carpenter, Journal of Physics: Condensed Matter **31**, 135403 (2019).

[186] J. G. Bednorz and K. A. Miiller, Z. Phys. B-Condensed Matter **64**, 189 (1986).

[187] M. R. Norman and C. Pépin, Reports on Progress in Physics **66**, 1547 (2003).

[188] J. Schwartz, K. M. Amm, Y. R. Sun, and C. Wolters, Physica B: Condensed Matter **216**, 261 (1996).

[189] E. Fradkin and S. A. Kivelson, Nature Physics **8**, 864 (2012).

[190] S. I. Uchida, Journal of the Physical Society of Japan **90**, 111001 (2021).

[191] G. Ghiringhelli, M. L. Tacon, M. Minola, S. Blanco-Canosa, C. Mazzoli, N. B. Brookes, G. M. D. Luca, A. Frano, D. G. Hawthorn, F. He, T. Loew, M. M. Sala, D. Peets, M. Salluzzo, E. Shierle, R. Sutarto, G. A. Sawatzky, E. Weschke, B. Keimer, and L. Braicovic, Science **337**, 821 (2012).

[192] S. Gerber, H. Jang, H. Nojiri, S. Matsuzawa, H. Yasumura, D. A. Bonn, R. Liang, W. N. Hardy, Z. Islam, A. Mehta, S. Song, M. Sikorski, D. Stefanescu, Y. Feng, S. A. Kivelson, T. P. Devereaux, Z.-x. Shen, C.-c. Kao, W.-s. Lee, D. Zhu, and J.-s. Lee, Superconductivity **350**, 6263 (2015).

[193] J. Chang, E. Blackburn, A. T. Holmes, N. B. Christensen, J. Larsen, J. Mesot, R. Liang, D. A. Bonn, W. N. Hardy, A. Watenphul, M. V. Zimmermann, E. M. Forgan, and S. M. Hayden, Nature Physics **8**, 871 (2012).

[194] J. J. Wen, H. Huang, S. J. Lee, H. Jang, J. Knight, Y. S. Lee, M. Fujita, K. M. Suzuki, S. Asano, S. A. Kivelson, C. C. Kao, and J. S. Lee, Nature Communications **10**, 10.1038/s41467-019-11167-z (2019).

[195] M. R. Norman, D. Pines, and C. Kallin, Advances in Physics **54**, 715 (2005).

[196] J. L. Tallon and J. W. Loram, Physica C **349**, 53 (2001).

[197] C. Renner, B. Revaz, J.-Y. Genoud, K. Kadowaki, and Ø. Fischer, Physical Review Letters **80**, 149 (1998).

[198] D. C. Johnston, Physical Review Letters **62**, 957 (1989).

[199] W. W. J. Warren, R. E. Walstedt, G. F. Brennert, R. J. Cava, R. Tycko, R. F. Bell, and G. Dabbagh, Physical Review Letters **62**, 1193 (1989).

[200] A. A. Kordyuk, Low Temperature Physics **41**, 319 (2015).

[201] I. M. Vishik, W. S. Lee, R. H. He, M. Hashimoto, Z. Hussain, T. P. Devereaux, and Z. X. Shen, New Journal of Physics **12**, 105008 (2010).

[202] I. M. Vishik, Rep. Prog. Phys **81**, 62501 (2018).

[203] J. W. Loram, J. Luo, J. R. Cooper, W. Y. Liang, and J. L. Tallon, Journal of Physics and Chemistry of Solids **62**, 59 (2001).

[204] J. R. Cooper, J. W. Loram, I. Kokanovic, J. G. Storey, and J. L. Tallon, Physical Review B **89**, 201104 (2014).

[205] R. M. Fleming, B. Batlogg, R. J. Cava, and E. A. Rietman, Physical Review B **35**, 7191 (1987).

[206] T. P. Croft, "X-ray and neutron scattering studies of high-t c cuprate superconductors" (University of Bristol, 2016).

[207] S. Badoux, S. A. Afshar, B. Michon, A. Ouellet, S. Fortier, D. LeBoeuf, T. P. Croft, C. Lester, S. M. Hayden, H. Takagi, K. Yamada, D. Graf, N. Doiron-Leyraud, and L. Taillefer, Physical Review X **6**, 021004 (2016).

[208] J. Chang, C. Niedermayer, R. Gilardi, N. B. Christensen, H. M. Rønnow, D. F. Mcmorrow, M. Ay, J. Stahn, O. Sobolev, A. Hiess, S. Pailhes, C. Baines, N. Momono, M. Oda, M. Ido, and J. Mesot, Physical Review B **78**, 104525 (2008).

[209] M. Kofu, S.-H. Lee, M. Fujita, H.-J. Kang, H. Eisaki, and K. Yamada, 10.1103/PhysRevLett.102.047001 (2009).

[210] S. Wakimoto, G. Shirane, Y. Endoh, K. Hirota, S. Ueki, K. Yamada, R. J. Birgeneau, M. A. Kastner, Y. S. Lee, P. M. Gehring, and S. H. Lee, Physical Review B **60**, 769 (1999).

[211] B. Lake, H. M. Rønnow, N. B. Christensen, G. Aeppli, K. Lefmann, D. F. McMorrow, P. Vorderwisch, P. Smeibidl, N. Mangkorntong, T. Sasagawa, M. Nohara, H. Takagi, and T. E. Mason, Letters to Nature **415**, 299 (2002).

[212] H. Kimura, K. Hirota, H. Matsushita, K. Yamada, Y. Endoh, S.-H. Lee, C. F. Majkrzak, R. Erwin, G. Shirane, M. Greven, Y. S. Lee, M. A. Kastner, and R. J. Birgeneau, Physical Review B **59**, 6517 (1991).

[213] Y. Wang, L. Li, and N. P. Ong, Physical Review B **73**, 024510 (2006).

[214] N. P. Armitage, P. Fournier, and R. L. Greene, Reviews of Modern Physics **82**, 2421 (2010).

[215] J.-L. Luo, *Advances of theoretical and experimental research of high temperature cuprate superconductivity* (June 2020), pp. 1–26.

[216] N. Barisic, M. K. Chan, Y. Li, G. Yu, X. Zhao, M. Dressel, A. Smontara, and M. Greven, PNAS **110**, 12235 (2013).

[217] K. V. Pierre and Cenzual, eds., *Lasrcuo4 crystal structure*, accessed 2023-02-04, (2016) https://materials.springer.com/isp/crystallographic/docs/sd_0558839.

[218] M. Nohara, T. Suzuki, Y. Maeno, T. Fujita, I. Tanaka, and H. Kojima, Physical Review B **52**, 570 (1995).

[219] Y. Ando, G. S. Boebinger, A. Passner, L. F. Schneemeyer, T. Kimura, M. Okuya, S. Watauchi, J. Shimoyama, K. Kishio, K. Tamasaku, N. Ichikawa, and S. Uchida, Physical Review B **60**, 12475 (1999).

[220] P. Konsin and B. Sorkin, Physica C: Superconductivity and its Applications **460-462**, 989 (2007).

[221] J. W. Loram and K. A. Mirza, *Electronic properties of high-tc superconductors and related compounds*, edited by H. Kuzmany, M. Mehring, and J. Fink, Vol. 99 (Springer Berlin Heidelberg, 1990), p. 92.

[222] F. Gugenberger, C. Meingast, G. Roth, K. Grube, V. Breit, T. Weber, H. Wühl, S. Uchida, and Y. Nakamura, Physical Review B **49**, 13137 (1994).

[223] M. Nohara, T. Suzuki, Y. Maeno, T. Fujita, I. Tanaka, and H. Kojima, Physica C **235-240**, 1249 (1994).

[224] J. Nyhus, "Resonant ultrasonic system design, and measurements of critical behaviour and flux-line elasticity in high temperature superconductors" (Norwegian University of Science and Technology, 2000).

[225] G. Demazeau, A. Marbeuf, M. Pouchard, and P. Hagenmuller, Journal of Solid State Chemistry **3**, 582 (1971).

[226] J. K. Vassiliou, M. Hornbostel, R. Ziebarth, and F. J. Disalvo, Journal of Solid State Chemistry **81**, 208 (1989).

[227] G. Catalan, Phase Transitions **81**, 729 (2008).

[228] M. L. Medarde, Journal of Physics: Condensed Matter **9**, 77266 (1997).

[229] D. Li, K. Lee, B. Y. Wang, M. Osada, S. Crossley, H. R. Lee, Y. Cui, Y. Hikita, and H. Y. Hwang, Nature **572**, 624 (2019).

[230] G. A. Pan, D. F. Segedin, H. LaBollita, Q. Song, E. M. Nica, B. H. Goodge, A. T. Pierce, S. Doyle, S. Novakov, D. C. Carrizales, A. T. N'Diaye, P. Shafer, H. Paik, J. T. Heron, J. A. Mason, A. Yacoby, L. F. Kourkoutis, O. Erten, C. M. Brooks, A. S. Botana, and J. A. Mundy, Nature Materials **21**, 160 (2021).

[231] J. F. Mitchell, Frontiers in Physics **9**, 753 (2021).

[232] C. R. Kalaiselvi, N. Muthukumarasamy, D. Velauthapillai, M. Kang, and T. S. Senthil, Materials Letters **219**, 198 (2018).

[233] H. Xu, P. H. Chien, J. Shi, Y. Li, N. Wu, Y. Liu, Y. Y. Hu, and J. B. Goodenough, PNAS **116**, 18815 (2019).

[234] H. T. Zhang, T. J. Park, A. N. Islam, D. S. Tran, S. Manna, Q. Wang, S. Mondal, H. Yu, S. Banik, S. Cheng, H. Zhou, S. Gamage, S. Mahapatra, Y. Zhu, Y. Abate, N. Jiang, S. K. Sankaranarayanan, A. Sengupta, C. Teuscher, and S. Ramanathan, Science **375**, 533 (2022).

[235] A. S. Disa, T. F. Nova, and A. Cavalleri, Nature Physics **17**, 1087 (2021).

[236] S. Catalano, M. Gibert, J. Fowlie, J. Iñiguez, J. M. Triscone, and J. Kreisel, Reports on Progress in Physics **81**, 046501 (2018).

[237] Y. M. Klein, M. Kozłowski, A. Linden, P. Lacorre, M. Medarde, and D. J. Gawryluk, Crystal Growth and Design **25**, 4230 (2021).

[238] J. A. Alonso, M. J. Martínez-Lope, M. T. Casais, M. A. G. Aranda, and M. T. Fernández-Díaz, Journal of American Chemical Society **121**, 4754 (1999).

[239] J. A. Alonso, M. J. Martínez-Lope, M. T. Casais, J. L. Martínez, G. Demazeau, A. Largeteau, J. L. García-Muñoz, A. Muñoz, and M. T. Fernández-Díaz, Journal of American Chemical Society **11**, 2463 (1999).

[240] J. A. Alonso, M. J. Martínez-Lope, and I. Rasines, Journal of Solid State Chemistry **120**, 170 (1995).

[241] P. Lacorre, J. B. Torrance, J. Pannetier, A. I. Nazzal, P. W. Wang, and T. C. Huang, Journal of Solid State Chemistry **91**, 225 (1991).

[242] J. L. García-Muñoz, J. Rodríguez-Carvajal, P. Lacorre, and J. B. Torrance, Physical Review B **46**, 4414 (1992).

[243] S. Rosenkranz, M. Medarde, F. Fauth, J. Mesot, M. Zolliker, A. Furrer, U. Staub, P. Lacorre, R. Osborn, R. S. Eccleston, and V. Trounov, Physical Review B **60**, 14857 (1999).

[244] L. Korosec, M. Pikulski, T. Shiroka, M. Medarde, H. Luetkens, J. A. Alonso, H. R. Ott, and J. Mesot, Physical Review B **95**, 60411 (2017).

[245] S. J. Kim, M. J. Martinez-Lope, M. T. Fernandez-Diaz, J. A. Alonso, I. Presniakov, and G. Demazeau, Chemistry of Materials **14**, 4926 (2002).

[246] M. T. Fernández-Díaz, J. A. Alonso, M. J. Martínez-Lope, M. T. Casais, and J. L. García-Munoz, Physical Review B **64**, 144417 (2001).

[247] J. Rodríguez-Carvajal, S. Rosenkranz, M. Medarde, P. Lacorre, M. T. Fernandez-Díaz, F. Fauth, and V. Trounov, Physical Review B **57**, 456 (1998).

[248] J. B. Torrance, P. Lacorre, A. I. Nazzal, E. J. Ansaldo, and O. C. Niedermayer, Physical Review B **45**, 8209 (1992).

[249] J. A. Alonso, M. J. Martínez-Lope, I. A. Presniakov, A. V. Sobolev, V. S. Rusakov, A. M. Gapochka, G. Demazeau, and M. T. Fernández-Díaz, Physical Review B **87**, 184111 (2013).

[250] J. A. Alonso, M. J. Martínez-Lope, M. T. Casais, J. L. García-Muñoz, M. T. Fernández-Díaz, and M. A. Aranda, Physical Review B **64**, 094102 (2001).

[251] T. Mizokawa, D. Khomskii, and G. Sawatzky, Physical Review B **61**, 11263 (2000).

[252] I. I. Mazin, D. I. Khomskii, R. Lengsdorf, J. A. Alonso, W. G. Marshall, R. M. Ibberson, A. Podlesnyak, M. J. Martínez-Lope, and M. M. Abd-Elmeguid, Physical Review Letters **98**, 176406 (2007).

[253] H. Park, A. J. Millis, and C. A. Marianetti, Physical Review Letters **109**, 156402 (2012).

[254] A. Subedi, O. E. Peil, and A. Georges, Physical Review B **91**, 075128 (2015).

[255] J. Ruppen, J. Teyssier, O. E. Peil, S. Catalano, M. Gibert, J. Mravlje, J. M. Triscone, A. Georges, and D. V. D. Marel, Physical Review B **92**, 155145 (2015).

[256] I. Ardizzone, J. Teyssier, I. Crassee, A. B. Kuzmenko, D. G. Mazzone, D. J. Gawryluk, M. Medarde, and D. V. D. Marel, Physical Review Research **3**, 33007 (2021).

[257] S. W. Cheong and M. Mostovoy, Nature Materials 2007 6:1 **6**, 13 (2007).

[258] G. Giovannetti, S. Kumar, D. Khomskii, S. Picozzi, and J. V. D. Brink, Physical Review Letters **103**, 156401 (2009).

[259] N. A. Spaldin and R. Ramesh, Nature Materials **18**, 203 (2019).

[260] J. M. Perez-Mato, S. V. Gallego, L. Elcoro, E. Tasci, and M. I. Aroyo, Journal of Physics: Condensed Matter **28**, 286001 (2016).

[261] C. Xin, Y. Wang, Y. Sui, Y. Wang, X. Wang, Y. Su, K. Zhao, and X. Liu, Computational Materials Science **82**, 191 (2014).

[262] X. F. Hao, A. Stroppa, P. Barone, A. Filippetti, C. Franchini, and S. Picozzi, New Journal of Physics **16**, 015030 (2014).

[263] I. V. Nikulin, M. A. Novojilov, A. R. Kaul, S. N. Mudretsova, and S. V. Kondrashov, Materials Research Bulletin **39**, 775 (2004).

[264] J. Shi, S. D. Ha, Y. Zhou, F. Schoofs, and S. Ramanathan, Nature Communications **4**, 3676 (2013).

[265] M. Kawai, S. Inoue, M. Mizumaki, N. Kawamura, N. Ichikawa, and Y. Shimakawa, Applied Physics Letters **94**, 082102 (2009).

[266] I.-C. Tung, G. Luo, J. H. Lee, S. H. Chang, J. Moyer, H. Hong, M. J. Bedzyk, H. Zhou, D. Morgan, D. D. Fong, and J. W. Freeland, Physical Review Materials **1**, 53404 (2017).

[267] A. Malashevich and S. Ismail-Beigi, Physical Review B **92**, 144102 (2015).

[268] M. Kotiuga, Z. Zhang, J. Li, F. Rodolakis, H. Zhou, R. Sutarto, F. He, Q. Wang, Y. Sun, Y. Wang, N. A. Aghamiri, S. B. Hancock, L. P. Rokhinson, D. P. Landau, Y. Abate, J. W. Freeland, R. Comin, S. Ramanathan, and K. M. Rabe, PNAS **116**, 21992 (2019).

[269] M. Crespin, P. Levitz, and L. Gatineau, Journal of the Chemical Society, Faraday Transactions 2 **79**, 1181 (1983).

[270] M. J. Sayagués, M. Vallet-Regí, A. Caneiro, and J. M. González-Calbet, Journal of Solid State Chemistry **110**, 295 (1994).

[271] A. Vinante, Applied Physics Letters **105**, 32602 (2014).

[272] G. Pillai, S.-S. Li, and S. Member, IEEE Sensors Journal **21**, 12589 (2021).

[273] D. A. Czaplewski, S. Strachan, O. Shoshani, S. W. Shaw, and D. López, Applied Physics Letters **114**, 254104 (2019).

Amelia Estry

amelia.estry@epfl.ch
ameliaestry

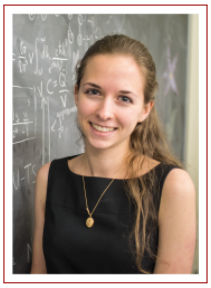

Education

2018-present **Ph.D.**, *Ecole Polytechnique Fédérale de Lausanne (EPFL)*, Lausanne, Switzerland, Laboratory of Quantum Materials
Thesis advisor: Prof. Philip Moll

2013-2017 **B.S. Physics**, *Florida State University (FSU)*, Tallahassee, Florida, USA, Summa Cum Laude
Minor in Mathematics

Research and Technical Experience

2018-present **Ph.D. Dissertation**, *EPFL*, Lausanne, Switzerland
- Developed novel technique to fabricate micro-scale cantilevers from challenging materials
- Designed and constructed measurement probe for low temperature (2K) and high magnetic field (16T) interferometry
- Conducted low-temperature and high magnetic field ultrasound studies on cantilevers built from quantum materials such as high-temperature unconventional superconductors

2017-2018 **Research Associate**, *Max Planck Institute for Chemical Physics of Solids*, Dresden, Germany
- Focused Ion Beam (FIB) fabrication of correlated electron systems for transport measurements

2014-2017 **Undergraduate Research Assistant**, *National High Magnetic Field Laboratory*, Tallahassee, FL, USA
- Constructed minimal vibration measurement probes for pulsed-magnetic fields
- Repaired and maintained laboratory equipment
- Analyzed data on correlated electron systems in high magnetic fields

2016 **Science Undergraduate Laboratory Internships (SULI) Intern**, *Ames National Laboratory*, Ames, IA, USA

- Synthesized heavy metal binary single and polycrystals using flux growth and arc-melting
- Identified materials through single-crystal and powder x-ray diffraction
- Conducted and analyzed magnetization and transport measurements

2015 **Research Experience for Undergraduations (REU) Intern**, *University of California, Davis*, Davis, CA, USA

- Characterized magnetic field drift of system used for Nuclear Magnetic Resonance (NMR) measurements, preventing the publication of faulty data
- Conducted NMR measurements on a topological material

2011-2013 **Instrument Repair Apprentice**, *DRF Music Studios*, Maitland, FL, USA

- Repaired woodwind and brass-wind musical instruments
- Studied the structure and design essential to producing high-quality sounds in wind instruments

Selected Honors and Awards

2017 **Lanutti Award for Undergraduate Research**, *FSU Department of Physics*

2017 **Marion Jewel Hay Award**, *FSU Phi Betta Kappa Honor Society*

2015 & 2016 **Goldwater Scholar, Honorable Mention**, *Bary Goldwater Scholarship and Excellence in Education Foundation*

2016 **Anna Runyan Award**, *FSU Department of Physics*

Languages

English, *Native*

German, *B1*

Computer Skills

Programming **Matlab, Labview**

Simulations **Comsol Multiphysics**

CAD **Autodesk Inventor**

Other **Latex, Photoshop, Illustrator, Microsoft Office**